
Doctoral Dissertations

Student Theses and Dissertations

Spring 2021

Evaluation of excavated surface irregularities and hardness of mechanical excavations and their relationship with excavator performance

Prosper Evaristus Akansah Ayawah

Follow this and additional works at: https://scholarsmine.mst.edu/doctoral_dissertations



Part of the [Geological Engineering Commons](#), and the [Mining Engineering Commons](#)

Department: Geosciences and Geological and Petroleum Engineering

Recommended Citation

Ayawah, Prosper Evaristus Akansah, "Evaluation of excavated surface irregularities and hardness of mechanical excavations and their relationship with excavator performance" (2021). *Doctoral Dissertations*. 2963.

https://scholarsmine.mst.edu/doctoral_dissertations/2963

This thesis is brought to you by Scholars' Mine, a service of the Missouri S&T Library and Learning Resources. This work is protected by U. S. Copyright Law. Unauthorized use including reproduction for redistribution requires the permission of the copyright holder. For more information, please contact scholarsmine@mst.edu.

EVALUATION OF EXCAVATED SURFACE IRREGULARITIES AND HARDNESS
OF MECHANICAL EXCAVATIONS AND THEIR RELATIONSHIP WITH
EXCAVATOR PERFORMANCE

by

PROSPER EVARISTUS AKANSAH AYAWAH

A DISSERTATION

Presented to the Graduate Faculty of the
MISSOURI UNIVERSITY OF SCIENCE AND TECHNOLOGY

In Partial Fulfillment of the Requirements for the Degree

DOCTOR OF PHILOSOPHY

in

GEOLOGICAL ENGINEERING

2021

Approved by:

Leslie Gertsch, Advisor
J. David Rogers
Norbert Maerz
Taghi Sherizadeh
VA Samaranayake

© 2021

Prosper Evaristus Akansah Ayawah

All Rights Reserved

ABSTRACT

This research involved lab and numerical excavation of a clastic sedimentary rock (Roubidoux Sandstone) using a long-bladed disc cutter in a Linear Rock Cutting Machine (LCM) with the aim of establishing relationships between the cutting parameters, excavated surface parameters (underbreaks, overbreaks and hardness), and performance parameters (specific energy and cutting rate). Three-dimensional cutting forces were recorded during the linear cutting. A structured laser imaging system was used to image the excavated surfaces for the estimation of the irregularities (ridge volumes (RV) and overbreak volumes (OV)). The excavated surface hardness was measured using the N-type Schmidt hammer. The numerical simulation was conducted in Itasca's Particle Flow Code 3D (PFC3D). It involved model calibration, a study of the effects of the cutting geometry and cutter scale on the cutting forces, validation of the models using the lab cutting data, and a study of the effects of cutter size on the cutting forces.

The results showed that the RV increased with increasing spacing-penetration (s-p) ratio for s-p ratios at which relieved cutting was achieved. However, the RV decreased with increasing s-p ratio under unrelieved cutting. The OV had a negative linear correlation with the s-p ratio under relieved cutting. In unrelieved cutting, the OV was independent of the s-p ratios. These findings can be used to determine the s-p ratio at which relieved cutting is first achieved. The specific energy decreased linearly with increasing surface hardness. The hardness was used together with the s-p ratio to develop a function for estimating SE. The numerical models yielded logarithmic functions for scaling forces from linear rock cutting simulations in PFC3D.

ACKNOWLEDGMENTS

The following individuals have been very instrumental in the completion of this research and I would like to acknowledge their contribution to this work. First, Dr. Leslie S. Gertsch, my academic advisor who was always ready to discuss any concepts that I thought of and suggested other ways that could yield better results. Her critical and rigorous evaluation of the outcomes of our experiments resulted in a more reliable research product. Second, the rest of my Ph.D. committee members, Dr. J. David Rogers, Dr. Norbert Maerz, Dr. Taghi Sherizadeh, and Dr. VA Samaranayake; thank you for your availability and contribution to the successful completion of this research. Third, thanks to Dr. Azupuri Kaba for the insightful discussions we had concerning this research. Thanks to Forsyth Kadingdi for the help during the lab experimentation phase of this work. I would also like to appreciate the family of Dr. Bruno Kansake. Charlotte, thanks very much for feeding me this whole time.

The contributions of the staff of the EMRGe center (formerly RMERC) cannot go unrecognized. Jeff Heniff, Fred, Stacey Fuller, thank you.

To my big family, especially my brother, Francis A. Akansah, and my mum, Victoria Ayawah; the motivation and moral support you gave me this whole time were immeasurable. Thanks for believing in me and cheering me on. I promise to keep making you proud. To all my friends who listened to me subtly complain without knowing that I'm complaining, thank you.

Finally, thanks to God for good health, inspiration, and good company. I couldn't have done it all by myself. Hallelujah!!!

TABLE OF CONTENTS

	Page
ABSTRACT.....	iii
ACKNOWLEDGMENTS	iv
LIST OF ILLUSTRATIONS	xii
LIST OF TABLES	xx
NOMENCLATURE	xxii
SECTION	
1. INTRODUCTION.....	1
1.1. INTELLECTUAL MERIT AND SIGNIFICANCE.....	3
1.2. OBJECTIVES.....	5
1.3. DISSERTATION ORGANIZATION	5
2. LITERATURE REVIEW.....	7
2.1. ROCK CUTTING.....	7
2.1.1. Cutting Tools.....	7
2.1.1.1. Drag bits.....	8
2.1.1.2. Roller cutters	9
2.1.2. Rock Fragmentation Mechanism by Indentation.	13
2.1.3. Linear Cutting Experiments.	17
2.1.3.1. Pressure distribution under the disc cutter.	23
2.1.3.2. Effect of confining stresses on cutting efficiency.....	24
2.1.4. Cutterhead Design	25

2.2. ROCK SURFACE HARDNESS	26
2.2.1. The Schmidt Hammer.	26
2.2.2. Rock Mass Characterization Using Schmidt Hammer Hardness.	28
2.2.3. Rock Hardness and Excavation.	29
2.3. ROUGHNESS OF EXCAVATED ROCK SURFACES	34
2.3.1. Measurement of Surfaces Roughness.....	34
2.3.2. Measurement of Overbreak and Underbreak in Excavations.....	40
2.3.3. Causes of Excavation Damage and Surface Roughness.	41
2.4. EXCAVATOR PERFORMANCE PREDICTION	43
2.4.1. Theoretical Models.....	43
2.4.2. Empirical Models from Field and Experimental Data.	47
2.4.3. Computational Models.	49
2.5. NUMERICAL MODELING OF ROCK EXCAVATION.....	50
2.5.1. Finite Element Methods and Rock Cutting.....	50
2.5.2. Discrete Element Methods and Rock Excavation.	51
2.5.2.1. Particle Flow Code (PFC).....	51
2.5.2.2. The flat-joint model (FJM) of PFC.....	52
2.5.2.3. Force-displacement law for the FJM.	53
2.5.3. Model Calibration.....	56
2.5.4. Size Effects and Scaling in Numerical Modeling.	58
2.5.5. Application of PFC in Rock Cutting Simulation.	61
3. ROCK SAMPLES, LAB EQUIPMENT, AND EXPERIMENTATION	65
3.1. ROCK SAMPLES	65

3.1.1. Rock Mechanical Properties.....	67
3.1.1.1. Uniaxial compressive strength.....	68
3.1.1.2. Measuring Young's modulus.....	68
3.1.1.3. Brazilian tensile strength.	68
3.1.2. Sample Preparation.....	70
3.2. LINEAR ROCK CUTTING MACHINE AND INSTRUMENTATION.....	72
3.2.1. The Cutter Assembly.....	73
3.2.2. Load Cells.....	75
3.2.3. Disc Cutter.....	75
3.2.4. Linear Displacement.....	77
3.2.5. Data Acquisition System.....	77
3.2.6. Schmidt Hammer.....	79
3.2.7. Laser Imaging System.....	79
3.3. EXPERIMENTAL SETUP AND EXECUTION.....	82
3.3.1. Instrument Calibrations.	82
3.3.1.1. Calibration of load cells.....	82
3.3.1.2. Calibration of string potentiometer.....	87
3.3.2. Linear Rock Cutting.	88
3.4. FRAGMENT SIZE ANALYSIS.....	90
3.5. IRREGULARITIES MEASUREMENT.....	91
3.5.1. Image Acquisition.	91
3.5.2. Processing of Surface Images.....	92
3.6. HARDNESS MEASUREMENT.....	93

4. NUMERICAL SIMULATIONS OF LINEAR ROCK CUTTING.....	96
4.1. THE PARTICLE FLOW CODE (PFC).....	96
4.1.1. Model Setup.	96
4.1.2. Boundary Conditions.....	98
4.1.3. Calibration of the Numerical Model.	99
4.1.4. The Cutting Tool.	102
4.2. THE NUMERICAL CUTTING SIMULATION	102
4.2.1. Experimental Design for the Simulation.....	105
4.2.2. Surface Irregularities from the Simulation Models.....	106
5. ROCK CUTTING EXPERIMENTAL RESULTS	107
5.1. ROCK CUTTING RESULTS	107
5.1.1. Cutting Forces.	107
5.1.2. Cutting Coefficient.	111
5.1.3. Specific Energy.	112
5.1.4. Instantaneous Cutting Rate.....	114
5.1.5. Cutting Efficiency.	115
5.1.6. Fragment Size Distribution.	116
5.1.6.1. Coarseness index.....	116
5.1.6.2. Large fragment percentage.	118
5.1.6.3. Absolute size constant (x') and distribution parameter (b).	119
5.2. SURFACE HARDNESS	121
5.3. SURFACE IRREGULARITIES.....	122
6. DISCUSSIONS OF LAB ROCK CUTTING RESULTS	126

6.1. PAIRWISE CORRELATION BETWEEN PARAMETERS.....	126
6.2. RELATIONSHIP BETWEEN CUTTING FORCES AND CUTTING GEOMETRY	130
6.2.1. Rolling, Normal, and Resultant Forces and Cutting Geometry.	130
6.2.2. Side Forces and Cutting Geometry.	135
6.3. SPECIFIC ENERGY, CUTTING EFFICIENCY, AND CUTTING GEOMETRY	137
6.3.1. Specific Energy and s-p Ratio.	137
6.3.2. Cutting Coefficient and s-p Ratio.....	139
6.4. INSTANTANEOUS CUTTING RATE	141
6.4.1. Instantaneous Cutting Rate and s-p Ratio.	141
6.4.2. Instantaneous Cutting Rate and Specific Energy.	142
6.4.3. Cutting Efficiency and s-p Ratio.....	144
6.5. UNDERBREAKS, OVERBREAKS, AND CUTTING GEOMETRY	145
6.5.1. Ridge Volume and s-p Ratio.	145
6.5.2. Ridge Volume and Specific Energy.	148
6.5.3. Overbreak Volume and s-p Ratio.....	149
6.5.4. Overbreaks and Specific Energy.	150
6.6. EXCAVATED SURFACE HARDNESS	150
6.6.1. Surface Hardness and s-p Ratio.....	150
6.6.2. Cutting Forces and Excavated Surface Hardness.....	153
6.6.3. Specific Energy and Excavated Surface Hardness.....	153
6.6.4. Specific Energy, s-p Ratio, and Surface Hardness.	154
6.6.5. Instantaneous Cutting Rate, s-p Ratio, and Surface Hardness.	158

7. RESULTS AND DISCUSSION OF NUMERICAL CUTTING SIMULATION.	161
7.1. MODEL SIZE AND CUTTING FORCES	162
7.1.1. Effect of the Cutting Geometry and Cutter Size Scale on the Cutting Forces.....	162
7.1.2. Effect of Scaling Spacing and Penetration at Constant s-p Ratio on Cutting Forces.....	165
7.1.3. Effect of Model Scale on Cutting Coefficient.....	168
7.1.4. Effect of the Cutter Tip Thickness on the Cutting Forces.....	169
7.2. CUTTING FORCES AND s-p RATIO	172
7.2.1. Effect of s-p Ratio on the Side Forces.....	172
7.2.2. Effect of s-p Ratio on the Rolling Forces	173
7.2.3. Effect of s-p Ratio on the Normal Forces.....	174
7.3. SURFACE IRREGULARITIES AND s-p RATIO	175
7.3.1. Effect of s-p Ratio on the Volume of Ridges.	176
7.3.2. Effect of s-p Ratio on the Volume of Overbreak.	178
8. CONCLUSIONS AND RECOMMENDATIONS.....	181
8.1. CONCLUSIONS	181
8.1.1. Relationships of Cutting Parameter.....	181
8.1.2. Relationship between Excavated Surface Parameters and Cutting Parameters.....	183
8.1.3. Numerical Simulations.	186
8.2. RECOMMENDATIONS.....	187
APPENDICES	
A. CALIBRATION OF 3D LOAD CELLS AND LVDT.....	189
B. LAB CUTTING FORCES DATA	199

C. NORMALITY AND OTHER STATISTICAL TESTS OF CUTTING PARAMETERS.....	203
D. NUMERICAL MODEL CUTTING FORCES	209
BIBLIOGRAPHY.....	211
VITA.....	223

LIST OF ILLUSTRATIONS

	Page
Figure 1.1. Modes of fracture development in mechanical rock excavation.	2
Figure 2.1. Modes of rock fragmentation by different cutting tools.....	8
Figure 2.2. Schematics of three main types of drag bits.	9
Figure 2.3. Disc cutters.	10
Figure 2.4. A schematic of a constant cross-section disc cutter with a zoom-in cutter ring on the right.....	11
Figure 2.5. Mode of cutting of conventional disc cutter (left) and undercutting disc cutters (right).	12
Figure 2.6. A typical undercutting operation in the field.....	12
Figure 2.7. Illustration of median crack propagation under a point-load with stress contours represented by dash arcs and the crack profile represented by the solid arc.	14
Figure 2.8. Illustration of stress distribution, and crack initiation and propagation under a wedge or conical indenter.	16
Figure 2.9. Relationship between boreability index and cutterhead penetration.....	19
Figure 2.10. Relationship between specific energy and cutter depth for different lithologies.....	20
Figure 2.11. A contour plot of normal forces associated with the three inner cuts (green arrows) showing a variation of forces without corresponding variation in cutting.	21
Figure 2.12. Plots of acoustic emissions and rolling force measured during a single cut showing high AE corresponding to force-drops.....	22
Figure 2.13. Postulated distribution of load under a disc cutter.	23
Figure 2.14. A 6.25 m diameter Robbins TBM with back-loading cutters.	25
Figure 2.15. Description of the N-type rock Schmidt hammer.....	27

Figure 2.16. Display of (a) settings of rock Schmidt (b) recorded hardness measurement.	27
Figure 2.17. Relationship between specific energy and Shore hardness.	30
Figure 2.18. Relationship between specific energy and Schmidt rebound hardness.	31
Figure 2.19. Relationship between optimum specific energy (SE) and Shore hardness. .	32
Figure 2.20. Relationship between optimum specific energy and coefficient of deformation.	32
Figure 2.21. Relationship between specific energy and rebound hardness.	33
Figure 2.22. Schematic of shadow profilometry setup.	35
Figure 2.23. Shadow profilometry.	36
Figure 2.24. Illustration of a 2D scene and shadowgram.	36
Figure 2.25. Reconstruction of a complex terrain from shadow data – the reconstructed surface on the left, and the original on the right.	37
Figure 2.26. A photo of a surface-scanning device.	38
Figure 2.27. Reconstruction of the summit craters of Piton de la Fournaise volcano using the SfM-MVS system.	39
Figure 2.28. Neptec 3D laser camera system in an underground setup.	39
Figure 2.29. A digitized image of a tunnel profile from an LSM image with the central light source as the reference point.	40
Figure 2.30. Relationship between rock mass quality, Q and (a) underbreak and (b) overbreak.	41
Figure 2.31. The effect of joint orientation of overbreaks percentage.	42
Figure 2.32. Linear pressure distribution under the disc cutter.	44
Figure 2.33. A plot of the CSM and AdjCSM model predictions against field data from the Queens water tunnel project.	48
Figure 2.34. Correlation between model predictions and observed FPI.	49
Figure 2.35. Illustration of the nature of the Flat-Joint model.	53

Figure 2.36. Numerical model calibration.	57
Figure 2.37. FJM calibration procedure.	58
Figure 2.38. A graded model used for rock cutting simulation.	62
Figure 2.39. Required thrust (left side) and torque (right side) for different joint orientations.	63
Figure 2.40. Thrust (left side) and torque (right side) required at different joint spacing.	63
Figure 3.1. Quartz grain of the Roubidoux Sandstone under the Mitutoyo Toolmaker's microscope.	65
Figure 3.2. A close-up view of the Roubidoux Sandstone sample with an iron nodule. ..	66
Figure 3.3. Roubidoux Sandstone with iron nodules and reddish banding.	66
Figure 3.4. Location of the Rosati quarry where the Roubidoux Sandstone was collected.	67
Figure 3.5. Setup for UCS test showing a failed 100 mm x 50 mm core.	69
Figure 3.6. Illustration of the determination of UCS and Young's modulus.	70
Figure 3.7. A block Roubidoux Sandstone.	71
Figure 3.8. Casting of rock in rock box.	71
Figure 3.9. Rock sample set to the rock table of the LRCM with indications of direction cutting and penetration.	72
Figure 3.10. Schematic of the full-scale linear rock cutting machine.	74
Figure 3.11. Cutter assembly.	74
Figure 3.12. A typical Omega LCHD-20K/N load cell.	75
Figure 3.13. Constant cross-section long-blade disc cutter and saddle donated by Robbins Company.	76
Figure 3.14. Schematic of disc cutter with force resolutions.	76
Figure 3.15. String potentiometer.	77
Figure 3.16. USB 6361 NBC DAQ module from National instruments.	78

Figure 3.17. Layout of the data acquisition system setup.....	78
Figure 3.18. Silver N-type Schmidt hammer.....	80
Figure 3.19. Schematic of the working principle of the Schmidt hammer.....	81
Figure 3.20. Setup for laser imaging with laser light and camera set at 45° in a perspective view.....	81
Figure 3.21. Schematic of rock surface imaging system in a side view.....	82
Figure 3.22. Setup for calibration of load cell 3.....	83
Figure 3.23. Free body diagram of load cells and cutter forces.....	84
Figure 3.24. Side view of the moment arms acting on the disc cutter.....	84
Figure 3.25. Setup for string potentiometer calibration.....	87
Figure 3.26. Illustration of cutting geometry, p – penetration.....	89
Figure 3.27. Set of Sieves for chip size analysis.....	90
Figure 3.28. Taking hardness measurements on the excavated rock surface.....	94
Figure 3.29. Illustration of hardness measurement locations on the surface of the excavated rock.....	95
Figure 4.1. Front view of a graded block model with fixed boundaries.....	97
Figure 4.2. Plan view of the block model with fixed boundaries.....	98
Figure 4.3. UCS versus axial strain from a UCS simulation of a synthetic rock core for the calibration of the model for the rock cutting simulations.....	100
Figure 4.4. Axial load versus axial displacement from a Brazilian strength test simulation of a synthetic rock disc for the calibration of the model for the rock cutting simulations.....	100
Figure 4.5. Flat-Joint model calibration procedure.....	101
Figure 4.6. Front and side views of the modeled disc cutter showing diameter and tip thickness.....	102
Figure 4.7. Three cutters cutting at a spacing of 30 mm and penetration of 4 mm.....	104

Figure 4.8. Flowchart of linear rock cutting simulation in PFC3D.	105
Figure 4.9. Digital elevation model of the excavated model surface free of dislodged particles– cutting at spacing 30 mm and penetration 5 mm.	106
Figure 5.1. Excavated rock surface with outline data window.	108
Figure 5.2. A typical trace of the cutting forces from a full-scale lab rock cutting test using a disc cutter at 76.2 mm spacing and 9.53 mm penetration.	110
Figure 5.3. Distribution of averaged rolling forces at different spacing-penetration ratios.	110
Figure 5.4. Distribution of averaged normal forces at different spacing-penetration ratios.	111
Figure 5.5. Distribution of averaged resultant forces at different spacing-penetration ratios.	111
Figure 5.6. Distribution of cutting coefficients at different spacing-penetration ratios..	112
Figure 5.7. Distribution of actual specific energy at different spacing-penetration ratios.	113
Figure 5.8. Distribution of instantaneous cutting rate at different spacing-penetration ratios.	114
Figure 5.9. Distribution of coarseness indexes at different spacing-penetration ratios..	118
Figure 5.10. Distribution of large fragment fraction at different spacing-penetration ratios.	118
Figure 5.11. Rosin-Rammler plot for determination of absolute size constant and fragment distribution parameter of pass 1 of penetration 6.35 mm.	120
Figure 5.12. Distribution of absolute size constants at different spacing-penetration ratios.	120
Figure 5.13. Distribution of excavated surface hardness at different spacing-penetration ratios.	122
Figure 5.14. Digital elevation model of pass 1 of penetration level 6.35 mm.	123
Figure 5.15. Distribution of volume of over-breaks on each pass over.	124
Figure 5.16. Distribution of volume of ridges on each pass over.	124

Figure 6.1. Pairwise correlation between cutting forces and fragment size parameters.	127
Figure 6.2. Pairwise correlation between cutting forces, hardness, and cutting rate.	128
Figure 6.3. Pairwise correlation between cutting energy, hardness, and fragment size parameters.	129
Figure 6.4. Relationship between cutting forces and spacing-penetration ratio.	131
Figure 6.5. Distribution of rolling forces at different s-p ratios.	134
Figure 6.6. Distribution of normal forces at different s-p ratios.	134
Figure 6.7. Distribution of resultant forces at different s-p ratios.	135
Figure 6.8. Relationship between side forces and s-p ratio.	136
Figure 6.9. Distribution of side forces at different s-p ratios.	136
Figure 6.10. Relationship between specific energy and spacing-penetration ratio.	138
Figure 6.11. Distribution of specific energy at different s-p ratios.	138
Figure 6.12. Relationship between cutting coefficient and s-p ratio.	140
Figure 6.13. Relationship between instantaneous cutting rate and s-p ratio.	141
Figure 6.14. Distribution of instantaneous cutting rate at different s-p ratios.	142
Figure 6.15. Relationship between linear or instantaneous cutting rate and specific energy.	143
Figure 6.16. Relationship between cutting efficiency and spacing-penetration ratio.	144
Figure 6.17. Distribution of ridge volume at different s-p ratios.	147
Figure 6.18. Illustration of deep unrelieved cutting having bigger ridges than shallow cutting.	147
Figure 6.19. Relationship between ridge volume and specific energy.	148
Figure 6.20. Distribution of overbreak volume at different spacing-penetration ratios.	149
Figure 6.21. Relationship between overbreak volume and specific energy.	150
Figure 6.22. Relationship between excavated surface hardness and s-p ratio.	151

Figure 6.23. Distribution of excavated surface hardness at different spacing-penetration ratios.....	152
Figure 6.24. Relationship between cutting forces and excavated surface hardness.	152
Figure 6.25. Relationship between excavated surface hardness and specific energy.	154
Figure 6.26. Relationship between specific energy, s-p ratio, and excavated surface hardness with the measured points and a modeled plane surface.	156
Figure 6.27. Relationship between specific energy and surface hardness within each s-p ratio.	156
Figure 6.28. Relationship between linear cutting rate, s-p ratio, and excavated surface hardness.....	159
Figure 6.29. Relationship between instantaneous cutting rate and excavated surface hardness.....	159
Figure 7.1. Cutting force traces from a simulation at spacing 30 mm and penetration 8 mm.....	161
Figure 7.2. Relationship between rolling forces and model scale with a plot of the full-scale lab LCM rolling force (blue square markers) and an extrapolated rolling force at a scaling factor of one (green X).	164
Figure 7.3. Relationship between normal forces and model scale with a plot of the full-scale lab LCM normal force (blue square markers) and an extrapolated normal force at a scaling factor of one (red X).....	164
Figure 7.4. Relationship between rolling forces and the scale of spacing and penetration at constant s-p ratio and different cutter sizes.	167
Figure 7.5. Relationship between normal forces and the scale of spacing and penetration at constant s-p ratio and different cutter sizes.	167
Figure 7.6. Relationship between cutting coefficient and the scale of spacing and penetration at constant s-p ratio and different cutter sizes.	168
Figure 7.7. Relationship between cutting coefficient and the cutter size.	169
Figure 7.8. Effect of cutter tip thickness on the cutting forces – obtained from numerical simulations.....	171
Figure 7.9. Relationship between the side forces and the spacing-penetration ratio – simulation.	173

Figure 7.10. Relationship between the rolling forces and the spacing-penetration ratio – simulation.	174
Figure 7.11. Relationship between the normal forces and the spacing-penetration ratio – simulation.	174
Figure 7.12. Relationship between ridge volume and s-p ratio at cut spacing 30 mm. ..	177
Figure 7.13. Relationship between ridge volume and s-p ratio at cut spacing 35 mm. ...	177
Figure 7.14. Relationship between overbreak volume and s-p ratio at cut spacing 30 mm.	179
Figure 7.15. Relationship between overbreak volume and s-p ratio at cut spacing 35 mm.	179
Figure 7.16. Illustration of deep relieved cutting having higher overbreak volume than shallow relieved cutting.	180

LIST OF TABLES

	Page
Table 2.1. Relationships between rock hardness and rock strength properties by different studies.....	29
Table 2.2. Rating of rock rebound hardness for excavatability classification.....	33
Table 3.1. Strength properties of the Roubidoux Sandstone.....	69
Table 3.2. Design of cutting process.....	89
Table 4.1. Properties of the Roubidoux Sandstone.....	99
Table 4.2. Microparameters for the synthetic rock model obtained through calibration.....	101
Table 4.3. Factorial experimental design.....	106
Table 5.1. Average and peak cutting forces, cutting coefficients, and specific energy per pass.....	109
Table 5.2. Instantaneous cutting rates and cutting efficiencies per pass.....	115
Table 5.3. Computation of coarseness index for pass 1 of penetration 6.35 mm.....	117
Table 5.4. Fragment size parameters.....	117
Table 5.5. Average surface hardness per cut at different penetrations.....	121
Table 5.6. Over-break and ridge volumes on each pass.....	125
Table 6.1. Analysis of variance results for the cutting forces at different s-p ratios.....	133
Table 6.2. Pairwise comparison of cutting forces at different s-p ratios.....	133
Table 6.3. Analysis of variance results for side forces at different s-p ratios.....	137
Table 6.4. Analysis of variance results for specific energy at different s-p ratios.....	139
Table 6.5. Pairwise comparison of specific energy at different s-p ratios.....	139
Table 6.6. Analysis of variance results for the instantaneous cutting rate at different s-p ratios.....	142

Table 6.7. Pairwise comparison of linear cutting rate at different s-p ratios.	142
Table 6.8. Analysis of variance of ridge volumes at different s-p ratios.	146
Table 6.9. Pairwise comparison of ridge volume at different s-p ratios.	146
Table 6.10. Analysis of variance of overbreak volume at different s-p ratios.	149
Table 6.11. ANOVA of excavated surface hardness at different s-p ratios.	153
Table 6.12. Pairwise comparison of excavated surface hardness at different s-p ratios.	153
Table 6.13. ANOVA of specific energy in relation to s-p ratio and surface hardness. ..	155
Table 6.14. Regression analysis with specific energy as the dependent variable.	157
Table 6.15. Analysis of variance of specific energy in relation to s-p ratio and surface hardness.	160
Table 7.1. Cutting forces at different model scales and from actual lab LCM rocking cutting.	163
Table 7.2. Average cutting forces at different spacing and penetration scales at a constant s-p ratio of 8.0.	166
Table 7.3. Cutting forces exerted by cutters with different thicknesses – simulation.	170
Table 7.4. Cutting forces at different spacing-penetration combinations.	172
Table 7.5. Underbreak and overbreak volumes at different spacing-penetration combinations.	175

NOMENCLATURE

Symbol	Description
BTS	Brazilian Tensile Strength
CC	Cutting coefficient
CCS	Constant Cross-Section
CE	Cutting efficiency
CI	Coarseness Index
F_N	Normal force (disc cutter)
F_R	Rolling force (disc cutter)
F_S	Side force (disc cutter)
ICR	Instantaneous cutting rate
LCM	Linear Rock Cutting Machine
LVDT	Linear Variable Differential Transducer
p	Cutter Penetration
s	Cut Spacing
s/p	Spacing to penetration Ratio
TBM	Tunnel Boring Machine
UCS	Uniaxial Compressive Strength
x'	Rosin-Rammler Absolute Size Constant
ρ	Rock Density
σ_c	Uniaxial Compressive Strength of Rock
σ_t	Brazilian Tensile Strength of Rock

1. INTRODUCTION

For millennia, mankind has manipulated the surface and near-surface of the earth to suit their interests. This manipulation includes excavation of earth materials, both soft (soil) and hard (rocks) using various means ranging from the use of simple tools and techniques to the use of very sophisticated machines and techniques. Until the 20th century, drill-and-blast has been the workhorse of the excavation industry (mining, tunneling, and construction). Various advancements have been made in this regard. Many other rock excavation methods have come into use in the face of those advancements. These excavation methods include thermal, electrical, pulsating laser, erosion, and mechanical methods. The use of water jets, which employs the mechanism of erosion for cutting and the use of mechanical tools have been successful and have gained popularity in recent times in the excavation industry (Ramezanzadeh and Hood, 2010). The popularity of mechanical excavation techniques in the excavation industry stems from high efficiency in large projects and are generally safer and more environmentally friendly (Vogt, 2016). Some of the machines that are used in mechanical rock excavation are roadheaders, continuous miners, longwall miners, impact hammers, tunnel boring machines (TBM), shearers, etc. (Vogt, 2016).

Generally, the principle of mechanical cutting is the application of thrust and rotary forces by the machine to induce fractures in the rock that coalesce to form chips that dislodge from the rock mass. Different cutting tools cause different fracturing mechanisms. One of these mechanisms is by indentation where disc cutters are pressed against the rock as they roll across the surface, inducing cracks in the rock, as shown in Figure 1.1a. Another

means of fracturing is achieved by plowing the rock surface with a conical or wedge-shaped bit causing a shearing action, as shown in Figure 1.1b. Various authors have hypothesized the formation of the fractures under different cutter types using laboratory experiments, empirical, and numerical methods. The brittleness and abrasiveness of the rock are factors considered in selecting the cutting tool for a given project.

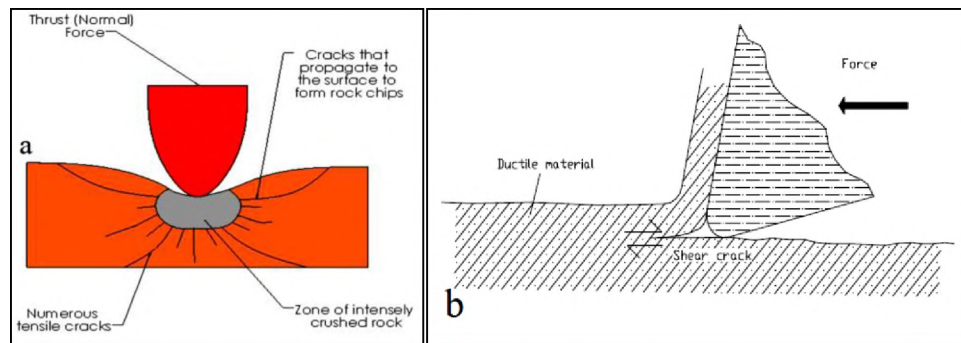


Figure 1.1. Modes of fracture development in mechanical rock excavation (Vogt, 2016).

Many other researchers (e.g., Rostami & Ozdermir, 1993; Balci, 2009; Khademi Hamidi et al., 2010; Hassanpour et al., 2011; Entacher et al., 2014; Rostami, 2016; Salimi et al., 2016) have tried to create a means to predict the performance of rock excavation machines. The researchers have, therefore, worked on finding easy-to-determine parameters that can be linked to excavation machine performance. Performance prediction is necessary for the optimization of excavation machines and cutting operations. Other researchers have worked on the optimization of excavator design parameters such as cutter spacing, thrust, and torque for various geologic conditions (e.g., Gertsch, 2000; Rostami, 2008; Han et al., 2017; Rostami & Chang, 2017).

Some of the methods in the literature for excavator performance evaluation were empirical and only applicable to the particular rock materials for which they were

developed. Others are more generic, but their input parameters were not easily obtainable, limiting the use of such models. Another concern is that most of these models tended to use intact rock properties. However, during rock cutting, the cutter mainly interacts with rocks that have been damaged by previous cutting. This damage causes changes in the mechanical and hydraulic properties of the rock. Therefore, using intact rock properties for predictions tend to result in errors.

In an effort to push the frontiers of knowledge in this area and address some of the issues outlined above, this research investigated the relationship between cutting parameters, excavated surface irregularities, and excavated surface hardness. The surface irregularities was measured in terms of the volume of underbreaks and overbreaks. Surface irregularities and hardness are direct properties of the damaged rock. Incorporation of these parameters into excavator performance evaluation is more realistic. However, in order to incorporate them, there was the need to first establish the relationship between these parameters and other cutting parameters. This research also evaluated the suitability of a three-dimensional numerical method, Particle Flow Code (PFC3D) for simulating linear rock cutting with the disc cutter. More sensitivity analysis can be conducted using validated numerical models. Such understanding is expected to enable more effective design and operation of rock excavation machines that use disc cutters as their cutting tools.

1.1. INTELLECTUAL MERIT AND SIGNIFICANCE

This research explored effective means of predicting the mechanical excavatability of rocks using surface and near-surface rock properties. Mechanical rock excavation has found favor in the mining and construction industries due to its efficiency (continuous

operation) in large projects and the general stability of the excavations that are made mechanically. In built-up locations, mechanical excavations are preferred over conventional drilling and blasting due to the vibration and noise caused by drill-and-blast excavation (Ramezanzadeh and Hood, 2010; Vogt, 2016). Since the inception of mechanical rock excavation, there has been a lot of research done to increase its efficiency by determining the optimum excavator parameters that are required for specific geological and operating conditions. Previous works have produced ways to predict the cutting forces and optimum machine parameters for rocks with various mechanical properties. Recent work by Kaba (2018) considered the surface hardness of the excavated surface as a means of predicting the cutter forces when drag picks were used as the cutting tools on an excavator. However, in Kaba (2018), the difference in resolution between the hardness data and the cutter forces data was vast, making the correlation difficult to assess. In this research, the resolution of the hardness data was increased, giving a better picture of the relationship between the surface hardness and other parameters.

No known previous research has related the irregularities of the excavated surface to the cutter forces or other cutting parameters like the cutting geometry. Rostami (2013) assumed a uniform surface when considering the pressure distribution under a disc cutter; however, the cutting surface is rarely uniform. It is believed that the unevenness of the rock surface will affect the pressure distribution, hence, the cutter forces. Therefore, consideration of excavated surface irregularities is an addition to the body knowledge and a possible improvement of the predictability of machine performance. The numerical simulations part of this research enabled sensitivity analysis for several parameters that are logistically expensive or impossible to conduct in laboratory testing. The results of this

research compare with recent research conducted on samples from the same rock (Roubidoux Sandstone) but using different cutting tools or cutting conditions (Abu Bakar, 2012 and Kaba, 2018).

1.2. OBJECTIVES

- This research aims to establish the relationships between:
 - The excavated rock surface hardness and instantaneous cutting rate
 - The excavated rock surface hardness and specific energy
 - The specific energy, excavated surface hardness, and cutting geometry
 - The excavated surface irregularities and the cutting geometry
- Compare the simulation results with those obtained from the lab to establish the suitability of numerical simulation for rock cutting experiments
- Establish relationships for upscaling cutting forces from numerical simulations for full-scale applications
- Develop a predictive model for specific energy and fragment involving excavated surface hardness and the cutting geometry

1.3. DISSERTATION ORGANIZATION

This dissertation was organized into eight sections introducing the research, describing the methods and results of the experiments conducted to achieve the stated objectives, and discussing the results. The dissertation layout is:

Section 1 – An exposition of the background for the research and its intellectual merits.

The objectives of the research and the layout of the dissertation are presented here.

Section 2 – A review of the literature relevant to this research was discussed in this section. It included the theory of rock fragmentation, the measurement of surface hardness using the Schmidt hammer, measurement and evaluation of excavation surface irregularities, and prediction of excavation machine performance.

Section 3 – This section described the linear rock cutting machine and all the instrumentations used to run the linear cutting tests. The rocking cutting procedure, surface hardness measurement, surface irregularities measurement, and the collection of data were also described here.

Section 4 – This section described the numerical model setup and calibration for the numerical linear rock cutting simulations. It also described the simulation of linear rock cutting.

Section 5 – The results from the lab tests were presented in this section in the form of charts and tables.

Section 6 – This section discussed the lab cutting forces, specific energy, instantaneous cutting rate, surface hardness, overbreaks, underbreaks, and their relationships among each other. Regression models for specific energy and instantaneous cutting rate were also discussed.

Section 7 – The results from the numerical simulations presented were discussed here, including the effects of the model scale on the cutting forces, effects of cutter thickness on the cutting forces, and the overbreak and underbreak volumes.

Section 8 – The major conclusions and limitations of the research were presented here. Recommendations for future research are also presented here.

2. LITERATURE REVIEW

This section reviewed previous research done in mechanical rock excavation relevant to the subject of this dissertation. Mechanical rock excavation has been an active area of research for the past century to improve excavation efficiency in the mining and civil engineering industries. The areas covered in this review included rock cutting and fragmentation mechanisms, excavated surface hardness, excavated surface irregularities, excavation machine performance prediction, and numerical simulation of linear rock cutting.

2.1. ROCK CUTTING

2.1.1. Cutting Tools. Generally, there are three main types of cutting tools used in mechanical excavation machines to execute mechanical rock fragmentation (Lislerud, 1997; Bilgin et al., 2014; Vogt, 2016). These are drag bits or picks, impact tools, and indenters including roller cutters (disc cutters). Disc cutters and drag picks are the commonly employed cutting tools in mechanical excavators like tunnel boring machines (TBMs), roadheaders, raise boring machines, continuous miners, mobile miners, etc.

Indenters and impact tools, like percussion tools, execute rock fragmentation through indentation. The tool exerts a load perpendicular to the surface of the rock, causing crushing directly beneath the tool and followed by dilation of the crushed material, resulting in the development of tensile stresses in the surrounding rock materials (Bilgin et al., 2014; Vogt, 2016). This eventually leads to tensile cracking (Figure 2.1a). Alternately, drag bits apply the load parallel to the surface of the rock, exerting shear

stresses, which initiate tensile cracking parallel to the rock surface (Figure 2.1b) (Hood and Alehossein, 2000; Bilgin et al., 2014).

According to Ramezanzadeh and Hood (2010), drag bits are more efficient than indenters in terms of specific energy. However, due to a higher susceptibility to wear and failure, drag bits are not suitable for hard and abrasive rocks. Using drag bits for cutting hard and abrasive rock will result in unnecessarily long and numerous machine downtime resulting in elongated project duration and cost.

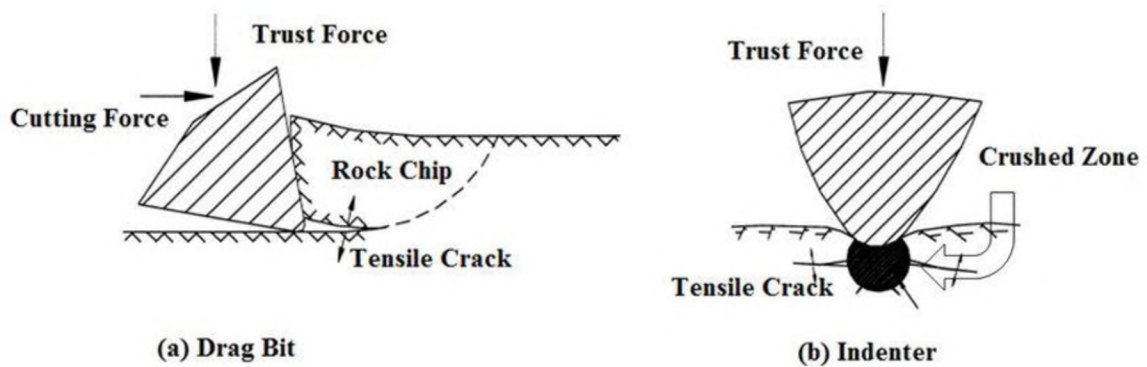


Figure 2.1. Modes of rock fragmentation by different cutting tools (Hood and Alehossein, 2000).

2.1.1.1. Drag bits. Due to the mode of fragmentation of drag bits, they are suited for cutting weak to moderate strength rocks with low abrasivity (Abu Bakar, 2012; Vogt, 2016). When the uniaxial compressive strength (UCS) of the rock is greater than 80 MPa, drag bits are unsuitable as cutting tools (Ramezanzadeh and Hood, 2010). The UCS limit is even lower for massive and abrasive rocks (Roxborough and Sen, 1986). This is because of frequent tool wear and failure. Drag bits are most suited for ductile rocks because ductile rocks are easier to break in shear than in tension (Ramezanzadeh and Hood, 2010). The

common machines that use different forms of drag bits include surface miners, roadheaders, trenchers, road planers, continuous miners, and drum shearers.

There are three subdivisions of drag bits—radial picks, point attack picks, and forward attack picks (Figure 2.2) (Summers, 1995). The radial pick is known to be the most efficient among the three in terms of specific energy though it has higher normal force requirements (Roxborough and Sen, 1986).

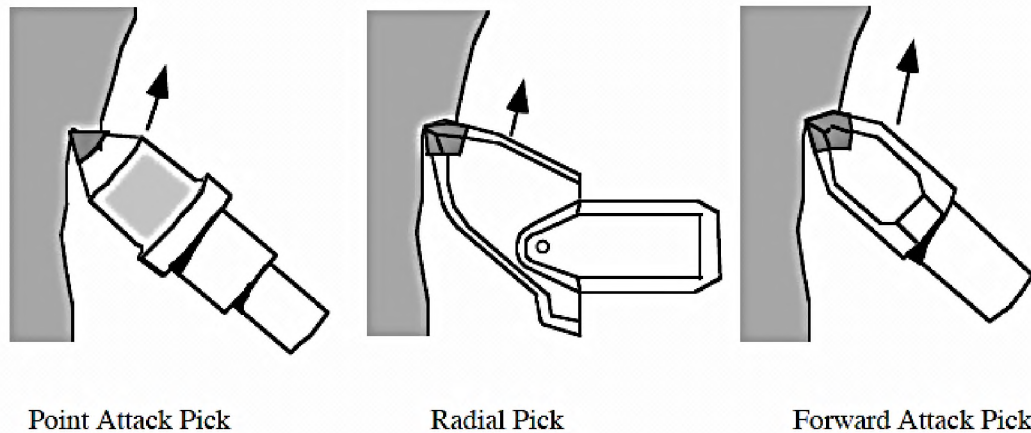


Figure 2.2. Schematics of three main types of drag bits (Summers, 1995).

2.1.1.2. Roller cutters. According to Plácido and Friant, (2004), the concept of roller cutters started in the petroleum industry. It was extended to full-face boring machines in the 1950s proving to be very efficient. Disc cutters became the main cutting tool for TBMs by 1980. Roller cutters are commonly used in TBMs, blind-hole drills, and raise and shaft borers (Abu Bakar, 2012). In the roller cutter, the generated heat load is distributed around the cutter circumference, thereby minimizing the level of wear and failure when compared to drag bits that have their tips in constant contact with the rock during cutting. This makes the roller cutter more suitable for cutting hard and abrasive rocks.

The disc cutters first used in full-face excavation machines had V-shaped disc tips (Plácido and Friant, 2004). They have high cutting efficiency when they are new, but wear out rapidly leading to a drastic drop in the efficiency due to increased force requirements for maintaining the level of penetration (Plácido and Friant, 2004; Abu Bakar, 2012). Due to the rapid wear and tear of V-shaped disc cutters, there have been several designs of disc cutters, including button disc cutters (Figure 2.3a), and constant cross-section (CCS) disc cutters (Figure 2.3b). However, these cutters do not have the same level of cutting efficiency as new V-shaped cutters, but they have longer life spans, thereby reducing machine downtime (Vogt, 2016). Constant cross-section cutters fall under a category of disc cutters known as single disc cutters. The other category is multi-row disc cutters on one shaft (e.g., double-disc cutters). Single disc cutters are known to be more efficient than multi-row disc cutters because the exerted thrust on the shaft is concentrated on one cutter, achieving deeper penetration, unlike the multi-row disc cutters where the thrust is distributed among two or more cutters (Ozdemir, 1995; Abu Bakar, 2012).

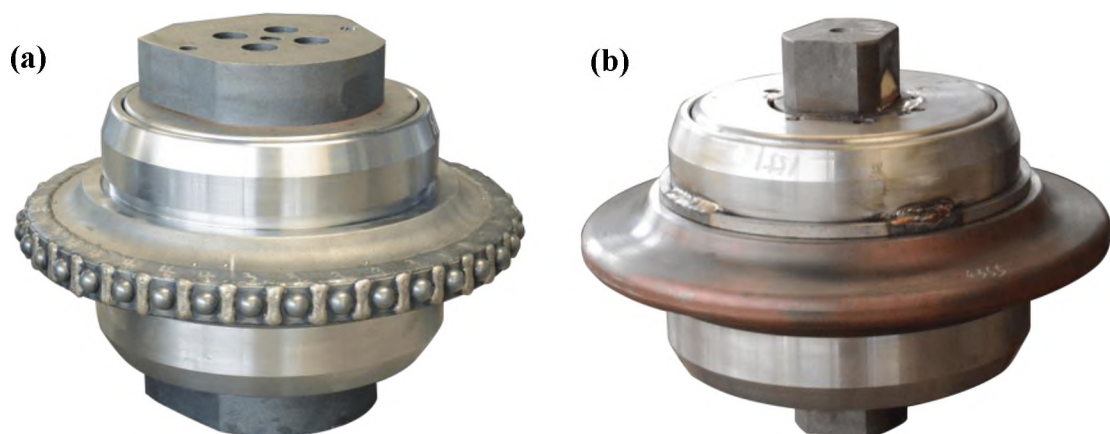


Figure 2.3. Disc cutters (a) Buttoned and (b) constant cross-section (USS, 2020).

The most common hard rock TBM cutting tool, the constant cross-section disc cutter, is composed of a replaceable cutter ring that fits on a hub (Figure 2.4). It has a shaft at the center of rotation surrounded by bearings that enable rotation of the cutter (Lin et al., 2019). The tip of the cutter ring has an almost constant cross-section yielding a balanced performance in terms of rock fragmentation and tool wear resistance. Tungsten carbides are sometimes used to make the ring tip for excavating extremely hard and abrasive rocks like fresh granite. According to Nelson (1993), the cutter tip width is typically 11-19 mm and can bear loads up to 270 kN.

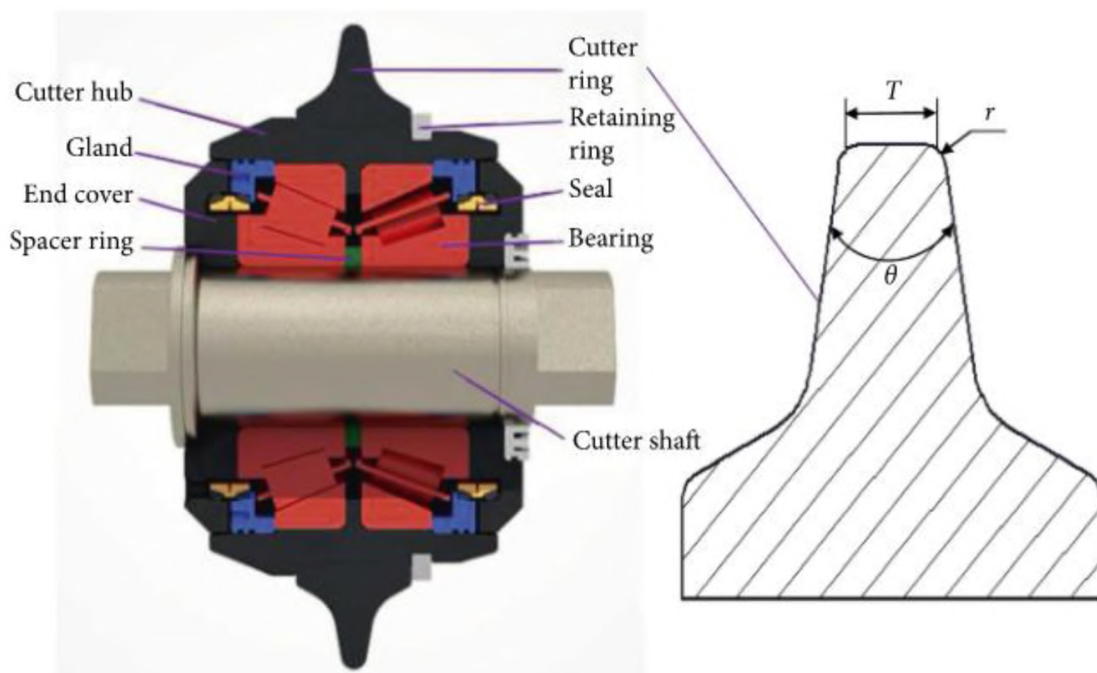


Figure 2.4. A schematic of a constant cross-section disc cutter with a zoom-in cutter ring on the right (Lin et al., 2019).

There have been modifications to disc cutters to undercut the rock, instead of indenting the rock perpendicularly. These modifications are said to be more efficient in

rock fragmentation because the generation of tensile cracks is more direct than the conventional indentation fragmentation (Ramezanzadeh and Hood, 2010) (Figure 2.5, Figure 2.6). Due to their mode of cutting, these tools are termed undercutting disc cutters.

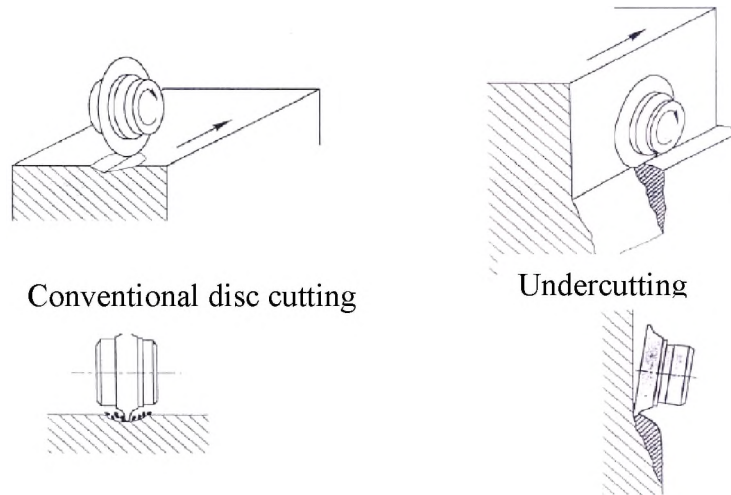


Figure 2.5. Mode of cutting of conventional disc cutter (left) and undercutting disc cutters (right) (Ramezanzadeh and Hood, 2010).



Figure 2.6. A typical undercutting operation in the field (Ramezanzadeh and Hood, 2010).

2.1.2. Rock Fragmentation Mechanism by Indentation. As mentioned in Section 2.1.1, rock fragmentation by disc cutters is achieved by indentation. The study of indentation in rocks was initiated by the theoretical studies of the stress fields under a point-load indenter (Boussinesq, 1885). The stress was studied in a half-space known as the Boussinesq field. Several researchers have followed with further theoretical, numerical, and experimental studies of the subject of rock fragmentation under indentation.

Paul and Sikarskie (1965) are researchers who attempted to explain the cracking process under a wedge indenter. They postulated that the Mohr-Coulomb failure criterion was critical and had to be satisfied for fracturing to occur under indentation. Their work was extended by Benjumea and Sikarskie (1969) to include the effects of anisotropies and heterogeneities like bedding planes. They also studied the effect of the wedge angle of the indenter and concluded that at wedge angles greater than 120° , the exerted load was dissipated through grain crushing, rather than chip formation.

In 1982, Lindqvist applied the principles of fracture mechanics to study fracturing under indentation. The length of the generated median crack was also investigated in relation to the indentation load (Figure 2.7). The following relationship was formulated (Eq. 2.1).

$$C = F \left(\frac{\psi(v)}{2\Gamma} \right) \left(\frac{\alpha}{\beta^2} \right) \left(\frac{H}{E} \right) \quad (2.1)$$

Where C – length of median crack;

F – applied load, kN;

$$\psi(v) = (1 - v^2)(1 - v)^2 / 2\pi^2 ;$$

v – Poisson's ratio;

Γ – crack surface energy, J/m²;

H – hardness;

E – Young's modulus, GPa;

α – rock constant;

$$\beta = z_0/a;$$

z_0 – depth of indentation, mm; and

a – indenter radius, mm (Lindqvist, 1982).

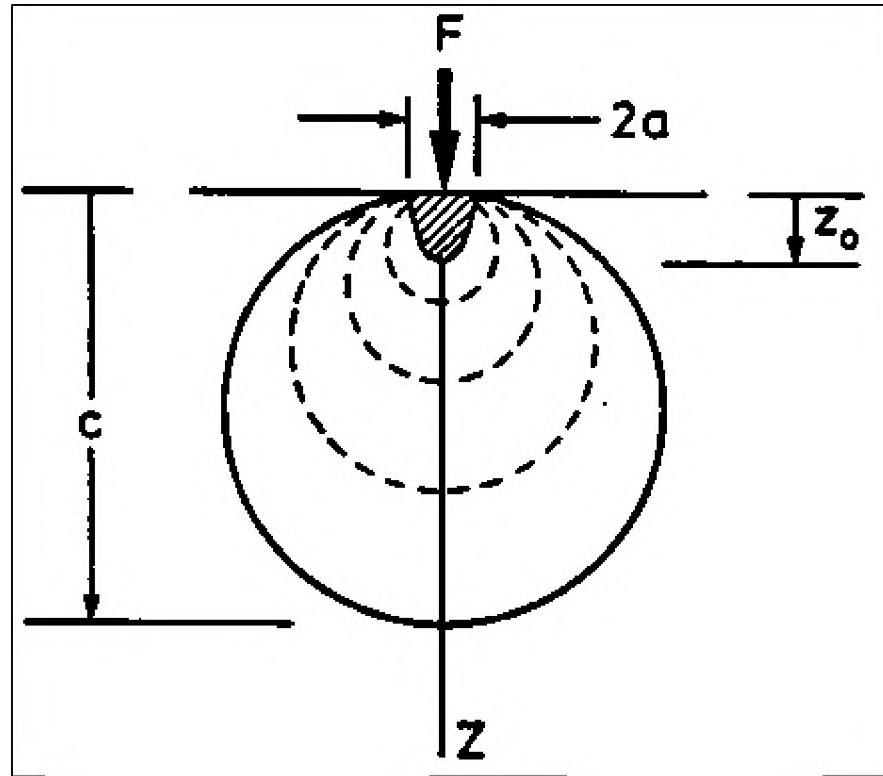


Figure 2.7. Illustration of median crack propagation under a point-load with stress contours represented by dash arcs and the crack profile represented by the solid arc. The hatched section is the inelastic zone (Lawn and Swain, 1975; Lindqvist, 1982).

Cook et al. (1984) also conducted lab indentation experiments on cores of the Seirra Granite using different sizes of circular flat-bottomed indenters. They discovered that

below 45% of the ultimate load, the rock deformed elastically but started to develop cracks as the load exceeded 45% of the ultimate load. They observed that the cracks initiated around the perimeter of the punch created by the indenter. According to the authors, the following relationship (Eq. 2.2) exists between the exerted normal stress and the indenter penetration depth.

$$\sigma_n = \frac{Ep}{0.54(1 - \nu^2)a} \quad (2.2)$$

Where σ_n – normal stress under indenter, kPa;

E – Young's modulus, GPa;

p – average indenter displacement;

ν – Poisson's ratio; and

a – indenter cross-sectional area, mm².

Cook et al.'s (1984) model was followed by Pang et al. (1989) who postulated relationships for estimating normal indentation forces when using wedge and conical indenters (Eqs. 2.3 and 2.4, respectively). They also noted that the Mohr-Coulomb criterion overestimated the required forces for chip formation.

$$F = \sigma_0(\sin\theta + \mu\cos\theta) \left(\frac{2wx}{\cos\theta} \right); \text{ Wedge} \quad (2.3)$$

$$F = \left[\sigma_0(\sin\theta + \mu\cos\theta) \left(\frac{\pi\tan\theta}{\cos\theta} \right) \right] x^2; \text{ Conical} \quad (2.4)$$

Where F – normal force;

σ_0 – constant stress in crushed zone;

θ – half-cone angle;

w – indenter width; and x – indentation depth.

More recently, Zhang et al. (2003) took cores from the bottom and side of a tunnel, and they measured the length of lateral and median cracks generated by a button roller cutter using a scanning electron microscope. They also measured the cutting forces and concluded that there was a relationship between the normal forces and the length of the median cracks. The length of the median crack increased with increasing normal force.

Entacher et al. (2014) studied the crack pattern during rock cutting. They observed prominent median cracks close to the edge of the rock block but no median cracks at the center where the confinement is higher. Based on this, the researchers believed that the role of the median cracks was overemphasized in previous research, such as Rostami & Ozdermir (1993) who illustrated a dominant role of the median crack in rock cutting. Gertsch (2000) had similar observations where confined rocks (semi-infinite surface) did not produce any median cracks, and the cemented core of the same rock produced median cracks. It was also noted that lateral cracks tended to increase in subsequent cuts due to the free face created by the previous cut.

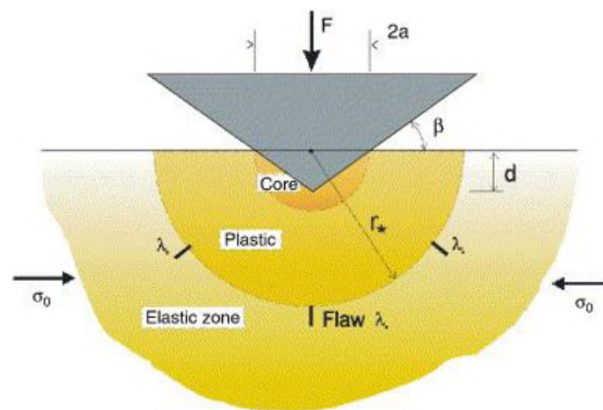


Figure 2.8. Illustration of stress distribution, and crack initiation and propagation under a wedge or conical indenter (β – wedge angle, σ_0 – confining stresses, λ – initiating cracks, r – crushed zone radius, d – depth of penetration of indenter) (Chen and Labuz, 2006).

In summary, all the work that has been done in rock fragmentation by indentation points to the following: the presence of a crushed zone directly under the tip of the cutter or indenter with an inner core (Figure 2.8). This zone behaves plastically and transfers the load from the indenter or cutter to the surrounding rock—the elastic zone. As the built-up stress in the rock exceeds its tensile strength, radial cracks begin to form. The initiation of cracks is facilitated by the presence of inherent flaws in the rock. The radial cracks are propagated deep into the rock, and some bend toward the surface as the load continues to increase. When these cracks coalesce or daylight, a chip is formed and dislodges from the surface of the rock. The crushing and chipping processes are accompanied by the release of built-up stresses. This results in saw-tooth shaped force profiles during loading representing the sequence of force or stress build-up and releases through crushing and chipping.

2.1.3. Linear Cutting Experiments. Roxborough and Philips (1975) conducted linear rock cutting experiments using disc cutters to investigate the influence of five principal parameters on excavation performance in the Bunter Sandstone. The parameters studied were the disc diameter, depth of penetration, cutter edge angle, cutting speed, and spacing between cuts. Five treatments of each parameter were conducted. It was observed that the normal force increased with increasing disc diameter, while the rolling force remained constant. For penetration, both normal and rolling forces increased with increasing depth of penetration, but the rate of increase of the normal force was greater than that of the rolling force. The effect of the edge angle on the cutting forces is similar to that of the depth of penetration. Increasing the edge angle increased the cutting forces. This corresponded with the results of the theoretical analysis. The study also revealed that the

cutting speed (between 76 and 178 mm/s) does not affect the cutting forces, yield, and specific energy. This was consistent with the behavior of other cutting tools. Both normal and rolling forces increased with increasing cut spacing, showing a power curve. This behavior is attributed to an interaction between adjacent cuts. They found the spacing-penetration (s-p) ratio at which interaction ceased to be 7.0 and observed slabbing occurring between s-p ratios of 3 and 7.

Balci (2009) conducted lab experiments on limestone and shale with a linear rock cutting machine (LCM). His study was connected with a tunneling project in Turkey. In his study, he used a constant cut spacing and varied the penetration at three levels under relieved cutting and at four levels under unrelieved cutting. The cutting forces obtained from the experiments were used to estimate the optimum TBM geometry and parameters for the rock formations studied. The normal force and rolling forces were used to estimate the machine thrust and torque, respectively. According to the author, the side forces were used in conjunction with the normal and rolling forces to balance the cutterhead. He obtained an optimum penetration of 8 mm for both rock types at a cutting spacing of 80 mm, thus an optimum s-p ratio of 10. The selection of 80 mm spacing is per industry practice. For both rock types, the normal and rolling forces both increased with increasing penetration, even though this phenomenon was not observed in the field data from the tunnel for which the LCM cutting experiments were conducted. He explained that the rock mass in the field was highly fractured and contained dykes, which resulted in collapses and chunking, respectively. As a result, it was observed that the cutting forces in the field did not show any unique trend with increasing penetration. He stated that the thrust, cutterhead torque, cutterhead power, and the number of cutters determined from the LCM experiments

compared favorably the actual TBM design parameters. The specific rock mass boreability index (SRMBI) is defined by Gong et al. (2007) as the boreability index (ratio of the average net thrust per cutter to the penetration per cutterhead revolution) at 1 mm/rev penetration rate was also studied in the field and the lab. The boreability indexes were fitted with power functions (Figure 2.9). The SRMBIs for the field data were higher than those obtained in the lab experiments (Figure 2.9). The explanation given for this was the highly fractured nature of the field rock mass, unlike the lab samples, which were intact rocks. He concluded that the SRMBI is a good measure for performance prediction but cautioned that large data should be accumulated before it can be used.

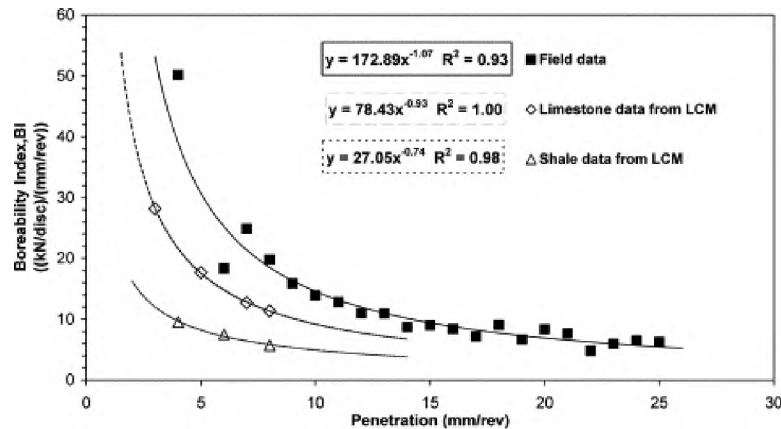


Figure 2.9. Relationship between boreability index and cutterhead penetration (Balci, 2009).

Balci and Tumac (2012) investigated the cuttability of different rocks—shale, arkose, and fossilized limestone—using v-shaped disc cutters. The rocks were said to have similar strength properties but different structural and textural fabric. Though the strength properties were similar, different cuttabilities were recorded for the three rock types (Figure 2.10), which were attributed to the structural and textural differences. They opined that using only strength parameters for theoretical models does not give accurate predictions.

They also compared the v-shaped cutter to the CCS cutter and concluded that for medium to soft, non-abrasive rock formations, the v-shaped cutter is a more efficient tool than the CCS cutter. The cutting forces increased with increasing penetration accompanied by decreasing specific energy.

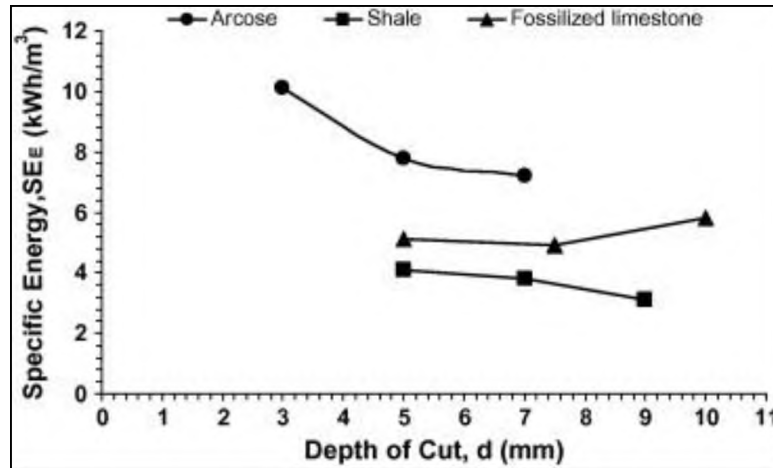


Figure 2.10. Relationship between specific energy and cutter depth for different lithologies (Balci and Tumac, 2012).

Entacher et al. (2014) considered a smaller scale linear rock cutting machine for TBM performance prediction. Their motivation was that the small-scale linear cutting tests are cheaper, less time-consuming, and the size of rock specimens required are easier to acquire compared to the full-scale rock block. They compared the small-scale test results with the full-scale cutting test results and results obtained from the Colorado School of Mines (CSM) model; they concluded that the CSM model results deviated largely from the test results for certain lithologies. They suggested that the discrepancy with the CSM model was in the input parameters, UCS and BTS. They concluded that cutting forces from scaled LCM tests are good alternative input parameters for TBM performance prediction models, instead of using intact rock properties (UCS and BTS) as input parameters.

Another study involving full-scale and small-scale rock cutting experiments was conducted by Entacher et al. (2014). The experiments were performed on the Brixen Granite and it was observed that low or high cutting forces from a pass corresponded with the opposite in the previous pass or subsequent. They plotted the distribution of the normal forces experienced over the whole block and obtained a non-uniform distribution of forces (Figure 2.11). They, therefore, asserted that a major fraction of the forces cannot be attributed to chip formation because the excavated volume is generally uniform, while the forces vary greatly. Gertsch (2000) earlier observed that many saw-tooth force wave-forms were not accompanied by chip formation. It is believed that most of the energy is consumed in crushing the zone directly beneath the cutter, and just a small percentage (about 3-15 %) contributes to crack propagation.

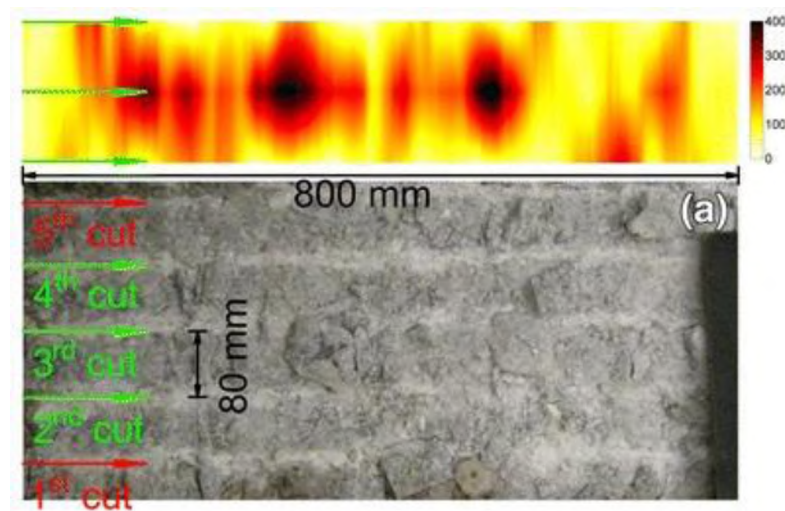


Figure 2.11. A contour plot of normal forces associated with the three inner cuts (green arrows) showing a variation of forces without corresponding variation in cutting (Entacher et al. 2014).

Entacher et al. (2014) tested the hypothesis that a small fraction of the cutting forces resulted in chip formation by recording the acoustic emissions (AE) during the cutting and

compared them with the cutting forces. High acoustic emissions were observed at the force-drop points (Figure 2.12). Higher rates of force-drops had higher AE. Only eight chips were formed in the process with fully developed primary and secondary crushed zones. They concluded that the high rate of force-drops was associated with grain crushing rather than chip formation. Therefore, the saw-tooth nature of the force traces is mostly explained by crushing and partly by chip formation. A similar finding was obtained by Rojek et al. (2010) who analyzed the frequency spectrum of the cutting process. They observed that the areas of high frequency, which represent force-drops in the time domain, result from grain crushing.

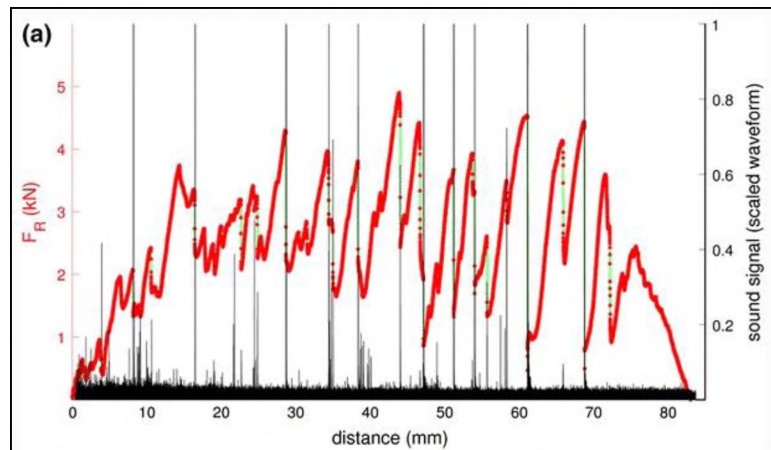


Figure 2.12. Plots of acoustic emissions and rolling force measured during a single cut showing high AE corresponding to force-drops (Entacher et al. 2014).

Qi et al., (2016) conducted lab experiments to determine the cutting forces and specific energies experienced by gauge cutters using a rotary cutting machine. They experimented with four angles of disc tilt the cutter, 0° , 10° , 20° , and 30° . It was observed that the cutting forces decreased with increasing tilt angle. This was attributed to the cutter-rock contact area decreasing with increasing tilt angle, as the tilted cutter had a sharper

edge in contact with the rock. The authors also observed that the specific energy increased with increased angle tilt.

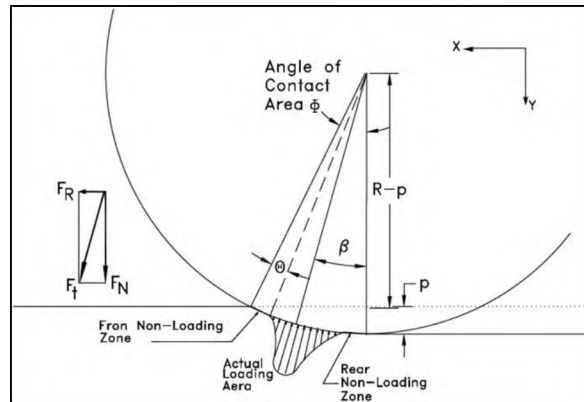


Figure 2.13. Postulated distribution of load under a disc cutter (Rostami, 2013).

2.1.3.1. Pressure distribution under the disc cutter. The pressure distribution under the disc cutter was previously theorized as a linear increasing profile where the contact pressure started from zero and increased to the maximum under the disc. However, according to Rostami (2013), a comparison of measured and calculated rolling coefficients for CCS disc cutters revealed that the pressure distribution under the cutter was not well represented by a linearly increasing function. He, therefore, set up experiments to determine the pressure distribution by installing strain gauges on the disc to measure the load distribution during cutting. After the cutting and analysis of the results, he discovered that the extent of the loading area was smaller than the nominal or theoretical contact area obtained from cutting geometry. It was observed that the loading was concentrated in the middle of the theoretical contact area (Figure 2.13). This implied that the front- and back-ends of the disc are no-load zones. The no-load zone at the back-end is supported by the observation of dust gushing from directly underneath the cutter in a direction opposite to

the cutting captured on a high-speed camera. He tested three rock types and noticed a general increase in the extent or span of the loading area with increased penetration. He postulated that the front-end no-loading zone represented the formation of chips and that the actual crushing or cutting occurred at the concentrated loading zone.

2.1.3.2. Effect of confining stresses on cutting efficiency. Ma et al. (2016) studied the influence of confining stresses on the cutting forces, cutting coefficient, and specific energy of a rock cutting machine in granitic rocks. Confining stresses of 5, 10, and 10 MPa were applied. According to their study, the normal forces increase with increased confinement stress for a given penetration. Studying the effect of directional confinement showed that the normal force is more sensitive to the confined stress perpendicular to the direction of cutting. The rolling force was not significantly sensitive to the confinement. The rolling force appeared to be more sensitive to the confining stress parallel to the direction of cutting. They found that the cutting coefficient decreased with increasing confinement. The specific energy decreased to a minimum and increased again when penetration increased, as expected. The optimum penetration for a constant spacing was found to increase with increasing confinement. This implies that for brittle rocks, higher confinements require higher thrust to obtain deeper penetration for efficient excavation. The thrust should, however, be within the limits of the cutter's bearing capacity.

Several other researchers conducted studies regarding the influence of confinement on the distribution of fractures in the rock under the disc cutter or indenter indentation (e.g., Cook et al., 1984; Pang and Goldsmith, 1990; Gertsch, 2000; Chen and Labuz, 2006; Innaurato et al., 2006; Entacher et al., 2014; and Yin et al., 2014). All these studies pointed to the fact that the presence of the median crack depends on the level of confinement. At

low or no confinement, the median crack is always prominent and disappears gradually as the confinement increases. Higher confinement tends to produce more lateral cracks than median cracks.

2.1.4. Cutterhead Design The tunnel boring machine (TBM) has been in existence since the mid-19th century and became a major part of the tunneling industry in the 1950s. It has become a method of choice for projects with tunnels longer than 1.5 km due to their continuous improvement (Vogt, 2016). Factors to be considered in the design of a TBM cutterhead include the cutter type, spacing of the cutters, shape and profile of the cutterhead, and the balance of the head (Rostami and Chang, 2017). These factors should be optimized for efficient excavation. In considering the cutter type, the cutter load-bearing capacity, required cutting forces, and cutter velocity limit should be taken into account. The load capacity, cutting forces, and velocity limits increase with increased cutter size for the same rock type.



Figure 2.14. A 6.25 m diameter Robbins TBM with back-loading cutters (Willis, 2014).

The typical s-p ratio for optimal cutting is in the range of 10-20 (Figure 2.14). The typical cut spacing, generally adopted by machine manufacturers, is in the range of 75-100 mm for hard rock TBMs to avoid ridge formation or groove-deepening (Bilgin et al., 2014). Wider cut spacings could be used for softer rocks. The spacing selection should be based on the hardest formation that covers a significant section of the tunnel path.

2.2. ROCK SURFACE HARDNESS

Rock surface hardness is a measure of the near-surface of the rock. It is the resistance of the rock to indentation or scratching. There are several means of measuring the hardness of a rock surface, including the use of the Shore Scleroscope hardness test, and the Schmidt hammer rebound test. In this research, the rock Schmidt hammer test was adopted due to its good estimation of rock hardness for rocks with uniaxial compressive strengths between 1 MPa and 100 MPa (ASTM, 2000; ASTM:D5873-14, 2014). Therefore, this section of the review concentrated on the literature of the Schmidt hammer rebound test.

2.2.1. The Schmidt Hammer. Ernest Schmidt, a Swiss engineer, developed the Schmidt hammer for concrete testing. It was presented at the Swiss Federal Institute of Experimental Testing in 1948 (Schmidt, 1951). It has since evolved through several phases to include measuring the near-surface hardness of rocks. Proceq, a leading producer of Schmidt hammers, has several types of hammers well suited for different purposes or different materials. They include the silver Schmidt OS8200 suitable for strong concrete, the original Schmidt OS8000, the original Schmidt suitable for measuring thin-walled material, the Schmidt OS-120 for testing softer material like fresh concrete, and the rock

Schmidt – a variation of the silver Schmidt particularly suited for rock testing (Proceq, 2020). There are two common rock Schmidt hammers for rock testing – the N-type with impact energy up to 2.207 Nm for harder material, and the L-type with impact energy up to 0.732 Nm for softer material (ASTM:D5873-14, 2014). The rock Schmidt hammer was used in this research, therefore, its detailed description is provided.

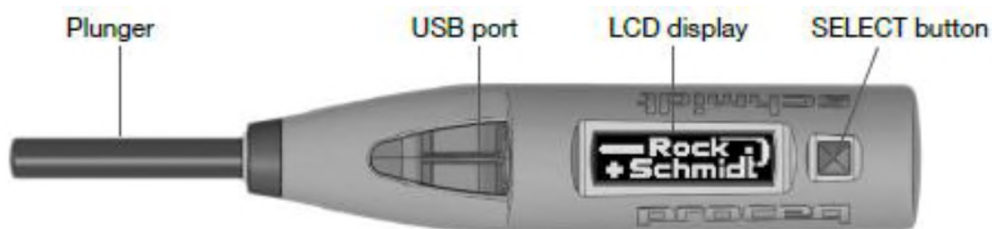


Figure 2.15. Description of the N-type rock Schmidt hammer (Proceq, 2017).



Figure 2.16. Display of (a) settings of rock Schmidt (b) recorded hardness measurement (Proceq, 2017).

The rock Schmidt consists of a plunger, a housing, a hammer mass, impact and loading springs, an electronic module, a mechanical module, a USB port, an LCD display, and a select button (Figure 2.15) (Proceq, 2017). The hammer is set up for measurement using the select button and the LCD display to choose options from the settings menu

(Figure 2.16a). The menu items of the display are changed by either rolling the hammer or tilting it. When the desired item is displayed, the select button is pressed to choose it. Measured hardness values are also displayed on the LCD screen (Figure 2.16b).

2.2.2. Rock Mass Characterization Using Schmidt Hammer Hardness. There have been several studies relating rock and concrete near-surface hardness to their engineering properties, such as the compressive strength and Young's modulus (Cargill and Shakoor, 1990; Sachpazis, 1990; Yilmaz and Sendir, 2002; Aydin and Basu, 2005; Buyuksagis and Goktan, 2007; Aydin, 2008; Hannachi and Guetteche, 2014). An exponential relationship was established between rock hardness and UCS, and Young's modulus by Yilmaz and Sendir (2002) upon testing several rocks using both the L- and N-type rock Schmidt hammers (Eqs. 2.5 and 2.6, respectively). They recommended the N-type for rock testing.

$$UCS = e^{0.818+0.059N} \quad (2.5)$$

$$E = e^{1.146+0.054N} \quad (2.6)$$

Where UCS – uniaxial compressive strength;

E – Young's modulus; and

N – Schmidt hammer rebound number.

Other studies have established similar relationships between rock hardness and rock strength properties (e.g., Deere and Miller, 1966; Aufmuth, 1975; Kidybiński, 1981; Sheorey et al., 1984; Singh et al., 1983; Xu et al. 1990). Some of the established relationships are presented in Table 2.1 along with the correlation coefficients obtained and the number of lithological units that were investigated.

Table 2.1. Relationships between rock hardness and rock strength properties by different studies (after Yilmaz and Sendir, 2002).

Authors	Equation	<i>R</i>	Rock type
Deere & Miller (1966)	$UCS=10^{(0.00014\gamma N+3.16)}$ $E=6.95\gamma^2N-1.14*10^6$	0.94 0.88	28 lithological unit, three base rock types
Aufmuth (1975)	$UCS=6.9*10^{[1.348\log(\gamma N)+3.16]}$ $E=6.9*10^{[1.061\log(\gamma N)+1.86]}$	–	25 lithological unit
Kidybiński (1981)	$UCS=0.447 \exp[0.045(N+3.5)+\gamma]$	–	Different rock types and coal
Singh et al. (1983)	$UCS=2N$	0.72	30 sedimentary unit
Sheorey et al. (1984)	$UCS=0.4N-3.6$	0.94	20 lithological unit
Sachpazis (1990)	$N=0.239 UCS+15.7244$ $N=0.515E+17.488$	0.96 0.88	33 different carbonates rocks
Xu et al. (1990)	$UCS=\exp(aN+b)$ a, b, c, and d coefficient based on rock types	0.88	Mica-schist, prasinite, serpentinite, gabbro, mudstone
UCS – uniaxial compressive strength; γ – unit weight; E – Young's modulus; and N – Rebound hardness.			

2.2.3. Rock Hardness and Excavation. An investigation conducted by Karpuz (1990) using 284 case studies in marl, tuff, and limestone postulated a rating system for rock diggability by different excavation methods. Rebound hardness, UCS, discontinuity spacing, weathering degree, and seismic velocity were some of the rock properties considered in the rating system. It was established that the rebound hardness of the rock significantly affects rock diggability by different equipment. Diggability is greater in softer rocks than in harder rocks.

Lislerud (1997) noted an established linear relationship between a relative rock hardness scale (known as the Protodyakonov rock hardness scale (f)) and rock UCS

(Eq.2.7). The hardness was then related to rock excavatability and concluded that excavatability is negatively correlated with rock hardness.

$$f = 0.1UCS \quad (2.7)$$

Tiryaki and Dikmen (2006) conduct bivariate regression analyses between rock properties of sandstone (mineralogical, physical, and mechanical properties) and the specific energy from full-scale linear rock cutting tests using drag picks. Among the properties were the Shore and Schmidt hardness of the rocks. The Shore hardness values were measured on rock cores, while the Schmidt rebound hardness was measured on outcrops. It was noted that both the Shore and Schmidt hardness values have a very strong positive correlation with the specific energy – with correlation coefficients of 0.92 and 0.89, respectively (Figure 2.17 and Figure 2.18, respectively).

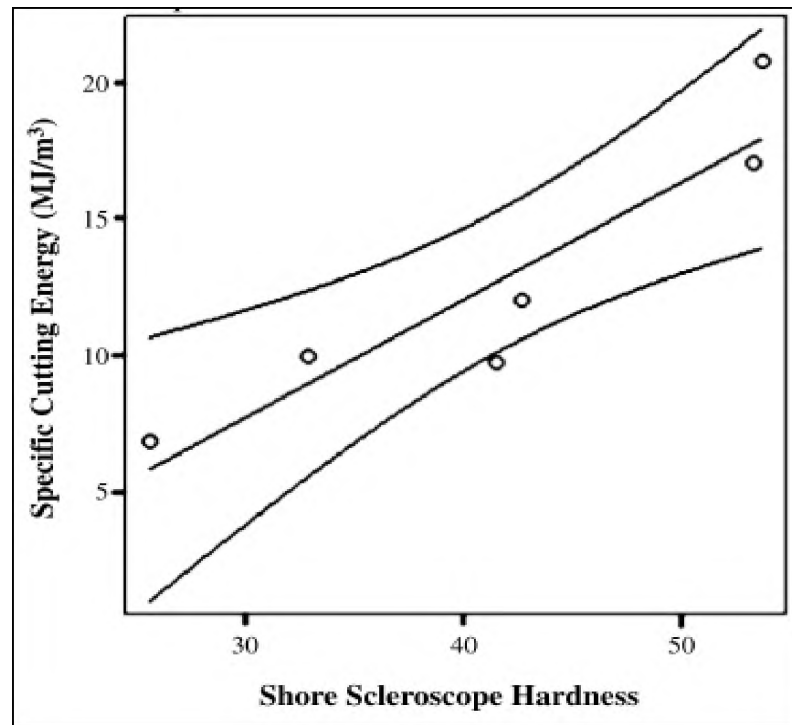


Figure 2.17. Relationship between specific energy and Shore hardness (Tiryaki and Dikmen, 2006).

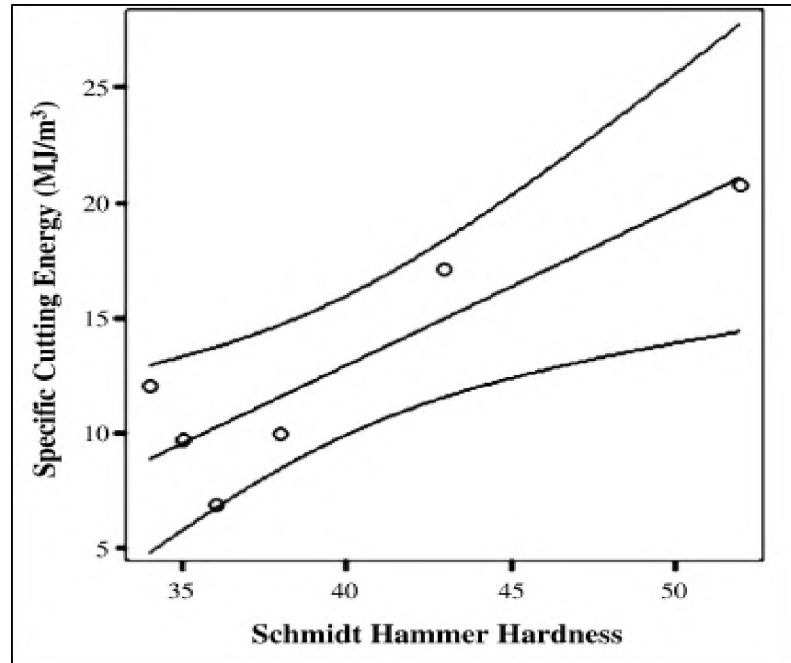


Figure 2.18. Relationship between specific energy and Schmidt rebound hardness (Tiryaki and Dikmen, 2006).

Another full-scale linear rock cutting investigation using conical drag cutters was conducted by Tumac et al. (2007) noting the optimum specific energy of different rock samples. They correlated the optimum specific energy with the Shore hardness and coefficients of deformation of 16 rock samples. They noted that the optimum specific energy is positively correlated with the Shore hardness of the rock (Figure 2.19). A power relationship was observed between the optimum specific energy and the coefficient of deformation (Figure 2.20). These relationships were validated by field excavations projects involving roadheaders in Turkey.

Liang et al. (2017) also established an excavability classification system using rebound hardness and other rock mass properties including joint spacing, joint number, joint extent, joint length, joint orientation, bedding planes, and intact rock properties. Their ratings for given rebound hardness ranges are presented in Table 2.2. A higher hardness

rating was given to rocks with lower rebound hardness. They investigated various sedimentary rocks and proposed the classification model based on statistical analysis. They then tested their model on different sedimentary excavation sites and found a good correlation between the model expectation and the observed excavatability values.

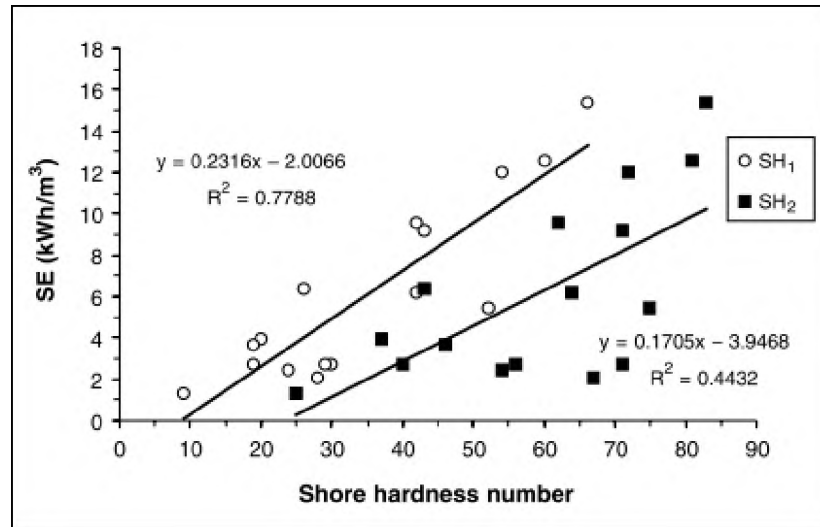


Figure 2.19. Relationship between optimum specific energy (SE) and Shore hardness (Tumac et al., 2007).

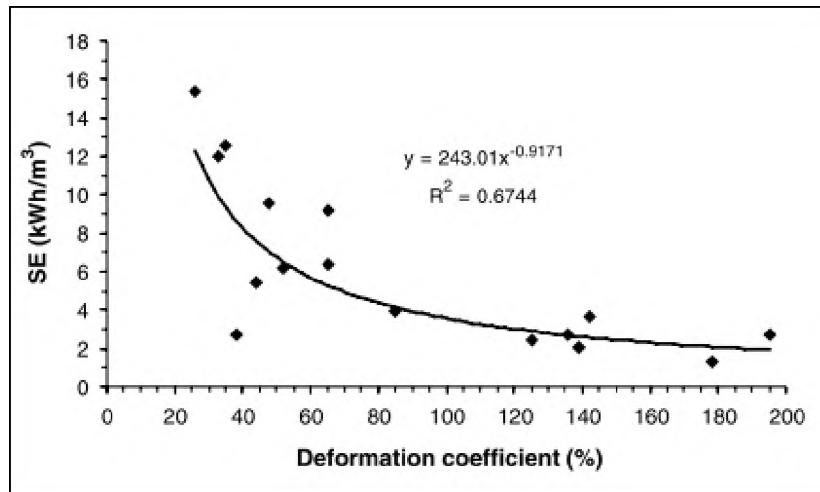


Figure 2.20. Relationship between optimum specific energy and coefficient of deformation (Tumac et al., 2007).

Table 2.2. Rating of rock rebound hardness for excavatability classification (after Liang et al., 2017).

Rebound hardness, R	<30	30-15	15-5	<5
Rating	0	1	2	3

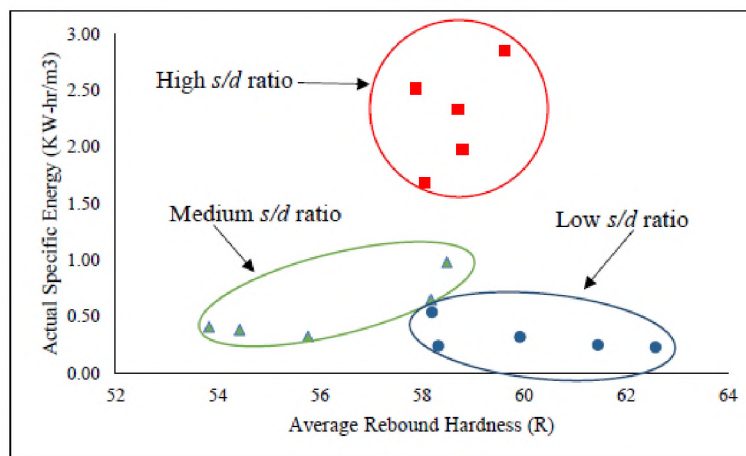


Figure 2.21. Relationship between specific energy and rebound hardness (s/d – spacing-penetration ratio) (Kaba, 2018).

Kaba (2018) used an N-type rock Schmidt hammer to measure the hardness of rock surfaces exposed by drag pick linear rock cutting. Hardness measurements were made after each pass of excavation. The hardness of the excavated surfaces was compared with that of a saw-cut surface of the same rock, and it was noted the average rebound hardness of the excavated surfaces was significantly lower than that of the saw-cut surface. This indicates that the excavation significantly affects the rock hardness. It was also observed that though there was no apparent relationship between the specific energy and the surface hardness, the specific energy at different spacing-penetration ratios tended to be in clusters (Figure 2.21). This observation is contrary to earlier researchers' observations (Tiryaki Dikmen, 2006; Tumac et al., 2007). This discrepancy could be attributed to the mode of

measurement of the rock hardness. While Tiryaki Dikmen (2006) and Tumac et al. (2007) measured the rock hardness on cores and outcrops, Kaba (2018) measured the hardness on the excavated surfaces. The inter-relationship between specific energy and excavated surface hardness, with other cutting parameters, could mask the actual relationship between the specific energy and surface hardness measured on the excavated surface.

2.3. ROUGHNESS OF EXCAVATED ROCK SURFACES

The roughness of an excavated surface is controlled by the overbreaks and underbreaks that occur during excavation. The overbreaks and underbreaks are, in turn, controlled by discontinuities in the rock mass, cutting geometry, and cutting forces. Some research on the causes and impact of overbreaks and underbreaks in excavations were reviewed in this section. Several methods for measuring rock surface roughness have been studied, and some of them were presented in this section.

2.3.1. Measurement of Surfaces Roughness. Raviv et al. (1989) explored the reconstruction of 3D surfaces using shadow profilometry. They placed the object on a reference surface at an elevation of zero, and they projected a beam of parallel light rays at the object at different angles. The images of the shadow cast by the object were taken by a camera placed vertically above the object (Figure 2.22). A 3D binary level shadow diagram (3DBL shadowgram) was then formed from the images taken. The camera resolution, height above the object, and the number of images were optimized to obtain a robust method.

Maerz et al. (1990), Maerz et al. (2001), Walker et al. (2005), and Maerz & Hilgers (2010) described a different version of shadow profilometry for surface roughness measurements that involves casting a shadow of a straight edge on the object of study. The shadow reveals the level of irregularity in the surface of the study object. A smooth surface will show a straight shadow edge, and a rough surface will show an irregular shadow edge. The method involves placing a flat long ruler on the study object, projecting light on the surface at an angle of 45° , and scanning the shadow cast by the ruler with a camera placed orthogonally to the study surface. The ruler is then moved to a new location along the length of the surface, and the process is repeated. This is done until the whole surface is examined. The edges of the shadows on each image are extracted using the Canny edge detection algorithm (Figure 2.23). The shadow edge profiles form a point cloud of the surface and are used for roughness analysis.

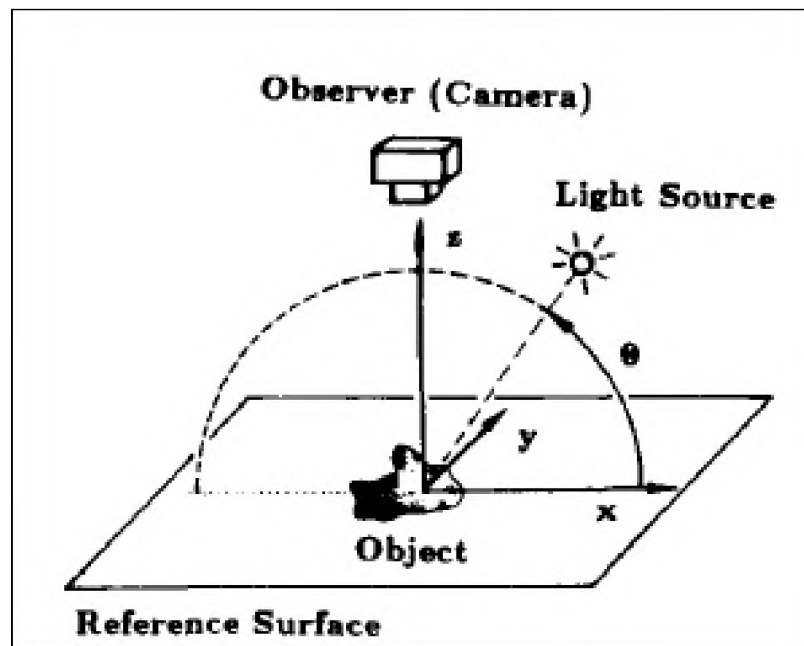


Figure 2.22. Schematic of shadow profilometry setup (Raviv et al., 1989).

The shadow profilometry described above has been applied for joint roughness measurement (Mearz et al., 1990), concrete roughness characterization (Maerz et al., 2001), surface reconstruction for forensic purposes (Walker et al., 2005), and fractured surface matching (Maerz and Hilgers, 2010).

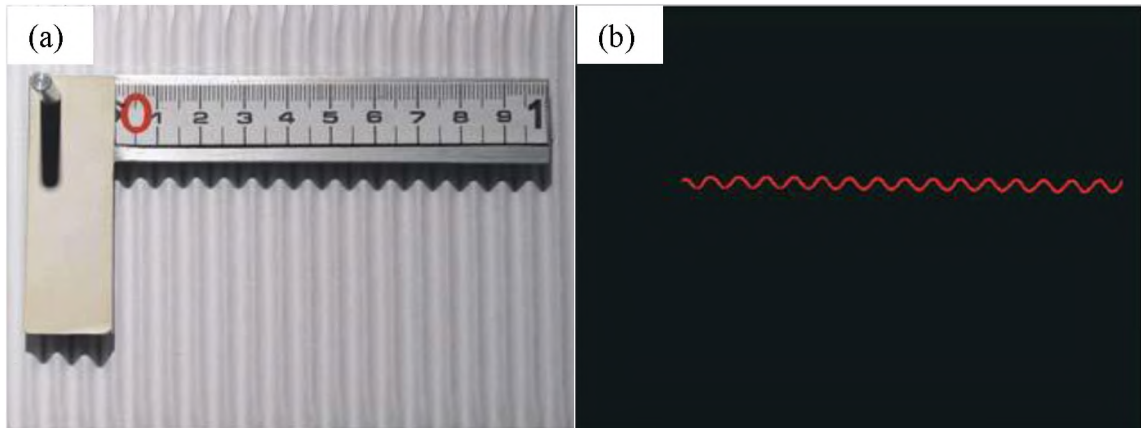


Figure 2.23. Shadow profilometry (a) Shadow cast on an undulating surface (b) extracted edge of the shadow showing profile of the surface (Maerz and Hilgers, 2010).

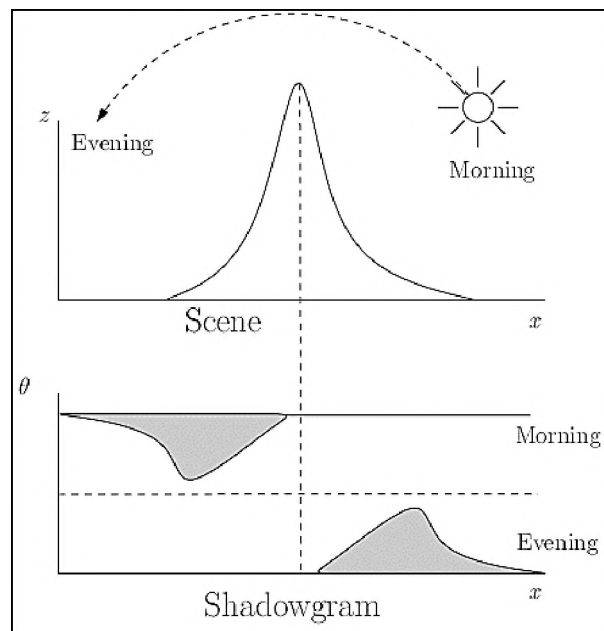


Figure 2.24. Illustration of a 2D scene and shadowgram (Daum and Dudek, 1998).

Another study was conducted by Daum and Dudek (1998) using the shape from shadows to reconstruct 3D surfaces. Their approach was for large-scale scenery reconstruction, though, the concept is similar to that described by Raviv et al. (1989). The light source and camera source are assumed to be infinite, thus, the light rays are considered parallel, and the camera projections are considered to be orthographic. They used the sun as a light source to illustrate the imaging method (Figure 2.24). The 3D surface is reconstructed from the series of 2D shadowgrams formed with the light source at different locations along its trajectory (Figure 2.25).

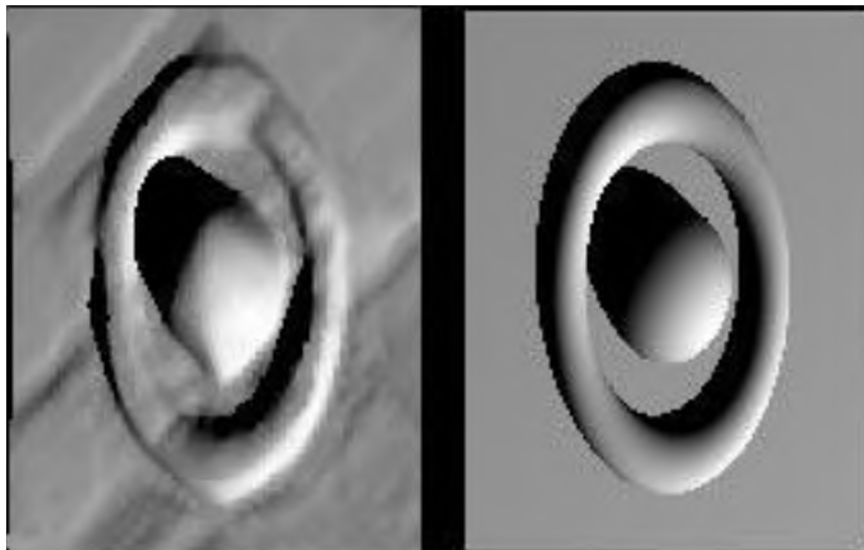


Figure 2.25. Reconstruction of a complex terrain from shadow data – the reconstructed surface on the left, and the original on the right (Daum and Dudek, 1998).

A computer-controlled surface mapping system consisting of a mechanical scanning device, and a circuit connected to a computer (Figure 2.26) was introduced by Develi et al., (2001). The scanning device is controlled by a software called SG1PRO installed on the computer. The mechanical device has a needle that is brought to the surface at a precise location, and the elevation of the needle is recorded. The needle was moved to

another location on the surface in a regular pattern based on the inputted scanning resolution and dimensions of the study surface. The sample size and scanning resolution are specified in the software before the scanning starts. The system is said to have a 1 mm maximum resolution in the x-y plane and 0.1 mm resolution in the z-axis. The authors noted that the system was well suited for imaging core-size samples. Evaluation of the surfaces generated by the system, after scanning synthetic and natural surfaces, led to the conclusion that the system is apt for quantitative surface roughness analyses.

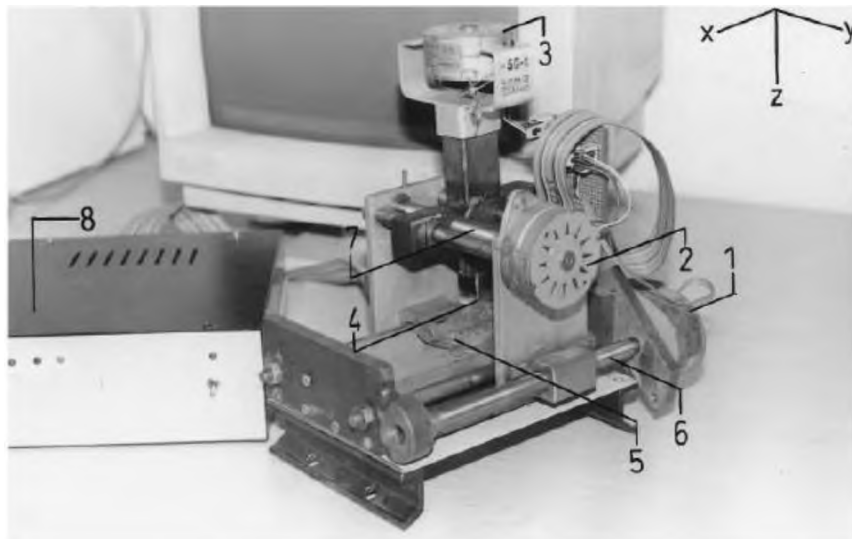


Figure 2.26. A photo of a surface-scanning device; (1) step motor 1; (2) step motor 2; (3) step motor 3; (4) needle; (5) fracture sample surface; (6) worm gear along x-direction; (7) wormgear along y-direction; (8) control unit of surface-scanning device. Dimensions of scanning device in x, y, and z-direction are 230, 160 and 245mm, respectively (Develi et al., 2001).

James and Robson (2012) proposed a structure-from-motion (SfM) and Multiview-stereo (MVS) algorithm for reconstructing surfaces from field photos for geoscience applications. They touted their system to be cheaper than laser scanners and less rigorous than conventional photogrammetry. Their system uses computer vision to match the texture

from different images. The matched images are used to generate 3D geometries of the imaged scene. It was assumed that the scene under observation is static. Figure 2.27 shows a 3D surface of the summit craters of Piton de la Fournaise volcano generated using the SfM-MVS system.

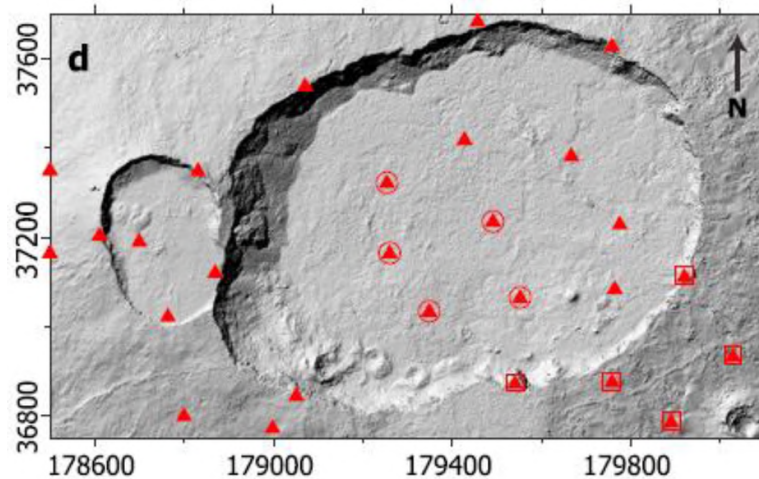


Figure 2.27. Reconstruction of the summit craters of Piton de la Fournaise volcano using the SfM-MVS system (James and Robson, 2012).

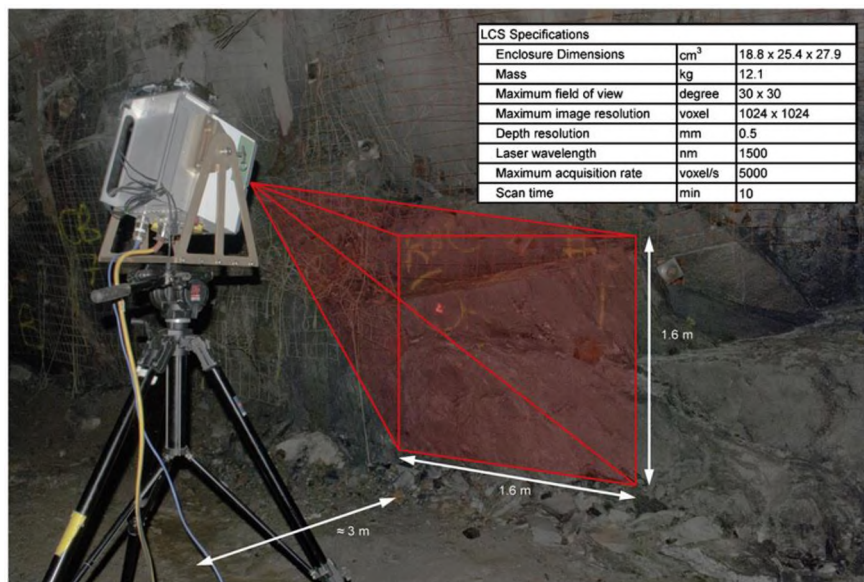


Figure 2.28. Neptec 3D laser camera system in an underground setup (Mah et al., 2012).

Laser imaging has also been employed to acquire surface data for roughness analysis. Mah et al. (2012) demonstrated the application of 3D laser imaging for collecting roughness data from the side wall of an underground drift. They adopted the Neptec 3D laser camera system (Figure 2.28), which was previously used for both surface and underground imaging (Samson et al., 2004; Mah et al., 2008; Mah et al., 2012). The camera collects a point cloud of the surface. The point cloud is later processed to reconstruct the surface for joint roughness and orientation analysis.

2.3.2. Measurement of Overbreak and Underbreak in Excavations. Maerz et al. (1996) introduced a method known as the light sectioning method (LSM) for measuring overbreaks and underbreaks in underground excavations. The method involves the projection of a thin sheet of light perpendicular to the excavation axis on the excavation walls. The intersection of the light and the tunnel walls represent the profile of the tunnel at that given point. An orthogonal image of the intersection is then taken, processed digitally (Figure 2.29), and superimposed on the designed profile of the tunnel. The overbreaks and underbreaks are then quantified and analyzed from the superimposed images.

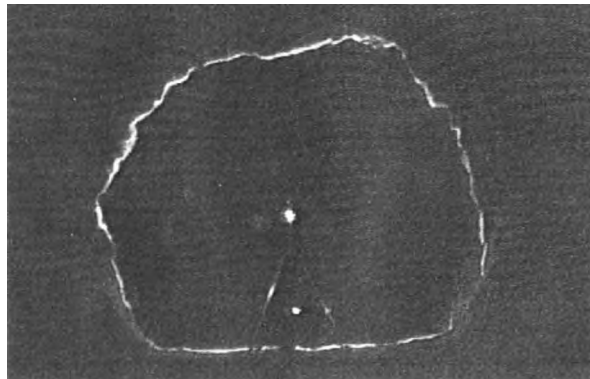


Figure 2.29. A digitized image of a tunnel profile from an LSM image with the central light source as the reference point (Maerz et al., 1996).

2.3.3. Causes of Excavation Damage and Surface Roughness. Ibarra et al.

(1996) measured the overbreaks and underbreaks in 92 sections of a tunnel constructed in Nayarit, Mexico. The rock masses at each of the 92 sections were classified based on the rock quality designation (RQD) (Deere and Miller, 1966), rock mass rating (RMR) (Bieniawski, 1979), and the Q system (Barton et al., 1974). They observed that the Q system had the best correlation with the overbreaks and underbreaks measured. The percentage of underbreaks had a positive linear relationship with the log of the rock mass quality (Q) (Figure 2.30a). Conversely, the percentage of overbreak had an inverse linear relationship with log Q (Figure 2.30b). The variations observed in the figures were attributed to other factors such as excavation design and execution methods.

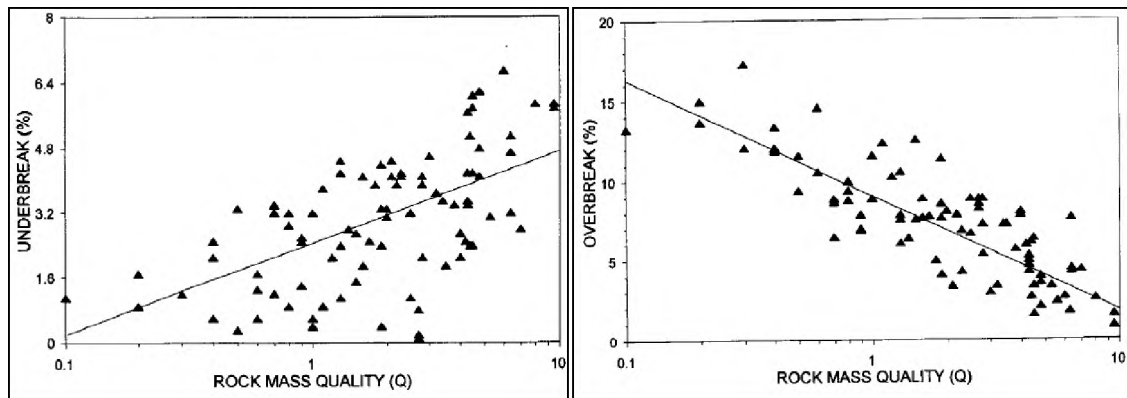


Figure 2.30. Relationship between rock mass quality, Q and (a) underbreak and (b) overbreak (Ibarra et al., 1996).

Singh & Xavier (2005) and Mandal & Singh (2009) studied the causes and impact of overbreaks in underground excavations. They outlined three factors: rock mass characteristics, explosive types and distribution, and the blast design, as noted earlier by Mahtab et al. (1997). The latter two are associated with blasting excavation, but the first is a general factor causing overbreaks in all excavation methods. Rock mass damage caused

by excavation can result in ore dilution in mining, create ground control problems, and increase the cost of excavation projects. One of the indices that were used to measure rock mass damage in their study was the percentage of overbreak. That is the percentage of the volume of rock excavated more than the designed volume. A physical concrete model was used to study how the rock mass characteristics influenced blast excavation damage. They observed that the geometry, distribution, orientation, and other discontinuity characteristics greatly affect the overbreak percentage. For example, in Figure 2.31, the percentage overbreak increases with increasing joint inclination from the excavation axis and peaks at 45° and decreases to the lowest at 90° . It was recommended that the orientation of major discontinuities be considered during the planning and design of the excavation. The in-situ stress field was also noted as one of the major causes of overbreaks and rock mass damage. Closely spaced joints are additionally associated with excessive rock mass damage and overbreaks. The percentage of overbreaks is directly related to the roughness of the excavation. Optimal excavations with little overbreaks and underbreaks produce smoother excavation walls.

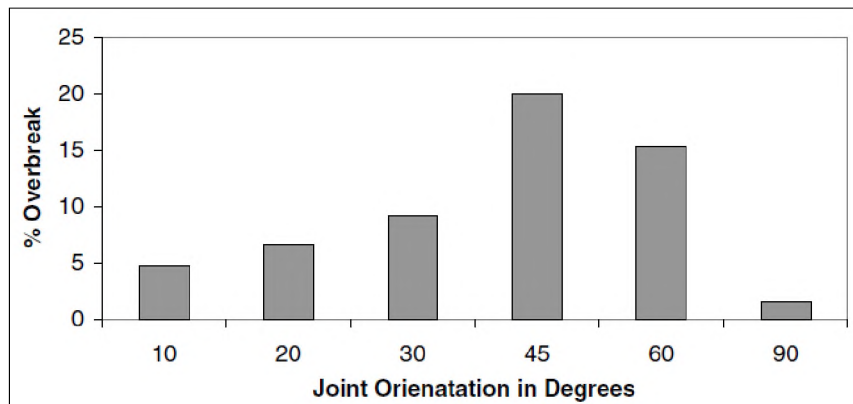


Figure 2.31. The effect of joint orientation of overbreaks percentage (Singh and Xavier, 2005).

Jang and Topal (2013) used the terms in the rock mass rating (RMR) criteria—point load strength (Sc), rock quality designation (RQD), joint spacing (Js), joint condition (Ja), and joint water condition (Jw)—as independent variables in linear and non-linear multi regression, and artificial neural networks (ANN) models to predict the magnitude of rock overbreak in excavations. They collected overbreaks and RMR data from 49 projects and used it for predictive modeling. They recorded over 94% coefficient of determination from the prediction of the ANN model. This implies that RMR or the rock mass conditions in the RMR criteria significantly influence the overbreaks that are observed in underground excavations.

2.4. EXCAVATOR PERFORMANCE PREDICTION

2.4.1. Theoretical Models. Rostami and Ozdermir (1993) developed models for estimating the cutting requirements of CCS disc cutters. They acknowledged the existence of the crushed zone and indicated that its extent is a function of the cutter tip geometry and the rock properties. The smaller the crushed zone, the better the cutting efficiency. Radial cracks propagate from the crushed zone under induced stresses from the cutter. These are caused by tensile stresses but are also subject to significant shear stresses. The researchers, therefore, believed that chip formation was a result of a mixed mode of failure. They postulated that the length of cracks generated was a function of pressure in the crushed zone, which is also a function of the normal forces exerted by the cutter. Based on this, they developed a theoretical model (Eq. 2.8) for estimating the pressure in the crushed zone considering the cutter geometry and the base pressure.

$$P = P' \left(1 - \frac{\theta}{\phi}\right)^{\psi} \quad (2.8)$$

Where P' is the base pressure; and

θ is an angle from the normal to face, ranging from 0 to ϕ .

Different pressure distribution models exist depending on the value of ψ , including linear distribution where $\psi = 1$ (Figure 2.32).

From Eq. 2.8, the force can be estimated as (Eq. 2.9):

$$dF = TRP' \left(1 - \frac{\theta}{\phi}\right) d\theta \quad (2.9)$$

Therefore, the normal and rolling forces can be estimated as follows (Eq. 2.10 and 2.11, respectively):

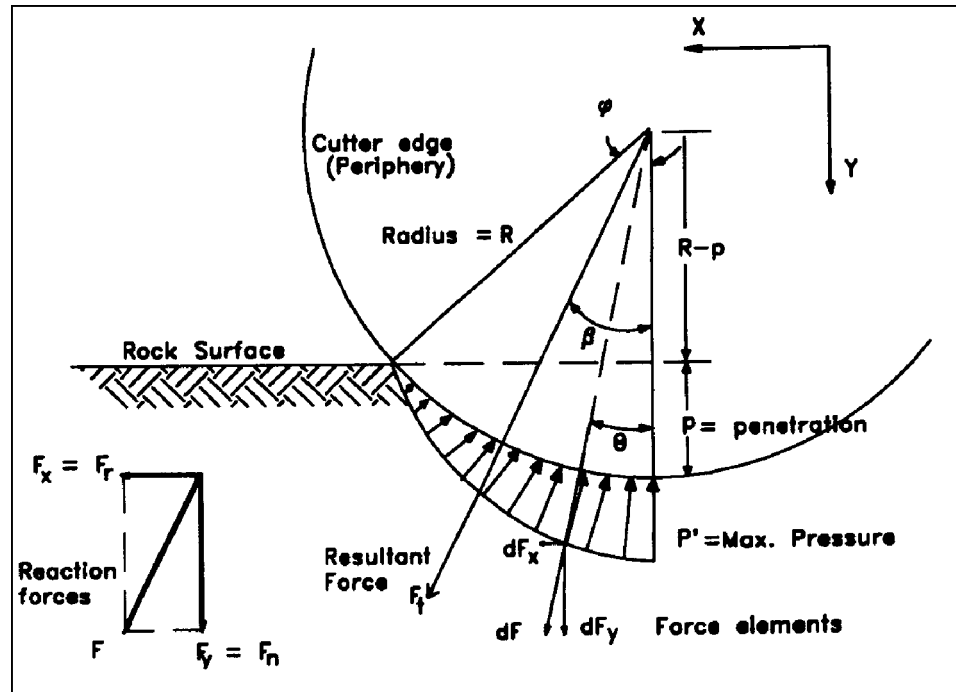


Figure 2.32. Linear pressure distribution under the disc cutter (Rostami and Ozdemir, 1993).

$$F_n = \int_0^\phi df_y = \int_0^\phi dF \cos \theta = \frac{TRP'}{\phi} (1 - \cos \phi) \quad (2.10)$$

and

$$F_r = \int_0^\phi df_x = \int_0^\phi dF \sin \theta = \frac{TRP'}{\phi} (1 - \sin \phi) \quad (2.11)$$

Where T is the cutter tip width in mm; and

R is the cutter radius.

Considering the optimum spacing between cutters, the number of cutters for a cutterhead design can be established. The thrust, torque, and power of the machine can also be calculated from the normal and rolling forces, respectively. This provides parameters for excavation machine design. For performance prediction, machine specifications and rock properties are used to estimate the maximum achievable rate of penetration. The advance rate can then be predicted, taking into consideration the machine utilization, which is the percentage of time the machine is excavating out of the total project duration.

Tumac and Balci (2015) suggested a modification to the Bilgin (1977) model (Eqs. 2.14 and 2.15) for predicting cutting forces under the V-shaped disc cutter. The modification was aimed at making the models applicable to CCS disc cutters. The modified models are presented in Eqs. 2.12 and 2.13. The input parameters for the suggested model include the edge radius, cutter penetration, and the uniaxial compressive strength of the rock. Their model was validated using linear rock cutting experimental data. According to the authors, the model reliably predicts the normal forces with a slight overestimation, but the prediction of the rolling forces shows significant variation from the measured experimental rolling forces, similar to what was observed by Rostami and Ozdermir

(1993). In their study, the experimental factors considered were rock type, cutting mode (relieved and unrelieved), cutter penetration, spacing, and cutter size. They observed that the cutter size effect was not uniform across all rock types. For shale and arkose, the rolling forces decreased with increasing cutter size, which is contrary to expectation. They attributed this to the structural and textural makeup of the rock. In all the rock types tested, however, the specific energy decreased with increasing cutter size. They obtained optimum s-p ratio between 10 and 11.4 and optimum penetrations between 7 mm and 9 mm at a constant spacing of 80 mm for all the rock types studied. They recommended further study on the accurate prediction of the rolling forces because all the models considered did not yield precise and accurate rolling force predictions.

$$FN_{Bil-M} = k \cdot FN_{Bil} \quad (2.12)$$

$$FR_{Bil-M} = k \cdot FR_{Bil} \quad (2.13)$$

$$FN_{Bil} = FN_{Rox} \cdot e^{A \cdot r} \quad (2.14)$$

$$FR_{Bil} = FR_{Rox} \cdot e^{B \cdot r} \quad (2.15)$$

$$A = 0.0354 + \frac{0.6554}{p} \quad (2.16)$$

$$B = 0.06 + \frac{0.383}{p} \quad (2.17)$$

Where FN_{Bil-M} and FR_{Bil-M} are the proposed normal and rolling forces modified after Bilgin (1977) in N;

FN_{Bil} and FR_{Bil} are the normal and rolling forces by Bilgin (1977) in N;

FN_{Rox} and FR_{Rox} are the normal and rolling forces by (Roxborough and Philips, 1975) in N;

k is the calibration or modification factor;

r is the cutter tip radius in mm; and

p is the cutter penetration in mm.

2.4.2. Empirical Models from Field and Experimental Data. Ramezanzadeh et al. (2008) used data from two tunneling projects to develop a modification to the famous CSM performance prediction model. They observed that there was no apparent correlation between the rate of penetration (ROP) and intact rock parameters (UCS, and BTS). Punch test index (PTI) was, however, said to have a good correlation with ROP. ROP increased with increasing PTI. Other parameters considered in their model were the discontinuity spacing (JS) and discontinuity orientation (α) with respect to the axis of the tunnel. Their models were developed based on data from the KCRC tunnel, as shown in Eqs. 2.18 and 2.19.

$$AdjROP = \frac{CSMROP^{0.453}}{Exp(0.001 \times JS - 0.002 \times PTI - 0.687)} \quad (2.18)$$

$$AdjROP = \frac{CSMROP^{0.407}}{Exp(0.001 \times JS - 0.002 \times \alpha - 0.002 \times PTI - 0.632)} \quad (2.19)$$

Where AdjROP is the adjusted rate of penetration; and

CSMROP is the rate of penetration calculated from the CSM model.

These models have correlation coefficients of 0.62 and 0.65, respectively, but the second model is only valid for $\alpha < 45^\circ$. They compared the performance of the adjusted models and that of the original CSM model in predicting the ROP of the Queens tunnel dataset and observed that the adjusted models performed better than the original CSM model (Figure 2.33).

Hassanpour et al. (2011) used a database collected from four tunneling projects to develop a performance prediction model for TBMs. They calculated the average ROP,

penetration per revolution (P), field penetration index (FPI), and specific energy from the obtained project data. The geological parameters considered in the model were UCS, RQD, basic RMR, discontinuity spacing, and discontinuities orientation. A correlation of the performance parameters revealed that FPI had a good correlation with the geological parameters, so it was used in developing the empirical model. The model includes the UCS and RQD of the formation. Their model is shown in Eq. 2.20 with a regression coefficient of 78.5%.

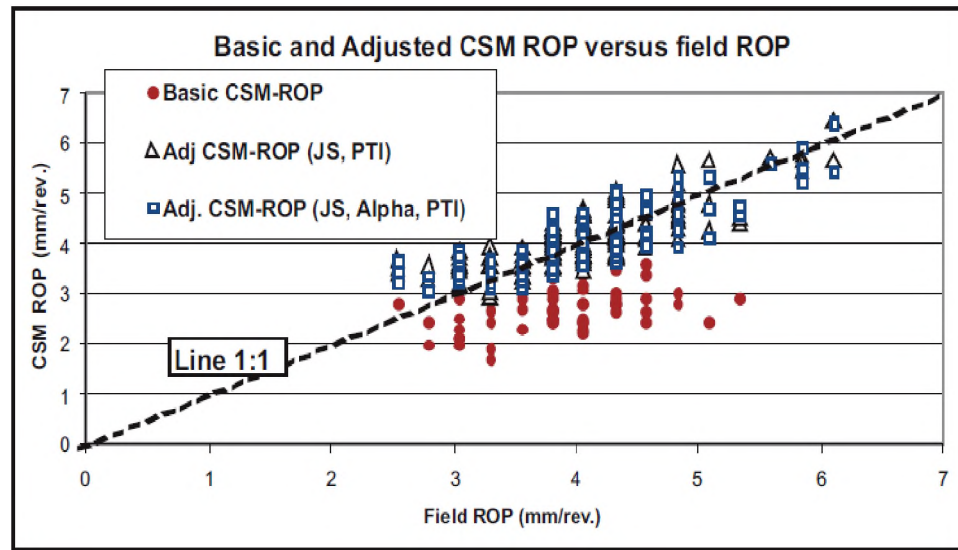


Figure 2.33. A plot of the CSM and AdjCSM model predictions against field data from the Queens water tunnel project (Ramezanzadeh et al., 2008).

$$FPI = e^{0.008UCS+0.015RQD+1.384} \quad (2.20)$$

They observed that higher values of FPI were recorded in strong and massive rocks, but lower FPI was recorded in weak rocks. It was, therefore, opined that FPI can be used as a rock mass boreability index. Predictions of their model were compared with the observed FPI and a good match was obtained, as shown in Figure 2.34.

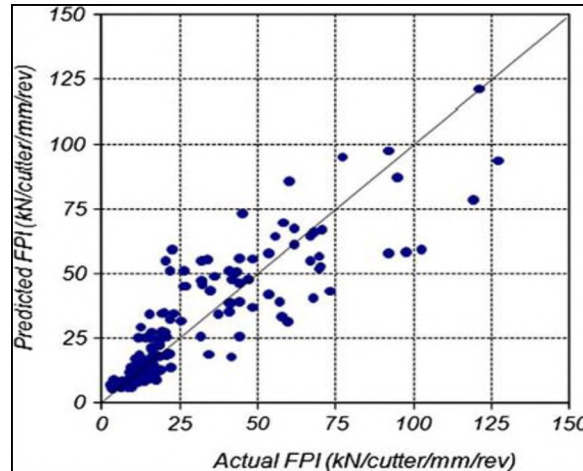


Figure 2.34. Correlation between model predictions and observed FPI (Hassanpour et al., 2011).

2.4.3. Computational Models. According to Dudt and Delisio (2016), the performance of a TBM can be predicted using the penalty factor model, which considers finite states of finite geo-parameter that affect the penetration rate of the TBM. In their model, they considered the degree of fracturing, UCS, water inflow, stress level, and abrasivity. The optimal advance rate was weighted based on the states of the geo-parameters considered. A weighting factor was included for the efficiency of the excavation crew. They validated their model using field data collected in a tunneling database from the New Technologies for Tunneling and Underground Works (NeTTUN).

Grima et al. (2000) criticized the lack of uniqueness in models used for the performance prediction of TBM. They compared prediction results from several models with a hybrid modeling framework and a Neuro-Fuzzy modeling method. They concluded that the neuro-fuzzy method was more accurate because it had the lowest root mean square error among the six models compared. The models compared were: multiple linear

regression (MLR) – stepwise, MLR – backward, Graham, Graham (>80 MPa), Adjusted Graham (>80 MPa), and Neuro-Fuzzy.

2.5. NUMERICAL MODELING OF ROCK EXCAVATION

2.5.1. Finite Element Methods and Rock Cutting. Cho et al. (2010) and Cho et al. (2013) conducted lab rock cutting experiments using a linear rock cutting machine and numerical rock cutting experiments in AUTOYN-3D, a finite element model. They aimed to determine the parameters for efficient cutting in granitic rocks. They studied three levels of penetration and six levels of spacing-penetration ratios. Specific energy was used as a measure of cutting efficiency. It was observed that earlier methods for obtaining the volume of excavated materials were unrealistic, as noted by Gertsch et al. (2007). As a result, they adopted a photogrammetric approach for measuring the volume of excavated material. The calculated volume of excavated material matched that of the measured volume closely until a certain s-p ratio (optimum s-p ratio) is reached where there is a significant deviation. The SE-s/p plot obtained from the measured volume gave a more realistic curve with an optimum s-p ratio between 7.5 and 10, as expected. They indicated that both normal and rolling forces increased until a certain s-p ratio was reached (15), and then it flattened. At this point, there was said to be no interaction between adjacent cuts. According to their study, the measured SE values at the optimum s-p ratio decreased slightly with increasing penetration. This agrees with the findings of Rostami (2008). Their numerical result matched the LCM results closely, with the forces and SE from the numerical experiments being slightly higher than those from the LCM, which they attributed to only non-zero forces used in calculating the mean forces in the simulation

results. A limitation of their study is that they used different cutter types in the LCM (CCS) and simulations (v-shape). The shape of the tip of the cutter has a significant effect on the cutter forces; therefore, comparing forces resulting LCM and simulation with different cutter types yielded a variation in the results.

Ma et al. (2011) studied the effect of confining stress on the chipping forces, crack angle, and effective crack length during TBM excavation. In their study, they simulated the indentation of a disc cutter in a 2D model in Rock Failure Process Analysis (RFPA2D). They observed that at higher confining stresses, the rate of increase of chipping forces, crack angle, and the effective crack length was not lower, as compared to that at lower confining stresses. They underscored that tensile failure occurred, even under high confining stresses, and that tensile failure is the main mode of chip formation during rock cutting using disc cutters.

2.5.2. Discrete Element Methods and Rock Excavation. Discrete element method (DEM) is a commonly used numerical simulation method in rock cutting due to its ability to simulate dynamic fracturing. A discrete element method – particle flow code – was used for the rock cutting simulations in this research; therefore, a detailed review of this method was given in this section. The motivation for modeling rocks as a homogeneous collection of balls is that the interaction between individual grains is largely random, making the specimen at an intact scale appear homogeneous (Potyondy, 2015).

2.5.2.1. Particle Flow Code (PFC). PFC is a distinct element method developed by Itasca® that employs an explicit dynamic solution approach in the computation of problems in both granular and solid material. The granular models are made up of cohesionless discs (2D) or spheres (3D) that are not bonded. The solid models, by contrast,

are collections of discs (2D) or spheres (3D) that are bonded either by a contact bond, linear bond, parallel bond, or flat-joint bond logic. The interaction between the particles at the contacts is pairwise based on interaction laws known as the contact models that update the internal forces and moments. Particles can move in rotation and translation. The solid model is known as the bonded particle model (BPM) (Potyondy and Cundall, 2004). This model can mimic the following emergent behaviors: elasticity, fracturing, acoustic emission, damage accumulation, producing material anisotropy, hysteresis, dilation, post-peak softening, and strength increase with confinement (Potyondy, 2015). Rock masses can be modeled by introducing discontinuities larger than the grain scale into the base intact rock model using the smooth-joint logic.

According to Paterson and Wong (2005), as the requirement for an adequate theory of failure, the BPM takes into consideration, the nucleation of microcracks from preexisting flaws and the growth in numbers and extent of these microcracks as the load is increased. As the extent and number of microcracks increase, the BPM allows for their interaction and possible localization, causing macroscopic failure (Lisjak and Grasselli, 2014; Potyondy, 2015).

2.5.2.2. The flat-joint model (FJM) of PFC. The interface between adjacent balls is segmented into a number of elements based on the user's definition. Each of the elements is either bonded or unbonded, depending on the gap between the balls. If the space between elements is within the specified bonding gap, then the elements are bonded, and linear elastic behavior is applied to the bonded pieces. Conversely, if the space between adjacent elements is wider than the specified gap, the interface elements are left unbonded, and linear elastic and frictional behavior are applied to the balls involved, accommodating slip

$$F = \sum_{\forall e} F^e \quad (2.21)$$

$$M = \sum_{\forall e} \{(r^e \times F^e) + M^e\} \quad (2.22)$$

Where r^e is the distance from the elemental centroid to the center of the contact.

The elemental forces are resolved into normal (F_n^e) and shear (F_s^e) forces and the moments resolved into twisting (M_t^e) and bending (M_b^e) moments (Eqs. 2.23 and 2.24, respectively).

$$F^e = -F_n^e \hat{n}_c + F_s^e \quad (2.23)$$

$$M^e = M_t^e \hat{n}_c + M_b^e \quad (2.24)$$

Where \hat{n}_c is a unit normal vector.

The normal elemental force (F_n^e) and elemental bending moment (M_b^e) are updated by integrating the normal stresses acting on the element. The effective portion of the relative shear displacement at the elemental centroid is used to update the elemental shear force (F_s^e) incrementally. The twisting moment is assumed to be equivalent to zero in 3D models. The normal (σ^e) and shear (τ^e) stresses over the elements are given by Eqs. 2.25 and 2.26, respectively.

$$\sigma^e = \frac{F_n^e}{A^e} \quad (2.25)$$

$$\tau^e = \frac{\|F_s^e\|}{A^e} \quad (2.26)$$

Where A^e is the area of the element.

The velocity algorithm proposed by Verlet (1967) is applied to solve the equations of motion used to update the displacement of each ball due to the application of external forces. For a force, $F(x)$, and moment, $M(x)$, acting on a particle, x , the linear and angular

accelerations (\ddot{r} and $\ddot{\theta}$) of the particle are determined using Newton's second law in Eqs. 2.27 and 2.28, respectively.

$$m_{(x)}\ddot{r}_i = \sum F_{(x)i} \quad (2.27)$$

$$I_{(x)}\ddot{\theta}_{(x)} = \sum M_{(x)} \quad (2.28)$$

Where $m_{(x)}$ is the mass of particles x ; and

$I_{(x)}$ is the moment of inertia of particle x .

An assumption of constant particle accelerations over the infinitesimal timesteps, δt , is made. Based on this assumption, the linear and angular velocities (\dot{r} and $\dot{\theta}$) are derived in Eqs. 2.29 and 2.30, respectively, while the linear and angular displacements (r and θ) are derived in Eqs. 2.31 and 2.32, respectively.

$$(\dot{r}_i)_{t+\frac{\delta t}{2}} = (\dot{r}_i)_{t-\frac{\delta t}{2}} + \left(\frac{\sum [F_{(x)i} + D_{(x)i}]}{m_{(x)}} \right)_t \times \delta t \quad (2.29)$$

$$(\dot{\theta}_i)_{t+\frac{\delta t}{2}} = (\dot{\theta}_i)_{t-\frac{\delta t}{2}} + \left(\frac{\sum [M_{(x)}]}{I_{(x)}} \right)_t \times \delta t \quad (2.30)$$

$$(r_i)_{t+\delta t} = (r_i)_t + (\dot{r}_i)_{t+\frac{\delta t}{2}} \times \delta t \quad (2.31)$$

$$(\theta_{(x)})_{t+\delta t} = (\theta_{(x)})_t + (\dot{\theta}_{(x)})_{t+\frac{\delta t}{2}} \times \delta t \quad (2.32)$$

Where $\sum D_{(x)}$ is the sum of all damping forces, and

$\sum M_{(x)}$ includes the damping forces moments.

At each timestep, Eqs. 2.27 through 2.32 are solved for all the contacts in the model. The forces and displacements of the particles are then updated based on these computations (Lim, 2004).

Several researchers have used FJM for rock material simulations, including rock cutting, and reported results that were in good agreement with those obtained from lab experiments (Potyondy, 2012, 2013; Wu & Xu, 2016; Xu et al., 2016; Castro-Filgueira et al., 2017; Chen, 2017; Li et al., 2018). These give the basis for the use of FJM in the current study.

2.5.3. Model Calibration. To create a PFC model that is representative of the real rock tested in the lab or the field, the model has to be calibrated with macro- mechanical properties (deformability and strength properties) of the real rock obtained from lab tests. In the process of calibration, micro-parameters of synthetic core specimens are adjusted, while the UCS, BTS, and/or direct tensile strength (DTS) tests are conducted. The UCS, tensile strength, Young's modulus, and Poisson's ratio of the model are matched with those obtained from lab tests of the actual rock samples. The micro-parameters that produce matching macro- mechanical properties are then used to create the rock model for further analyses (Potyondy and Cundall, 2004). Wu and Xu (2016) studied the effects of the micro-parameters of the FJM and published the following calibration procedure, in Figure 2.36a, based on the macro-parameters that are directly affected by corresponding micro-parameters. Li et al. (2018) suggested a slightly different calibration procedure for the FJM models. Their procedure accounted for the Hooke-Brown parameter, m_i , and the macroscopic friction angle. Figure 2.36b shows the flowchart of their calibration procedure.

Chen (2017) classified the micro-parameters into deformability and strength parameters. The deformability parameters are the stiffness ratio and the bond effective modulus, which directly affect the specimens Poisson's ratio and elastic modulus. The

strength micro-parameters are the bond cohesion, bond tensile strength friction coefficient, and friction angle. They conducted sensitivity analyses and determined the extent of influence each micro-parameter has on the respective macro-parameters, then suggested a calibration flowchart, as shown in Figure 2.37.

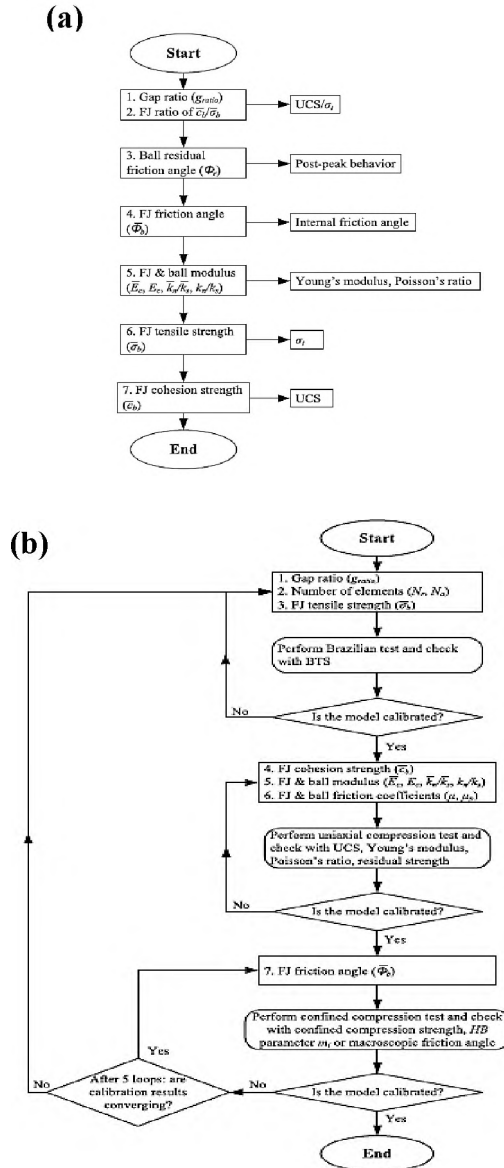


Figure 2.36. Numerical model calibration (a) Wu and Xu's calibration procedure (after Li et al. (2018)) (b) FJM calibration flowchart (Li et al., 2018).

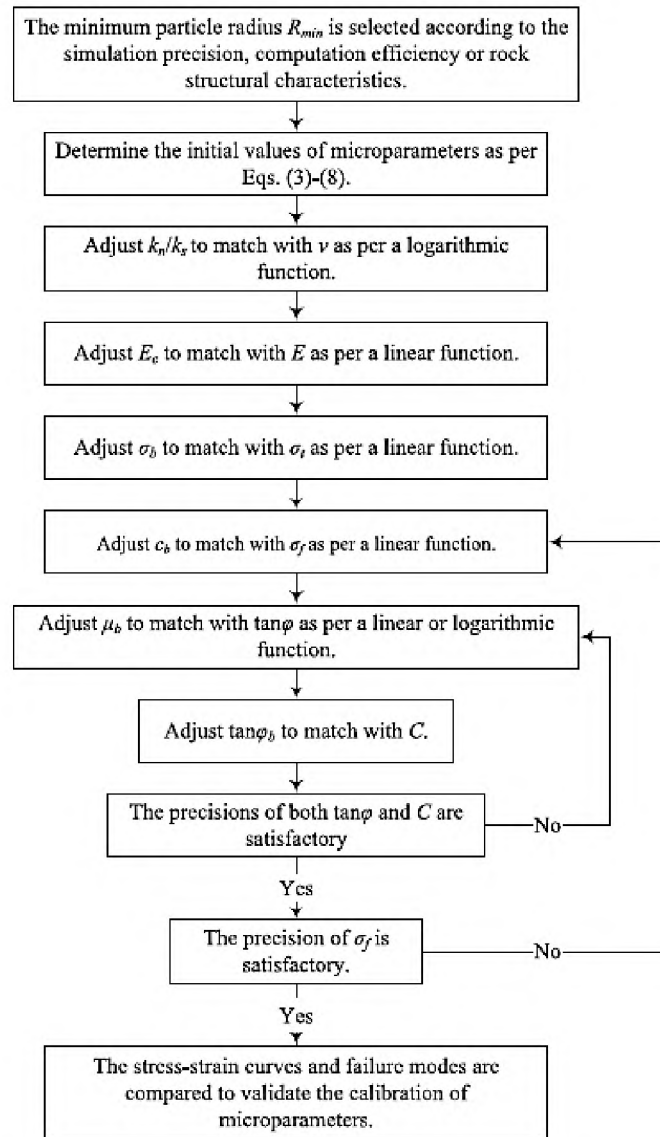


Figure 2.37. FJM calibration procedure (Chen, 2017).

2.5.4. Size Effects and Scaling in Numerical Modeling. The effect of lab samples on the strength of materials tested has been studied thoroughly by many researchers. Generally, smaller sized samples appear to be stronger than larger samples due to more flaws in the large samples than the smaller specimen. In numerical modeling, the same effect was realized where the tested strength varies with respect to the model size.

Koyama and Jing (2007) studied the effect of model scale and particle size on the micro-properties and rock failure processes. They used statistical methods to determine the representative elemental volume REV for 2D PFC models. They concluded that the REV for the 2D PFC model is 5 x 5 cm. At this dimension, the coefficient of variation is within an acceptable limit of 5%. They also observed that the REV increased with increasing heterogeneity of the particle sizes.

The effect of micro-structure and micro-parameters on the BTS of an FJM was studied by Xu et al. (2016). They divided the micro-structure into model size, model resolution, and degree of heterogeneity. They observed that as the thickness to diameter ratio increased, the tensile strength increased. They concluded that even though ISRM (2014) recommends a ratio of 1:2, if the coefficient of variation should be less than 7%, then the thickness to diameter ratio should be less than 1:2. Model resolution, which is the ratio of the smallest model dimensions to the average particle diameter, was found to inversely affect the tensile strength of the model. A resolution of 16.7:1 was recommended to achieve 5% coefficient of variation. The tensile strength was observed to decrease as degree of heterogeneity increased and leveled off at d_{\max}/d_{\min} of 1.67:1. In effect, these micro structural limits, if not met in any FJM simulation, the model will either underestimate or overestimate the tensile strength of the material.

Bahrani and Kaiser (2016) used a grain-based model and the regular PFC parallel bond model to investigate the influence of model size on the UCS of intact and defected rocks. They used the discrete fracture network (DFN) logic to model the defects in the intact rock. According to them, the strength of intact rock is independent of the model size, but they failed to account for the model resolution. They also observed that the influence

of the model size on the strength of a defected rock depends on the orientation and distribution of the discontinuities or defects. Generally, the strength decreased with increasing model size, until the size was large enough to capture all the defects representative of the defects in the rock mass.

Li et al. (2018) studied the roles of model size and particle size distribution on the macro-mechanical properties of granite using PFC. They tested seven different model sizes and four different particle size distributions. From their study, they realized that model porosity tended to decrease with increasing model size and increasing particle size heterogeneity. It was also realized that both tensile and compressive strengths are inversely related to model porosity. As a result, the pure effect of model size and particle size distribution was studied at constant model porosity. They concluded that at constant model porosity, strength decreased with increasing model size to a point ($D/d_{\max} \geq 20$; D is core diameter and d_{\max} is maximum particle diameter) and then leveled. This implies that for a reliable strength test, the model size (D/d_{\max}) should be at least, 20. They also concluded that all macro-mechanical properties decreased with increasing particle size heterogeneity.

Wang et al. (2018) applied the theory of similitude for the calibration of the micro-parameters of PFC models. Their purpose was to cut down the time required for trial-and-error calibration of PFC models by scaling known micro-parameters from previous tests. They discovered that the effect of the similitude constants was minimal with the similarity between the model and the prototype. The main determinant of the similarity is the model fabric. The fabric is dependent on the model resolution (i.e., the ratio of the smallest characteristic model length to the median particle diameter). As the sample resolution increased, the similarity of the model fabric to that of the prototype increased. Therefore,

to apply the similitude method to scale micro-parameters for PFC model calibration, the model resolution should be large enough (greater than 30) for the model to be similar enough to the prototype. Earlier, Huang et al. (2013) used similitude analysis and obtained the height to length ratio of 0.54 and a height to particle radius ratio of 112 to be sufficient for 2D rock cutting simulation in PFC.

2.5.5. Application of PFC in Rock Cutting Simulation. The success of PFC for rock cutting simulation is attributed to its ability to simulate the process of fracture formation during cutting. Studies that have used PFC to simulate rock cutting include Rizo (2010) who successfully simulated rock cutting with a drag pick using PFC2D; Zhao et al. (2012) used PFC2D to study the cutter-rock interaction during mechanical excavation. According to Ledgerwood III (2007), PFC2D yielded results of rock cutting that were comparable with results obtained from actual tests when cutting under confinement.

The simulation of a single roadheader pick cutting of a synthetic sandstone model was achieved by Rojek et al. (2011) using PFC2D and PFC3D. A similar study was conducted by van Wyk et al. (2014) using PFC3D in which they simulated the rock cutting with chisel-shaped and button-shaped picks.

Moon and Oh (2011) investigated the optimum rock cutting conditions of hard rock TBM. In their investigation, they simulated disc cutter indentation of the LCM during an excavation in PFC2D. The dimensions of their model were 20 cm x 7 cm. Multi-indentation was simulated while varying spacing and penetration. A linear relationship between the s-p ratio and the square of the brittleness of the rock was observed. They concluded that the optimized s-p ratio is governed by the brittleness of the rock and the thickness of the cutter.

Su and Akcin (2011) used graded particle assembly in PFC3D (Figure 2.38) to study rock cutting using a point attack cutter. The idea of modeling larger particles on the outside is to reduce computational time and keep the model large enough to avoid edge effects during cutting.

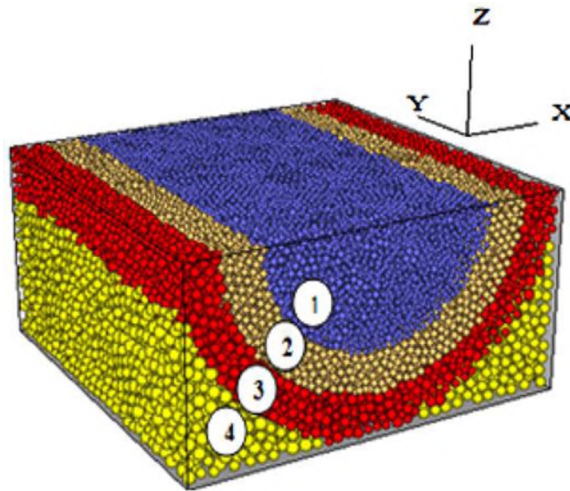


Figure 2.38. A graded model used for rock cutting simulation (Su and Ali Akcin 2011).

Choi and Lee (2015) studied the rock cutting process using disc cutter indentation. They used PFC3D to study the optimal spacing-penetration ratio at which specific energy is lowest, and they compared it with results obtained using AUTODYN3D and results from linear rock cutting machine experiments, concluding that the PFC3D results were closer to the LCM results than the AUTODYN3D results were. Therefore, it can be deduced that PFC3D gives a better rock cutting simulation than AUTODYN3D. The authors also observed that the effective magnitude and direction of the side forces were indicative of the level of interaction between adjacent cuts. Cuts with no interaction had symmetrical side forces, but the level of symmetry decreased as interaction increased. In their research,

they modeled the V-shaped disc cutter, which has a different geometry than the constant cross-section disc cutter.

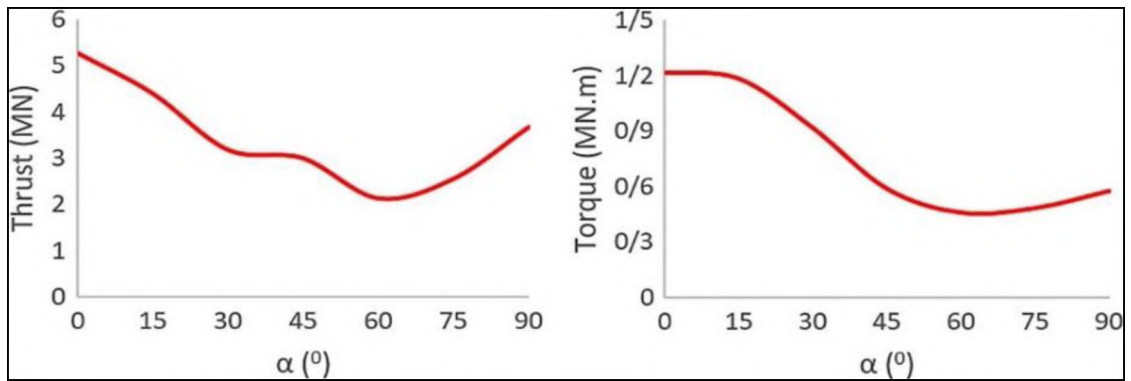


Figure 2.39. Required thrust (left side) and torque (right side) for different joint orientations (Afrasiabi et al., 2019).

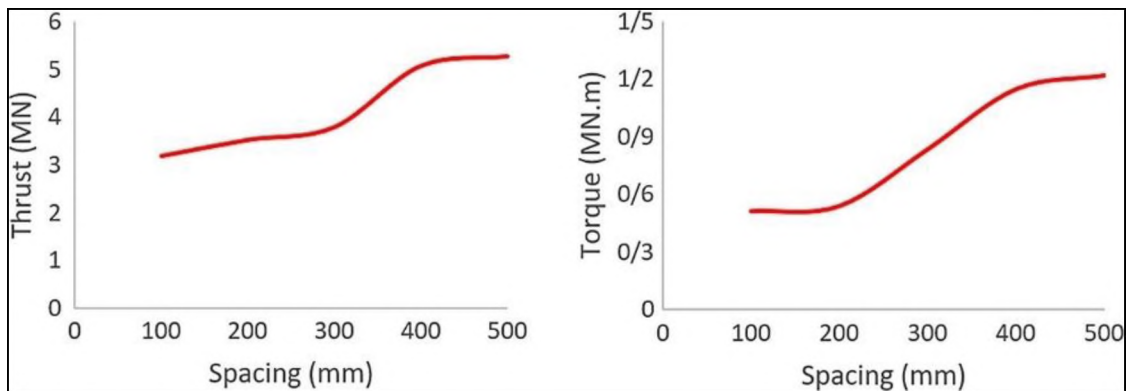


Figure 2.40. Thrust (left side) and torque (right side) required at different joint spacing (Afrasiabi et al., 2019).

A full-face simulation of a TBM excavation through a discontinuous rock using PFC3D was conducted by Afrasiabi et al. (2019) to study the effect of geometric parameters of discontinuities on TBM performance. According to them, discontinuities parallel to the tunnel axis had the least influence on machine performance, while the best performance was achieved when the discontinuities were at 60° to the tunnel axis (Figure

2.39). They also investigated the effect of joint spacing on TBM performance and concluded that the effect was highest with closely spaced joints and decreased as the spacing increased. At joint spacing greater than 400 mm, the influence of the joints on TBM performance was negligible (Figure 2.40). In their model, however, they used the parallel bonding logic, which is known to have issues with matching tensile and compressive strengths with those of the rock being modeled (Potyondy, 2013).

3. ROCK SAMPLES, LAB EQUIPMENT, AND EXPERIMENTATION

This section described the rock sample used for this research, including its mechanical properties, its preparation, and the linear cutting test procedure.

3.1. ROCK SAMPLES

The rock, Roubidoux Sandstone, is a slightly friable whitish quartz sandstone with reddish bands parallel to the bedding planes. The reddish banding is due to the presence of iron oxides in those layers. The rock also contains iron nodules that are visible in outcrops and the sample (Figure 3.2 & Figure 3.3). The grain size of the sandstone ranges from 0.10 mm to 1.00 mm (medium-grained sandstone). The grain sizes were measured under the Mitutoyo Toolmaker's microscope in the mineral processing laboratory of the Energetic Materials, Rock Characterization and Geomechanics (EMRGe) center at Missouri S&T (Figure 3.1).

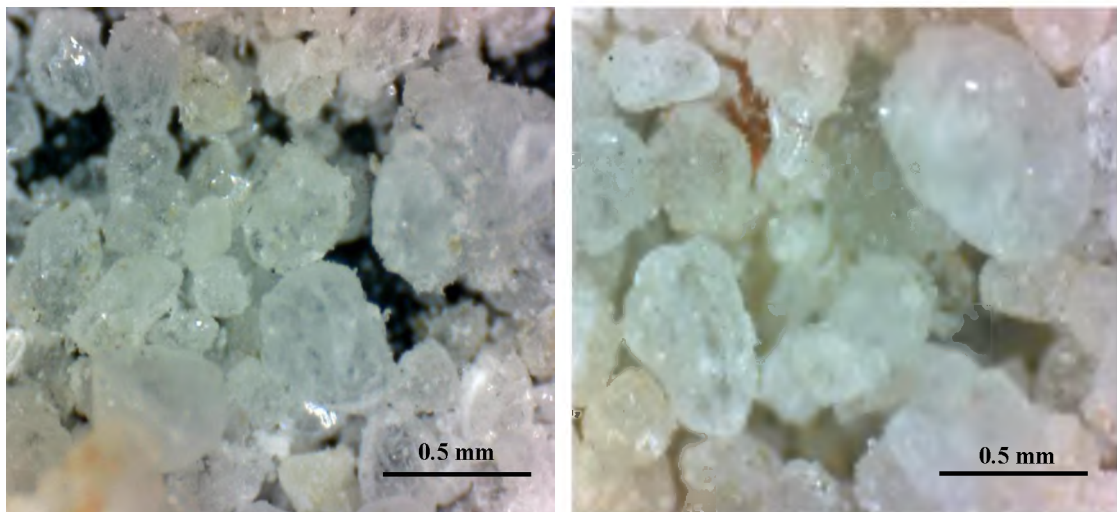


Figure 3.1. Quartz grain of the Roubidoux Sandstone under the Mitutoyo Toolmaker's microscope.

The Roubidoux Sandstone is part of the Roubidoux Formation whose age is early Ordovician (Bain and Ulrich, 1905). It is used as dimension stones and serves as a major aquifer (Heller, 1954). It is also a potential source of proppant for hydraulic fracturing.

The samples used for this research were obtained from the Rosati Sandstone Quarry in northeastern Phelps County, Missouri (Figure 3.4).



Figure 3.2. A close-up view of the Roubidoux Sandstone sample with an iron nodule.



Figure 3.3. Roubidoux Sandstone with iron nodules and reddish banding.

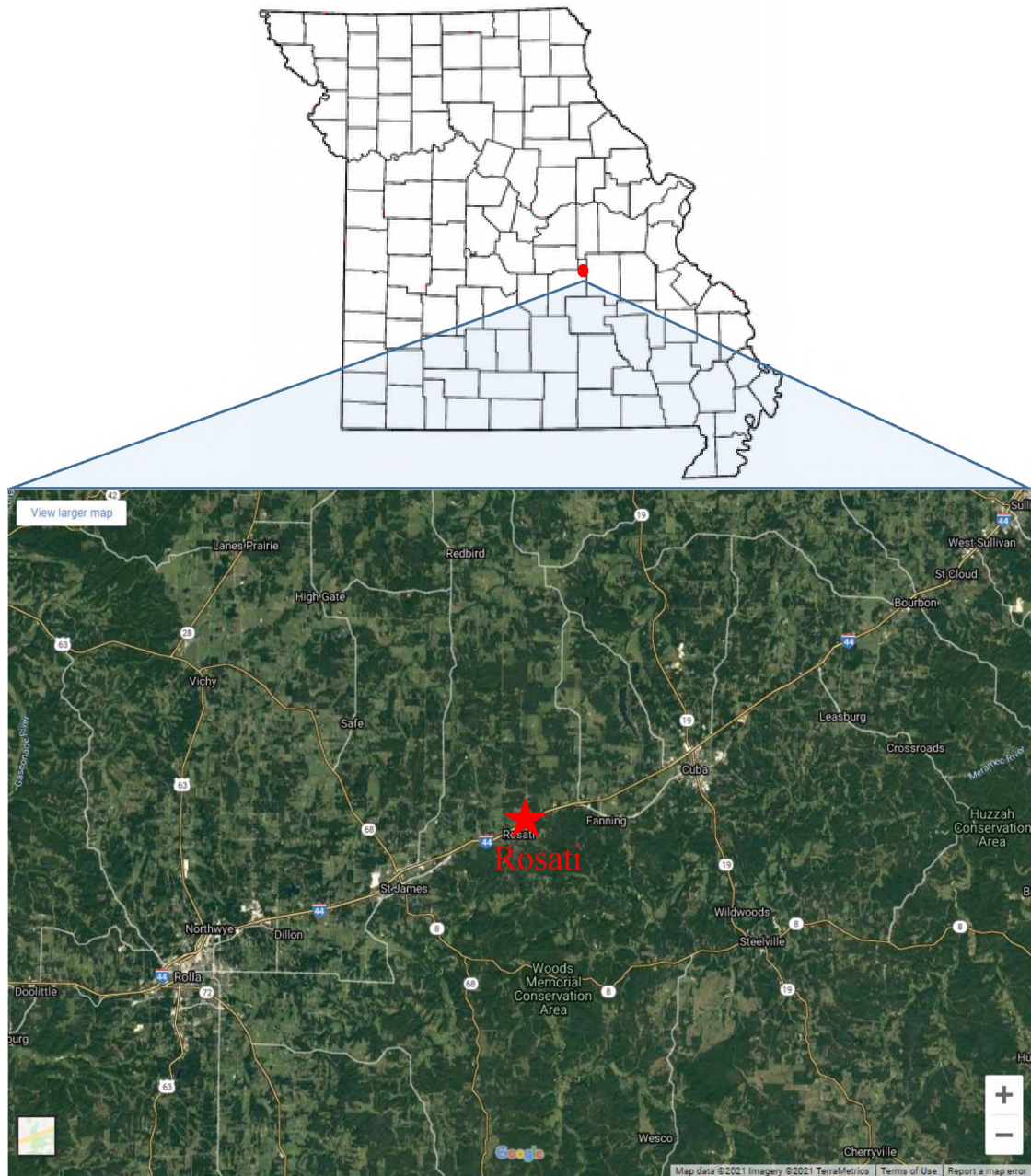


Figure 3.4. Location of the Rosati quarry where the Roubidoux Sandstone was collected.

3.1.1. Rock Mechanical Properties. The mechanical properties of the rock sample that were considered important for this research were tested in the core lab in RMERC. Uniaxial compressive strength (UCS) and Brazilian tensile strength (BTS) tests were conducted. The Young's modulus of the rock was obtained from the UCS test.

3.1.1.1. Uniaxial compressive strength. Ten (10) rock cores of length, 100 mm, and diameter, 50 mm (2:1 length to diameter ratio) were drilled from a block of the Roubidoux Sandstone following the procedures recommended in ASTM D4543. These cores were tested in the core lab according to ASTM D7012-10 under air-dried conditions (Figure 3.5). The formula for the calculation of the UCS is given in Eq. 3.1.

$$\sigma_c = \frac{4P_{max}}{\pi D^2} \quad (3.1)$$

Where; σ_c = uniaxial compressive strength;

P_{max} = maximum applied force/load at failure; and

D = diameter of core specimen in contact with load.

3.1.1.2. Measuring Young's modulus. During the compressive testing, the strain in the cores due to the applied load was recorded. The young's modulus was determined by plotting a stress-strain curve and computing the slope of the proportional portion of the curve (Figure 3.6) (ASTM E111, 1981). Young's modulus (E) is computed using Eq. 3.2.

$$E = \frac{\sigma_2 - \sigma_1}{\varepsilon_2 - \varepsilon_1} \quad (3.2)$$

Where σ_2 and σ_1 are stresses on the linear portion of the stress-strain curve; and

ε_2 and ε_1 are strains on the linear portion of the stress-strain curve.

3.1.1.3. Brazilian tensile strength. Ten (10) discs were drilled from the rock sample. The dimensions of the discs were of length 25 mm, and diameter 50 mm, per ASTM D4543. The samples were air-dried and tested in the core lab according to ASTM D3967-08. Brazilian tensile strength is calculated using Eq. 3.3. The strength sample dimensions and test results are shown in Table 3.1.

$$\sigma_t = \frac{2P_{max}}{\pi DL} \quad (3.3)$$

Where; σ_t = tensile strength

P_{\max} = maximum applied load at failure.

D = diameter of core sample.

L = length of core sample.

Table 3.1. Strength properties of the Roubidoux Sandstone (Kaba, 2018).

Rock Properties	Min., MPa	Max., MPa	Avg., MPa	Number of samples	Diameter, mm	Height, mm
UCS	62	82	72.8	11	50	100
BTS	4.6	8.1	6.0	13	50	25



Figure 3.5. Setup for UCS test showing a failed 100 mm x 50 mm core.

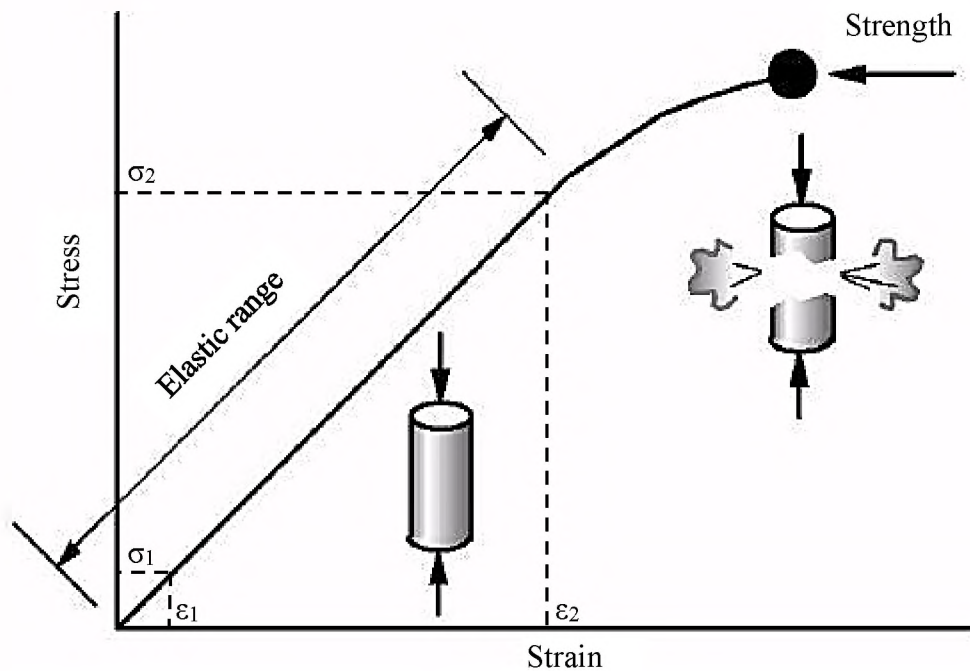


Figure 3.6. Illustration of the determination of UCS and Young's modulus.

3.1.2. Sample Preparation. The Roubidoux Sandstone block was sized approximately 100 x 50 x 40 cm (Figure 3.7) and placed in a rock box with concrete cast around the block to hold it firmly to the box (Figure 3.8). The rock box is a trapezoidal prism. The face of the rock to be cut was exposed at the wider side of the box. A black plastic was placed between the rock box and the concrete for easy removal of the rock remnant after the excavation experiments. The rock block was cast such that the bedding planes were horizontal. This was because of the dimensions of the available rock and the fact that the cutting was intended to excavate the rock across the layers simulating excavation perpendicular to discontinuities. The box was then welded to the top of the table of the LRCM, as shown in Figure 3.9.

A suite of laboratory property measurements was made on core samples from the rock sample to be excavated, including uniaxial compressive strength (UCS), Brazilian tensile strength (BTS), and Young's modulus (E), as discussed in Section 3.1.1.



Figure 3.7. A block Roubidoux Sandstone.



Figure 3.8. Casting of rock in rock box.

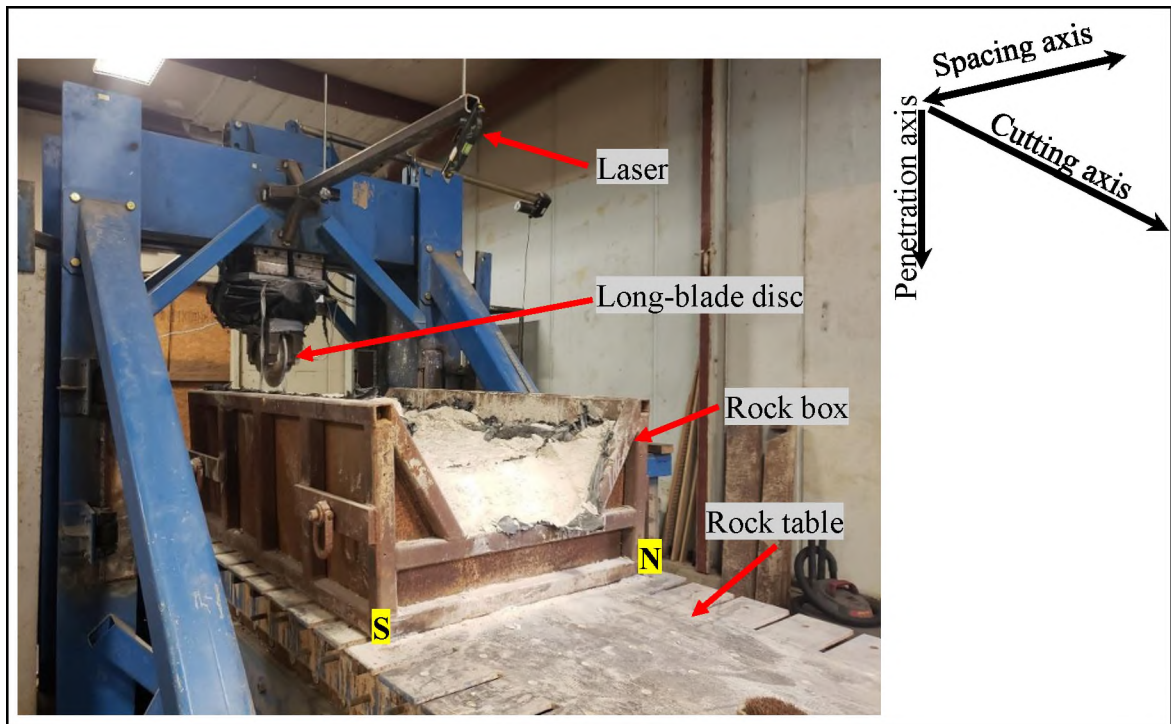


Figure 3.9. Rock sample set to the rock table of the LRCM with indications of direction cutting and penetration.

3.2. LINEAR ROCK CUTTING MACHINE AND INSTRUMENTATION

The linear rock cutting machine (LRCM) is composed of a movable rock table controlled by hydraulic systems, and an overhead load frame to which the cutter assembly is attached. The table can only move in the longitudinal direction, that is the direction of linear cutting. The cutter assembly is also movable but only in the transverse (side) direction relative to the direction of motion of the rock table. This is used to control the position of cutting (offsetting the cutter from one cut to the next). The cutter assembly is also adjustable in the vertical direction to control the depth of penetration of the cutter into the rock during cutting.

All the movable parts of the LRCM are hydraulically controlled. The motion of the rock table executes the cutting by moving the rock under the stationary cutter assembly at a fixed penetration depth. The cutter indents the rock based on the set depth of penetration and then rolls as the rock moves past it.

3.2.1. The Cutter Assembly. The cutter assembly is hydraulically movable vertically and laterally, when not cutting rock, as described previously. Between the assembly and the load frame is a stack of spacers, which adjusts the elevation of the cutter above the rock surface (Figure 3.10, Figure 3.11). The cutter holder has upper and lower plates that sandwich the 3D load cells (Section 3.2.2). The cutter is the last component of the assembly. It is held by a saddle through the cutter shaft. It is fixed such that it spins about its center and in a direction parallel to the motion of the rock table. The cutter is composed of the shaft which forms the rotating axis for the cutter. Roller bearings are arranged around the shaft controlling the rotational motion of the cutter ring and the amount of load that can be exerted on the cutter. A hub with a disc ring is set on the roller bearings (see Figure 2.4). The length of the ring blade used in this research was 60 mm, giving it the name long-bladed disc cutter. A shaft retainer encloses the bearings with seals between the hub and shaft retainer. Figure 3.11 is a photo of the cutter assembly on the LRCM. Lateral adjustments are made when the position of the cutter needs to change after making one complete cut. When the position and depth of penetration are set, the cutterhead is pulled firmly against the main frame by hydraulic means so that it is stable during cutting. After a pass is completed, the cutter assembly is lowered, so a spacer of specific thickness can be inserted between the cutter assembly and the frame to lower the cutter further into the rock.

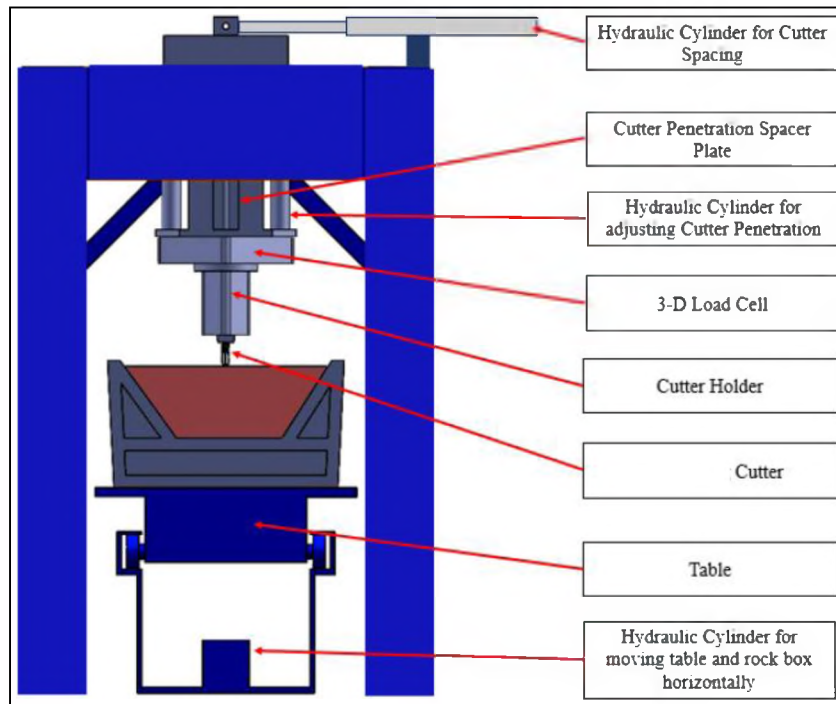


Figure 3.10. Schematic of the full-scale linear rock cutting machine (Kaba, 2018).

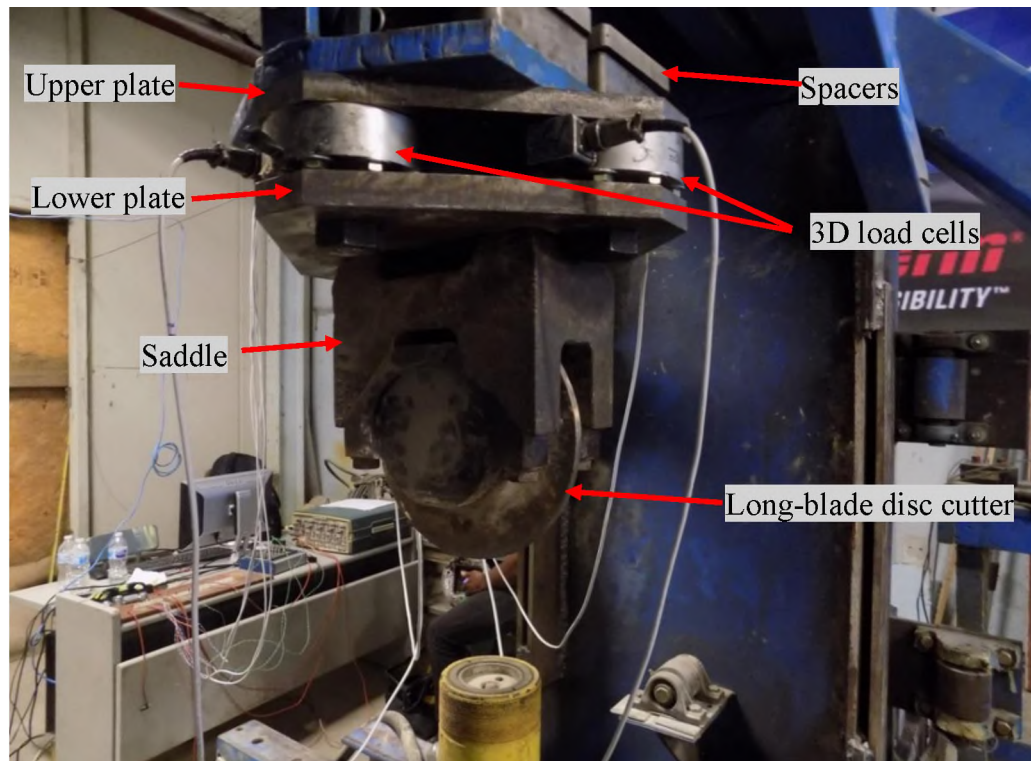


Figure 3.11. Cutter assembly.

3.2.2. Load Cells. The 3D load cell is comprised of four load Omega LCHD-20K/N load cells (Figure 3.12), which are arranged in a diamond shape such that two are aligned in the direction of motion of the rock table and the other two are aligned perpendicular to the cutting direction. Each has a load capacity of 89 kN (20,000 lbf). They are arranged such that their readings can be combined to measure the two horizontal forces acting parallel and perpendicular to the cutter, as well as the vertical force.

A known voltage is sent through the input terminals. The voltage returned through the output terminals corresponds to the amount of stress exerted on the load cells. The input terminals are connected to a power source, which supplies the known voltage. The output terminals are connected to a data acquisition system that measures the amount of voltage output from the load cells.



Figure 3.12. A typical Omega LCHD-20K/N load cell.

3.2.3. Disc Cutter. The cutter used in this study was the long-bladed constant cross-section (CCS) disc cutter from the Robbins Company. The dimensions of the cutter are a diameter of 292 mm and a blade thickness of 11 mm. Figure 3.13 is a long-bladed CCS disc cutter, and Figure 3.14 is a schematic of a disc cutter with the lines of action of the various forces acting on the cutter relative to the direction of cutting.

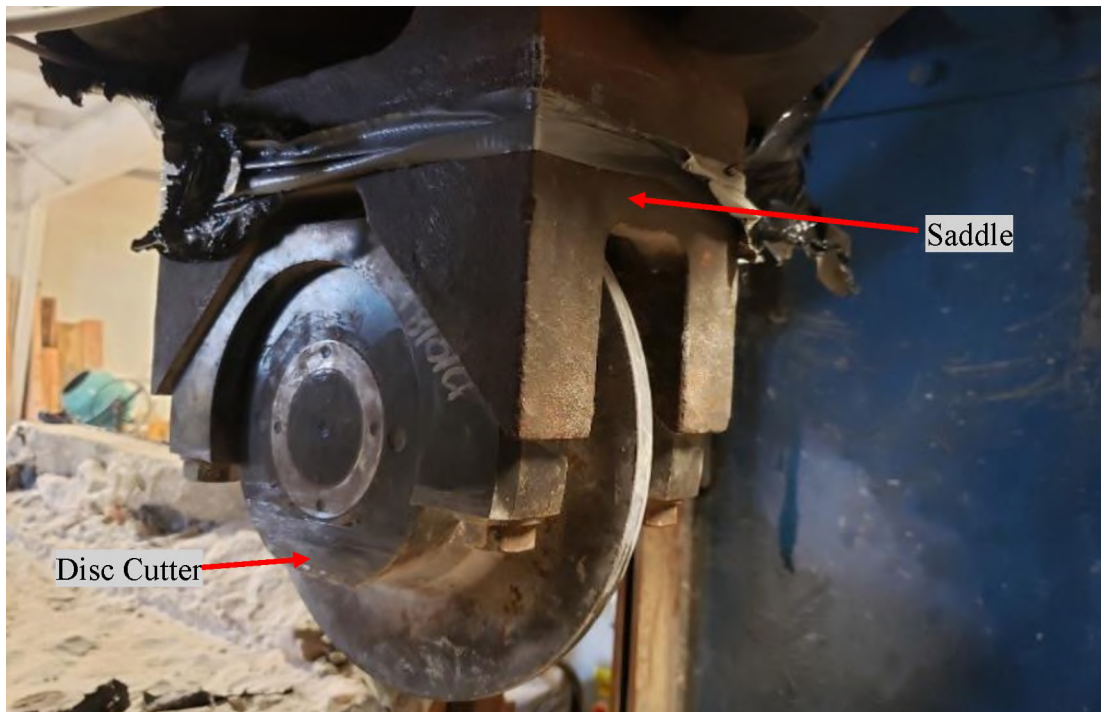


Figure 3.13. Constant cross-section long-blade disc cutter and saddle donated by Robbins Company.

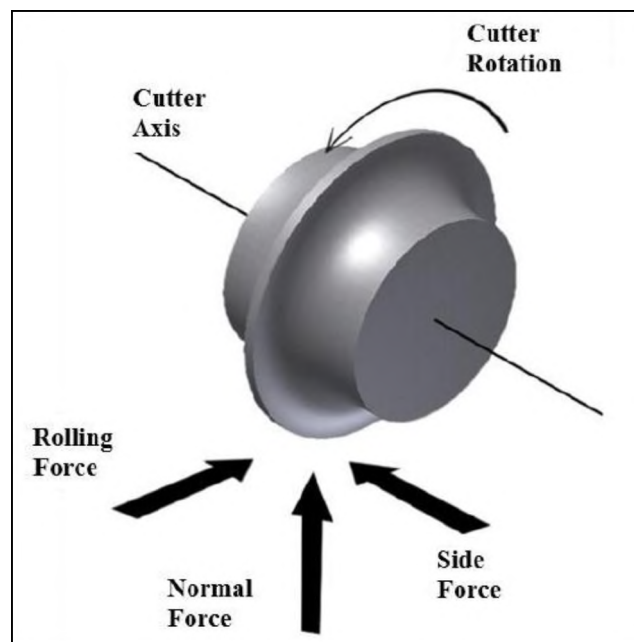


Figure 3.14. Schematic of disc cutter with force resolutions.

3.2.4. Linear Displacement. A string potentiometer (string pot) was used to measure the position of the rock table at every point in time during the cutting. It consists of a measuring cable, a spool, a spring, and a rotational sensor. The cable or wire is wound on a precisely machined cylindrical spool. A spring is coupled to the spool to maintain the tension in the wire, and the spool is also coupled to the rotational sensor. The spool and the sensor rotate when the wire is drawn, creating an electrical signal that is proportional to the length of the wire that has been drawn.

The string potentiometer was attached to the non-movable frame of the LRCM and the end of the wire was attached to the end of the movable part of the rock table. It was ensured that the wire was horizontal. The output terminal of the string pot was connected to the data acquisition system that reads and records the electrical signal generated by reeling and unreeling the wire. This system measures the exact location of the rock during cutting. Figure 3.15 is a photo of a string potentiometer.



Figure 3.15. String potentiometer.

3.2.5. Data Acquisition System. The data acquisition (DAQ) system includes sensors, transducers, cables that connect the various components, the NI USB 6361 BNC module (Figure 3.16), and the control software (LabVIEW). The DAQ system was connected to a Windows 10 operating desktop computer through a USB cable. The

computer had the LabVIEW software installed on it. The output terminals of the load cell components and the LVDT were connected to the BNC (Bayonet Neill-Concelman) pinouts of the DAQ system. The input terminals of the load cells were connected to a power source supplying a known voltage. The USB 6361 BNC module read the output voltages from the load cells and the string pot. These voltages were visualized and recorded by the LabVIEW software and later exported into Excel. The setup for the data acquisition system is presented in Figure 3.17.



Figure 3.16. USB 6361 NBC DAQ module from National instruments.

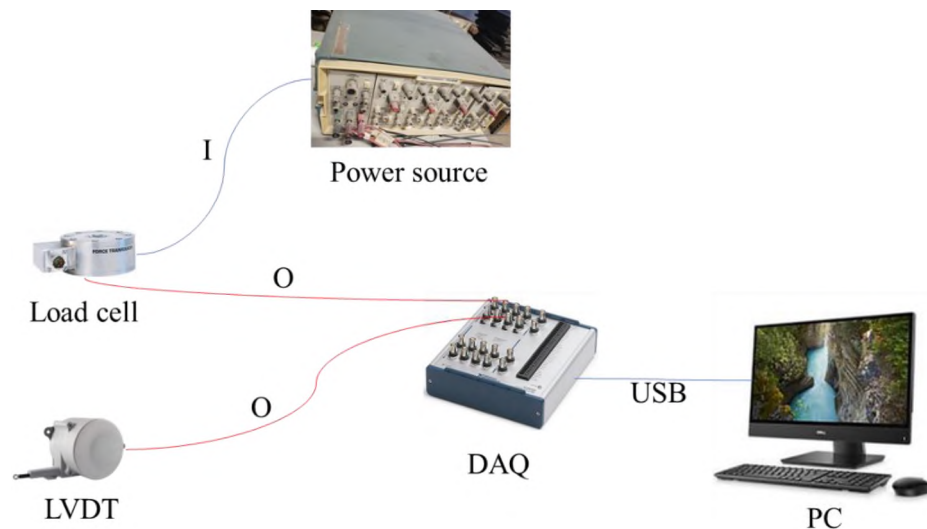


Figure 3.17. Layout of the data acquisition system setup (I – input signal, O – output signal).

3.2.6. Schmidt Hammer. The Schmidt hammer used in this study to measure the rock surface hardness was manufactured by Proceq. The N-type hammer in Figure 3.18 is particularly useful for assessing the integrity of rocks with a uniaxial compressive strength between 1 MPa and 100 MPa. It meets the ASTM D5873 standards. The Schmidt hammer consists of a tubular housing enclosing a mass that is controlled by a spring. The mass slides on a plunger attached to the tip of the hammer. Measurements are obtained by pressing the hammer gently against the rock surface. When the hammer tip is pressed against the surface, the spring-controlled mass with constant energy is released and impacts the rock surface through the plunger and tip (Figure 3.19). The mass rebounds upon impacting the surface, and the level is recorded on a graduated scale or digitally and stored in the hammer memory. The level of rebound depends on the hardness of the surface. Softer surfaces absorb more energy, resulting in a lower rebound and harder surfaces absorb little energy, yielding a higher rebound (Mishra, 2014). Due to the gravitational effect on the hammer mass, it is recommended that it be used in the vertical position. However, it must always be perpendicular to the surface being tested. In case the angle of application deviates from the vertical, a correction factor should be applied to the results to compensate for the gravitational effect.

3.2.7. Laser Imaging System. The imaging system was composed of a laser light source that produces red light structured linearly and a GoPro Hero 4 Black camera. These were mounted on a metal frame hanging directly over the rock surface. The camera was mounted on the load frame of the LRCM. The frame extended 20 cm from the overhead frame of the LRCM. The laser was mounted at the end of the frame at an angle of 45° from the horizontal towards the camera (Figure 3.21), and it was adjustable vertically adjustment

according to the elevation of the rock surface, thus allowing for imaging of the rock surface as it was lowered due to excavation. The camera was mounted at 6.30 cm from the cutterhead frame and pointed vertically downward, making a 90° angle with the rock surface. The elevation of the camera was also made adjustable vertically. During imaging, the height of the laser and the camera were set such that the structured laser light was projected to the center of the camera's field of view. The arrangement of the laser and camera used in this setup was to eliminate the need for height correction after capturing the images (Maerz et al., 2001). The setup is presented in Figure 3.20.



Figure 3.18. Silver N-type Schmidt hammer.

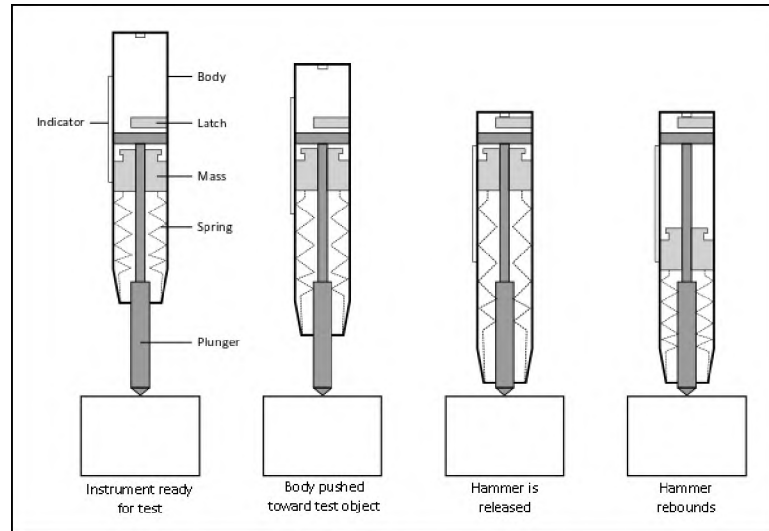


Figure 3.19. Schematic of the working principle of the Schmidt hammer (Schick, 2019).

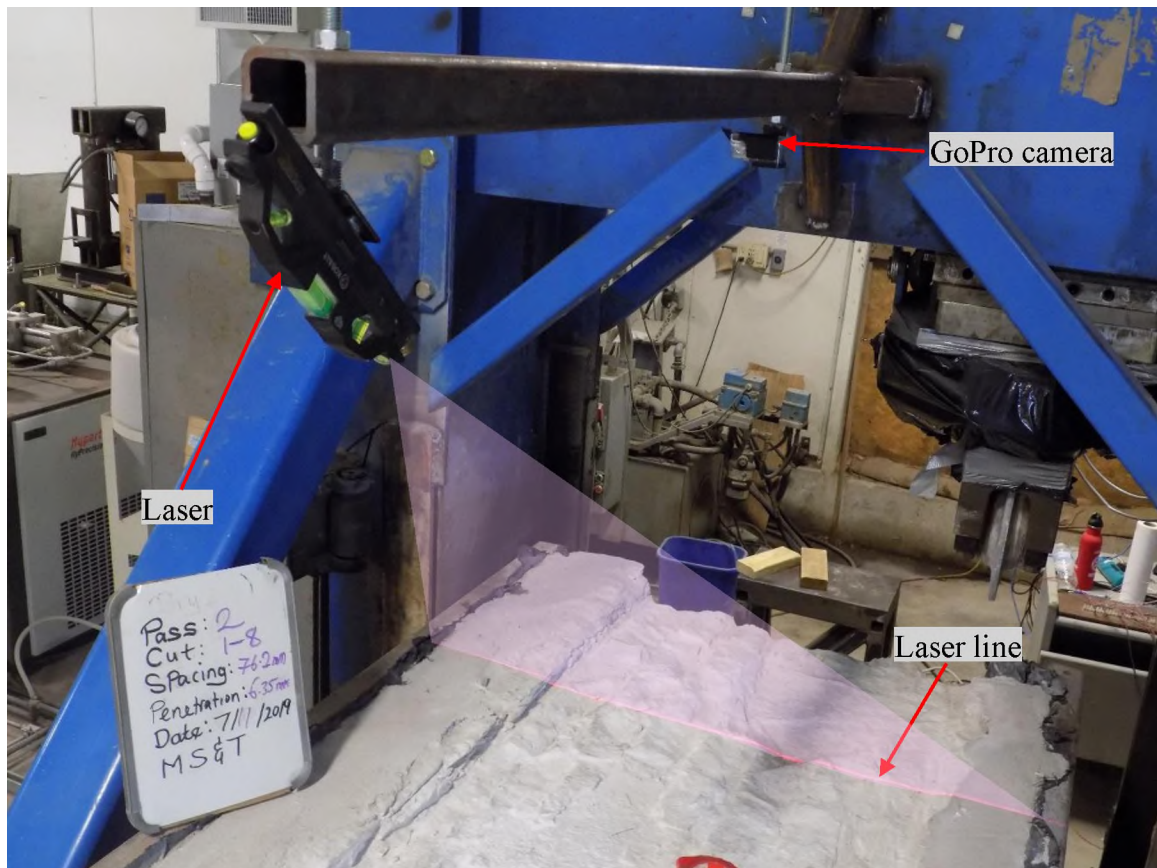


Figure 3.20. Setup for laser imaging with laser light and camera set at 45° in a perspective view.

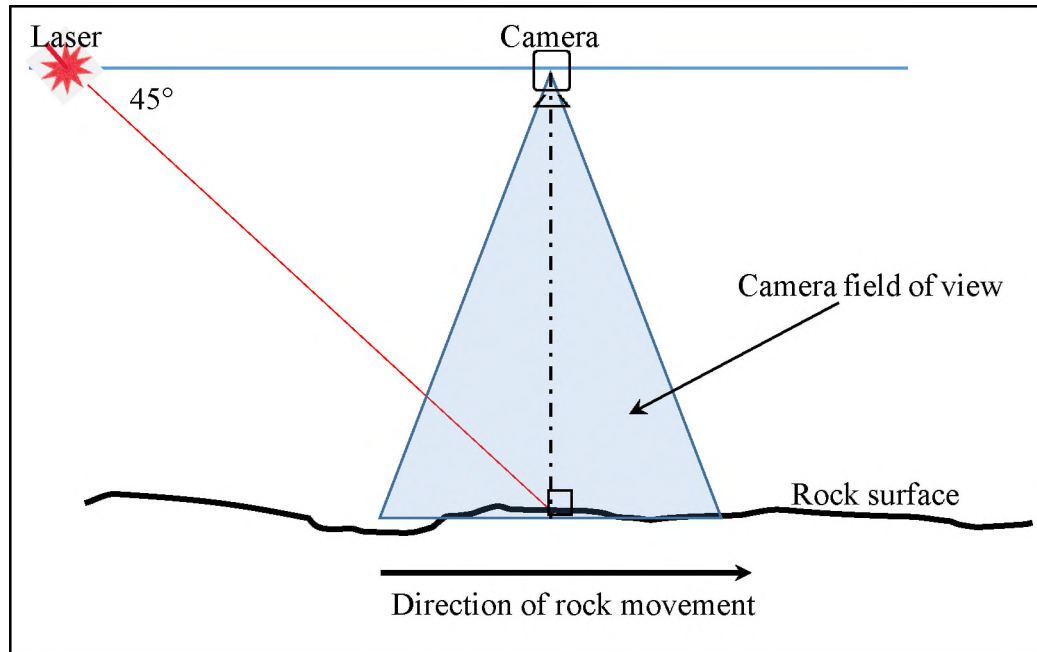


Figure 3.21. Schematic of rock surface imaging system in a side view.

3.3. EXPERIMENTAL SETUP AND EXECUTION

3.3.1. Instrument Calibrations. The load cells were calibrated for measuring 3D cutting forces and the LVDT was calibrated for measuring the position of the rock being cut. These calibrations were necessary for computing the cutting forces and rock location from the output voltages.

3.3.1.1. Calibration of load cells. Before starting the cutting experiments, the 3D force sensor, which is used to measure the 3D cutting forces, was calibrated using an Enerpac[®] hydraulic pump and jack and the DAQ system. A 7.5° wedge was used to set the hydraulic jack at 7.5° in a direction opposite to the load cell to be calibrated. This was necessary to exert the load in the same direction as the loading direction experienced during cutting, and to enable the resolution of the load into its three orthogonal components – side force, rolling force, and normal force (Gertsch, 2000). The hydraulic pump was then used

to increase the stress exerted on the cutter by the jack in increments of $6.89\text{E}3$ kPa ($1.00\text{E}3$ psi). Six increments were made from 0 kPa to a maximum pressure of $3.44\text{E}4$ kPa ($5.00\text{E}3$ psi) followed by six decrements of $6.89\text{E}3$ kPa from $3.44\text{E}4$ kPa to 0 kPa. At each pressure point, output voltages from all the load cells were read by the DAQ system and recorded using the LabVIEW software. This process was repeated for each load cell by changing the position of the 7.5° wedge. The setup for the load cell calibration is shown in Figure 3.22.

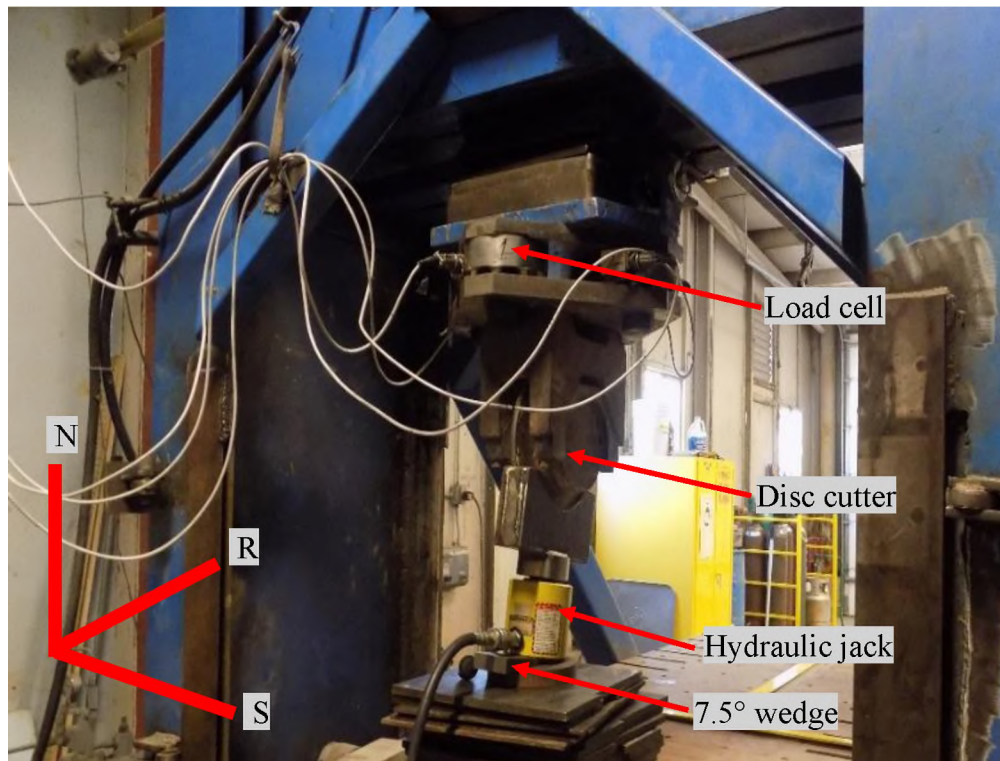


Figure 3.22. Setup for calibration of load cell 3.

Equilibrium analysis of the forces and moments on the disc cutter based on the stresses recorded by the various load cells yielded equations that relate the side, rolling, and normal forces to the output voltages of the load cells. The equilibrium analyses were

based on the free body diagram in Figure 3.23 with the moment arms shown in Figure 3.24. Under quasi-static equilibrium conditions, the sum of all external forces acting on a body is equal to zero and the sum of the moments of the external forces about a point is equal to zero. The equilibrium analyses are presented in the following section.

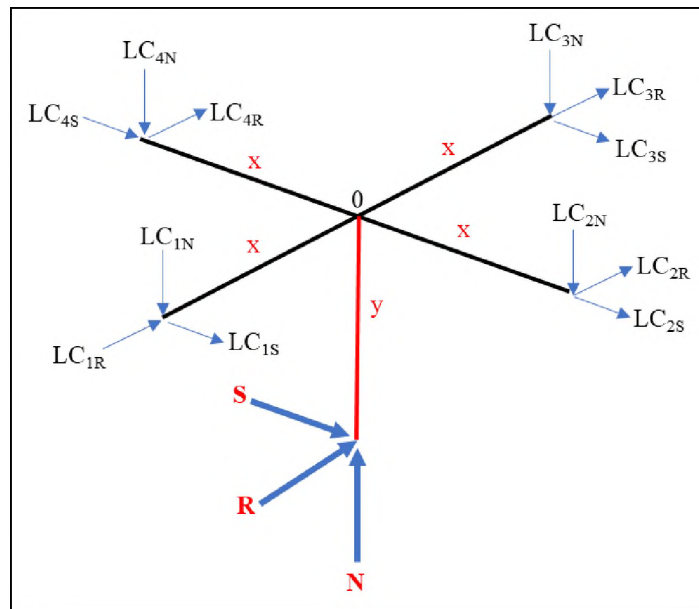


Figure 3.23. Free body diagram of load cells and cutter forces.

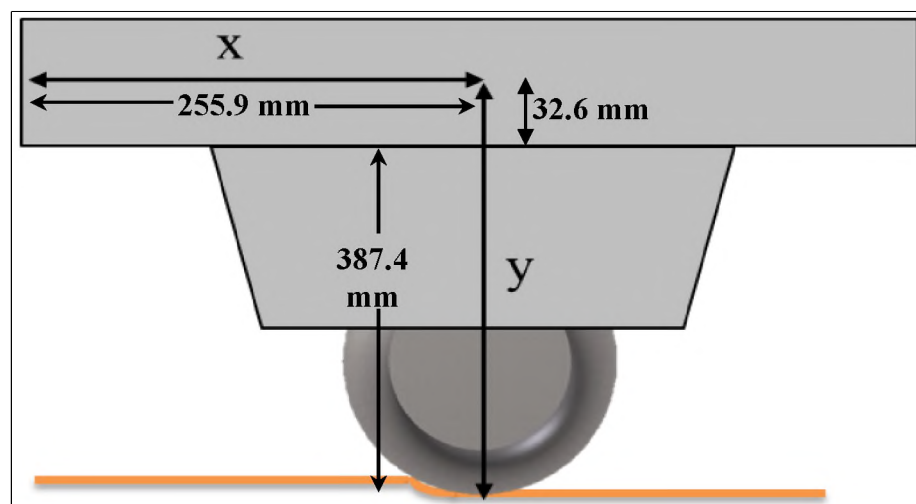


Figure 3.24. Side view of the moment arms acting on the disc cutter.

Force equilibrium

$$\Sigma F_N = 0;$$

$$N - (LC_{1N} + LC_{2N} + LC_{3N} + LC_{4N}) = 0$$

$$N = \Sigma LC_N \quad (3.4)$$

$$\Sigma F_R = 0;$$

$$R - (LC_{1R} + LC_{2R} + LC_{3R} + LC_{4R}) = 0$$

$$R = \Sigma LC_R \quad (3.5)$$

$$\Sigma F_S = 0;$$

$$S - (LC_{1S} + LC_{2S} + LC_{3S} + LC_{4S}) = 0$$

$$S = \Sigma LC_S \quad (3.6)$$

Moment equilibrium

$$\Sigma M_N = 0;$$

$$(LC_{3S} - LC_{1S}).x + (LC_{2R} + LC_{4R}).x = 0 \quad (3.7)$$

$$\Sigma M_R = 0;$$

$$(LC_{2N} - LC_{4N}).x + S.y = 0 \quad (3.8)$$

$$\Sigma M_S = 0;$$

$$(LC_{3N} - LC_{1N}).x + R.y = 0 \quad (3.9)$$

From equation 3.6;

$$(LC_{1S} - LC_{3S}) = (LC_{2R} - LC_{4R})$$

From equation 3.7;

$$S = (LC_{4N} - LC_{2N}).\frac{x}{y} \quad (3.10)$$

From equation 3.8;

$$R = (LC_{1N} - LC_{3N}) \cdot \frac{x}{y} \quad (3.11)$$

Where N = normal force;

R = rolling force;

S = side force;

LC₁ = load cell one;

LC₂ = load cell two;

LC₃ = load cell three;

LC₄ = load cell four;

x = horizontal distance between the load cell and cutter-rock contact (horizontal moment arm to the center of the load cell); and

y = vertical distance between the load cell and cutter-rock contact (vertical moment arm to the center of the load cell).

Moment arm ratio for the long-bladed disc cutter

$$x = 255.9 \text{ mm}$$

$$y = 355.6 \text{ mm (disc cutter + saddle)} + 31.75 \text{ mm (lower plate thickness)} + 9.53 \text{ mm (bottom of load cells)} + 23.02 \text{ mm (half of load cell thickness)} = 419.9 \text{ mm}$$

$$\text{Moment Arm Ratio} = x/y = 0.6094$$

Equations 3.4, 3.11, and 3.10 give the output voltages representing the normal force, rolling force, and side force, respectively. The calibration load increments were plotted against the normal, rolling, and side voltages, and the straight lines were fitted to them. The best-fit linear equations of these curves were used to convert output voltages recorded during cutting into the 3D cutting forces.

3.3.1.2. Calibration of string potentiometer. The rock travel under the cutter was monitored by a string potentiometer attached at one end to the fixed frame on which the cutter was mounted, and at the other end to the rock table. To calibrate it, a meter-ruler was attached to the rock table and positioned parallel to the travel direction (Figure 3.25). The rock table was moved incrementally in the direction of cutting and the output voltage from the string potentiometer was recorded by the DAQ (section 3.2.5) at 5 cm intervals from 0 to 25 cm. This provided the voltages corresponding to each position (5 cm interval) of the rock table. The distances were plotted against the measured voltages and a straight line was obtained. The equation of this line was then used to convert all voltages into distances during the rock cutting process. This gave a continuous reading of the location of the rock during the cutting and imaging.

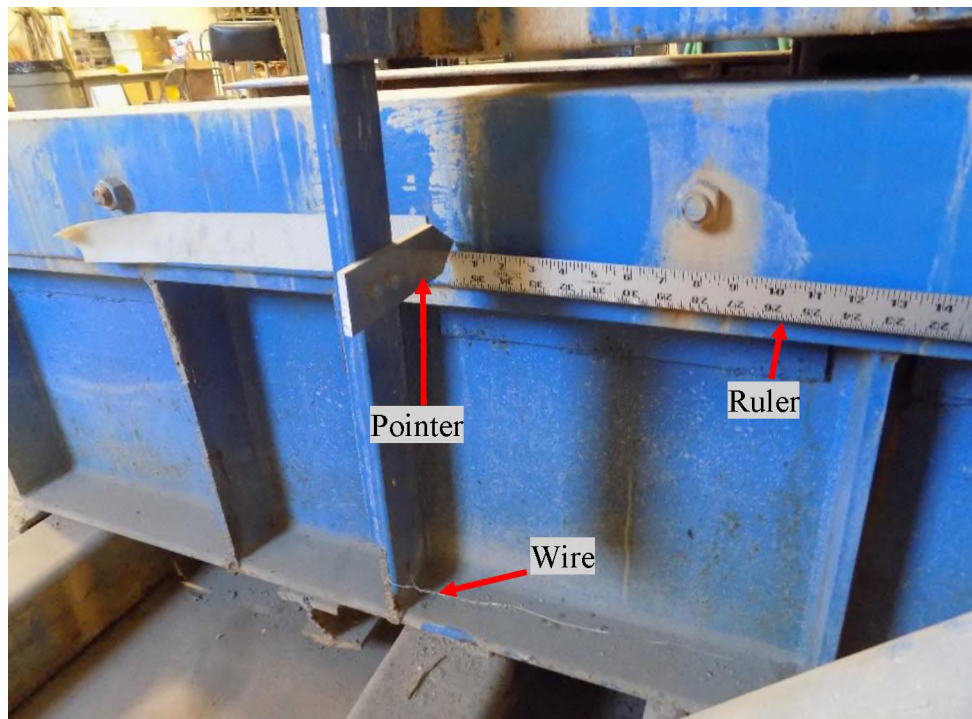


Figure 3.25. Setup for string potentiometer calibration.

3.3.2. Linear Rock Cutting. To set up the calibrated LCM for the cutting, the cutter assembly was moved to the northern end (see Figure 3.9 and Figure 3.9) of the crossbeam, where the first cut was designed to start. The cutter was lowered using the hydraulic controls and spacers stacked between the saddle and crossbeam such that the cutter overlapped the rock surface by 6.35 mm (the designed penetration) (Figure 3.26). The cutter assembly was tightened using the overhead hydraulic controls to ensure that it was stiff during cutting. The rock was then forced past the cutterhead by moving the LCM table to the east. The table was moved at a constant speed until the eastern end of the rock block had passed through the cutter. This completed one cut. As the rock moved past the cutter, the cutter indented the rock surface while rolling on it. The indentation and rolling caused fracturing resulting in rock fragmentation immediately or in subsequent cuts and passes. The cutter assembly was lifted by removing one or two spacers, and the LCM table was returned to its original position. The cutter assembly was indexed sideways (to the south) by 76.2 mm to the position of the second cut using the overhead hydraulic controls. The cutter elevation was set again, and the second cutting was done. Eight such cuts were made in this manner completely planing the target area, forming one pass. After the last cut on a pass, the cutter assembly was moved to the position of the first cut, and the cutter was lowered to a new elevation and the cutting process repeated.

The first three passes were conditioning passes, meant to get the condition of the rock to the level of damage that the first penetration was expected to cause so that the first data pass was consistent with subsequent data passes. The cutter penetration used for the first three conditioning passes was 6.35 mm and the spacing was 76.2 mm.

After the last conditioning pass, four passes were excavated at the same penetration (data passes). These four passes represent repetitions of the cutting at this level of penetration (6.35 mm) and spacing (76.2 mm).

The process of conditioning and cutting was repeated with penetrations of 9.53 mm and 12.70 mm at a constant cut spacing of 76.2 mm. Two conditioning passes were made for penetrations 9.53 mm and 12.70 mm, totaling seven conditioning passes and 12 data passes. All the passes consisted of eight cuts, except the last three passes of penetration 12.7 mm in which the size of the rock box restricted the number of cuts to seven on each pass. The design of the cutting experiments is presented in Table 3.2.

Table 3.2. Design of cutting process.

Penetration, mm	No. of conditioning passes	No. of passes	No. of cuts per pass
6.35	2	4	8
9.53	2	4	8
12.70	2	4	8 (pass1) & 7 (passes 2-4)

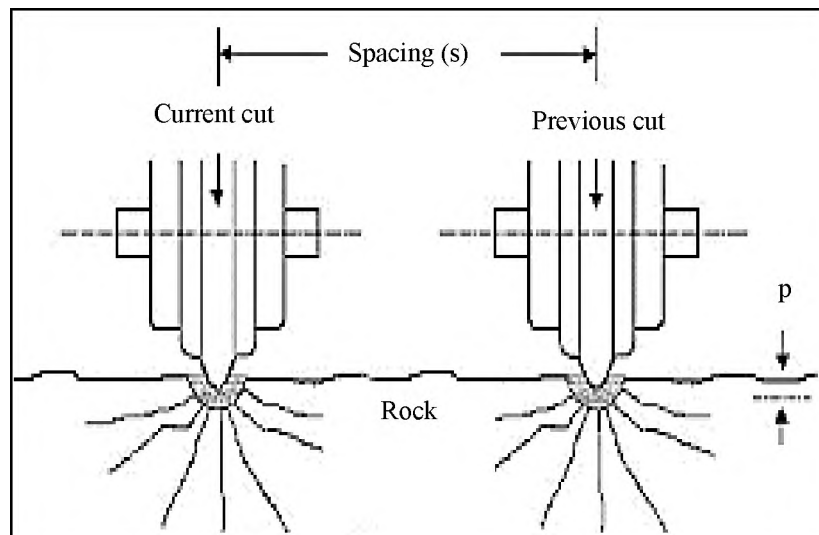


Figure 3.26. Illustration of cutting geometry, p – penetration (Rostami and Ozdemir, 1993).

During the cutting, the voltage outputs from the load cells and the LVDT were recorded by the DAQ system. These were converted to 3D forces and linear position of the rock table, respectively, for each cut.

3.4. FRAGMENT SIZE ANALYSIS

After excavation of each complete pass, the rock fragments—including the dust—were collected into a container. Sieve analysis was conducted on each set of excavation pass fragments. A set of four sieves was used for the fragment size analysis, with openings sized 50.80 mm, 25.40 mm, 9.40 mm 1.65 mm. Fines were captured in a pan at the bottom of the stack (Figure 3.27). The container of fragments was poured on the top sieve, and the set was manually shaken such that finer materials dropped to the sieve with a smaller mesh size.

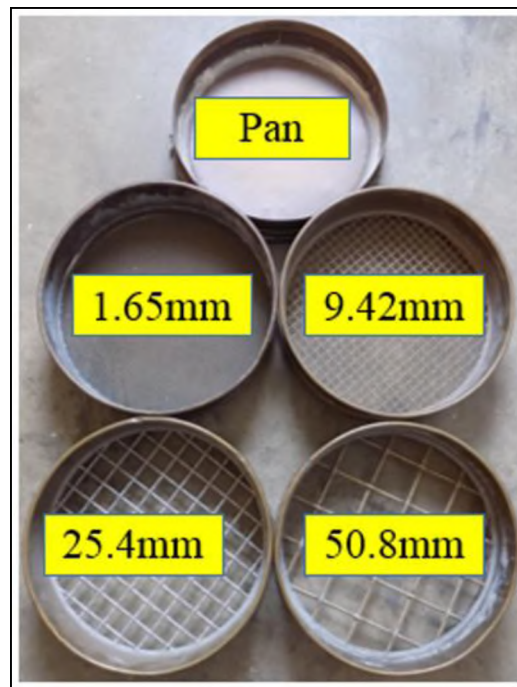


Figure 3.27. Set of Sieves for chip size analysis.

The mass of fragments retained by each sieve was weighed and recorded. This process was repeated for all the passes, including the conditioning passes. The fragment masses obtained from the sieve analysis were used to calculate several fragment size distribution parameters such as coarseness index, absolute size constant, and large fragments fraction (see Section 5.1.6).

3.5. IRREGULARITIES MEASUREMENT

The irregularities measurement was achieved by a simple structured laser light and GoPro Black 4 camera. The camera was fixed at a 90° angle to the surface of the rock to be imaged. The laser light source was fixed at 45° to the camera. The height of the laser light and the camera was adjustable in order to keep the distance from them to the surface of the rock relatively constant when the surface of the rock was lowered during the cutting. The setup of the imaging system is illustrated in Figure 3.20.

3.5.1. Image Acquisition. After each pass, the chips were collected, and the surface of the rock was cleaned of any dust to prepare it for imaging. The imaging was achieved by moving the rock table with excavated rock under the camera and light at a constant velocity so that the laser line is perpendicular to the direction of cutting. To get maximum contrast between the rock and the laser light, the imaging was done at night. During the imaging, the light in the lab was turned off leaving the laser light as the only light in the room. The camera was set to capture the video at 50 fps. A mobile phone app was used to control the camera. After all the instrumentation was set for the recording, the video mode of the camera was switched on from the phone app, and the hydraulic controls of the rock table were used to move the rock in the direction of cutting. Videos were recorded for both

forward and backward strokes of the table for quality check purposes. The edges of the data window were marked with wooden bars. A bar of 25.4 mm thickness was fixed to the edge of the rock box to serve as a scale for the vertical magnitude of the amplitude of the surface irregularities.

3.5.2. Processing of Surface Images. The laser images were processed using MATLAB[®]. The videos were cropped to the size of the data window, and all the picture frames were extracted using video-to-jpg software. In MATLAB, codes were written to extract the edges of the illuminated area (the edge of the laser light) for each picture frame, and noises were removed to increase the accuracy of irregularities measurements. This resulted in millions of 3D coordinates (point cloud) of the surface. The density of these points depended on the speed at which the surface was moved across the light and the fps at which the videos were captured. Triangulation was then applied to the point cloud collected to generate a triangulated irregular network (TIN). The coordinates were plotted in MATLAB to generate the 3D surface from which irregularities parameters—like ridge volume and overbreak volumes—were calculated. The volume of rock material left above the nominal cutting depth on the ridges between cuts (ridge volume) and the volume of rock material that was excavated beyond the nominal cutting depth (overbreak volume) was also determined from the digital elevation models generated from the surface imaging.

The edge detection was achieved using Canny's edge detection algorithm. This algorithm involves three stages (Canny, 1986). It first applies a Gaussian blur to reduce the noise in the images. The second stage applies the Sobel kernel for finding the light intensity gradient. The intensity gradient helps isolate areas with a high potential of being edges (areas with high light intensity gradient). Thresholding is the final stage of the algorithm.

Minimum and maximum threshold values were selected such that all points that fall above the maximum threshold value were traced as a continuous edge. All points below the minimum were omitted. Points between the minimum and the maximum were only considered as edges if they were connected with points above the maximum threshold.

3.6. HARDNESS MEASUREMENT

The hardness of the rock surface is a measure of the integrity of the rock material (ASTM, 2000). In this research, it was set out to determine how the excavation affected the hardness of the rock surface and to establish the relationship between excavated surface hardness and specific energy. An established relationship will be useful in the prediction of the penetration rate of TBM and hence, its efficiency.

The common measure of surface hardness of geomaterials is the rebound number measured using the Schmidt hammer. According to ASTM (2000), the uniaxial compressive strength range for which the use of the Schmidt hammer is applicable for hardness measurement is 1-100 MPa. The rock sample studied in this research, the Roubidoux Sandstone has a UCS range of 43-51 MPa (Abu Bakar et al., 2013); therefore, the Schmidt hammer was suitable for the surface hardness determination. The rebound hardness number, H_R , is a dimensionless number representing a relative measure of the hardness of the rock material. The rebound hardness value can be related to the strength of the rocks near the excavated surface.

The hardness measurement was done after the imaging of the excavated surface was completed. To measure the hardness, it is required that the hammer be perpendicular to the surface being measured (ASTM, 2000). The hammer was positioned perpendicular

to the surface and pushed gently until it rebounded. The rebound value was recorded, the hammer moved to the next marked location, and the measurement repeated. To have a regular outline of hardness measurement locations and ensure verticality of the Schmidt hammer, two lasers were mounted on perpendicular bars fixed to the edges of the rock box. Each of the bars was grooved at 25.4 mm (1 in) intervals such that the laser indexed at 25.4 mm for each measurement. The setup for the hardness measurement is shown in Figure 3.28.

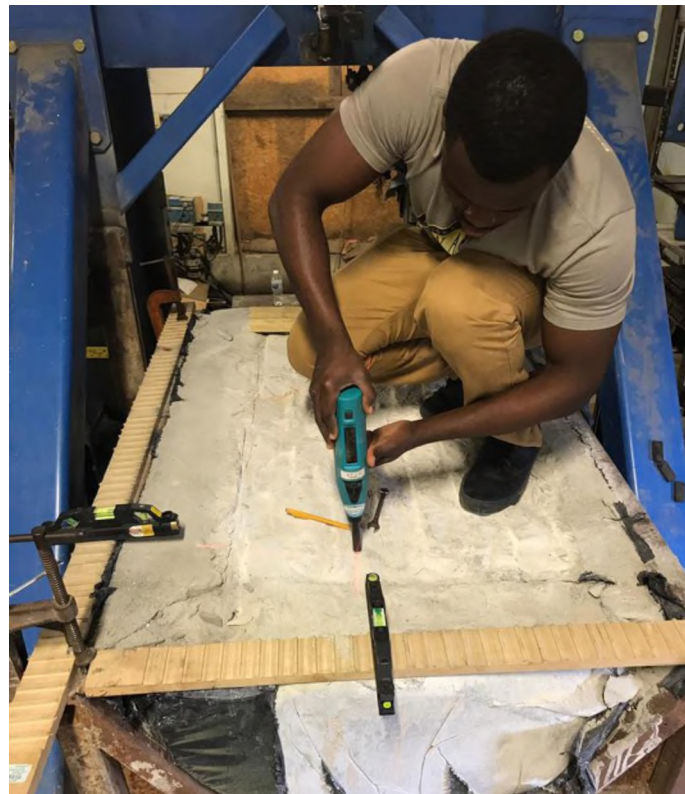


Figure 3.28. Taking hardness measurements on the excavated rock surface.

Two lines of measurements, 25.4 mm apart, were made on the ridge between two successive cuts. To reduce the data resolution gap between the cutter forces data and the hardness data, the hardness was measured at the lowest resolution possible (i.e. 3 radii of

the hammer tip apart). The measurement was done in a zig-zag fashion (see Figure 3.29) to cover most of the excavated surface. The measurement on one line was offset by 12.7 mm from the previous line's measurements to achieve maximum resolution in the zig-zag fashion. Along each line, 35 measurements were made.

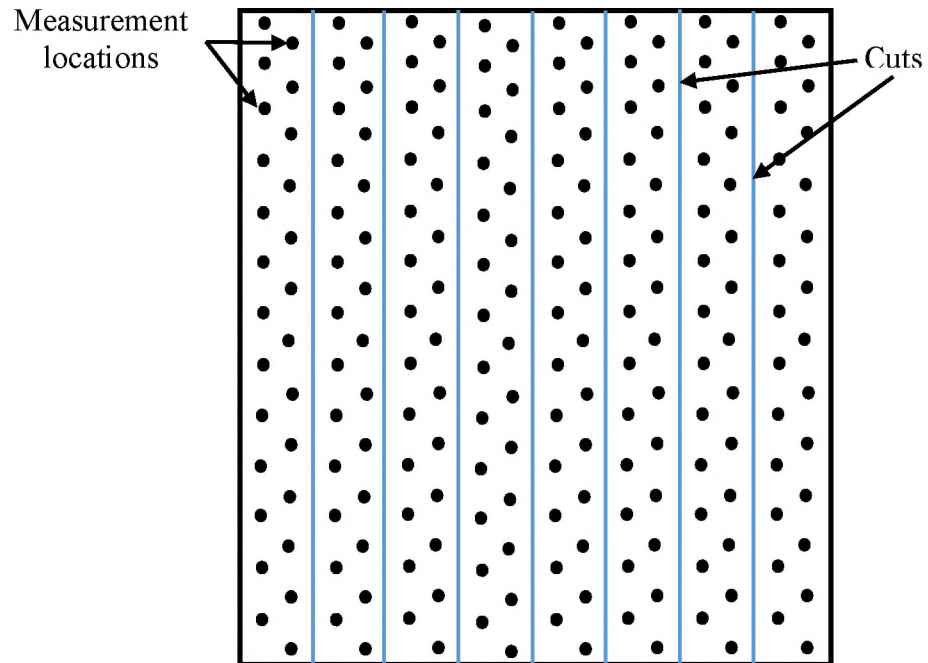


Figure 3.29. Illustration of hardness measurement locations on the surface of the excavated rock.

4. NUMERICAL SIMULATIONS OF LINEAR ROCK CUTTING

This section described the numerical experimental procedure for simulating linear rock cutting in PFC3D 5.0. It included the creation of the numerical model, as well as its calibration, verification, and validation.

4.1. THE PARTICLE FLOW CODE (PFC)

Particle Flow Code in 3D (PFC3D), an Itasca[®] software that is based on distinct element method (DEM), was used in this research to numerically simulate the linear rock cutting experiments conducted in the lab. According to Su & Ali Akcin (2011), PFC3D has been used to model the fracturing process of sedimentary rocks successfully. That is the motivation for the use of PFC3D in this study. In the PFC domain, the flat-joint bonded-particle model (FJ-BPM) was used because it is the best representation of synthetic rock material currently (Potyondy, 2012). A detailed review of the Itasca particle flow code and the flat-joint model is presented in Sections 2.5.2.1 & 2.5.2.2

4.1.1. Model Setup. In the PFC3D environment, a domain extent was first established to represent the working space where the models were created, and the simulations conducted. The domain extent was set to five times the dimensions of the block model to allow for the importation of the cutting tools and execution of the cutting. Rectangular blocks with dimensions 8 x 12 x 10 cm were modeled for the simulation in this study (Figure 4.1). The particles in the model were graded vertically. That is, the top of the model where the cutting took place was composed of smaller particles, 2-4 mm in radii. The particle size increased gradually to the base of the model, which was composed

of particles with radii ranging from 11 mm to 15 mm. The graded models were adopted to save computational time and maintaining a model large enough to be representative of the lab linear cutting experiment (Su and Akcin, 2011; Ayawah et al., 2019). The model was initialized by zeroing the ball displacements, contact forces, and contact moments. Gravity was introduced into the model. The model was then run to equilibrium at an average ratio of less than 1×10^{-4} , where the average ratio is the ratio of the average value of the unbalanced force magnitude (i.e., magnitude of the sum of the contact forces, body forces, and applied forces) over all the bodies to the average value of the sum of the magnitudes of the contact forces, body forces and applied forces over all the bodies (Itasca, 1988).

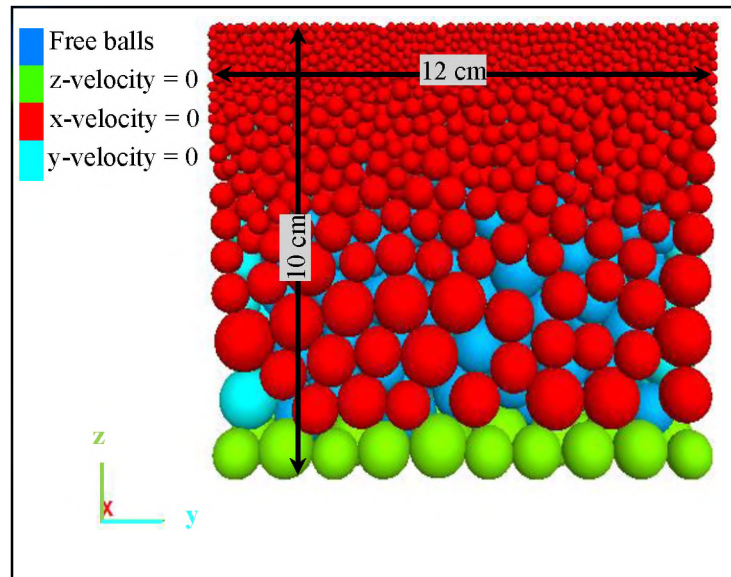


Figure 4.1. Front view of a graded block model with fixed boundaries.

The Flat-Joint logic described in Section 2.5.2.2 was then implemented in the created model to produce a rock-like model. Microparameters were assigned to make the model exhibit macro strength properties similar to the actual Roubidoux Sandstone rock

sample that was tested in the lab. The microparameters were obtained from a calibration process described in Section 4.1.3.

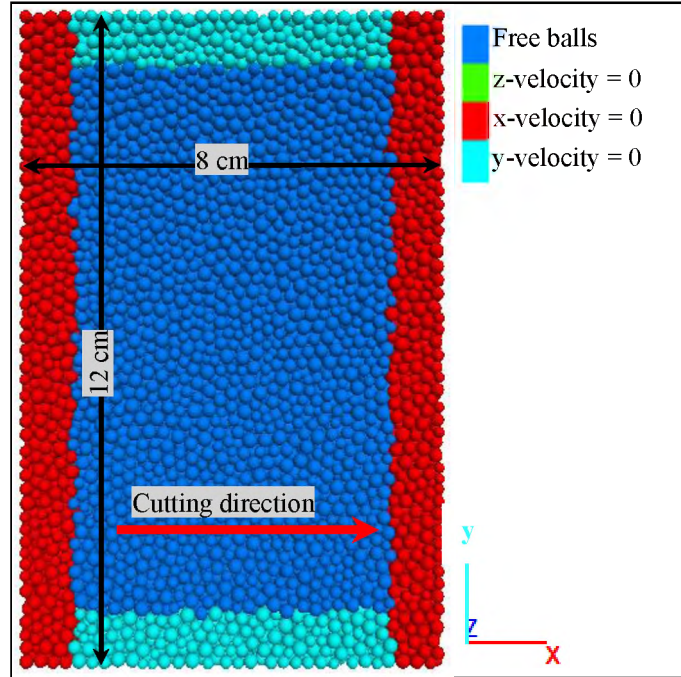


Figure 4.2. Plan view of the block model with fixed boundaries.

4.1.2. Boundary Conditions. To establish boundary conditions in the block models, three to four layers of particles on the edges of the blocks were fixed by setting their lateral velocities to zero (Figure 4.2). In the x-direction, the x-velocity of the particles on both extremes were set to zero. Similarly, the y-velocity of the edge particles in the y-direction was set to zero. The z-velocity of the particles at the base of the model was also set to zero to prevent downward movement of the block (Figure 4.1). These fixed boundaries served as no-motion boundary conditions, keeping the block in place during cutting. The rest of the particles, including the top surface of the block, were free to move in any direction. This mimics the lab linear rock cutting where the rock block was cast in a rock box and welded to the cutting table to ensure stability during cutting. The model

with boundary conditions was saved as a base model to be restored and used for different experimental runs.

4.1.3. Calibration of the Numerical Model. To calibrate the numerical model, rock strength tests (UCS, BTS, and E) were simulated with synthetic rock cores in PFC3D 5.0. The results matched with the UCS, BTS, and E obtained from testing of the real rock sample in the lab. The objective of this procedure was to tune the microparameters of the model to produce a synthetic rock model that exhibited similar strength properties as the actual rock tested in the lab (Labra et al., 2016). The strength properties of the Roubidoux sandstone were obtained from lab tests, as presented in Table 4.1. Simulation of uniaxial compressive strength (Figure 4.3) and Brazilian tensile strength (Figure 4.4) tests were conducted using synthetic rock cores and discs with dimensions that satisfy the ASTM guidelines (2:1 height to diameter ratio for UCS and 1:2 height to diameter ratio for BTS) (ASTM D4543-19, 2019). The tests were conducted iteratively while adjusting the model microparameters, as shown in the flowchart in Figure 4.5. The set of microparameters that yielded UCS, BTS, and E that matched those obtained from the actual rock were noted (Table 4.1). These (Table 4.2) were the microparameters that were used to create the rock block models used for the cutting simulation.

Table 4.1. Properties of the Roubidoux Sandstone (Kaba, 2018).

Rock Properties	Min.	Max.	Avg.	Number of samples
UCS (MPa)	62	82	72.8	11
BTS (MPa)	4.6	8.1	6	13
Point Load Test (I50) (MPa)	2.7	3.6	2.5	10
Bulk density (kg/m ³)	2.05	2.25	2.1	4

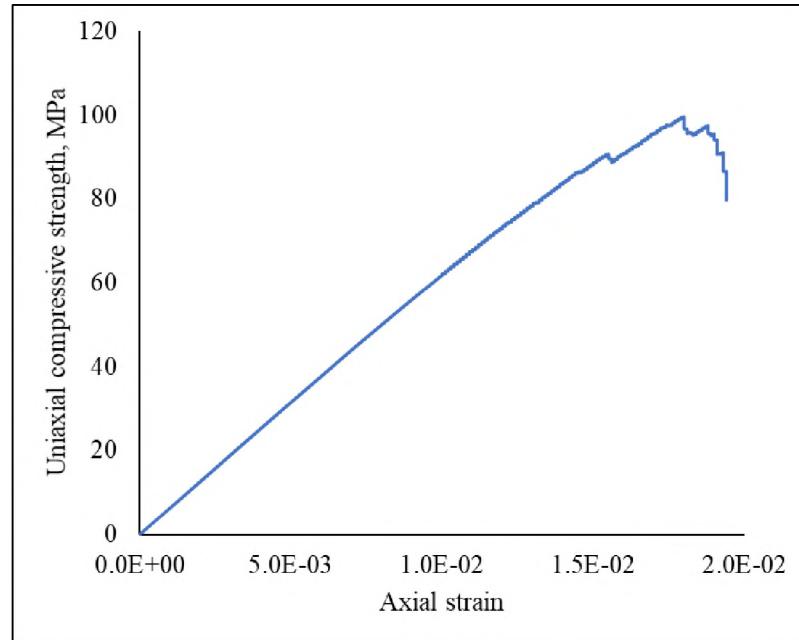


Figure 4.3. UCS versus axial strain from a UCS simulation of a synthetic rock core for the calibration of the model for the rock cutting simulations.

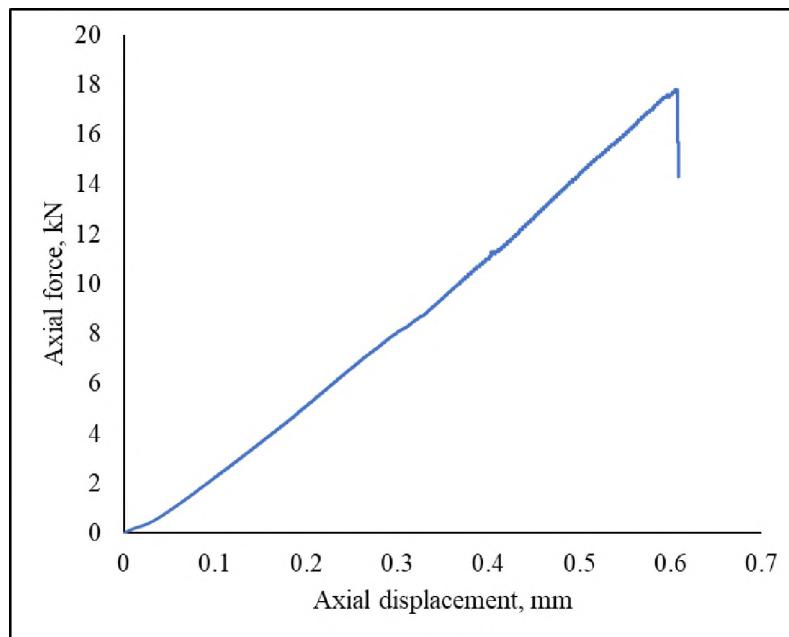


Figure 4.4. Axial load versus axial displacement from a Brazilian strength test simulation of a synthetic rock disc for the calibration of the model for the rock cutting simulations.

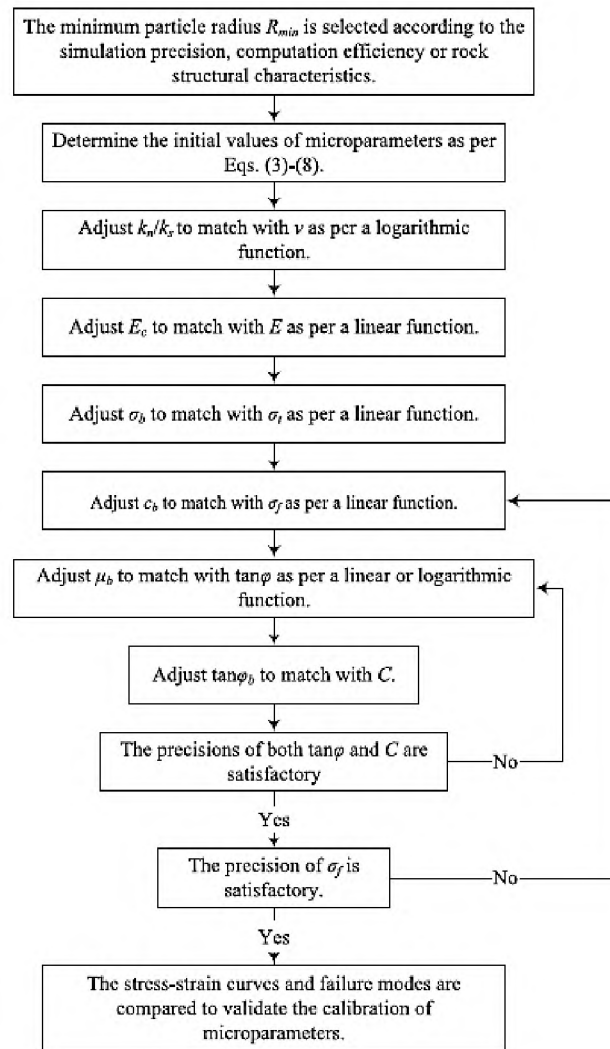


Figure 4.5. Flat-Joint model calibration procedure (after Chen, 2017).

Table 4.2. Microparameters for the synthetic rock model obtained through calibration.

Microparameter	Value
Bulk density (kg/m^3)	2760.0
Porosity (%)	20.0-25.0
Effective modulus (GPa)	7.0
Normal to shear stiffness ratio	1.0
Tension (MPa)	14.0
Cohesion (MPa)	175.0

4.1.4. The Cutting Tool. A model of the disc cutter was built in AutoCAD and imported into PFC as a rigid wall with both normal and shear stiffnesses of 50.0 GPa. The cutter was modeled as a flat disc with a slightly rounded tip (Figure 4.6). The modeled cutter only represented the disc ring of the actual TBM cutter. It did not include hub or shaft retainer, which would have increased computational expenses by adding more facets and their inclusion or exclusion do not influence the cutting outcome. The diameter of the modeled cutter is 95 mm, and its tip thickness is 4 mm (Figure 4.6). These dimensions are one-third the dimensions of the actual Robins disc cutter used in the lab experiments. This cutter was used in all the numerical experimental runs.

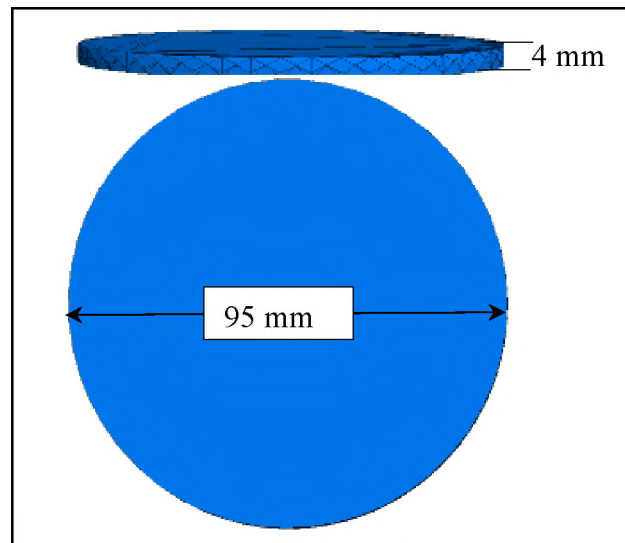


Figure 4.6. Front and side views of the modeled disc cutter showing diameter and tip thickness.

4.2. THE NUMERICAL CUTTING SIMULATION

The saved base model was restored in a new domain. A disc cutter was also imported as a rigid wall into the domain, and it was oriented such that its axis of rotation

was parallel to the y-axis so that the direction of cutting was along the x-direction. The initial position of the first cutter was 3 cm from the negative y-edge of the block. In the x-direction, it was positioned such that its movement started in the air before it came into contact with the block at the negative x-edge. The elevation of the cutter was set such that there was a specific overlap distance between the top of the block and the cutter. This overlap was equivalent to the cutter penetration in the LCM experiment. It was the depth to which the cutter penetrated the rock during cutting. The cutting was designed to proceed from the negative x-direction toward the positive x-direction.

After the cutter was imported and oriented in position, its center was set as the axis of rotation. An angular velocity about the y-axis, 105.26 rad/s, was applied to it in the clockwise direction, so it spun about its axis of rotation. A translational velocity, 5 m/s, was applied in the x-direction to move the spinning disc horizontally, simulating the rolling of the disc cutter on the rock face during cutting. The values of the translational and angular velocities were calculated using the relationship in Eq 4.1, assuming no slip between the rock model and the cutter. The principles of similitude and preliminary studies showing no significant influence of cutting velocity on the cutting forces were the basis for choosing the velocities used in this research.

$$v = r\omega \quad (4.1)$$

Where v = translational velocity;

r = disc cutter radius; and

ω = angular velocity.

After the first cutter progressed about 25 mm into the block, another cutter was imported with the same orientation, elevation, and x-position as the starting point of the

first cutter, but it indexed lateral (in the positive y -direction) by a predetermined distance, cut spacing (s), to start cutting the next line. This was repeated until the last cut (see Figure 4.7). This procedure conserved computational time, while still mimicking the actual cutting process where two adjacent cutters were offset by some distance, one ahead of the next. A total of three cuts were simulated on each rock block model. Figure 4.8 illustrates the procedural flow of steps involved in the simulation of linear rock cutting.

The history command in PFC was used to record the contact forces between the rock model and each cutter in the x -, y -, and z -directions at a sampling interval of 100 timesteps. The contact forces in the y -direction represented the side forces, the forces in the x -direction represented the rolling forces, and the z -direction forces represented the normal forces. The position of the cutter was also recorded at the same sampling interval to enable ‘georeferencing’ of the cutter forces.

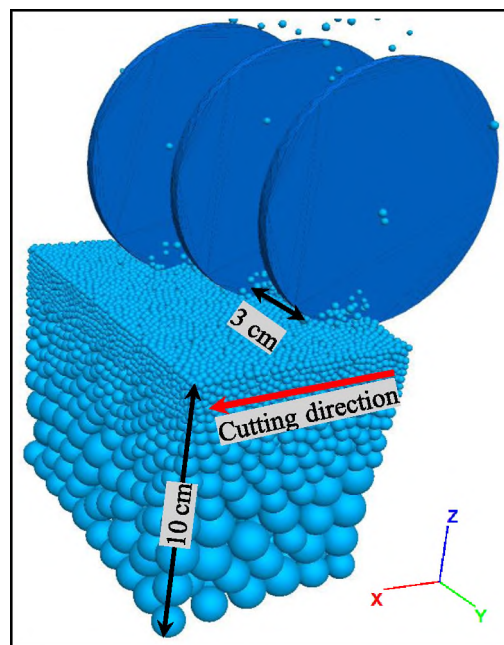


Figure 4.7. Three cutters cutting at a spacing of 30 mm and penetration of 4 mm.

A code was written to track the interparticle bond breakage in the model during the cutting simulation. This provided a count of the microcracks that were associated with each excavation run. It also tracked the location of these microcracks. This was done to study the influence of spacing-penetration combinations on the intensity of microcracks and their distribution within the rock block.

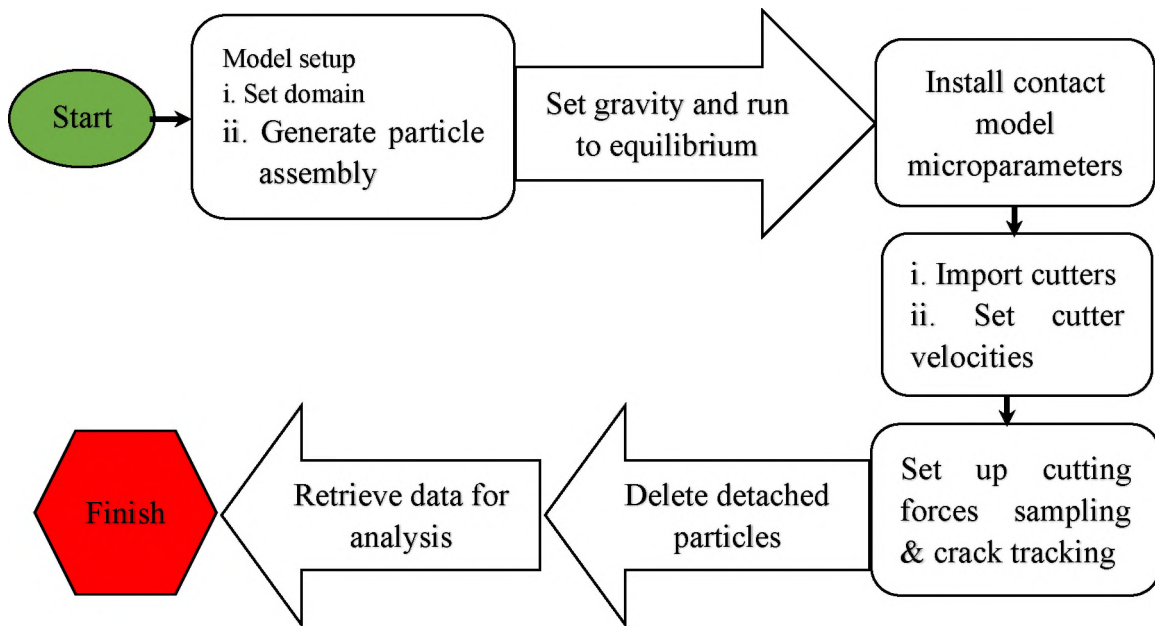


Figure 4.8. Flowchart of linear rock cutting simulation in PFC3D.

4.2.1. Experimental Design for the Simulation. In this study, a factorial design was set up with two factors: the cut spacing and the depth of penetration of the cutter. The spacing had three levels: 25 mm, 30 mm, and 35 mm; and the penetration had 12 levels. For the 12 levels of penetration and three spacing values, 36 runs were made, one for each spacing-penetration combination. The three cuts were repetitions of each s-p combination. The experimental treatment of this design is presented in Table 4.3.

Table 4.3. Factorial experimental design.

Spacing	Penetration											
25	2.5	3.0	3.5	4.0	4.5	5.0	5.5	6.0	6.5	7.0	7.5	8.0
30	2.5	3.0	3.5	4.0	4.5	5.0	5.5	6.0	6.5	7.0	7.5	8.0
35	2.5	3.0	3.5	4.0	4.5	5.0	5.5	6.0	6.5	7.0	7.5	8.0

4.2.2. Surface Irregularities from the Simulation Models. After excavation of each model, the dislodged fragments were deleted from the model leaving a clean excavated surface. The 3D positions of the top-most particles on the excavated model surfaces were extracted and used to generate digital elevation models (DEMs) of the excavated surfaces in MATLAB (Figure 4.9). Surface irregularities analyses similar to those conducted on the lab rock surface in Section 3.5.2 were then conducted on the DEMs.

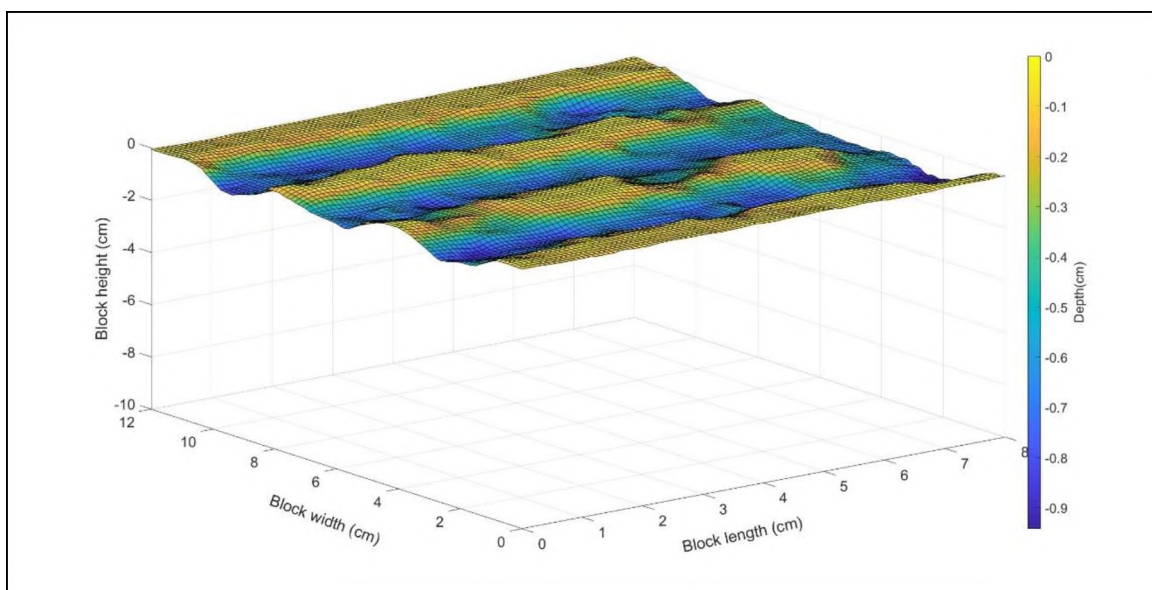


Figure 4.9. Digital elevation model of the excavated model surface free of dislodged particles– cutting at spacing 30 mm and penetration 5 mm.

5. ROCK CUTTING EXPERIMENTAL RESULTS

The results from the lab linear rock cutting experiments are presented in this section. The results include primary parameters that were directly measured from the experiments and secondary parameters that were derived from the primary parameters. The information gleaned is presented in tables and charts.

5.1. ROCK CUTTING RESULTS

All the data pieces (rock fragments, cutting force, surface hardness, and surface irregularities) considered for analysis were taken from the outlined data window (Figure 5.1). The data window was 76.2 mm (3 in) from all the edges of the rock block. This was done to eliminate the influence of the edge on the cutting data. Data from the outer cuts on each pass were discarded because they fell outside the data window.

5.1.1. Cutting Forces. The forces recorded during the rock cutting were the side forces that acted laterally on the cutter, the rolling forces that acted parallel to the direction of cutting, and the normal forces that acted perpendicular to the surface of the rock. The resultants of these forces were calculated for each cut using Eq. 5.1. These forces had highly irregular traces that resulted from a sequence of stresses build-up in the rock under the cutter and sudden release of those stresses due to crack initiation and propagation (chip formation) and/or grain crushing (Gertsch, 2000; Rojek et al., 2010; Entacher et al., 2014). This phenomenon formed saw-tooth shaped force traces in all the forces along the cuts (see Figure 5.2). As a result, the average and the peak (maximum) (Table 5.1) of each force were analyzed for excavator design and evaluation. A detailed presentation of all the forces

data can be found in Appendix B. The cutting forces were averaged over each cut for pass-based analysis. For penetration-based analysis, the forces were averaged over each pass.

$$\text{resultant force} = \sqrt{S^2 + R^2 + N^2} \quad (5.1)$$

Where S – side force (kN);

R – rolling force (kN); and

N – normal force (kN).

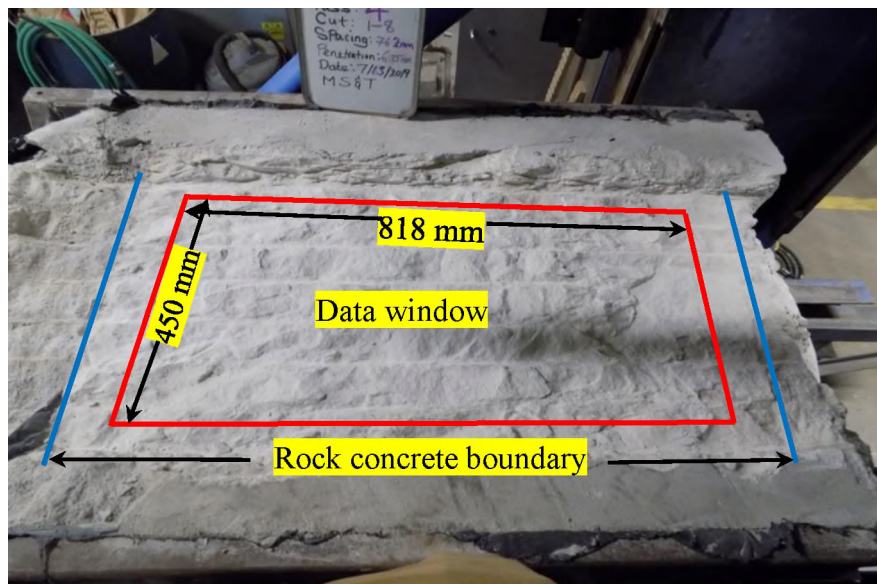


Figure 5.1. Excavated rock surface with outline data window.

The average rolling, normal, and resultant forces for all the passes in each penetration category were plotted on dot plots to show the median and range of their distributions (Figure 5.3, Figure 5.4, and Figure 5.5). From these plots, it was observed that on average, the forces increased with increasing penetration. This is in agreement with the literature (e.g. Gertsch, 2000; Gertsch et al., 2007; Balci, 2009; Abu Bakar, 2012; Balci & Tumac, 2012; Kaba, 2018).

Table 5.1. Average and peak cutting forces, cutting coefficients, and specific energy per pass.

Penetration, 6.35 mm				
Pass	1	2	3	4
Avg side force, kN	-3.3	-8.0	-6.2	-2.0
Avg rolling force, kN	10.8	10.2	10.6	11.0
Avg normal force, kN	54.6	47.8	54.1	55.8
Avg resultant force, kN	58.5	52.3	58.0	59.6
Peak side force, kN	49.7	38.1	45.5	49.7
Peak rolling force, kN	88.4	42.2	34.7	38.8
Peak normal force, kN	178.5	178.5	172.7	161.9
Peak resultant force, kN	180.0	190.3	173.7	164.3
Cutting coefficient, %	19.8	21.4	19.5	19.7
Specific energy, kW.hr/m ³	5.4	4.4	5.9	7.0
Penetration, 9.5 mm				
Avg side force, kN	-6.3	-7.8	-5.1	-7.2
Avg rolling force, kN	13.1	16.5	15.3	16.1
Avg normal force, kN	55.9	68.4	68.2	67.1
Avg resultant force, kN	61.1	73.8	73.5	73.0
Peak side force, kN	43.4	52.9	57.1	59.2
Peak rolling force, kN	53.7	57.0	69.4	64.5
Peak normal force, kN	189.2	168.8	221.4	224.3
Peak resultant force, kN	191.5	173.6	225.4	230.2
Cutting coefficient, %	23.4	24.1	22.4	24.0
Specific energy, kW.hr/m ³	5.4	4.7	4.7	5.7
Penetration, 12.7 mm				
Avg side force, kN	-9.8	-9.8	-5.0	-9.0
Avg rolling force, kN	18.9	19.4	16.7	19.2
Avg normal force, kN	68.9	69.6	61.4	69.9
Avg resultant force, kN	75.1	76.2	67.3	77.0
Peak side force, kN	51.8	47.6	57.1	71.9
Peak rolling force, kN	66.9	72.7	55.4	56.2
Peak normal force, kN	203.9	195.1	221.4	209.7
Peak resultant force, kN	214.0	207.6	225.1	222.5
Cutting coefficient, %	27.5	27.9	27.1	27.5
Specific energy, kW.hr/m ³	4.8	4.2	4.2	4.4

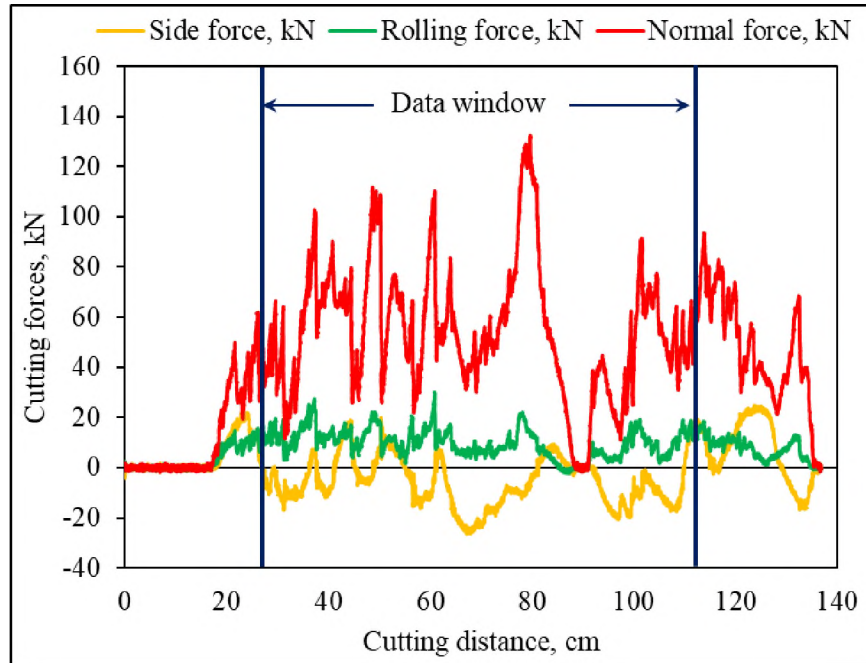


Figure 5.2. A typical trace of the cutting forces from a full-scale lab rock cutting test using a disc cutter at 76.2 mm spacing and 9.53 mm penetration.

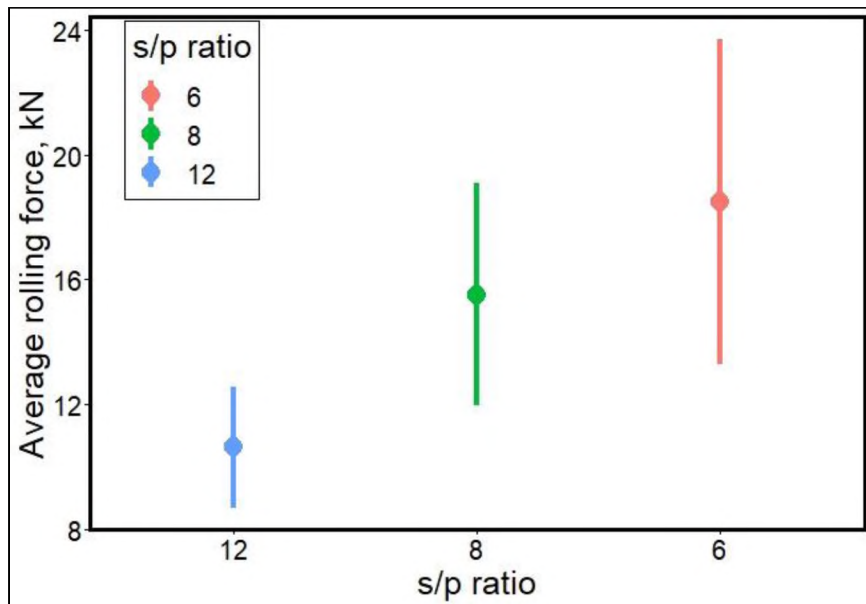


Figure 5.3. Distribution of averaged rolling forces at different spacing-penetration ratios.

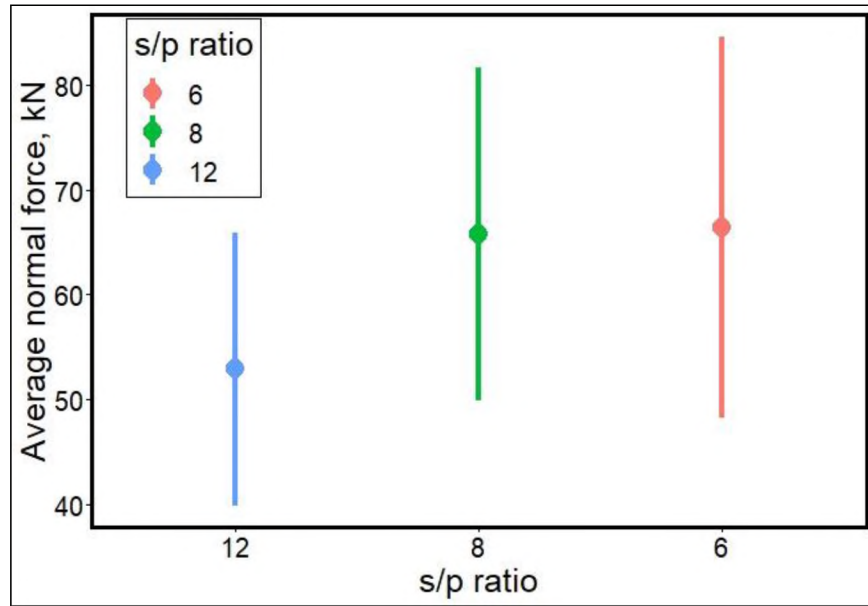


Figure 5.4. Distribution of averaged normal forces at different spacing-penetration ratios.

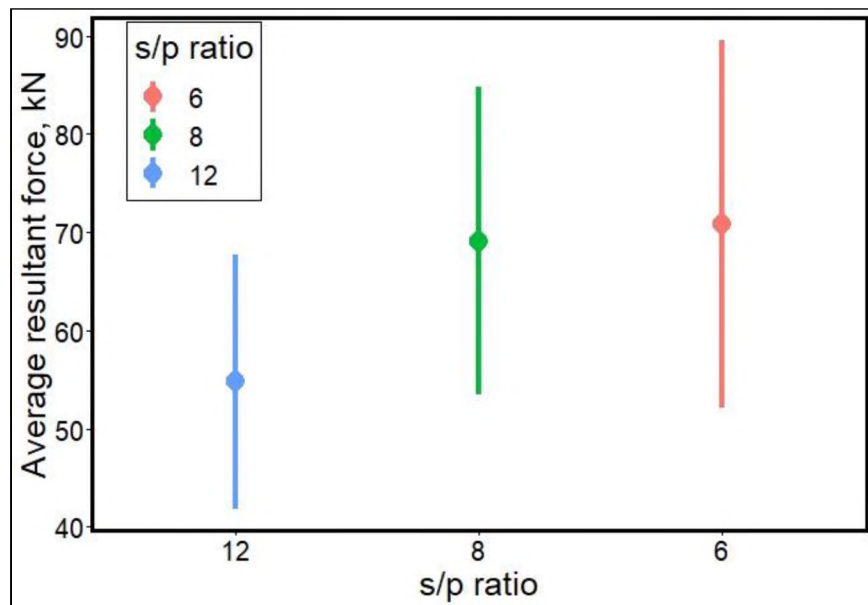


Figure 5.5. Distribution of averaged resultant forces at different spacing-penetration ratios.

5.1.2. Cutting Coefficient. The cutting coefficient (CC) is a ratio of the rolling force to the normal force expressed as a percentage. It is a measure of the required amount

of torque for a given amount of thrust of a TBM. On average, CC increased almost linearly with increasing depth of penetration (Figure 5.6), as expected, because the increased depth of penetration had more torque requirement due to the increased contact length, which resulted in more cutter bite. This observation was also consistent with what was observed in the literature (e.g., Gertsch et al., 2007; Abu Bakar, 2012).

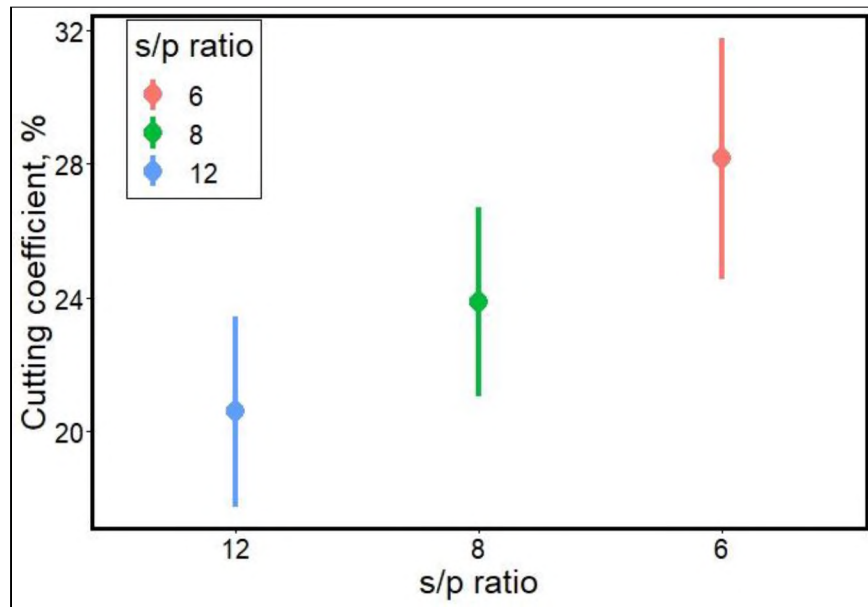


Figure 5.6. Distribution of cutting coefficients at different spacing-penetration ratios.

5.1.3. Specific Energy. Specific energy is the amount of energy required to excavate a unit amount (volume or mass) of rock (Teale, 1965). This parameter is computed either as an expected or nominal specific energy (SE_E) or actual specific energy (SE_A). The expected specific energy is computed using the average rolling forces and the expected volume of materials to be excavated (based on the spacing and penetration dimensions). By contrast, the actual specific energy is computed using the average rolling force and the actual mass of the chips produced from the excavation. The SE_E is volumetric,

and the SE_A is mass related. The distribution of the actual specific energy is presented in Figure 5.7, showing a linear increase in specific energy with an increasing spacing-penetration ratio. The formulas for SE_E and SE_A calculations are shown in Eqs. 5.2 and 5.3, respectively.

$$SE_E = 0.278 \frac{\bar{R}L}{spL} \quad (5.2)$$

$$SE_A = 0.278 \frac{\bar{R}L\rho}{m} \quad (5.3)$$

Where; \bar{R} = average rolling force, kN

s = cut spacing, mm

p = cutter penetration, mm

L = cutting length, mm

m = mass of chips produced, kg

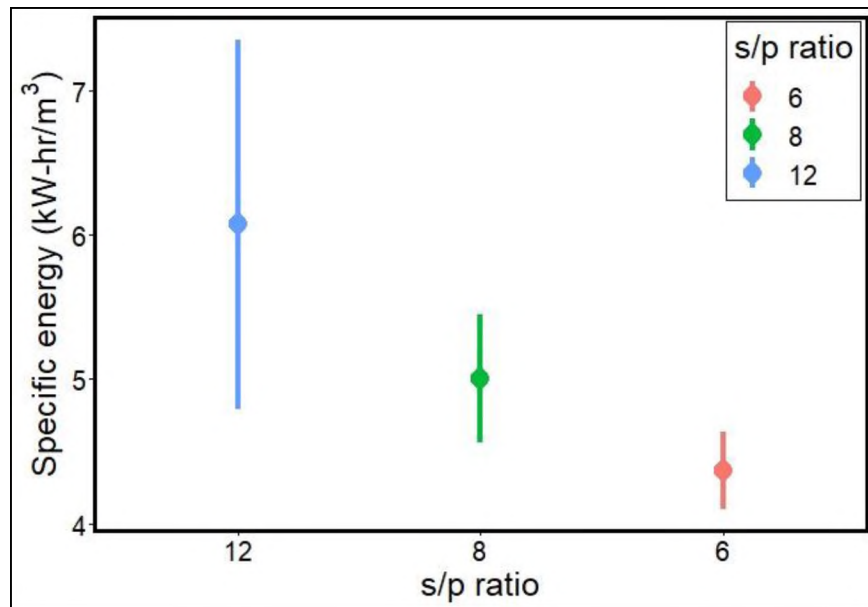


Figure 5.7. Distribution of actual specific energy at different spacing-penetration ratios.

5.1.4. Instantaneous Cutting Rate. The instantaneous cutting rate is the amount of rock fragments produced per unit time. It is also known as linear cutting rate. Like the specific energy, the instantaneous cutting rate is also classified as expected (ICR_E) and actual (ICR_A) instantaneous cutting rate. The expected cutting rate involves the cutting velocity, cut spacing and cutter penetration, and density of the rock (Eq. 5.4). Conversely, the instantaneous cutting rate involves the actual mass of fragments produced per unit time (Eq. 5.5). The relationship between ICR_A and spacing-penetration ratio is shown in Figure 5.8.

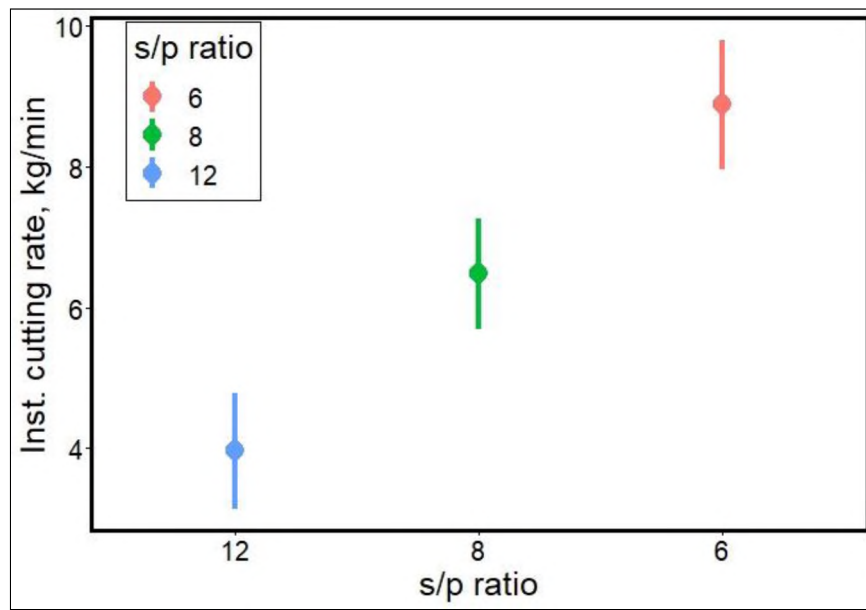


Figure 5.8. Distribution of instantaneous cutting rate at different spacing-penetration ratios.

$$ICR_E = \frac{s}{1000} \times \frac{p}{1000} \times vp \quad (5.4)$$

$$ICR_A = \frac{mv}{1000 \times L} \quad (5.5)$$

Where; m = mass of chips produced, kg;

s = cut spacing, mm;

p = cutter penetration, mm;

v = cut speed, m/min;

ρ = mass density, kg/m³; and

L = cutting length, mm.

Table 5.2. Instantaneous cutting rates and cutting efficiencies per pass.

Penetration	Pass	Actual instantaneous cutting rate (kg/min)	Nominal instantaneous cutting rate (kg/min)	Cutting efficiency (%)
6.35 mm	1	4.37	3.79	115.33
	2	5.11	3.85	132.84
	3	3.88	3.76	103.11
	4	3.45	3.83	90.21
9.5 mm	1	5.20	5.60	92.74
	2	7.30	5.39	135.28
	3	6.83	5.51	123.87
	4	5.93	5.47	108.25
12.7 mm	1	8.30	7.26	114.38
	2	9.57	7.15	133.75
	3	8.34	7.35	113.52
	4	8.86	7.13	124.29

5.1.5. Cutting Efficiency. A ratio of the actual cutting rate to the nominal or cutting rate gives a measure of the cutting efficiency of the excavation. For a perfect excavation, the cutting efficiency will be 100%. That is, the actual amount of rock fragments produced is equal to the amount of rock fragments expected or intended. However, the amount of rock fragments produced is rarely equal to the expected amount. In some instances, ridges

form between cuts resulting in cutting efficiency lower than 100%. This is common when full interaction between adjacent cuts has not been achieved. Over-breaks can also occur (the rock dislodges beyond the designed spacing-penetration dimensions) resulting in cutting efficiency greater than 100%. For passes in which more ridges than over-breaks form, the overall cutting efficiency on that pass is lower than 100%. Conversely, when a pass has more over-breaks than ridges, then the overall cutting efficiency on that pass is greater than 100%. The instantaneous cutting rates and cutting efficiencies on a pass basis are presented in Table 5.2.

5.1.6. Fragment Size Distribution. The rock fragments produced during the excavation were collected after each pass within the data window and weighed. Sieve analysis was conducted. Coarseness index (CI), large fragment percentage, and absolute size constant (x') were the parameters estimated from the fragment size analysis results. These are discussed in Sections 5.1.6.1- 5.1.6.3.

5.1.6.1. Coarseness index. Coarseness index (CI) is the sum of the cumulative mass percentages of rock fragments retained on each sieve, starting from the largest sieve. According to Roxborough & Rispin (1973), CI is a comparative fragment size distribution using sieve analysis of rock fragments produced from an excavation. It is a measure of the coarse fragment generation characteristics and size distribution (Kumar et al., 2017).

The procedure for determining the coarseness index was: The sieve analysis results were arranged in descending order of mesh sizes and the percentage of rock fragments retained on each sieve was calculated. The cumulative percentage was then calculated, and the sum of the cumulative percentages represented the coarseness index. This procedure was outlined in detail in Tuncdemir et al., (2008). An example of this procedure for pass 1

of penetration level 6.35 mm is presented in Table 5.3. The coarseness indexes for all the passes are presented in Table 5.4, along with large fragment percentage, and absolute size constant. Figure 5.9 shows the distribution of CI at different spacing-penetration ratios.

Table 5.3. Computation of coarseness index for pass 1 of penetration 6.35 mm.

Mesh size, mm	Mass retained (kg)	Cum. % retained
50.8	1.29	21.47
25.4	1.57	47.49
9.4	0.99	63.92
1.7	0.49	72.04
Pan	1.69	100.00
Total	6.03	304.93

Table 5.4. Fragment size parameters.

Penetration, mm	6.35			
Pass	1	2	3	4
Coarseness index, %	304.9	297.9	285.5	276.8
Absolute size constant, mm	32.8	28.2	25.1	21.3
Large fragments fraction, %	21.5	14.6	18.1	14.5
Penetration, mm	9.5			
Coarseness index, %	268.1	284.3	306.6	287.2
Absolute size constant, mm	18.5	24.5	33.2	25.8
Large fragments fraction, %	8.8	15.2	20.6	16.6
Penetration, mm	12.7			
Coarseness index, %	289.6	288.6	281.8	291.4
Absolute size constant, mm	26.7	25.9	22.3	26.6
Large fragments fraction, %	17.4	16.5	13.4	18.4

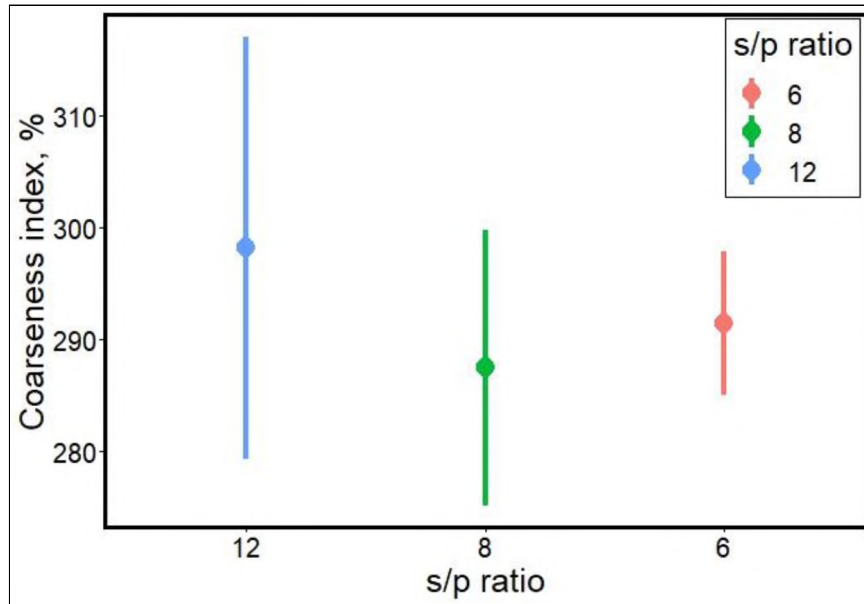


Figure 5.9. Distribution of coarseness indexes at different spacing-penetration ratios.

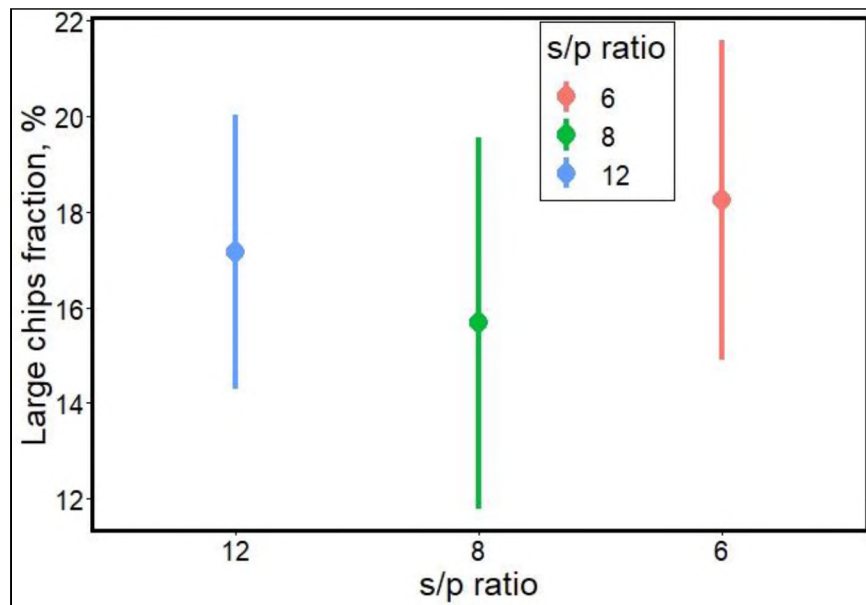


Figure 5.10. Distribution of large fragment fraction at different spacing-penetration ratios.

5.1.6.2. Large fragment percentage. Large fragment fraction (PRL) is the proportion of the total fragment volume or mass that is retained on the 50.8 mm sieve. For

each pass, the mass of rock fragments retained on the 50.8 mm sieve was divided by the total rock fragment mass and expressed as a percentage to obtain PR_L (see Table 5.4). Figure 5.10 is a distribution plot of PR_L for each penetration level. This parameter is important because, in excavation, the production of large fragments is more energy-efficient than the production of dust. Therefore, the proportion of the fragments that fall in this category is a major determining factor of the efficiency of the excavation.

5.1.6.3. Absolute size constant (x') and distribution parameter (b). To further characterize the distribution of the rock fragments, a Rosin-Rammler distribution (Figure 5.11) was used to determine absolute size constants (x') and distribution parameters (b). The Rosin-Rammler distribution expresses the mass distribution in an exponential functional form, as shown in Eq. 5.6 (Rosin et al., 1933):

$$R_R = 100 \exp \left[- \left(\frac{x}{x'} \right)^b \right] \quad (5.6)$$

Where R_R = cumulative mass (volume) % retained on sieve of size x

x' = absolute size constant or size parameter, and

b = distribution parameter.

This can also be expressed as Eq. 5.7.

$$\log \left[\log \left(\frac{100}{R_R} \right) \right] = b \cdot \log x + \text{constant} \quad (5.7)$$

The Rosin-Rammler chart is a plot of $\log[\log(100/R_R)]$ against $\log x$, yielding a straight line whose slope is b – the fragment distribution parameter. The mesh size, x , at which $R_R = 36.79\%$ is known as the absolute size constant (x'). These calculations and plots were completed using a function written in MATLAB[®] by Brezani (2020).

A small value of b indicates a wider fragment size range, while a higher b indicates a narrow fragment size range. The absolute size constant is the most common fragment size class in the fragment distribution (Rosin et al., 1933). Figure 5.12 shows the distribution of absolute size constant in each penetration level.

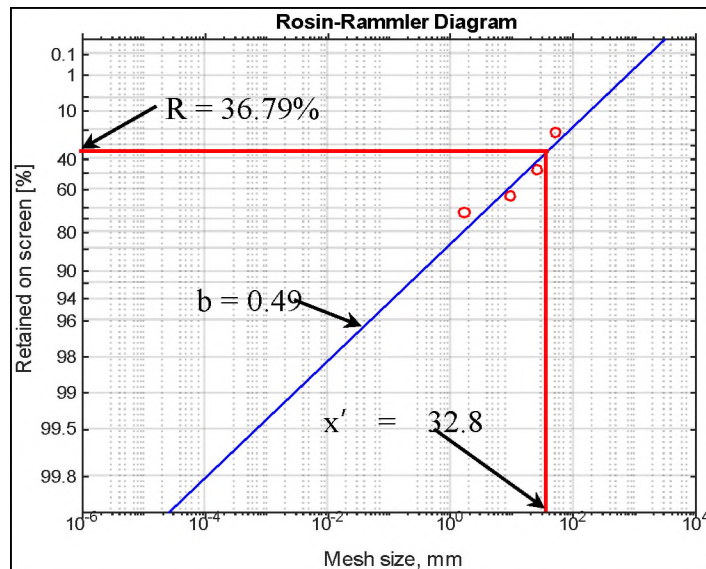


Figure 5.11. Rosin-Rammler plot for determination of absolute size constant and fragment distribution parameter of pass 1 of penetration 6.35 mm.

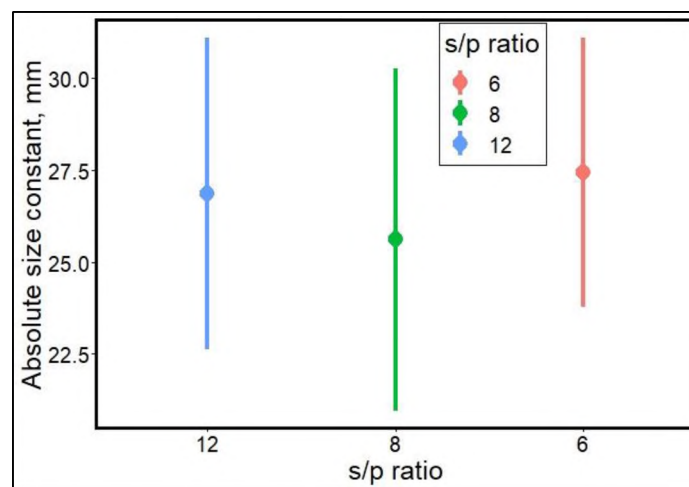


Figure 5.12. Distribution of absolute size constants at different spacing-penetration ratios.

5.2. SURFACE HARDNESS

On each pass, 420 hardness measurements were made within the data window. Therefore, a total of 5040 measurements were made for all twelve data passes. The hardness of the surface bordering each cut was averaged from two lines of hardness values on either side of the cut. This yielded six average hardness values for each pass. Table 5.5 presents the average hardness along cuts within the data window on each data pass. The distribution of these values at different spacing-penetration ratios is shown in Figure 5.13. It was observed that on average, the surface hardness decreased with increasing depth of penetration. This phenomenon is further explored in the discussion section.

Table 5.5. Average surface hardness per cut at different penetrations.

Penetration, mm	Pass	Cut2, R	Cut3, R	Cut4, R	Cut5, R	Cut6, R	Cut7, R
6.35	1	40.2	42.5	41.7	42.3	41.5	39.9
	2	41.2	48.7	49.8	47.7	43.7	38.5
	3	37.5	46.3	47.0	44.5	42.5	37.5
	4	36.8	43.1	45.6	44.1	39.7	41.3
9.5	1	32.1	35.3	39.9	41.5	41.6	42.3
	2	37.3	37.3	36.3	40.6	39.6	41.6
	3	33.3	39.3	41.0	37.5	39.8	41.4
	4	30.5	38.7	39.1	40.6	41.4	38.2
12.7	1	32.4	32.7	39.3	36.3	36.5	36.8
	2	37.6	40.0	36.7	35.8	32.1	
	3	37.5	37.6	35.4	36.4	36.0	
	4	36.9	41.5	37.6	32.7	29.0	

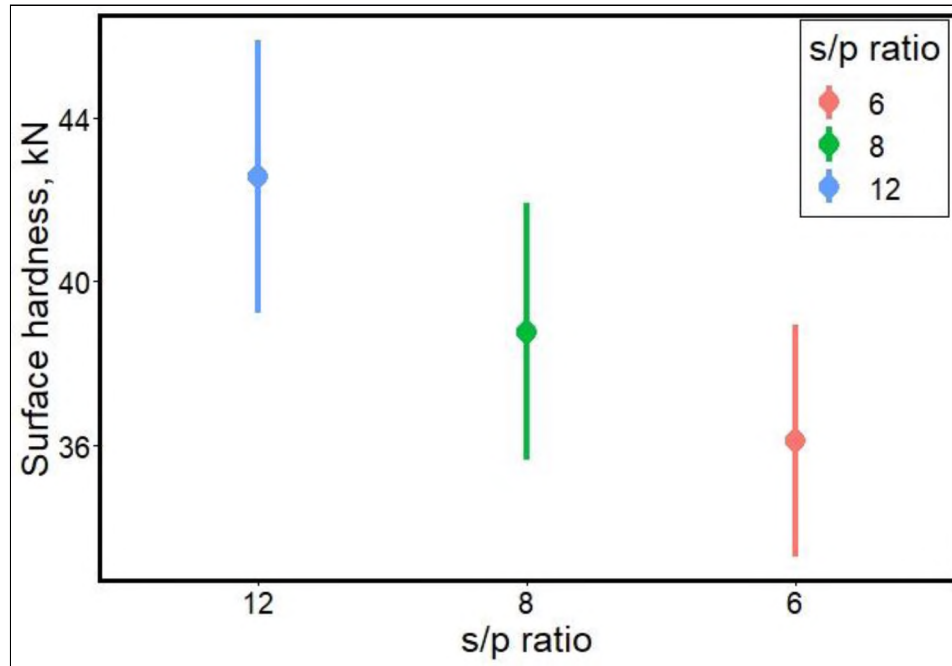


Figure 5.13. Distribution of excavated surface hardness at different spacing-penetration ratios.

5.3. SURFACE IRREGULARITIES

The videos of the excavated surface captured using the laser imaging system described in the experimentation section were converted into overlapping image frames containing point clouds covering the entire excavated rock surface. These point clouds were extracted using a MATLAB[®] code. The point clouds were used to generate digital elevation models (DEMs) of the surfaces (e.g., Figure 5.14). The DEMs were then used to estimate the volume of ridges (material above the nominal cutting level), and the volume of overbreaks (i.e., the volume of material that has been removed beyond the nominal cutting level).

From the DEM of each pass, the nominal elevation of the cutter tip was identified and used as a reference elevation for over-breaks and ridges evaluation. Elevations higher

than the reference elevation were considered ridges, while elevations lower than the reference elevation were considered over-breaks. Trapezoidal numerical integration in MATLAB was used to compute the volume of material above the nominal cutting level from the elevations greater than the reference elevation. The volume of rock material removed below the nominal cutting level – the volume of over-break – was also calculated from the elevations lower than the reference, using the trapezoidal numerical integration method in MATLAB. A summary of the over-break and ridge volumes is presented in Table 5.6. The distribution of the over-break volume and ridge volume at each spacing-penetration ratio is presented in Figure 5.15 and Figure 5.16, respectively.

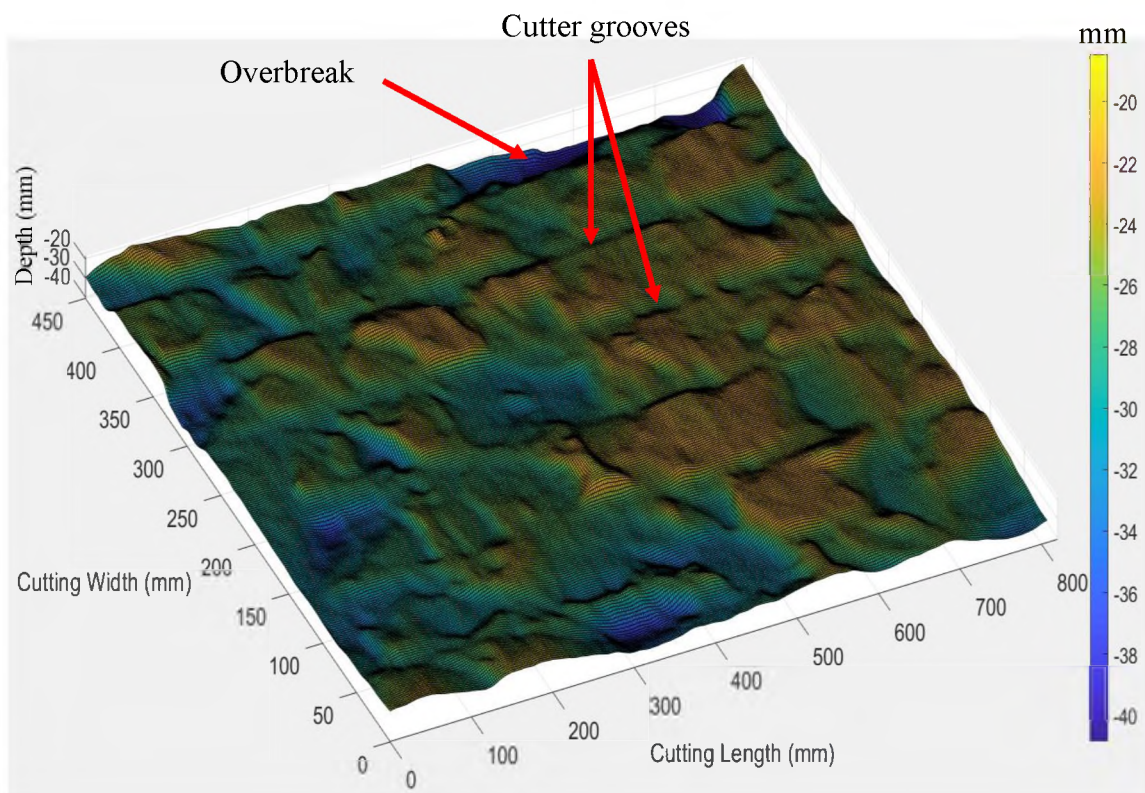


Figure 5.14. Digital elevation model of pass 1 of penetration level 6.35 mm.

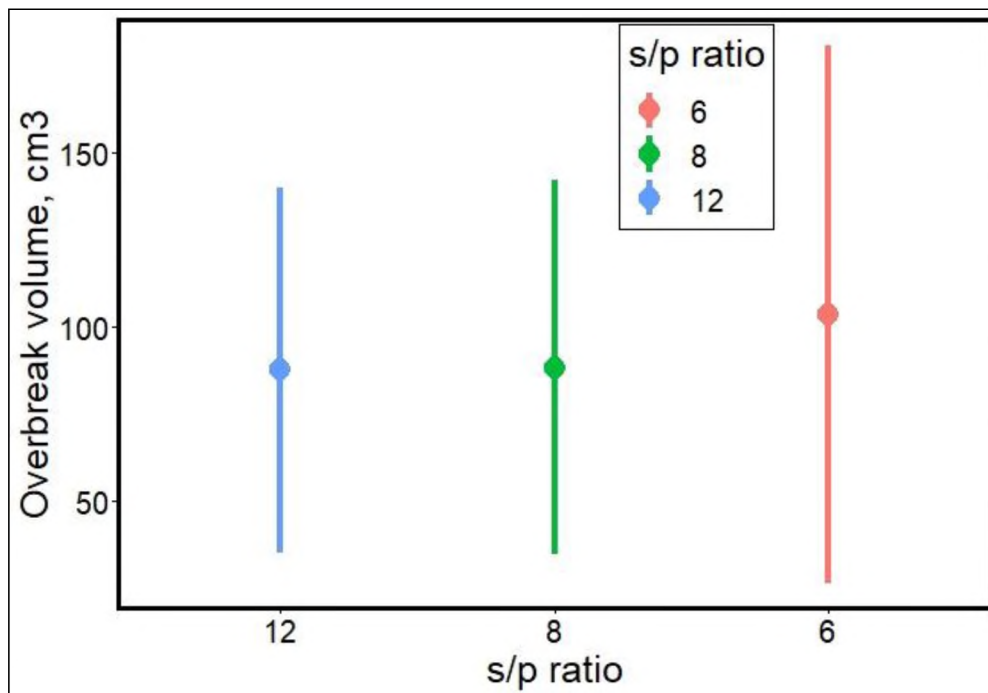


Figure 5.15. Distribution of volume of over-breaks on each pass over.

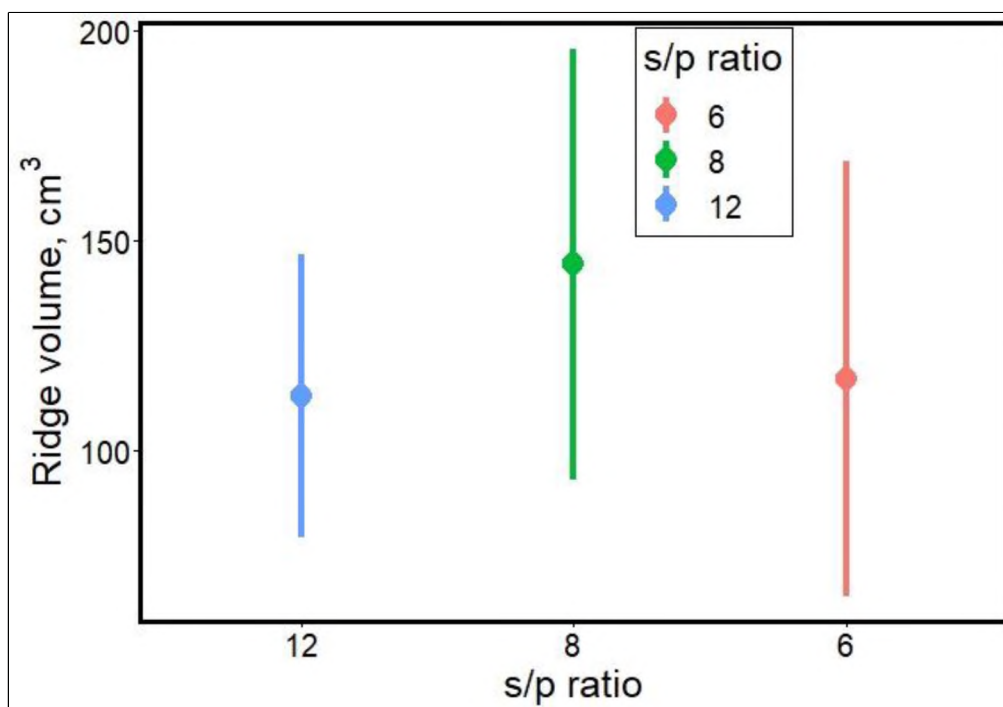


Figure 5.16. Distribution of volume of ridges on each pass over.

Table 5.6. Over-break and ridge volumes on each pass.

Penetration, mm	Pass	Ridge volume, cm ³	Over-break volume, cm ³
6.35	1	5.22E+02	4.02E+02
	2	7.68E+02	3.52E+02
	3	7.15E+02	9.59E+02
	4	6.28E+02	5.75E+02
9.5	1	8.87E+02	5.53E+02
	2	9.47E+02	5.82E+02
	3	6.73E+02	4.51E+02
	4	8.64E+02	6.27E+02
12.7	1	6.45E+02	7.18E+02
	2	7.18E+02	6.31E+02
	3	5.83E+02	4.28E+02
	4	5.38E+02	4.86E+02

6. DISCUSSIONS OF LAB ROCK CUTTING RESULTS

This section discusses the results of the laboratory full-scale linear rock cutting experiments. The results discussed here focus on the cutting forces, cutting geometry, excavation efficiency parameters such as specific energy, cutting coefficient, and surface hardness of the excavated rock and the relationship between these parameters.

6.1. PAIRWISE CORRELATION BETWEEN PARAMETERS

The first step in analyzing the linear rock cutting data was determining the pairwise correlations between the parameters, both measured and calculated. Pearson's correlation coefficients were calculated for each parameter combination (Figure 6.1, Figure 6.2, and Figure 6.3).

The rolling and normal forces had a strong positive correlation with Pearson's correlation coefficient of 0.91 (Figure 6.1). This was generally expected because high rolling forces which imply high TBM torque as associated with deep cutter penetration or cutting very hard rock. Either of these scenarios will also yield high normal force corresponding to high TBM thrust.

Both the rolling and normal forces had very weak correlations with rock fragment size distribution parameters – coarseness index, large fragments proportion, and absolute size constant. This could be because the size combination of rock fragments produced is a function of the level of interaction between adjacent cuts. The same level of cutting forces could produce large fragment size muck at optimal cut interaction or fine muck due to

crushing at suboptimal cut interaction, depending on the spacing penetration ratio. The fragment size parameters had strong positive correlations among each other, as expected.

As anticipated, there was a negative correlation between the cutting forces and specific energy (Figure 6.2). This is an established phenomenon (e.g., Gertsch, 2000; Gertsch et al., 2007; Abu Bakar, 2012; Kaba, 2018). This is because as cutting transitions from unrelieved cutting to relieved cutting, the interaction between cuts increases, resulting in more material being excavated with a slight increase in the cutting forces. This trend, however, changes as the spacing-penetration ratio surpasses the optimum values.

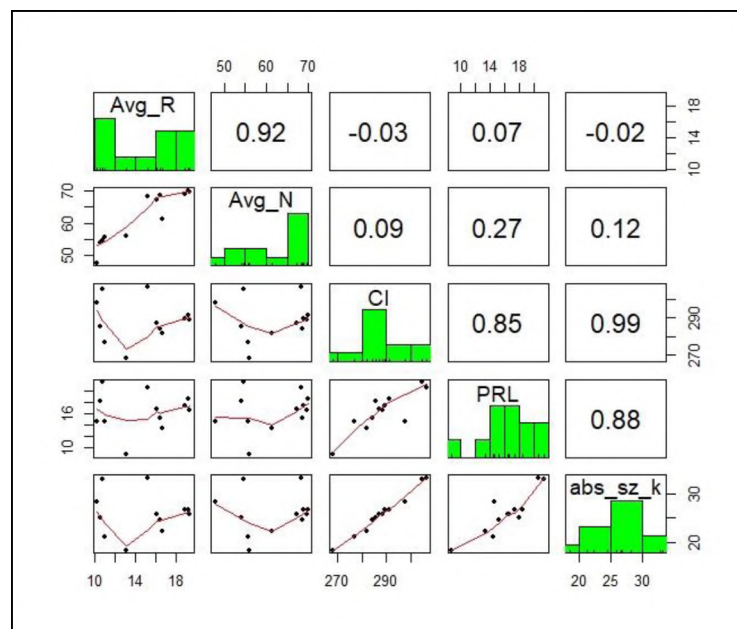


Figure 6.1. Pairwise correlation between cutting forces and fragment size parameters (Avg_R – average rolling force, Avg_N – average normal force, CI – coarseness index, PRL – large fragments proportion, abs_sz_k – absolute size constant).

Another observation was the relationship between cutting forces and surface hardness. The cutting forces had a strong negative correlation with the excavated surface hardness (Figure 6.2). Higher forces result in more invasive fracturing of the rock,

weakening its integrity and lowering the surface hardness. This is contrary to what was observed by Kaba (2018) where there was a positive correlation between the cutting forces and the surface hardness. The contradiction could be due to the different cutting tools used in the two studies. Kaba (2018) used a drag bit, which fragments the rock through a shearing action; however, this study used a disc cutter whose mode of fragmentation is through mostly tensile fracturing under indentation. Tensile forces tend to produce more radial cracks, which compromise the surface integrity as compared to the shearing action of a drag pick.

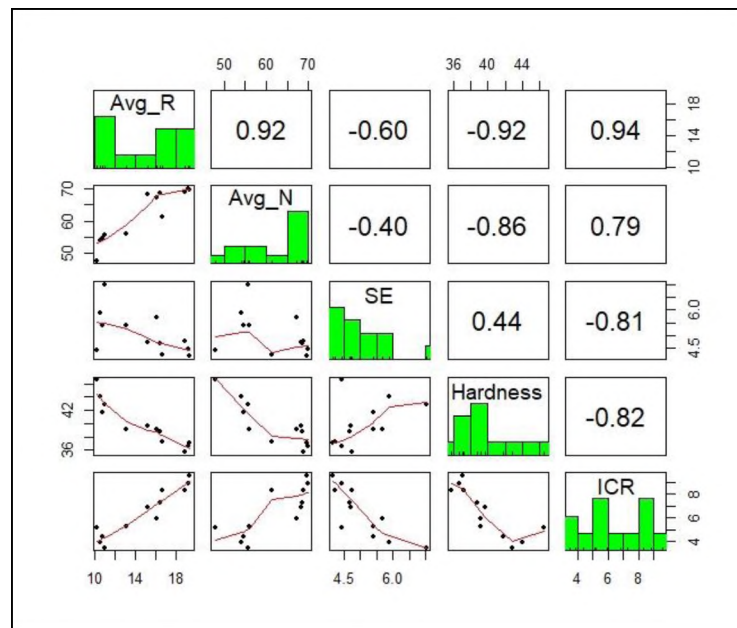


Figure 6.2. Pairwise correlation between cutting forces, hardness, and cutting rate (Avg_R – average rolling force, Avg_N – average normal force, SE – specific energy, Hardness – excavated surface hardness, LCR – linear cutting rate).

Also, there was an expected strong positive correlation between the cutting forces and the instantaneous cutting rate (ICR) (Figure 6.2). Intuitively, the cutting forces and ICR are positively correlated because the ICR is a function of the total mass of rock

fragments produced and the fragment mass is directly related to the cutting forces.

Specific energy has a negative correlation with ICR, which was also anticipated because specific energy has a negative relationship with the cutting forces (Figure 6.2). Excavated surface hardness and specific energy were positively correlated (Figure 6.2). This is because both surface hardness and specific energy are negatively correlated with the cutting forces.

From Figure 6.3, generally, specific energy had a negative correlation with the fragment size parameters. This is because, the production of coarser fragments is more energy efficient (lower specific energy) than the production of finer fragments (Roxborough and Rispin, 1973; Abu Bakar, 2012). Consequently, higher specific energy corresponds to finer fragments while lower specific energy corresponds to coarser fragments.

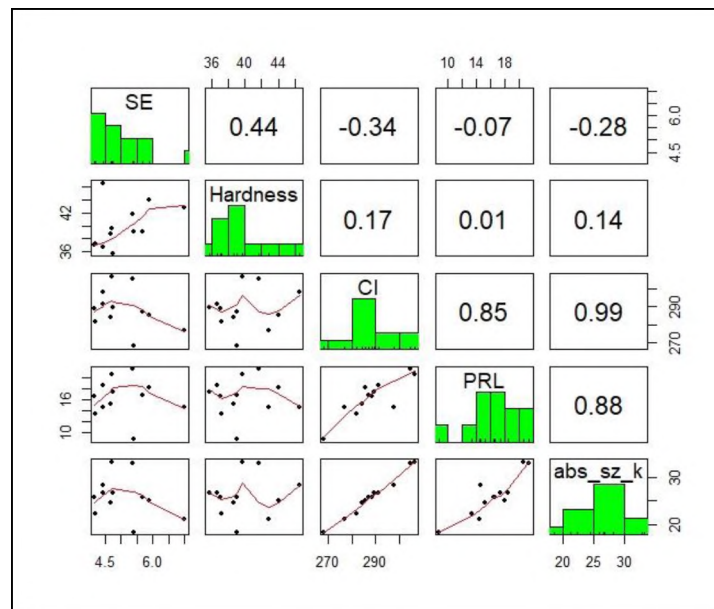


Figure 6.3. Pairwise correlation between cutting energy, hardness, and fragment size parameters (SE – specific energy, Hardness – excavated surface hardness, CI – coarseness index, PRL – large fragments proportion, abs_sz_k – absolute size constant).

The excavated surface hardness generally had a weak positive correlation with fragment size parameters. This could be due to the hardness range not being wide enough to change the mode of fracturing from brittle to ductile which will result in a significant change in the size distribution of the fragments.

6.2. RELATIONSHIP BETWEEN CUTTING FORCES AND CUTTING GEOMETRY

In this research, cutting geometry refers to the combination of cut spacing and depth of penetration of the cutter (s-p ratio) at which a pass was excavated. As stated earlier, three s-p ratios were investigated, 6, 8, and 12. That is, at a constant cut spacing of 76.2 mm, three levels of penetrations were used for the rock cutting, 6.35 mm, 9.53 mm, and 12.7 mm.

6.2.1. Rolling, Normal, and Resultant Forces and Cutting Geometry. For the investigated s-p ratios, the rolling force, the normal force, and the resultant force generally decreased with increasing s-p ratio (Figure 6.4). This was logical and consistent with the literature (e.g., Gertsch et al., 2007; Abu Bakar, 2012). Due to the constant cutting space, increasing s-p ratios implies decreasing penetration level. At higher penetration, higher forces are required for the indentation and fragmentation of the rock as compared to lower levels of penetration at constant cut spacing.

There was a notable relatively higher variability in the normal forces than in the rolling forces. This is contrary to what was observed by Gertsch (2000). He noted that there was a consistently higher variability in the rolling force compared to the normal force, which he attributed to the rolling force being more reactive to chip formation. He also associated it with the difference in the vertical and horizontal stiffnesses of the cutterhead

of the LCM used in his experiment (the Colorado School of Mines LCM). It was noted that the cutterhead was stiffer in the vertical direction than in the direction of cutting, possibly resulting in the high variability in the rolling forces. However, there was no observed difference in the vertical and horizontal cutterhead stiffness in the LCM used in the current study (the Missouri S&T LCM). The higher variability of the normal forces than the rolling forces in this research was also observed by Abu Bakar (2012) who used the Missouri S&T LCM to cut the Roubidoux Sandstone as in the current study. This observation could be attributed to the heterogeneity of the sandstone which has visible iron nodules and color banding. It could also be attributed to overbreaks due to layering in the rock.

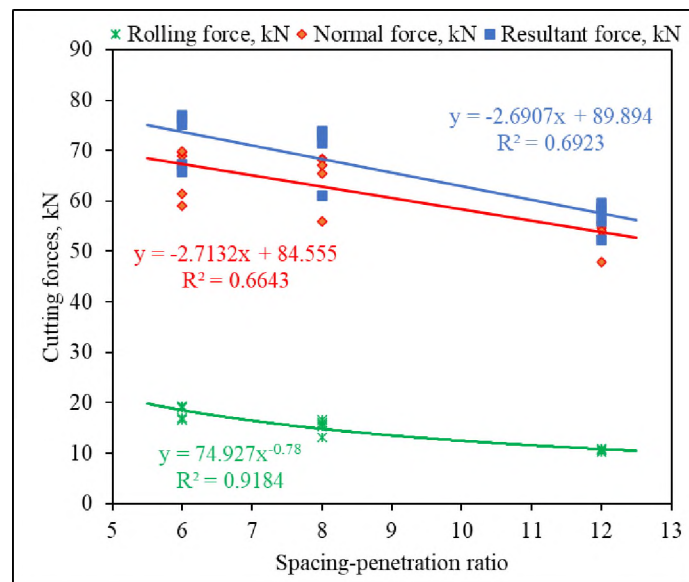


Figure 6.4. Relationship between cutting forces and spacing-penetration ratio.

Overbreaks were commonly observed during the cutting in almost every pass. The magnitude of the normal forces was much higher than that of the rolling forces, and because of that, an overbreak resulting in zero forces affected the magnitude of the average normal

forces more than that of the average rolling forces. Also, the iron nodules had different effects on the rolling and normal forces. The rolling forces acted to dislodge the nodules from the host rock and since the bond strength between the nodules and the host rock is almost the same as the bond strength within the host rock itself (Scholle & Ulmer-Scholle, 2003; Albar et al., 2019), this action did not significantly disrupt the rolling forces. Conversely, the normal forces acted to crush the nodules and because the nodules were significantly harder than the host rock, the normal forces varied significantly.

From the equations of the best-fit equations in Figure 6.4, the slope of the normal forces was steeper than that of the rolling forces. This indicates that the normal forces are more sensitive than the rolling forces to the s-p ratio. This can be attributed to the fragmentation mechanism of the rolling cutter. Higher normal forces were applied to achieve deeper penetration indentation. However, the incremental rolling force required for the forward advancement of the cutter at a deeper penetration was not as much as the incremental normal force required to achieve the deeper penetration.

The resultant forces, though slightly higher than the normal forces, had a slope close to that of the normal forces (Figure 6.4). This was because the magnitude of the normal forces was much higher than those of the side and rolling forces. Therefore, the resultant was more influenced by the normal forces, making the resultant forces mimic the trend of the normal forces.

Furthermore, hypothesis testing was conducted to determine if the change in the cutting forces with changing s-p ratio was statistically significant. The results showed that for the rolling and normal forces, at least one s-p ratio was statistically different from the rest, at a 95% confidence interval (see Table 6.1). Similar results were obtained for the

resultant forces. Further analysis was conducted to ascertain which s-p ratios differed from the other. The Tukey post hoc test was adopted. The Tukey post hoc test does a pairwise comparison of the s-p ratios. The results from the Tukey test showed that the rolling forces for all the s-p ratios were significantly different from one another (Table 6.2, Figure 6.5). The normal forces at s-p ratio 12 were significantly different from those in s-p ratios of 6, and 8 at a 95% confidence interval. However, the normal forces at s-p ratio 6 were not statistically different from those at s-p ratio 8 (Table 6.2). This can be seen in Figure 6.6 where the median normal force for s-p ratios 6 was close to that of s-p ratio 8. The resultant forces had the same relationship with the s-p ratios as did the normal forces (Table 6.2, Figure 6.7).

Table 6.1. Analysis of variance results for the cutting forces at different s-p ratios.

Parameter		Df	Sum Sq	Mean Sq	F value	Pr(>F)
Rolling force	s/p ratio	2	987.1	493.6	33.3	1.04E-11
	Residuals	96	1422.9	14.8		
Normal force	s/p ratio	2	3651	1825.7	7.221	1.20E-03
	Residuals	96	24272	252.8		
Resultant force	s/p ratio	2	4861	2430.3	9.447	1.80E-04
	Residuals	96	24696	257.2		

Table 6.2. Pairwise comparison of cutting forces at different s-p ratios.

Parameter	s/p ratio pair	difference	lower	upper	p-value
Rolling force	8-12	4.89	2.63	7.16	4.30E-06
	6-12	7.87	5.56	10.18	0.00E+00
	6-8	2.98	0.77	5.19	5.06E-03
Normal force	8-12	12.87	3.51	22.23	4.17E-03
	6-12	13.56	4.01	23.11	2.98E-03
	6-8	0.69	-8.43	9.81	9.82E-01
Resultant force	8-12	14.32	4.88	23.76	1.40E-03
	6-12	16.08	6.45	25.71	3.98E-04
	6-8	1.76	-7.44	10.97	8.92E-01

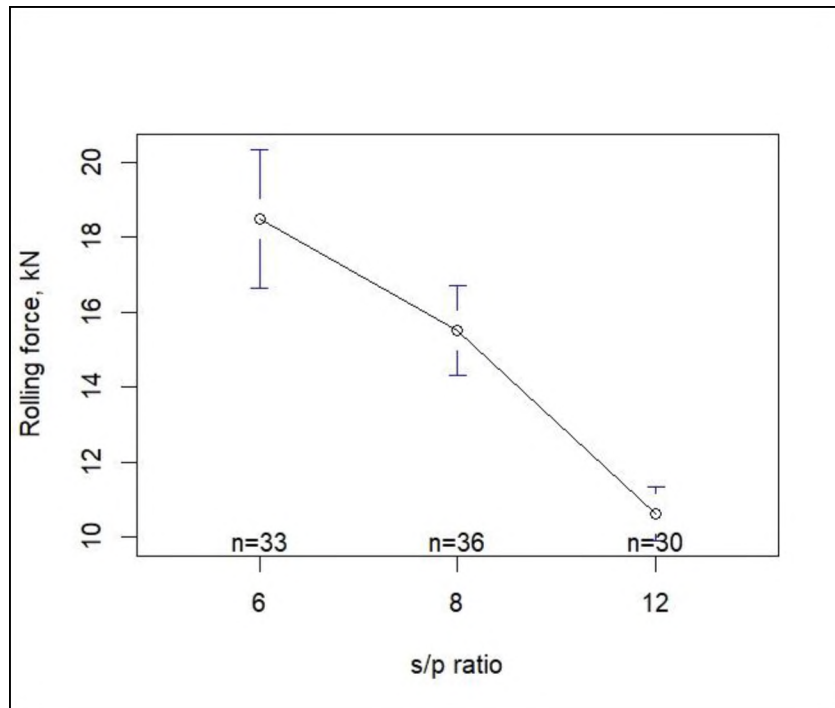


Figure 6.5. Distribution of rolling forces at different s-p ratios.

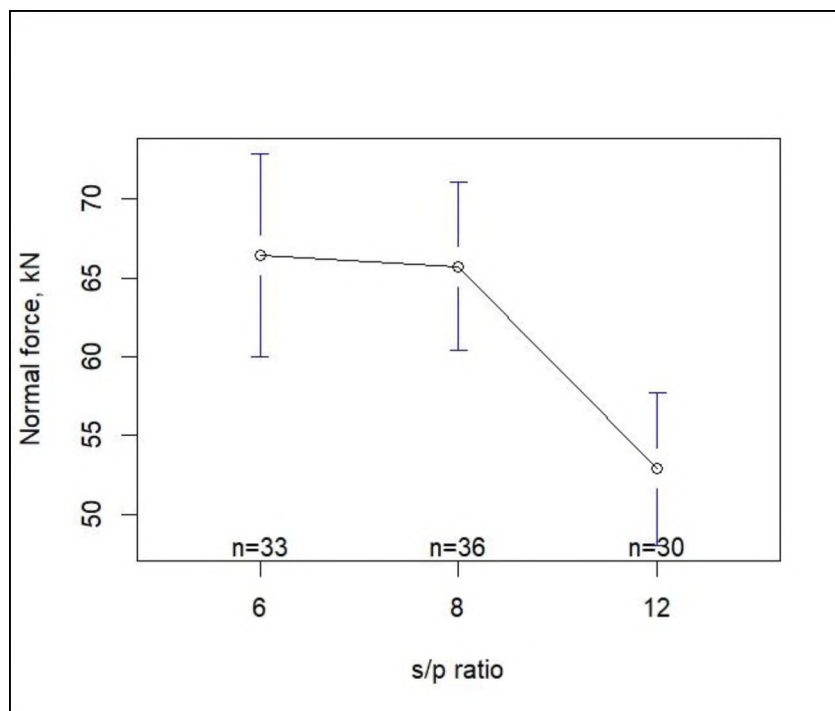


Figure 6.6. Distribution of normal forces at different s-p ratios.

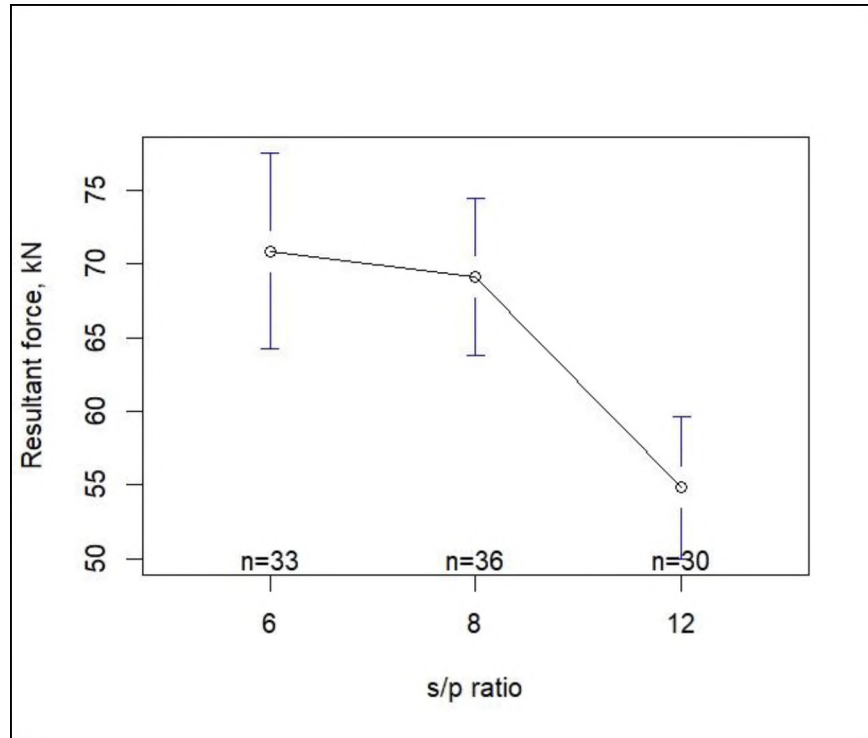


Figure 6.7. Distribution of resultant forces at different s-p ratios.

6.2.2. Side Forces and Cutting Geometry. Unlike the rolling and normal forces, the side forces had an apparent positive relationship with the s-p ratio (Figure 6.8). The side forces also had higher variability than the rolling and normal forces. The largely negative magnitude of the side forces was due to the deflection of the cutter towards the direction of the previous cut, where there was a relief from the previous cut. This deflection assertion explains the positive relationship between the side forces and the s-p ratio. At a lower s-p ratio, the high cut interaction causes more deflection of the cutter towards the relieved side, making the magnitude of the side force more negative. At a higher s-p ratio, the cut interaction is low, resulting in low cutter deflection, hence, the side forces tend to approach zero.

In Table 6.3, the results of the analysis of variance of the side forces show that the side forces at the different s-p ratios investigated were not statistically different at a 95% confidence interval. This can be seen in the overlapping dot-plot whiskers in Figure 6.9.

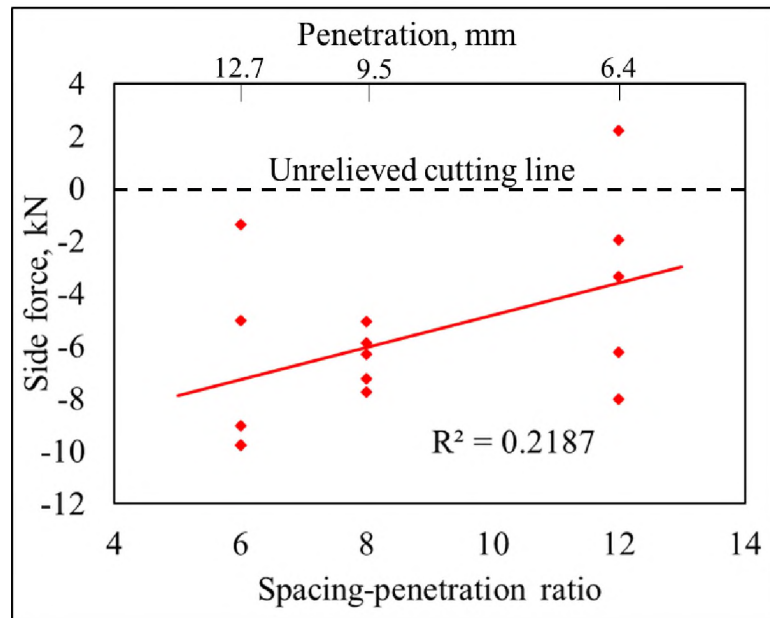


Figure 6.8. Relationship between side forces and s-p ratio.

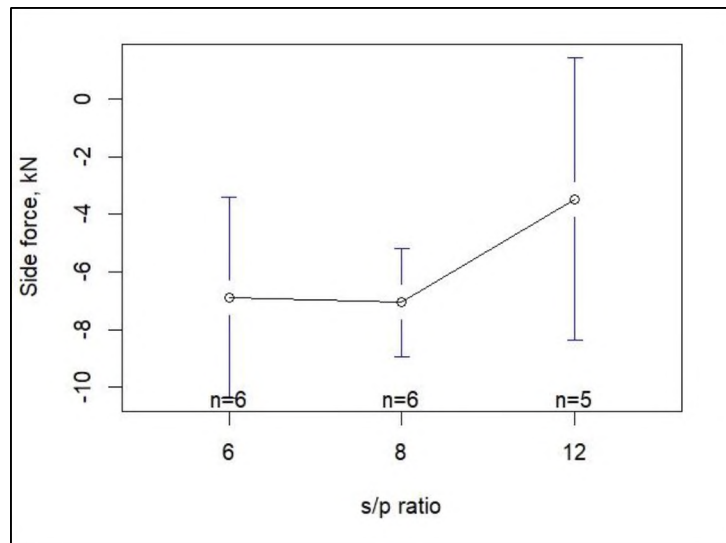


Figure 6.9. Distribution of side forces at different s-p ratios.

Table 6.3. Analysis of variance results for side forces at different s-p ratios.

Parameter	Df	Sum Sq	Mean Sq	F value	Pr(>F)
s-p ratio	2	43.6	21.8	2.27	0.14
Residuals	14	134.3	9.59		

6.3. SPECIFIC ENERGY, CUTTING EFFICIENCY, AND CUTTING GEOMETRY

6.3.1. Specific Energy and s-p Ratio. Generally, specific energy increased with increasing s-p ratio (Figure 6.10). This is consistent with Roxborough and Philips (1975) who observed a uniform upward trend of specific energy between s-p ratios 5 and 12. The variability in the specific energy increased with increasing s-p ratio, similar to the observation by Kaba (2018). This can be attributed to the level of interaction between cuts at the various s-p ratios. At a high s-p ratio, there is partial interaction between adjacent cuts. As a result, the formation of chips is not consistent, and ridges commonly form between cuts. This leads to more variability because the amount of rock fragments produced for the same amount of cutting forces is variable, depending on other factors such as pre-existing flaws in the rock and the presence of inclusions. At a low s-p ratio, there is complete interaction between adjacent cuts leading to more consistent production of rock fragments, therefore, less variability in the specific energy.

ANOVA test results showed that, at least, the specific energy at one s-p ratio was significantly different from the rest (Table 6.4). Based on a Tukey pairwise comparison (Table 6.5), the specific energy at s-p ratio 12 was significantly different from those at s-p ratios 6 and 8. However, there is no evidence that the specific energy at s-p ratio 6 is significantly different from that at s-p ratio 8 (Table 6.5, Figure 6.11).

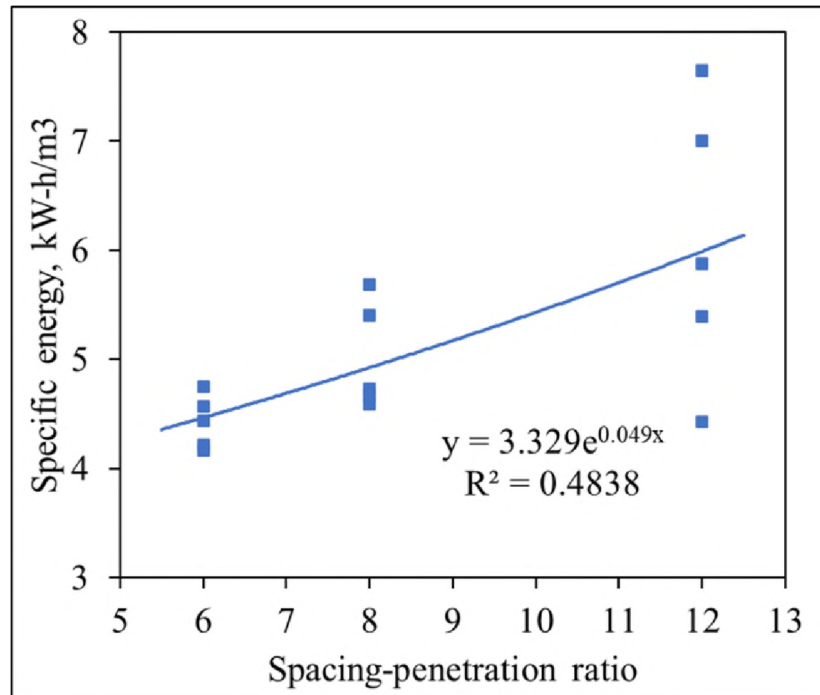


Figure 6.10. Relationship between specific energy and spacing-penetration ratio.

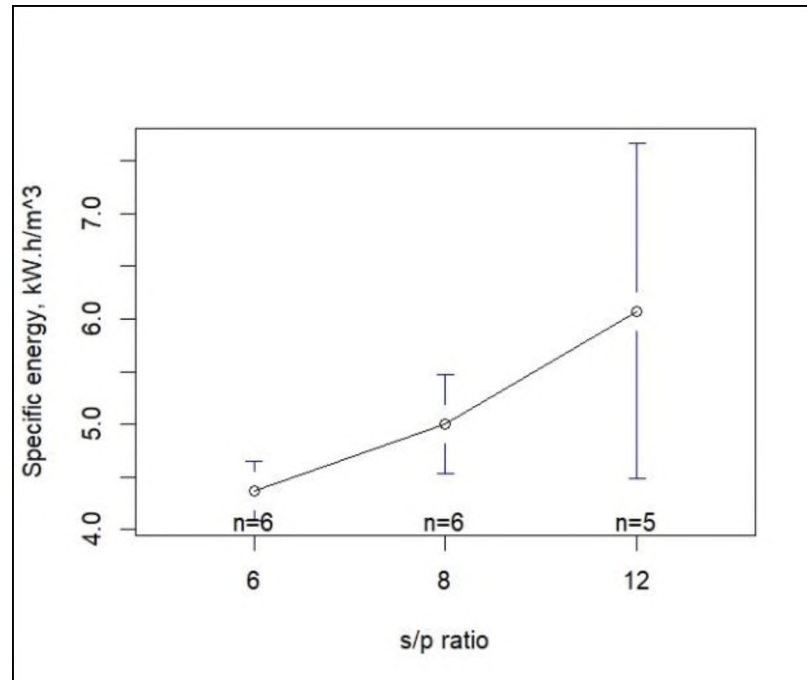


Figure 6.11. Distribution of specific energy at different s-p ratios.

An explanation for the normal forces and the specific energy being statistically significantly different at s-p ratio 12, but not at s-p ratios 6 and 8, is that relieved cutting (complete cut interaction) was achieved at s-p ratios 6 and 8. It is believed that the optimal s-p ratio in which complete cut interaction was first achieved in this rock was between s-p ratios 8 and 12, even though there was no observable change in direction of the specific energy curve. Tumac and Balci (2015) also observed the optimal s-p ratio to be 8 and 12 for several rocks using different disc cutter types. Han et al. (2017) recorded an optimal s-p ratio of 10 in sandstone. Therefore, only partial unrelieved cutting was realized in s-p ratio 12, thus, making it different. The non-observable turning point of the specific energy curve is possibly due to the high variability in the specific energy and the sparseness of the tested s-p ratios.

Table 6.4. Analysis of variance results for specific energy at different s-p ratios.

Parameter		Df	Sum Sq	Mean Sq	F value	Pr(>F)
Specific Energy	s/p ratio	2	8.004	4.002	7.081	7.50E-03
	Residuals	14	7.912	0.565		

Table 6.5. Pairwise comparison of specific energy at different s-p ratios.

Parameter	s/p ratio pair	difference	lower	Upper	p-value
Specific energy	8-12	-1.07	-2.26	0.12	8.22E-02
	6-12	-1.71	-2.90	-0.51	5.75E-03
	6-8	-0.64	-1.77	0.50	3.34E-01

6.3.2. Cutting Coefficient and s-p Ratio. The cutting coefficient—the required torque for a given amount of TBM thrust—was estimated as the ratio of rolling forces to normal forces expressed as a percentage. There was a power relationship between the s-p

ratio and cutting coefficient (Figure 6.12). The cutting coefficient decreased with increasing s-p ratio, consistent with the observations of Abu Bakar (2012), but he observed a linear relationship.

This relationship shows that for a given cut spacing, the torque requirements increase with increasing cutter penetration (Rostami & Ozdemir, 1993; Rostami, 1997; Gertsch et al., 2007). This is also consistent with the observed trends in the rolling and normal forces. The power relationship exhibited in Figure 6.12 is possibly an expression of a combination of partial unrelieved cutting at s-p ratio 12 and relieved cutting at s-p ratios 6 and 8.

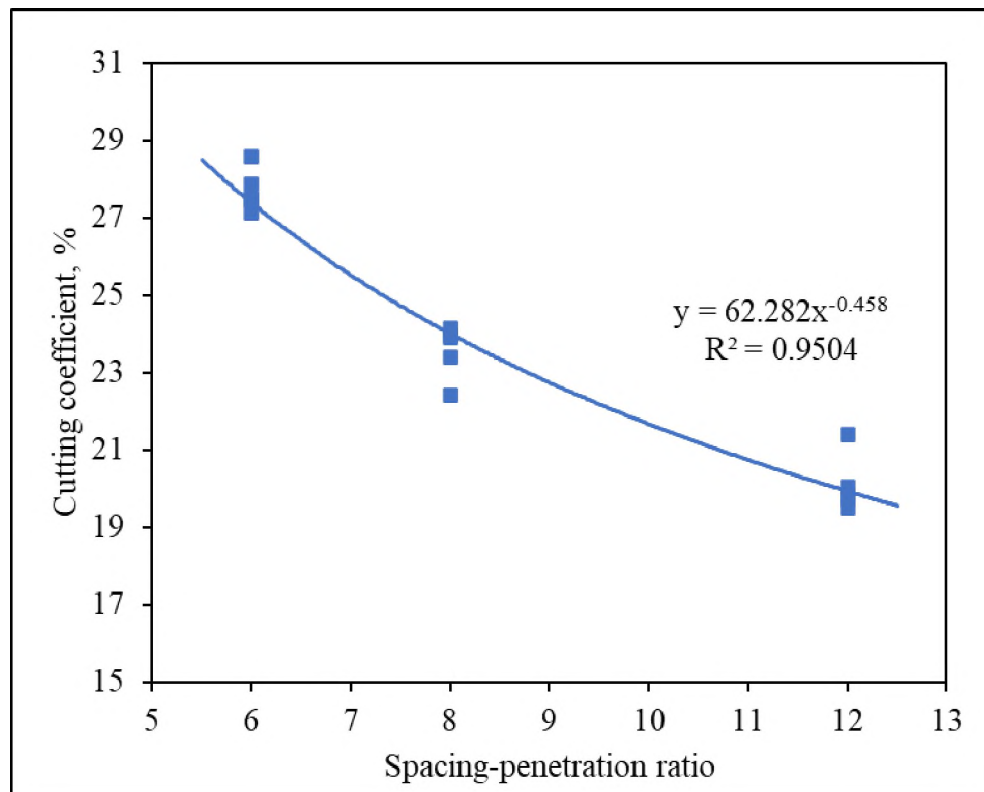


Figure 6.12. Relationship between cutting coefficient and s-p ratio.

6.4. INSTANTANEOUS CUTTING RATE

6.4.1. Instantaneous Cutting Rate and s-p Ratio. The ICR is the mass of rock fragments produced per unit time. As shown in Figure 6.13, ICR decreases with increasing s-p ratio. At constant cut spacing, deeper penetration means more cut interaction resulting in more rock fragmentation, consequently, the relationship depicted in Figure 6.13. The findings in the current research are consistent with those of Kaba (2018) who conducted linear rock cutting experiments on samples from the same rock using a drag pick.

An analysis of variance of ICR at different s-p ratios showed that, on average, the ICR at each s-p ratio tested was statistically different from the other two (Table 6.6). This was exemplified in Figure 6.14 where there were no visible error bars while the median points were different.

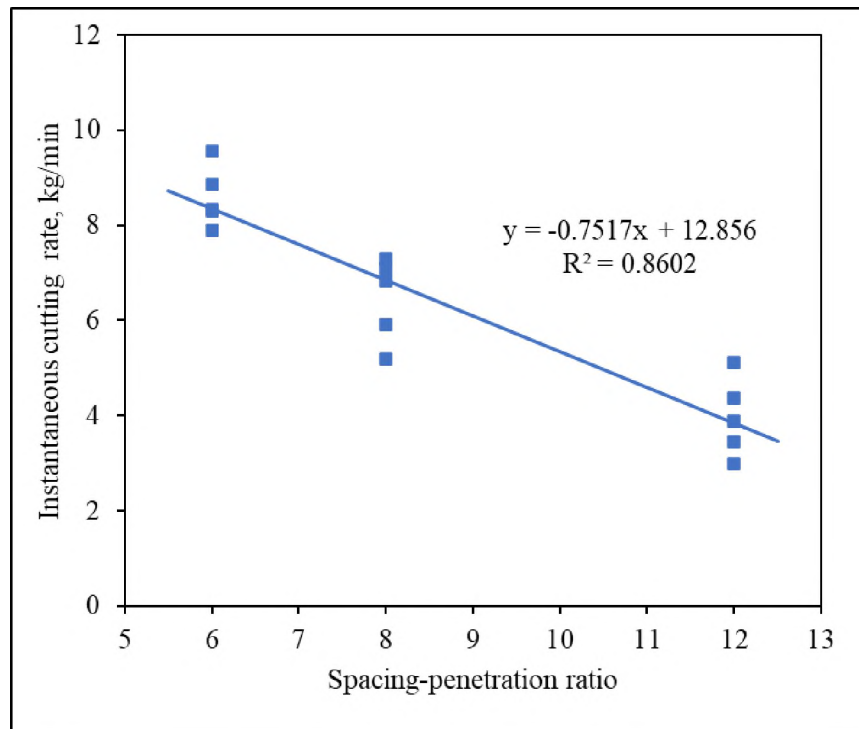


Figure 6.13. Relationship between instantaneous cutting rate and s-p ratio.

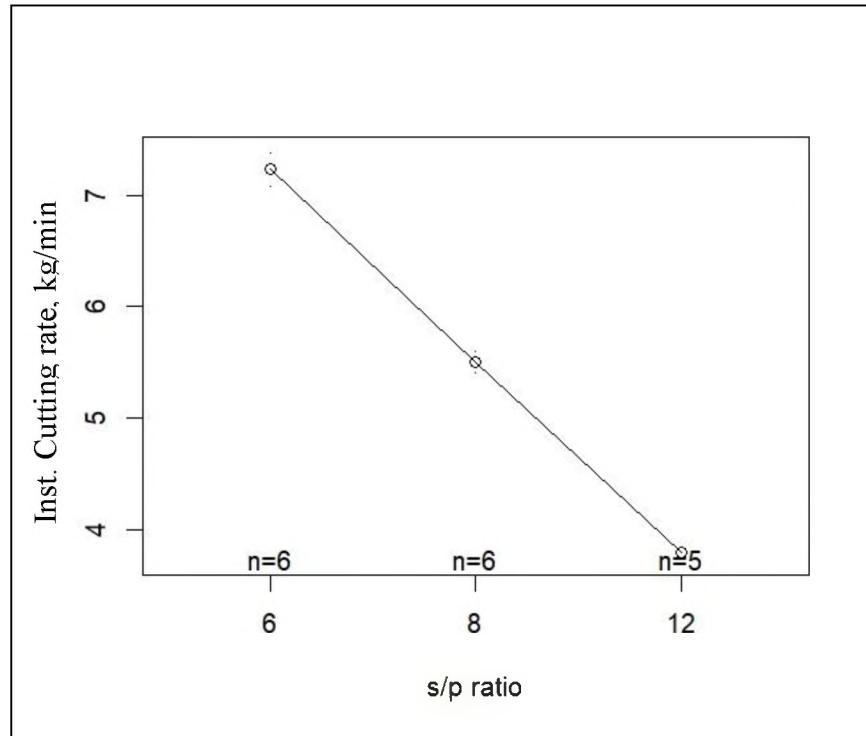


Figure 6.14. Distribution of instantaneous cutting rate at different s-p ratios.

Table 6.6. Analysis of variance results for the instantaneous cutting rate at different s-p ratios.

Parameter		Df	Sum Sq	Mean Sq	F value	Pr(>F)
Inst. Cutting rate	s/p ratio	2	32.23	16.12	1567	<2e-16
	Residuals	14	0.14	0.01		

Table 6.7. Pairwise comparison of linear cutting rate at different s-p ratios.

Parameter	s/p ratio pair	difference	Lower	upper	p-value
Inst. Cutting rate	8-12	1.71	1.55	1.87	0.00E+00
	6-12	3.43	3.27	3.59	0.00E+00
	6-8	1.72	1.57	1.87	0.00E+00

6.4.2. Instantaneous Cutting Rate and Specific Energy. The relationship between ICR and SE is consistent with the relationships reported in the literature (e.g.,

Gertsch, 2000; Copur et al., 2017; Kaba, 2018; Xia et al., 2018). There was a power relationship between the instantaneous cutting rate and the specific energy with a negative gradient (Figure 6.15). This is also in conformity with the theoretical relationship between ICR and specific energy (Eq. 6.1). From the relationship shown in Figure 6.15, as the specific energy increased, the rate at which ICR changes decreased. It implies that at a higher specific energy, the change in ICR is insignificant.

$$ICR = \eta \frac{P}{SE_{opt}} \quad (6.1)$$

Where; P is cutterhead power;

ICR – Instantaneous cutting rate;

SE_{opt} is optimal specific energy; and

η is the total system efficiency coefficient (Rostami et al., 1994; Copur et al., 2017).

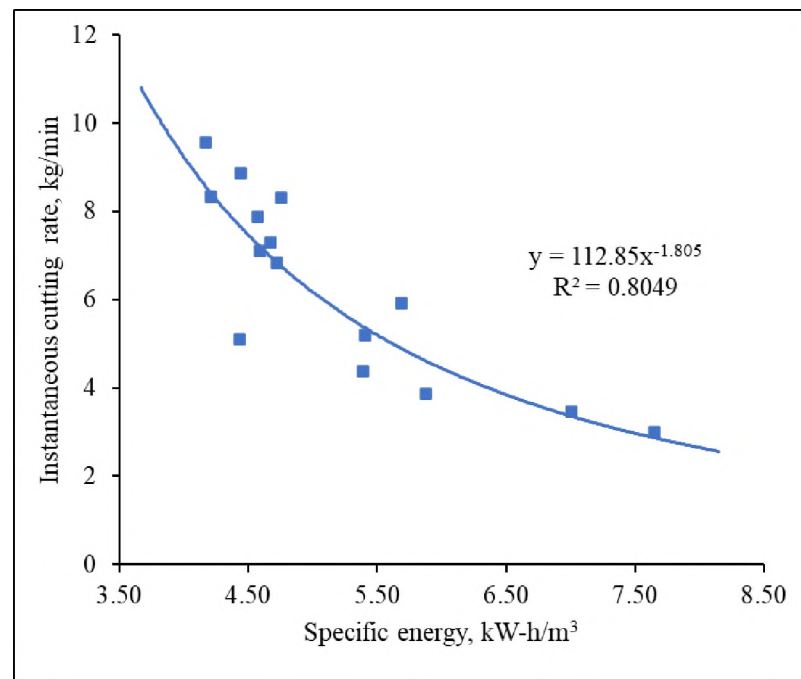


Figure 6.15. Relationship between linear or instantaneous cutting rate and specific energy.

6.4.3. Cutting Efficiency and s-p Ratio Cutting efficiency is the proportion of the rock material designed to be excavated, that is excavated. It is the ratio of actual instantaneous cutting rate to nominal or designed cutting rate expressed as a percentage.

In this study, there was no unique trend of the cutting efficiency in relation to the s-p ratio (Figure 6.16). However, it was observed that at s-p ratio 6, where there was full relieved cutting with a lot of overbreaks, all the cutting efficiencies were greater than 100% with relatively lower variability. At higher s-p ratios, there were instances of sub-optimal cutting with cutting efficiencies less than 100%. The high variability and lack of a definite trend can be attributed to the bedding planes, and other discontinuities in the rock that resulted in overbreaks even in the partial unrelieved cutting, which compensated for the underbreaks.

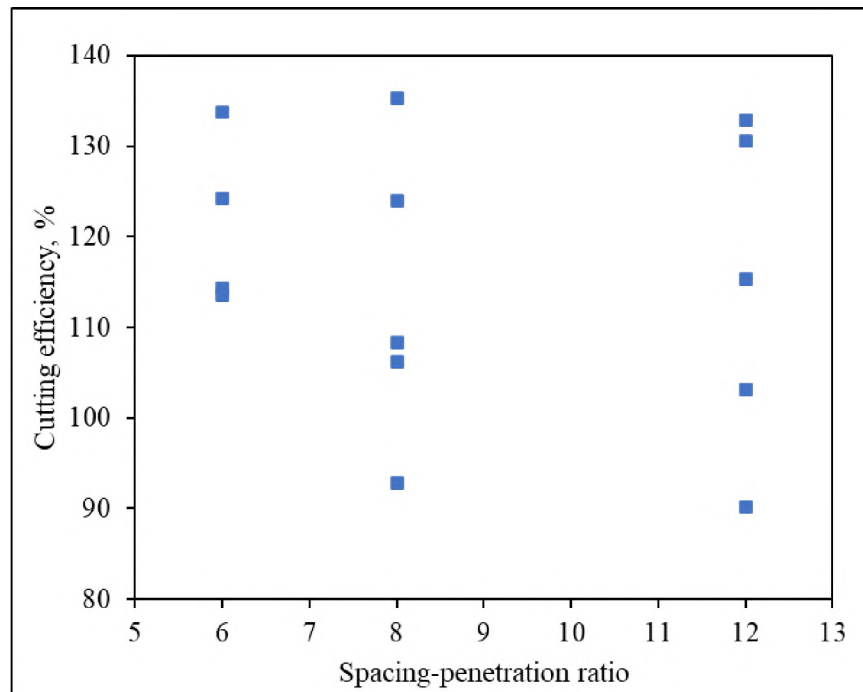


Figure 6.16. Relationship between cutting efficiency and spacing-penetration ratio.

6.5. UNDERBREAKS, OVERBREAKS, AND CUTTING GEOMETRY

Ideal excavation is when all the material between successive cuts is completely removed to the depth of the cutter penetration. However, this is rarely achieved in practice. In the field or lab, underbreaks occur resulting in ridge formation between cuts due to unrelieved cutting or rock heterogeneity. Overbreaks also occur where rock material breaks beyond the cutter penetration and/or beyond the cut spacing. Overbreaks are controlled by inherent flaws and discontinuities in the rock such as bedding planes, fractures, and iron nodules. In this research, the volume of the ridges (amount of uncut rock) created between cuts and the troughs (areas of overbreak) were computed from the digital elevation models of the excavated surfaces obtained from the excavated surface of each pass. The digitization of the excavated surfaces was described in Section 3.5.2. Sections 6.5.1-6.5.4 discuss the relations between these volumes, cutting geometry, and specific energy.

6.5.1. Ridge Volume and s-p Ratio. To ascertain the behavior of the ridge volume in relation to the s-p ratio, an analysis of variance was conducted. The results of this analysis are presented in Table 6.8. The results indicated that at a 95% confidence interval, at least, the ridge volume at one s-p ratio was statistically different from the others. A post hoc analysis using a Tukey test (Table 6.9) showed that the ridge volume at s-p ratio 8 was statistically different from those at s-p ratios 6 and 12. The ridge volumes at s-p ratios 6 and 12, however, were not statistically different. This can be seen in Figure 6.17 where the median ridge volumes at s-p ratios of 6 and 12 were approximately the same level while the median ridge volume at the s-p ratio of 8 was significantly higher.

A possible explanation for the trend seen in Figure 6.17 is that, as the s-p ratio increased beyond the optimum value (between 7 and 10), unrelieved cutting was realized

and a significant volume of ridges formed between cuts. As the s-p ratio increased further, corresponding to decreasing penetration (at constant cut spacing), the nominal volume of material to be excavated decreased; therefore, the volume of ridges decreased. As the penetration increased at the same cut spacing reaching an s-p ratio of 8, the expected (nominal) excavation volume increased. The partial cut interaction at deeper penetration resulted in the formation of ridges bigger than those formed at shallower penetration (Figure 6.18). Further increase in the penetration at the same cut spacing led to complete interaction between cuts, resulting in the removal of almost all the material between successive cuts, which was the case at s-p ratio 6. This implies that optimal s-p operations result in complete planing of the rock surfaces if there are no discontinuities and rock heterogeneities to cause excessive overbreaks. Partial or no cut interaction results in groove deepening where the grooves created by successive passes are progressively deepened without the formation of chips (Lislerud, 1997; Bilgin et al., 2014). This can cause cutting tool failure due to shock loads or stalling of the excavation machine as a result of the machine face coming into contact with the rock surface.

Table 6.8. Analysis of variance of ridge volumes at different s-p ratios.

Parameter		Df	Sum Sq	Mean Sq	F value	Pr(>F)
Ridge volume	s/p ratio	2	19649	9825	4.465	1.40E-02
	Residuals	96	211215	2200		

Table 6.9. Pairwise comparison of ridge volume at different s-p ratios.

Parameter	s/p ratio pair	difference	lower	upper	p-value
Ridge volume	8-12	31.23	3.63	58.84	2.25E-02
	6-12	4.09	-24.08	32.26	9.36E-01
	6-8	-27.14	-54.05	-0.23	4.76E-02

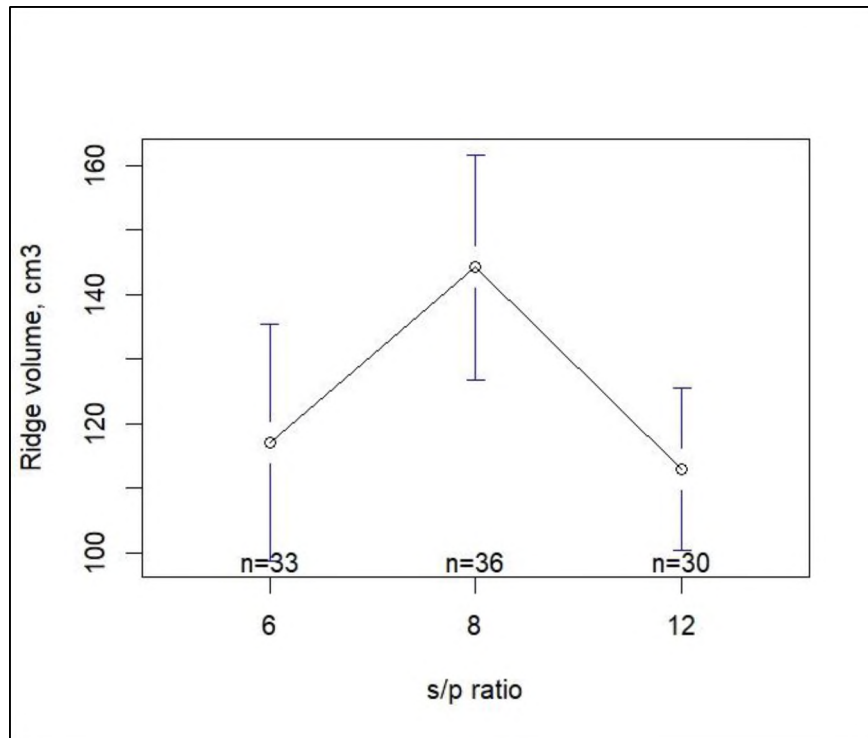


Figure 6.17. Distribution of ridge volume at different s-p ratios.

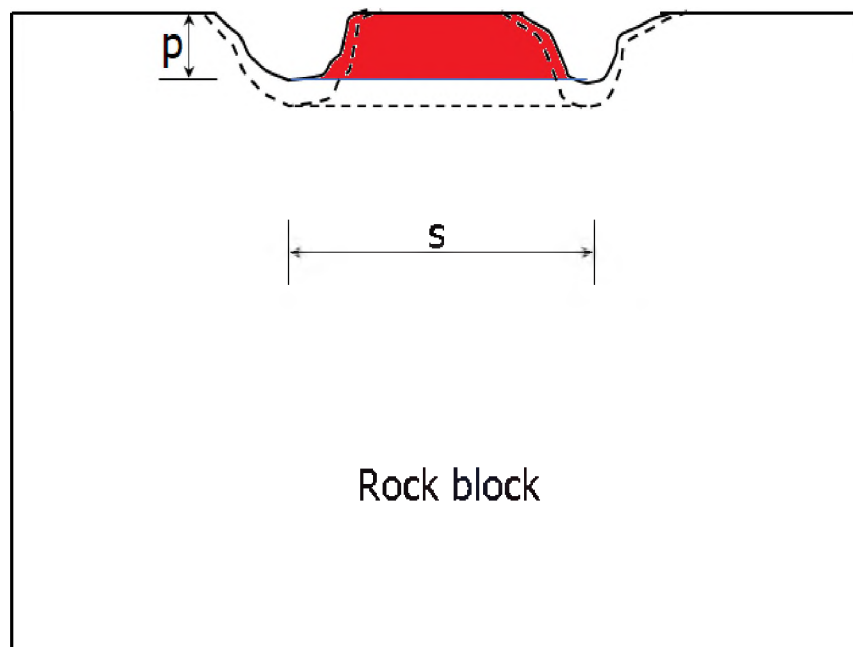


Figure 6.18. Illustration of deep unrelieved cutting having bigger ridges than shallow cutting.

6.5.2. Ridge Volume and Specific Energy. Ridges are more common when there is unrelieved cutting or when there is partial interaction between successive cuts. When relieved cutting is achieved, the volume of ridges is expected to be minimal. It is, therefore, not strange that the volume of rock material in the ridges has a positive power relationship with specific energy for the range of specific energy recorded in this research (Figure 6.19).

Both the ridge volume and specific energy were dependent on the s-p ratio. Because the relationship between the specific energy and s-p ratio was linear in this research (see Figure 6.10), the relation between the ridge volume and specific energy (Figure 6.19) mimicked the relationship between the ridge volume and s-p ratio (see Figure 6.17). Due to the structure of the experiments in this research, the independent effect of specific energy on ridge volume cannot be assessed.

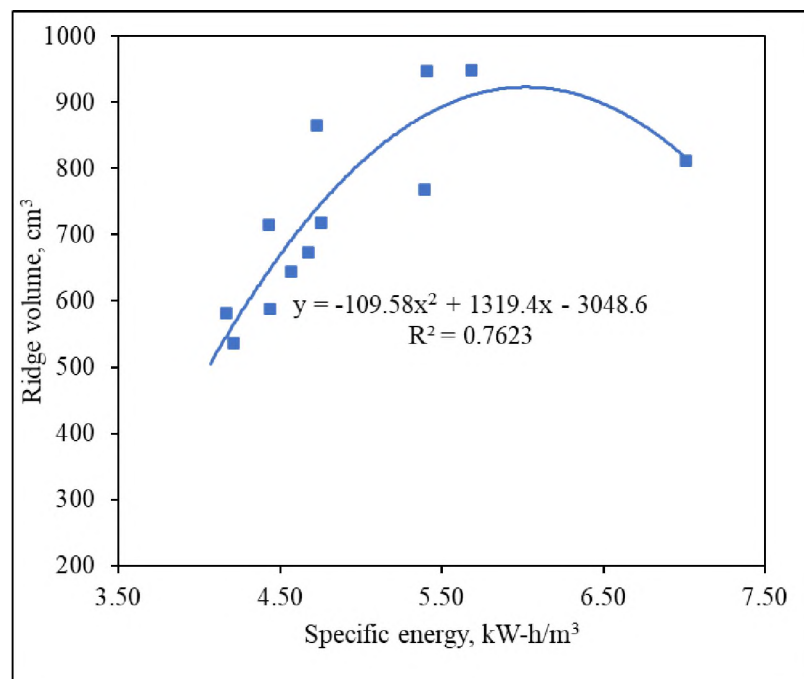


Figure 6.19. Relationship between ridge volume and specific energy.

6.5.3. Overbreak Volume and s-p Ratio. The median volume of overbreak material at s-p ratio 6 appeared to be higher than those of s-p ratios 8 and 12 (Figure 6.20). This is intuitive because there was complete cut interaction at s-p ratio 6. However, based on analysis of variance conducted (Table 6.10), the overbreak volume at the three s-p ratios was not significantly different at 5% level of significance. This was also obvious in the overlap of the error whiskers in Figure 6.20.

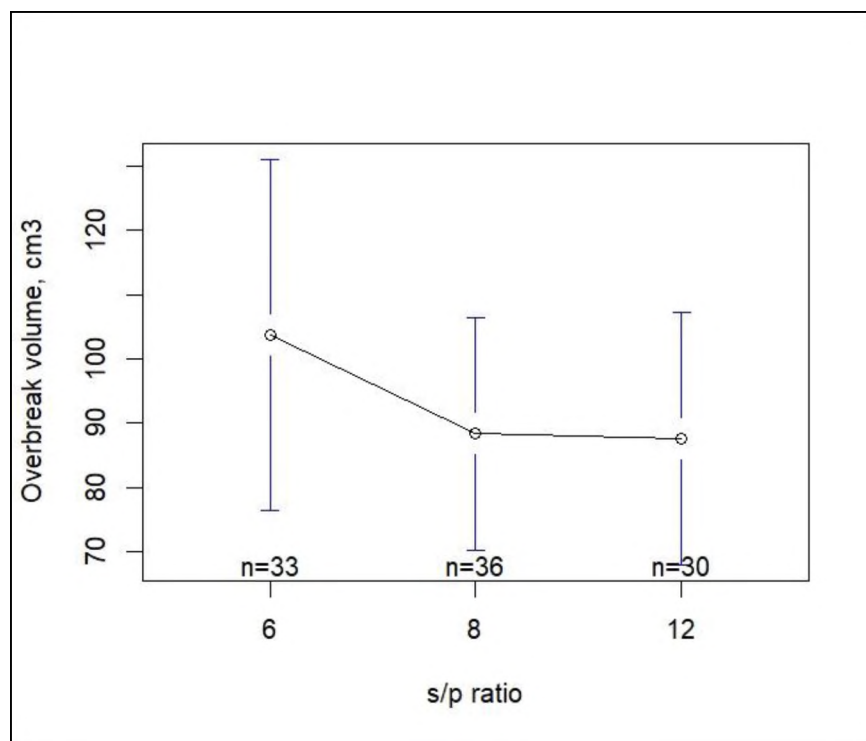


Figure 6.20. Distribution of overbreak volume at different spacing-penetration ratios.

Table 6.10. Analysis of variance of overbreak volume at different s-p ratios.

Parameter		Df	Sum Sq	Mean Sq	F value	Pr(>F)
Overbreak volume	s/p ratio	2	5439	2720	0.701	4.98E-01
	Residuals	96	372272	3878		

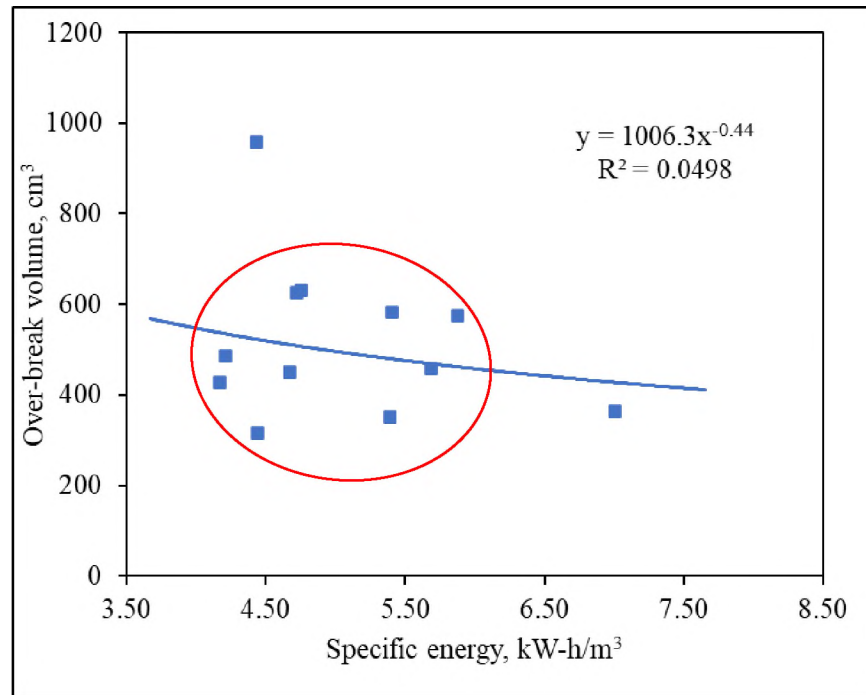


Figure 6.21. Relationship between overbreak volume and specific energy.

6.5.4. Overbreaks and Specific Energy. The overbreak volume is mostly controlled by discontinuities and flaws in the rock. It can also result from groove deepening in unrelieved cutting. After several passes of groove deepening, the ridges finally broke out, taking material beyond the designed spacing and penetration. As a result of these controlling factors, it is expected that the overbreak volume is less related to the specific energy. The results from this study confirm this expectation as shown in Figure 6.21. With an $R^2 = 0.05$, there was virtually no relationship between the overbreak volume and the specific energy.

6.6. EXCAVATED SURFACE HARDNESS

6.6.1. Surface Hardness and s-p Ratio. The hardness of the excavated surface—a measure of the integrity of the rock after excavation—was measured using the rock

Schmidt hammer. Surface hardness increased with increasing s-p ratio (Figure 6.22).

At constant cut spacing, fracturing becomes more intense with increasing cutter penetration. Fractures penetrate deeper and the fracture density increases due to the increased level of interaction between cuts. This results in the rock becoming weaker at lower s-p ratios, thereby creating lower surface hardness values. The surface hardness had more variability at s-p ratio of 12 than at 6, and 8 (Figure 6.22). This can be attributed to low cut interaction at s-p ratio 12, making the surface hardness more dependent on inherent rock heterogeneities, rather than the effects of cutting.

Based on an analysis of variance and a pairwise post hoc test presented in Table 6.11 and Table 6.12, respectively, the surface hardness at each s-p ratio was statistically significantly different from the others. A visual representation of this is shown in Figure 6.23, where there is essentially no overlap between the whiskers of the dot plots.

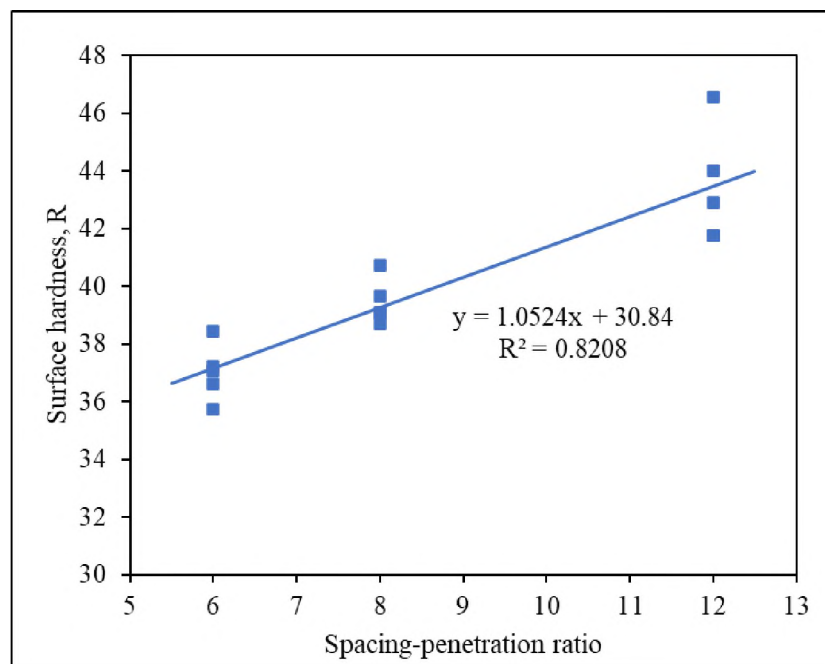


Figure 6.22. Relationship between excavated surface hardness and s-p ratio.

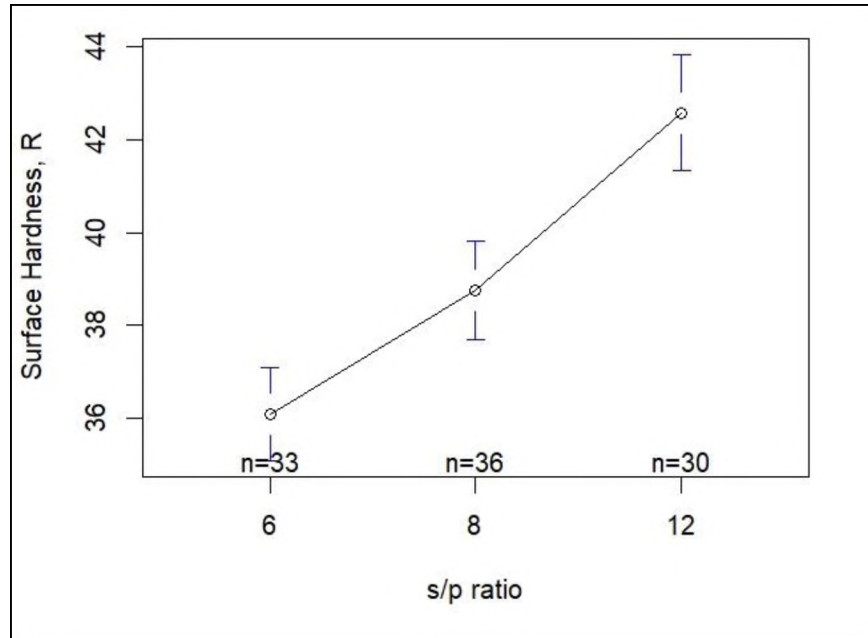


Figure 6.23. Distribution of excavated surface hardness at different spacing-penetration ratios.

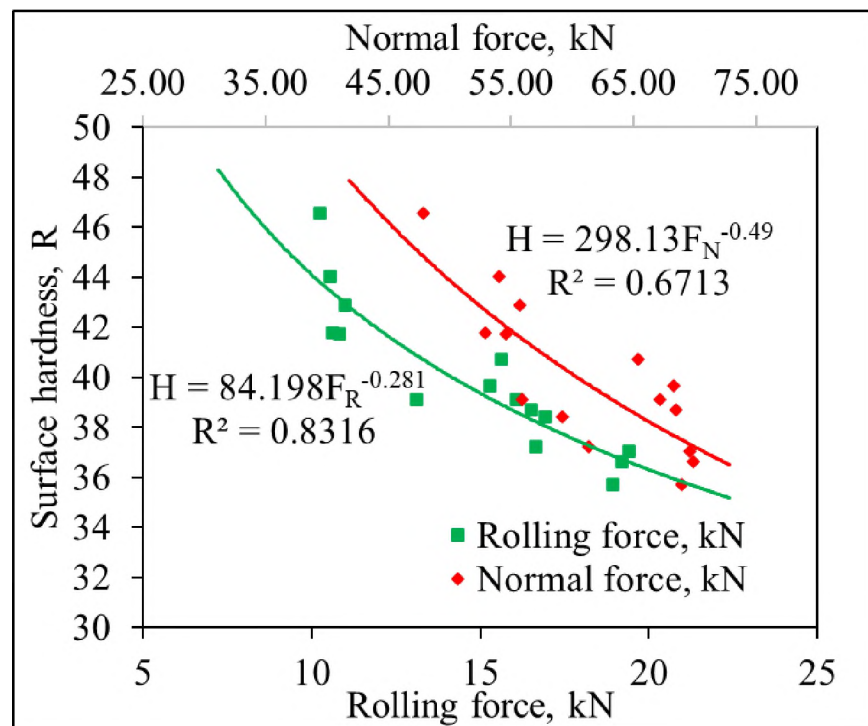


Figure 6.24. Relationship between cutting forces and excavated surface hardness.

Table 6.11. ANOVA of excavated surface hardness at different s-p ratios.

Parameter		Df	Sum Sq	Mean Sq	F value	Pr(>F)
Surface Hardness	s/p ratio	2	662.8	331.4	34.22	6.04E-12
	Residuals	96	929.8	9.7		

Table 6.12. Pairwise comparison of excavated surface hardness at different s-p ratios.

Parameter	s/p ratio pair	difference	lower	upper	p-value
Surface Hardness	8-12	-3.81	-5.64	-1.98	9.30E-06
	6-12	-6.47	-8.34	-4.61	0.00E+00
	6-8	-2.66	-4.45	-0.88	1.71E-03

6.6.2. Cutting Forces and Excavated Surface Hardness. A plot of the cutting forces against the excavated surface hardness (Figure 6.24) showed that the cutting forces had negative power relationships with the hardness. That is, lower cutting forces yield harder excavation faces, while higher forces yield weaker excavation faces. The rolling force had a higher correlation coefficient with the hardness than the normal force. This is because the normal force was more variable with respect to the cutter penetration when compared to the rolling force as discussed in Section 6.2.1 (see Figure 6.4). Like the relationship between the cutting forces and s-p ratio, the normal force-hardness curve had a steeper slope than the rolling force-hardness curve.

6.6.3. Specific Energy and Excavated Surface Hardness. There was an apparent weak positive linear relationship between specific energy and surface hardness. This conforms with Tiryaki and Dikmen (2006) and Tumac et al. (2007) who recorded a positive relationship between specific energy and the hardness of sandstone excavated with a drag pick. This phenomenon may be because weaker rock surfaces correspond to a low s-p ratio,

which in turn corresponds to low specific energy. The variability of specific energy was lower when the surface hardness was low, and it increased as the surface hardness increased (Figure 6.25). This is because the harder rock surface occurred at a higher s-p ratio. From the discussion in Section 6.3.1, the variability of specific energy increased with increasing s-p ratio (Figure 6.10). This relationship may be different at ranges of specific energy or surface hardness values other than what was investigated in this study. Also, it must be noted that, in this case, the observed trend cannot be fully attributed to the effect of surface hardness on specific energy because the cutting geometry (s-p ratio) also had an influence on specific energy.

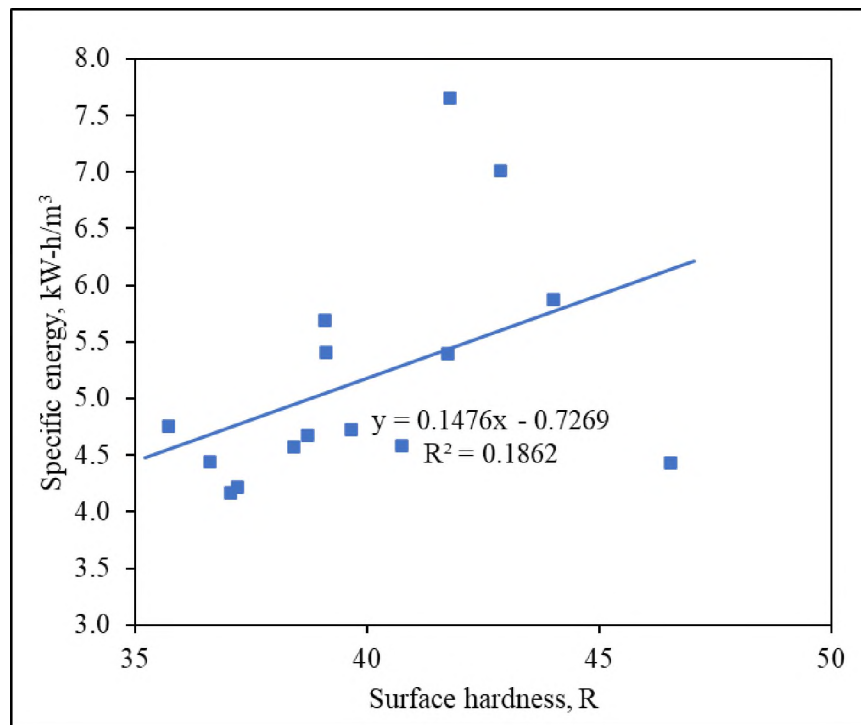


Figure 6.25. Relationship between excavated surface hardness and specific energy.

6.6.4. Specific Energy, s-p Ratio, and Surface Hardness. The combined effect of the s-p ratio and surface hardness on the specific energy was studied (Figure 6.26). The

points represent the observed values while the planar surface is a model relating the specific energy to the s-p ratio and surface hardness. The figure shows that the specific energy was highest at high s-p ratio and low surface hardness, and it was lowest at low s-p ratio and high surface hardness. This is contrary to the relationship shown in Figure 6.25, where the specific energy increased with increasing surface hardness. Further investigation revealed that there was a negative relationship between specific energy and surface hardness within each s-p ratio though, the overall fit across s-p ratios appeared to be positive (Figure 6.27). This implies that the overall positive relationship recorded in Figure 6.25 was due to the confounding of the s-p ratio (Glen, 2020).

The negative relationship between specific energy and surface hardness can be attributed to the fragmentation mechanism of rolling cutters. Rock fragmentation under disc cutters is by tensile fracturing due to the indentation effect of the cutters. The tensile cracks initiate and propagate faster and more efficiently in harder, brittle rocks than in softer rocks (Vogt, 2016). Therefore, fragmentation by disc cutters is more efficient in harder rocks when compared to softer or weaker rocks.

Table 6.13. ANOVA of specific energy in relation to s-p ratio and surface hardness.

Parameter	Df	Sum Sq	Mean Sq	F value	Pr(>F)
s-p ratio	2	6.90	3.45	8.58	5.70E-03
Hardness	1	2.60	2.60	6.45	2.75E-02
s-p ratio*Hardness	2	0.89	0.45	1.11	3.65E-01
Error	11	4.42	0.40		

An analysis of variance showed that the combined effect of s-p ratio and surface hardness was not statistically significant at a 95% confidence interval (Table 6.13).

However, the main effects of both s-p ratio and surface hardness were statistically significant. This implies that, though, both s-p ratio and surface hardness influence the specific energy independently, the influence of one does not depend on the other.

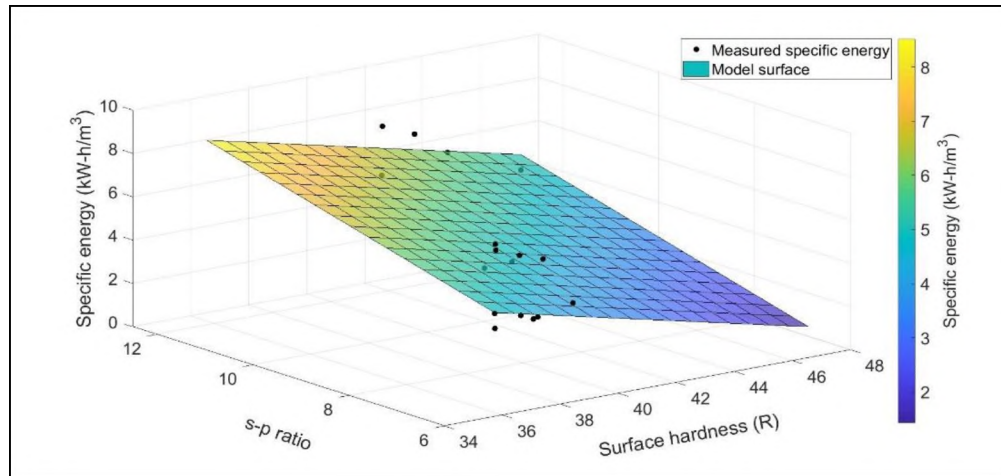


Figure 6.26. Relationship between specific energy, s-p ratio, and excavated surface hardness with the measured points and a modeled plane surface.

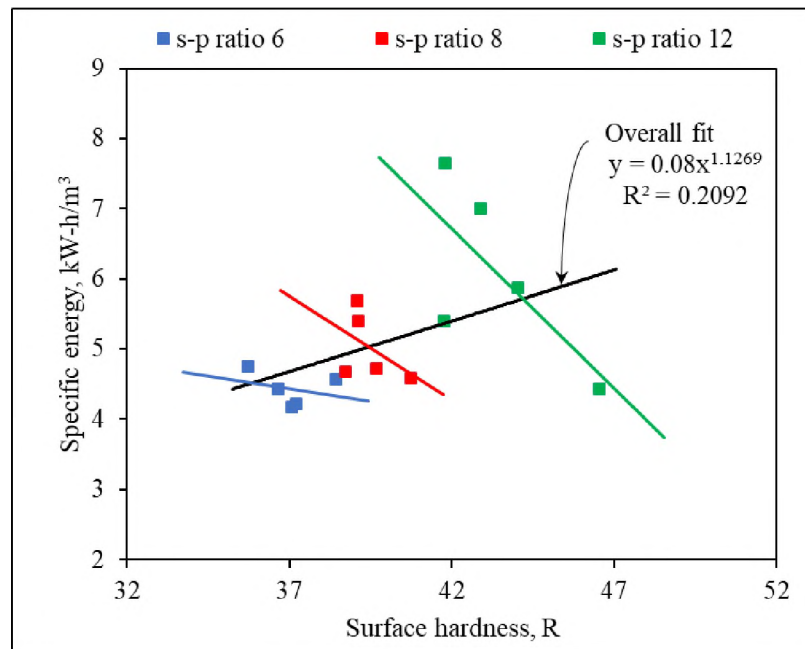


Figure 6.27. Relationship between specific energy and surface hardness within each s-p ratio.

A regression analysis involving specific energy as a dependent variable, s-p ratio, and surface hardness as independent variables was conducted and presented in Table 6.14. This analysis was meant to establish a relationship between specific energy and s-p ratio, and surface hardness. The interaction term between s-p ratio and surface hardness was statistically insignificant (Table 6.13), and because of that, it was left out of the regression formulation. The regression results show that specific energy had a positive relationship with s-p ratio when surface hardness is kept constant and has a negative relationship with surface hardness at a constant s-p ratio. The regression formulation is given in Eq. 6.2.

Table 6.14. Regression analysis with specific energy as the dependent variable.

Variable	Estimate	Standard error	Pr(> t)
Intercept	13.99	4.16	5.69E-03
s-p ratio	0.65	0.16	1.21E-03
Surface hardness	-0.36	0.13	1.89E-02

$$SE = 0.65\left(\frac{s}{p}\right) - 0.36H + 13.99 \text{-----} R^2 = 83.8\% \quad (6.2)$$

Where: SE – specific energy (kW-h/m³);

s – cut spacing (mm);

p – cutter penetration depth (mm); and

H – excavated surface hardness (R).

The accuracy metrics of the formulation (Eq. 6.2) are as follows:

Root Mean Squared Error (RMSE) = 0.635;

R-squared (R^2) = 0.838.

6.6.5. Instantaneous Cutting Rate, s-p Ratio, and Surface Hardness. The combined effect of the s-p ratio and surface hardness on the instantaneous cutting rate was also studied and presented in Figure 6.28 and Table 6.15. Figure 6.28 shows that surface hardness does not have a significant effect on the instantaneous cutting rate. This was confirmed by the analysis of variance results. These results showed that the combined effect of s-p ratio and surface hardness was not statistically significant on the cutting rate. Similarly, the main effect of surface hardness was not statistically significant. The main effect of the s-p ratio was, however, statistically significant at a 95% confidence interval. The non-significance of the main effect of surface hardness is inconsistent with Tumac et al. (2007). They observed a power relationship between the instantaneous cutting rate and Shore hardness of excavated rock surface with a negative gradient, similar to the observation depicted in Figure 6.29. This prompted a more detailed study of the relationship between the instantaneous cutting rate and surface hardness in Figure 6.29. The hardness values recorded at each s-p ratio were plotted with different color codes. This revealed that the apparent power relationship between the linear cutting rate and surface hardness was because of the changing s-p ratio (resulting in changing cutting forces). Within each s-p ratio, there was no unique trend that indicated a decrease in instantaneous cutting rate with increasing surface hardness (Figure 6.29). This explains why when the instantaneous cutting rate was plotted against s-p ratio and surface hardness, only s-p ratio influenced the instantaneous cutting rate (Figure 6.28). In statistical terms, considering the relationship between instantaneous cutting rate and surface hardness alone confounds s-p ratio; thereby, resulting in a false relationship between instantaneous cutting rate and surface hardness (Glen, 2020).

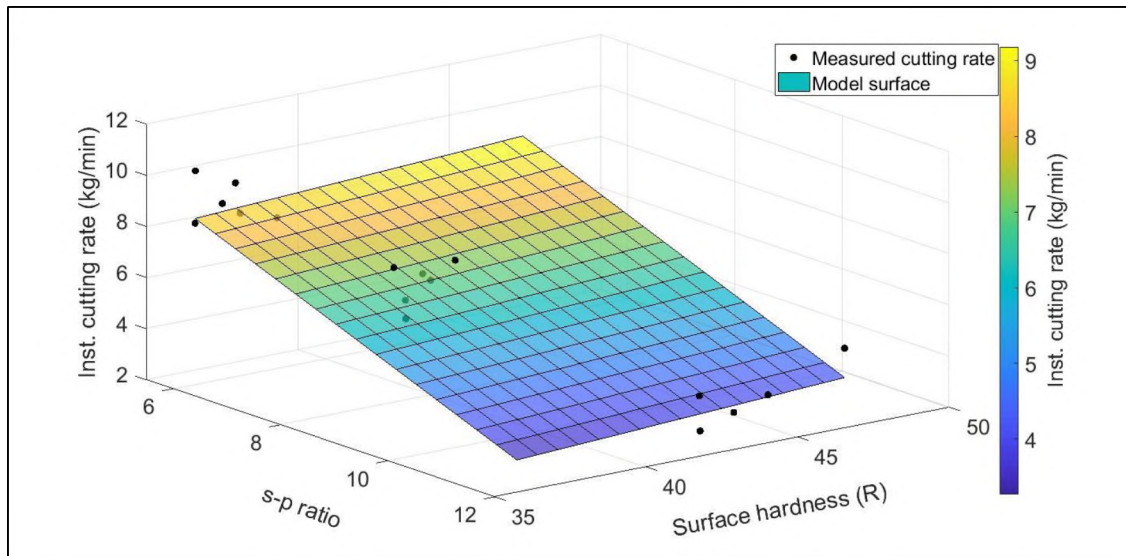


Figure 6.28. Relationship between linear cutting rate, s-p ratio, and excavated surface hardness.

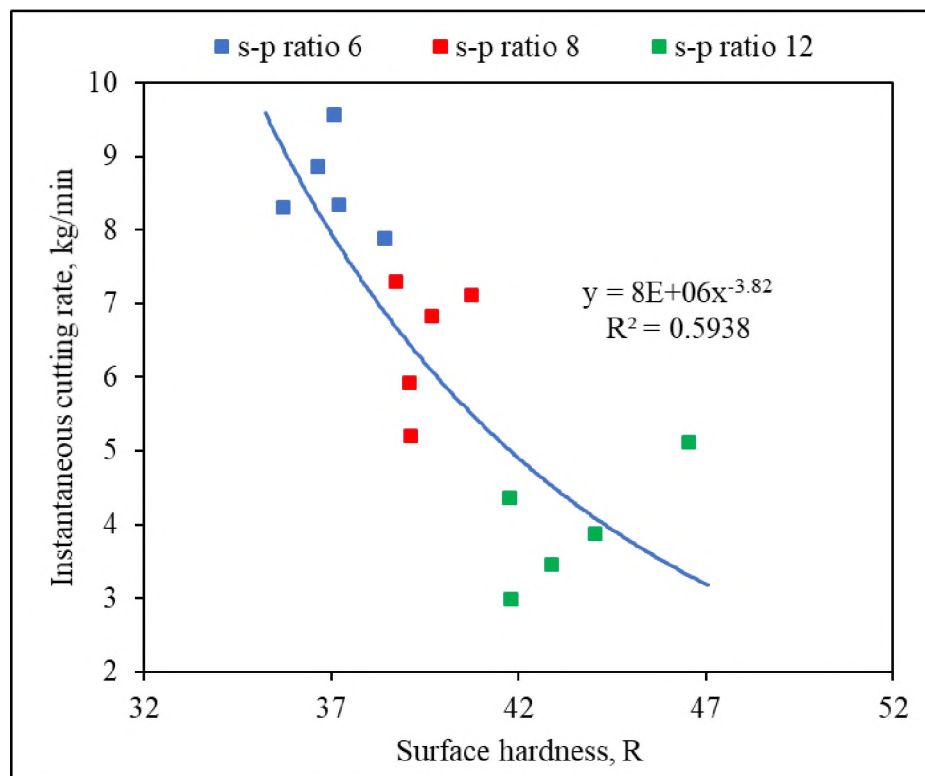


Figure 6.29. Relationship between instantaneous cutting rate and excavated surface hardness.

Table 6.15. Analysis of variance of specific energy in relation to s-p ratio and surface hardness.

Parameter	Df	Sum Sq	Mean Sq	F value	Pr(>F)
s-p ratio	2	15.5827	7.79136	12.18	0.0016
Hardness	1	0.3939	0.39393	0.62	0.4491
s-p ratio*Hardness	2	2.6481	1.32407	2.07	0.1726
Error	11	7.0356	0.6396		

7. RESULTS AND DISCUSSION OF NUMERICAL CUTTING SIMULATION

In this section, the results from the numerical simulation of linear rock cutting experiments were discussed. First, the scaling effects of the cutter and cutting geometry obtained from sensitivity analysis were explored. Second, the measured cutting forces were examined in conjunction with those obtained from the lab LCM experiments. Finally, the occurrence of underbreaks and overbreaks and their relationship with the spacing-penetration ratio were discussed.

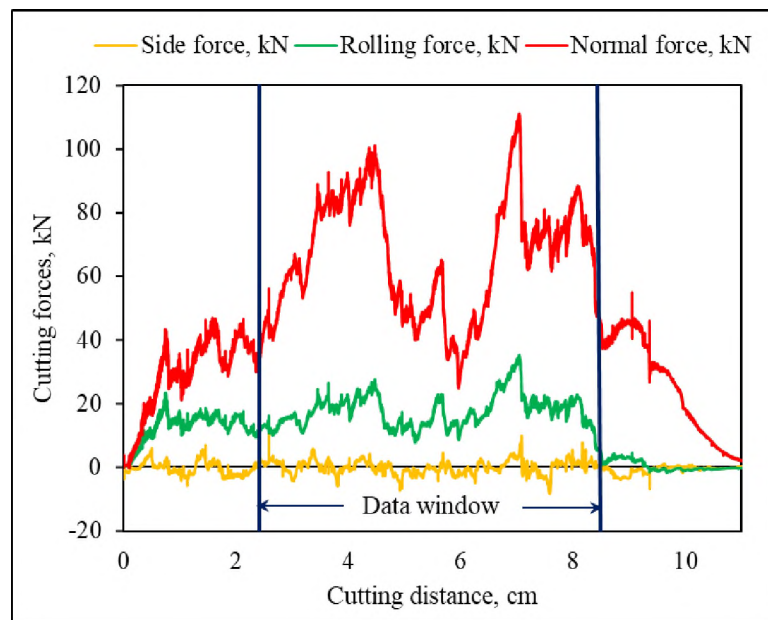


Figure 7.1. Cutting force traces from a simulation at spacing 30 mm and penetration 8 mm.

Figure 7.1 is a plot of typical traces of cutting forces recorded during one of the cutting simulations. As the cutter made contact with the rock block, the rolling and normal forces built up. They increased to full form when the cutter was fully in contact with the rock model. The side forces remain relatively low and alternate between positive and

negative, depending on the direction of deflection of the cutter deflection. At the other end of the block, as the cutter exited the block, all the forces dropped to zero.

7.1. MODEL SIZE AND CUTTING FORCES

7.1.1. Effect of the Cutting Geometry and Cutter Size Scale on the Cutting Forces. Numerical models are mostly scaled down for computational efficiency. The scale of the model is known to affect the cutting forces recorded from simulations (e.g., Koyama and Jing, 2007; Xu et al., 2016). To establish a baseline for estimating the full-scale cutting forces from scaled numerical models, linear rock cutting was simulated at four different model scales – 0.10, 0.25, 0.35, and 0.50 times of the full-scale LCM prototype. The cutting geometry (spacing and penetration), and the cutter size were scaled by the same factor simultaneously for each experimental run. The full-scale dimensions are as follows: cutter diameter = 292 mm, cutter tip thickness = 11 mm, cut spacing = 76.2 mm, and penetration = 9.525 mm. For each scaling factor, the cutting forces from five cuts were recorded (Table 7.1).

Figure 7.2 and Figure 7.3 plot the rolling and normal forces, respectively, against the model scaling factors. The plots indicate logarithmic relationships between the cutting forces and scaling factors. The rolling and normal forces obtained from the full-scale lab LCM tests are also plotted in Figure 7.2 and Figure 7.3 (blue square markers) with a scaling factor of 1.0 (full-scale).

In both the rolling and normal forces relationships, the logarithmic curves closely matched the lab rolling and normal forces. This implies that the logarithmic models – Eq. 7.1 and Eq. 7.2 – can be used to scale up rolling forces and normal forces obtained from

scaled numerical models to full-scale cutting forces with correlation coefficients of 98% and 93%, respectively.

$$F_R = 10.35 \ln(f) + 16.67 \quad (7.1)$$

$$F_N = 25.86 \ln(f) + 65 \quad (7.2)$$

Where F_R – rolling force;

F_N – normal force; and

f – model scaling factor.

Table 7.1. Cutting forces at different model scales and from actual lab LCM rocking cutting (cutter diameter = 292 mm, spacing = 76.2 mm, and penetration = 9.525 mm).

Scaling factor	Side force, kN	Rolling force, kN	Normal force, kN
Numerical model			
0.10	0.33	0.55	8.61
0.10	-1.57	0.47	5.39
0.10	-1.41	0.43	5.03
0.10	-0.67	0.60	9.15
0.10	-2.06	0.37	3.92
0.25	-0.35	2.86	30.78
0.25	-0.83	2.37	27.15
0.25	-1.56	2.45	32.15
0.25	-0.56	2.93	26.67
0.25	-1.58	1.86	29.15
0.35	0.27	5.91	41.10
0.35	-5.59	5.64	32.83
0.35	-1.69	5.52	32.84
0.35	-2.49	5.28	32.31
0.35	-2.33	5.05	28.35
0.50	1.69	9.66	53.88
0.50	-5.08	9.20	46.32
0.50	-0.61	10.32	51.88
0.50	2.14	9.70	54.95
0.50	-4.60	9.42	45.29
1.00		16.67	65.00
Full-scale - Lab			
1.00		15.02	63.53
1.00		15.64	65.40
1.00		16.52	68.44
1.00		15.29	68.23
1.00		16.08	67.10

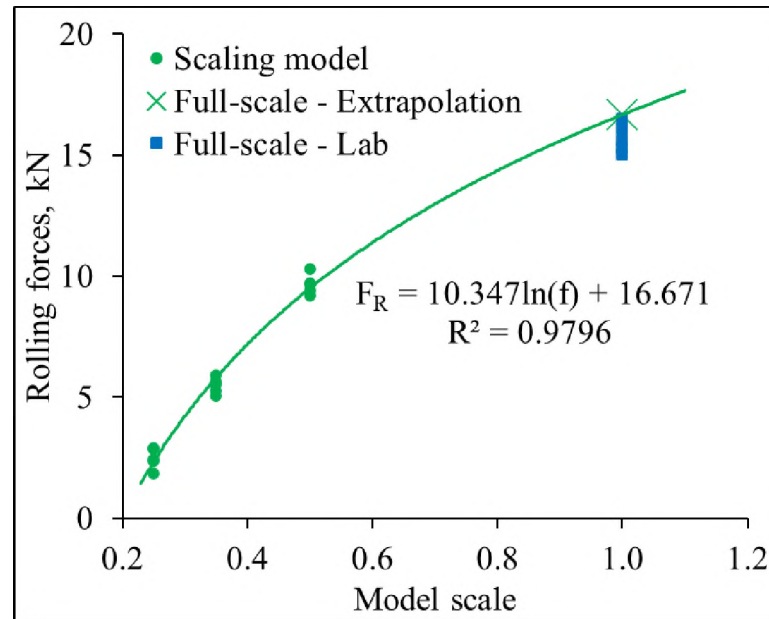


Figure 7.2. Relationship between rolling forces and model scale with a plot of the full-scale lab LCM rolling force (blue square markers) and an extrapolated rolling force at a scaling factor of one (green X). The full-scale cutter diameter, spacing, and penetration are 292 mm, 76.20 mm, and 9.53 mm, respectively.

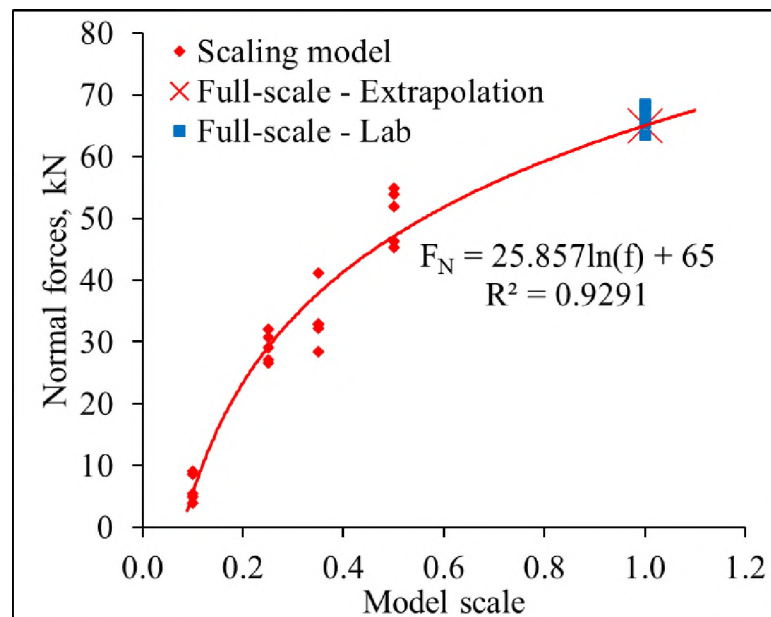


Figure 7.3. Relationship between normal forces and model scale with a plot of the full-scale lab LCM normal force (blue square markers) and an extrapolated normal force at a scaling factor of one (red X). The full-scale cutter diameter, spacing, and penetration are 292 mm, 76.20 mm, and 9.53 mm, respectively.

7.1.2. Effect of Scaling Spacing and Penetration at Constant s-p Ratio on

Cutting Forces. In the previous section, the cutting geometry and the cutter were scaled by the same factor simultaneously. In this section, the effect of scaling the cutting geometry and cutter size separately was also investigated. Four cutter sizes modeled with diameters 29.2 mm, 73.0 mm, 102.2 mm, and 146.0 mm were used to simulate linear rock cutting at three different spacing and penetration scales. The full-scale spacing and penetration were 76.2 mm and 9.525 mm respectively and the scales investigated were 0.10, 0.35, and 0.50. The spacing and penetration were scaled by the same factor simultaneously to retain a fixed s-p ratio. The cutting forces recorded from all the simulation runs are presented in (Table 7.2).

It was observed that for each cutter size, the rolling forces increased linearly with increasing spacing and penetration scale at a constant s-p ratio (Figure 7.4). To achieve deeper penetration at a larger spacing higher forces were required. This conformed with the literature (e.g., Selimoglu, 2009; Abu Bakar, 2012). It was also observed that the rolling forces increased with increasing cutter scale. This is attributed to the contact area between the cutter and the rock model. Larger cutters have larger contact areas and require higher forces to execute cutting at the same level of penetration. However, the rate of increase of the rolling forces is higher for larger cutters than for smaller cutters. The rolling forces from all the cutters tend to approach zero at lower spacing and penetration scales. This phenomenon was also observed by Gertsch et al. (2007). It is attributed to shallower penetration. At very shallow penetration (0.95 mm in this case), there was minimal rolling resistance because the cutter did not have enough bite of the rock to cause any cutting, thereby, very low rolling forces were generated. At this point, the rolling forces were

independent of the cutter size, hence, the convergence of the rolling forces at very low spacing and penetration scales. As the penetration increased, the cutter penetrated and cut the rock, generating more rolling resistance, and consequently, there was an increase in the rolling forces.

Table 7.2. Average cutting forces at different spacing and penetration scales at a constant s-p ratio of 8.0.

Scaling factor	Spacing, mm	Penetration, mm	Side force, kN	Rolling force, kN	Normal force, kN	Cutting Coeff., %
Cutter diameter = 146 mm						
0.10	7.62	0.95	1.38	0.57	25.67	2.22
0.10	7.62	0.95	1.15	0.51	28.59	1.80
0.35	26.67	3.33	-4.21	6.23	40.43	15.40
0.35	26.67	3.33	-4.19	6.58	39.21	16.79
0.50	38.10	4.76	-5.08	9.20	46.32	19.85
0.50	38.10	4.76	-4.60	9.42	45.29	20.80
Cutter diameter = 102 mm						
0.10	7.62	0.95	-1.32	0.53	20.08	2.65
0.10	7.62	0.95	-0.46	0.49	22.25	2.18
0.35	26.67	3.33	-5.59	5.64	32.83	17.18
0.35	26.67	3.33	-2.33	5.05	28.35	17.81
0.50	38.10	4.76	-2.42	7.86	39.84	19.72
0.50	38.10	4.76	-1.54	7.32	33.40	21.92
Cutter diameter = 73 mm						
0.10	7.62	0.95	-0.91	0.46	13.62	3.41
0.10	7.62	0.95	-1.11	0.64	14.16	4.49
0.35	26.67	3.33	-2.01	3.25	15.63	20.79
0.35	26.67	3.33	-1.44	3.26	16.40	19.89
0.50	38.10	4.76	-1.44	5.42	20.12	26.92
0.50	38.10	4.76	-1.59	5.11	20.92	24.41
Cutter diameter = 29 mm						
0.10	7.62	0.95	-1.57	0.47	5.39	8.64
0.10	7.62	0.95	-2.06	0.37	3.92	9.33
0.35	26.67	3.33	-1.04	1.54	5.61	27.44
0.35	26.67	3.33	-0.72	1.69	5.44	31.06
0.50	38.10	4.76	-0.52	2.51	6.91	36.29
0.50	38.10	4.76	-0.52	2.33	6.71	34.67

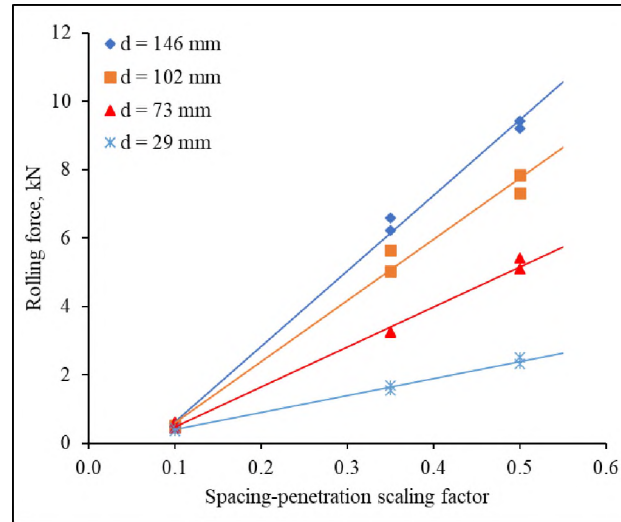


Figure 7.4. Relationship between rolling forces and the scale of spacing and penetration at constant s-p ratio and different cutter sizes. The full-scale spacing and penetration are 76.20 mm and 9.53 mm, respectively. d – cutter diameter.

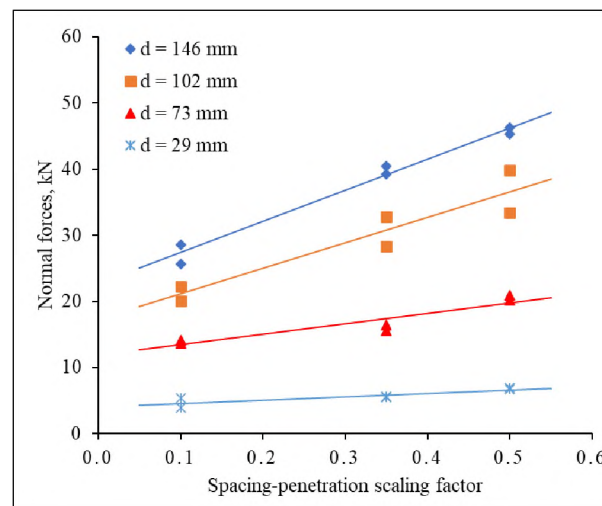


Figure 7.5. Relationship between normal forces and the scale of spacing and penetration at constant s-p ratio and different cutter sizes. The full-scale spacing and penetration are 76.20 mm and 9.53 mm, respectively. d – cutter diameter.

The normal forces, like the rolling forces, increased with increasing spacing and penetration scale (Figure 7.5). The normal forces also increased with increasing cutter sizes due to the increased contact area. Unlike the rolling forces that approached zero at very

shallow penetration, the normal forces were significantly high (greater than 5 kN even for the smallest cutter) at the shallowest penetration tested. This is because, at very shallow penetration there was significant resistance to the cutter penetration to develop substantial normal forces (Gertsch et al., 2007). The normal forces then increased linearly with increasing penetration.

7.1.3. Effect of Model Scale on Cutting Coefficient. The cutting coefficients for all the four cutters were computed (Table 7.2) and plotted against the spacing-penetration scaling factors (Figure 7.6). The plots show logarithmic relationships between the cutting coefficient and scaling factors. This indicates that the TBM torque required for a given TBM thrust to achieve a certain cutter penetration increased logarithmically with increasing spacing and penetration.

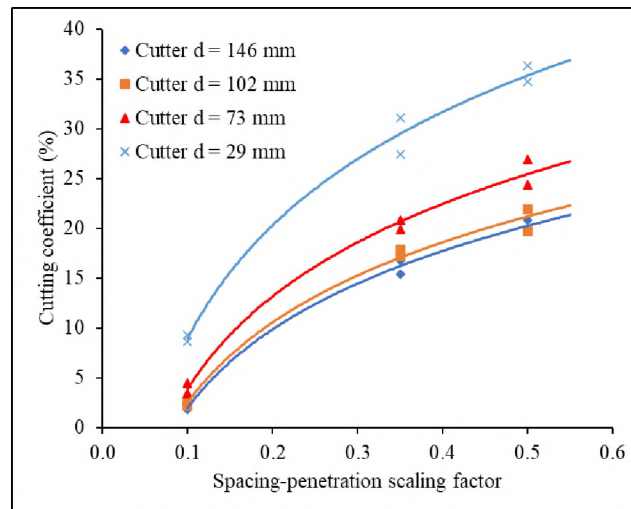


Figure 7.6. Relationship between cutting coefficient and the scale of spacing and penetration at constant s-p ratio and different cutter sizes. The full-scale spacing and penetration are 76.20 mm and 9.53 mm respectively. d – cutter diameter.

In terms of the effect of the cutter size, the cutting coefficient decreased with increasing cutter sizes (Figure 7.7). The curve exhibits a power relationship because the

smaller cutters have lower normal forces than the larger cutter. The cutting coefficient is the ratio of the rolling force to the normal force, thereby the relationship is logical. This implies that for a given thrust, the TBM torque requirement for smaller cutters is higher than that for larger cutters.

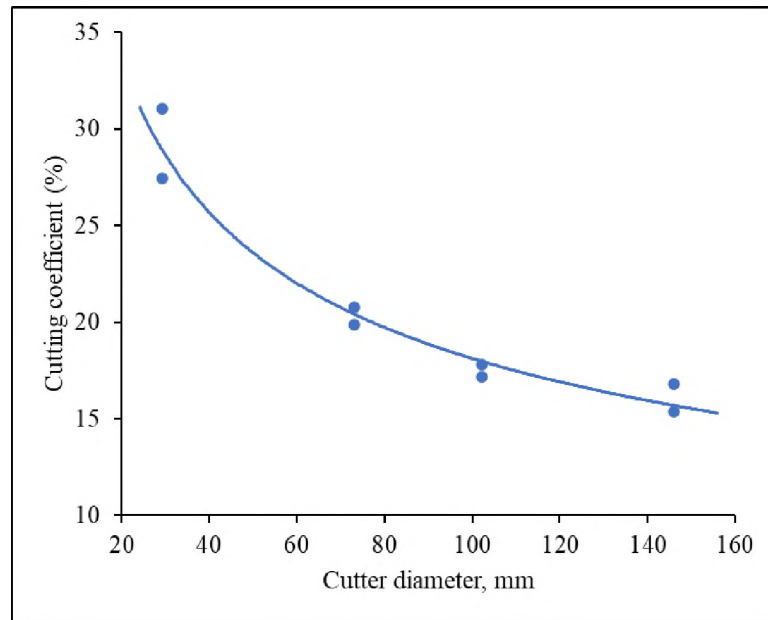


Figure 7.7. Relationship between cutting coefficient and the cutter size. The spacing and penetration are 26.67 mm and 3.33 mm, respectively.

7.1.4. Effect of the Cutter Tip Thickness on the Cutting Forces. Five cutters with different thicknesses were created and used to simulate linear rock cutting while measuring the forces involved in the rock fragmentation. Three simulation runs were made for each cutter thickness. Each experimental run had a different randomized packing of the particles in the model. The cutting simulations were run at a constant penetration of 3.096 mm with cutters of a constant diameter of 94.9 mm. The average cutting forces for all the experimental runs are presented in Table 7.3.

Table 7.3. Cutting forces exerted by cutters with different thicknesses – simulation.

Simulation run	Cutter thickness, mm	Side forces, kN	Rolling forces, kN	Normal forces, kN
run1	1.10	-0.16	1.98	17.25
	2.75	0.11	3.96	25.17
	3.63	0.95	4.70	31.44
	3.85	0.67	4.83	29.68
	5.50	0.76	5.63	37.12
run2	1.10	2.19	1.88	14.99
	2.75	1.57	3.59	22.25
	3.63	2.62	4.09	27.38
	3.85	2.42	4.56	28.04
	5.50	2.62	6.21	43.35
run3	1.10	-2.14	2.14	13.19
	2.75	1.01	3.79	32.03
	3.63	-0.21	4.40	34.10
	3.85	0.77	4.77	38.34
	5.50	0.63	6.43	46.92

From Figure 7.8, both the normal forces and rolling forces have positive linear relationships with the cutter thickness, but the slope of the normal force is steeper than that of the rolling force. These observations match closely to plots of Eqs. 7.3 and 7.4 (Figure 7.8), which were formulated theoretically by Lislérud (1997). In the theoretical equations, while the normal force depends on both the cutter thickness and diameter, the rolling force depends on only the cutter thickness. The formulation is such that when the disc diameter is greater than one, the rate of increase of the normal force with cutter thickness is higher than that of the rolling force. This conformed with the literature that touted a new V-shaped disc cutter as having better cutting efficiency than the constant cross-section disc cutter (Plácido and Friant, 2004; Vogt, 2016). A thinner cutter, like a new V-shaped cutter, has a

smaller contact area; therefore, a smaller amount of force is required to achieve the same level of penetration into a rock of constant strength.

Similar to what was observed in the lab linear cutting, the normal force exhibited higher variability than the rolling force.

$$F_R = k \cdot \sigma \cdot W \cdot 2\pi \cdot p \quad (7.3)$$

$$F_N = k \cdot \sigma \cdot W \cdot 2\pi \cdot \sqrt{d \cdot p} \quad (7.4)$$

Where F_R – rolling force, kN;

F_N – normal force, kN;

k – a constant defined the rock failure criterion and the cutting geometry;

σ – uniaxial compressive strength of the rock;

d – diameter of the cutter; and

W – tip thickness of the cutter.

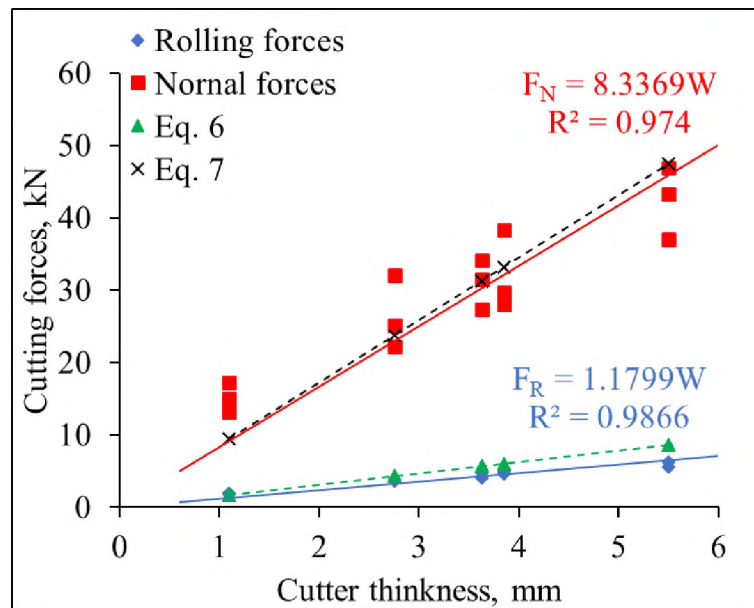


Figure 7.8. Effect of cutter tip thickness on the cutting forces – obtained from numerical simulations.

7.2. CUTTING FORCES AND s-p RATIO

To investigate the relationship between the cutting forces and the s-p ratio, three cut spacings, and twelve penetrations were simulated. The cutting forces were recorded for all the spacing-penetration combinations (Table 7.4).

Table 7.4. Cutting forces at different spacing-penetration combinations.

P, mm	s = 25 mm			s = 30 mm			s = 35 mm		
	F _s , kN	R, kN	N, kN	F _s , kN	R, kN	N, kN	F _s , kN	R, kN	N, kN
2.5	-0.45	5.77	38.39	0.02	5.38	44.82	-0.03	5.66	46.49
3.0	-0.62	6.62	45.25	-0.84	6.43	45.47	-0.09	6.99	46.79
3.5	-0.66	7.47	48.24	-1.56	7.30	52.12	-0.10	7.66	52.69
4.0	-0.75	8.64	47.04	-0.84	9.06	54.41	0.24	9.27	55.35
4.5	-1.18	9.43	45.01	-1.21	9.97	49.76	-0.01	9.91	53.69
5.0	-1.00	10.00	46.93	-1.42	10.89	55.29	-0.36	11.10	57.70
5.5	-1.05	10.85	47.05	-1.00	12.01	57.96	-0.14	12.36	61.81
6.0	-1.01	11.92	52.73	-1.03	13.06	57.99	-0.83	12.85	63.57
6.5	-1.03	13.22	51.06	-0.34	13.66	56.53	-0.41	14.22	60.72
7.0	-0.94	13.29	49.96	-0.77	14.94	61.60	-0.85	15.03	63.21
7.5	-0.79	14.34	55.40	-1.20	15.34	57.61	-0.76	15.10	65.12
8.0	-0.79	15.88	56.25	-1.10	17.10	63.26	-0.71	16.40	62.44
s – cut spacing; p – penetration; F _s – side force; R – rolling force; N – normal force									

7.2.1. Effect of s-p Ratio on the Side Forces. As seen in the linear rock cutting tests in the lab, the side forces had a high degree of variation. Generally, there was a positive linear relationship between the side forces and the s-p ratio (Figure 7.9). There was no unique trend of the side forces with respect to the cut spacing. The explanation in Section 6.2.2 about the lab test side forces is applicable in this case as well.

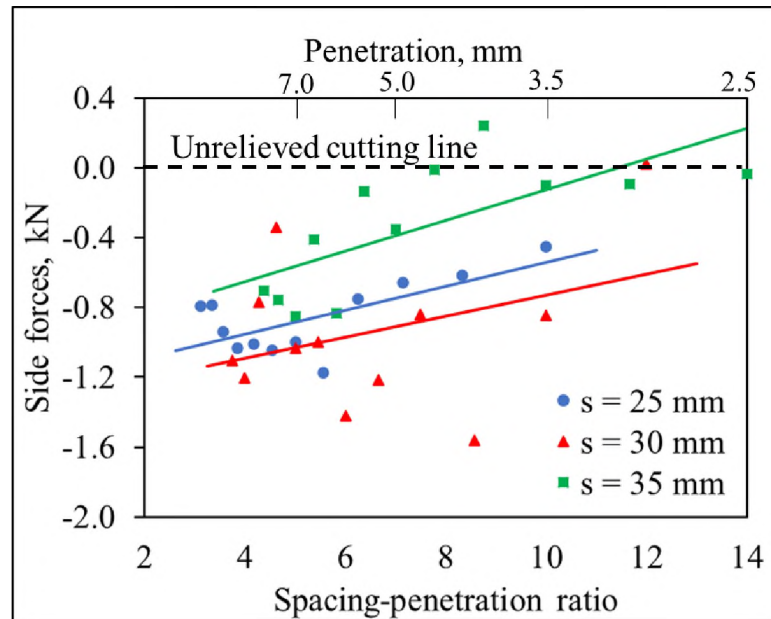


Figure 7.9. Relationship between the side forces and the spacing-penetration ratio – simulation.

7.2.2. Effect of s-p Ratio on the Rolling Forces. The relationship between the rolling forces and the s-p ratio was a power relationship with a negative gradient (Figure 7.10). This was seen in all the cut spacings investigated including the rolling forces obtained from the lab experiments. The magnitude of the rolling forces increased with increasing cut spacing. The rolling forces obtained from the lab were higher than the model rolling forces because the spacing tested in the lab was higher (76.2 mm), and the size of the cutter used in the lab was larger (292 mm diameter and 11 mm tip thickness) than that used in the numerical models. At a constant s-p ratio, an increase in cut spacing corresponded to an increase in the cutter penetration. Increasing spacing and penetration are both known to result in corresponding increases in the cutting forces (e.g., Roxborough and Philips, 1975), hence, the increasing rolling forces with decreasing s-p ratio observed in Figure 7.10.

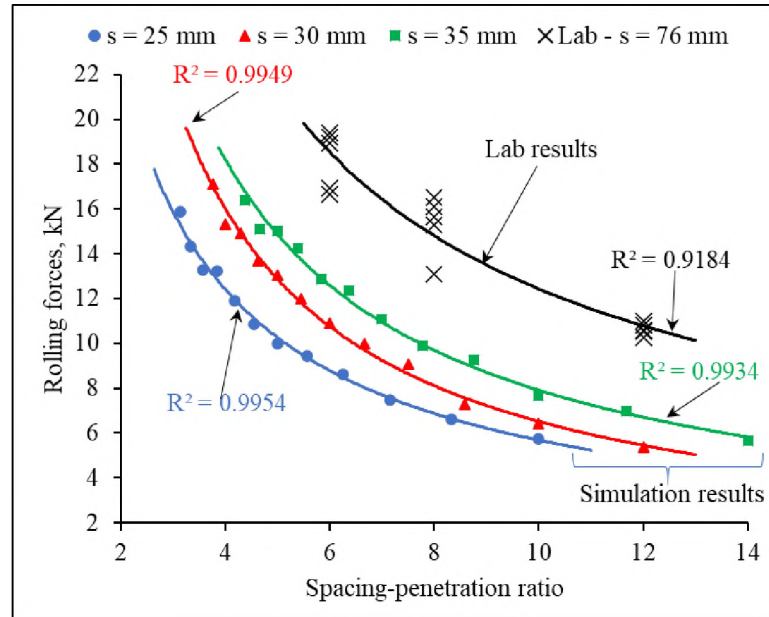


Figure 7.10. Relationship between the rolling forces and the spacing-penetration ratio – simulation.

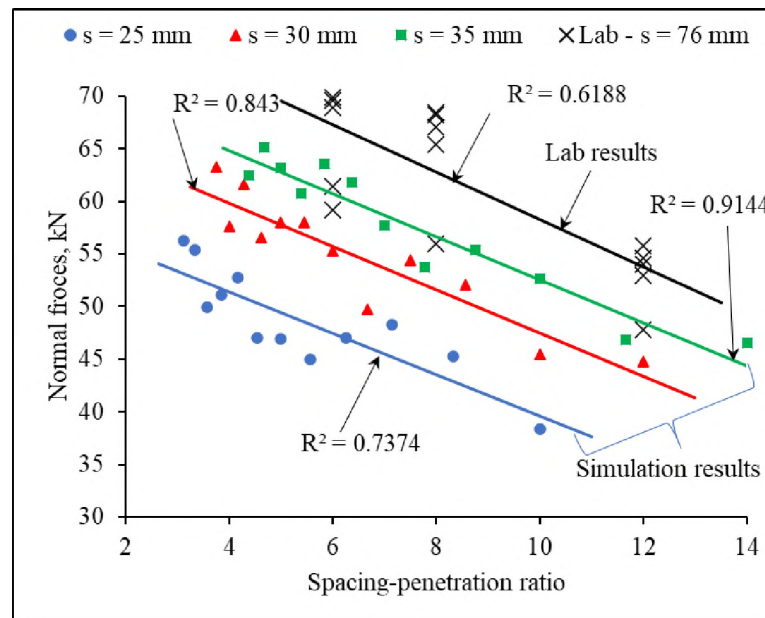


Figure 7.11. Relationship between the normal forces and the spacing-penetration ratio – simulation.

7.2.3. Effect of s-p Ratio on the Normal Forces. The simulated normal forces produced trends similar to those obtained in the lab tests. They had negative linear

7.3.1. Effect of s-p Ratio on the Volume of Ridges. The formation of ridges (underbreaks) between cuts occurs when all the rock material between adjacent cuts is not removed to the depth of the cutter. Ridges are more pronounced when complete relieved cutting is not achieved. That is, when the s-p ratio is sub-optimal and there is incomplete cut interaction between adjacent cuts. This leads to more groove deepening than chip formation, leaving a substantial volume of material between cuts (ridges). From the foregoing, it was expected that the volume of material in the ridges had a relationship with the spacing and penetration of the cutter.

Figure 7.12 and Figure 7.13 depict the relationship between the volume of ridges and the s-p ratios at cut spacings 30 mm and 35 mm, respectively. In both charts, it was observed that for s-p ratios less than 7.0, the ridge volume decreased with decreasing s-p ratios. The explanation for this is; at s-p ratio < 7.0 , complete relieved cutting was achieved, and as the penetration increased at a constant spacing (decreasing s-p ratio), there was more interaction between adjacent cuts, resulting in a decrease in the volume ridges that formed. Conversely, for s-p ratios greater than 7.0, the volume of ridges decreases linearly with increasing s-p ratio. The trend of the ridge volume observed at higher s-p ratios (s-p ratio > 7.0) can be attributed to a combination of unrelieved cutting and a decrease in the nominal (expected) excavated volume. All cuts in this region produced ridges. However, cuts with deeper cutter penetration produced bigger ridges than those with shallower penetration, hence the increasing ridge volume with decreasing s-p ratio (increasing penetration at

constant cut spacing) beyond 7.0. These trends were also observed in the lab LCM test results discussed in Section 6.5.1 (see Figure 6.17).

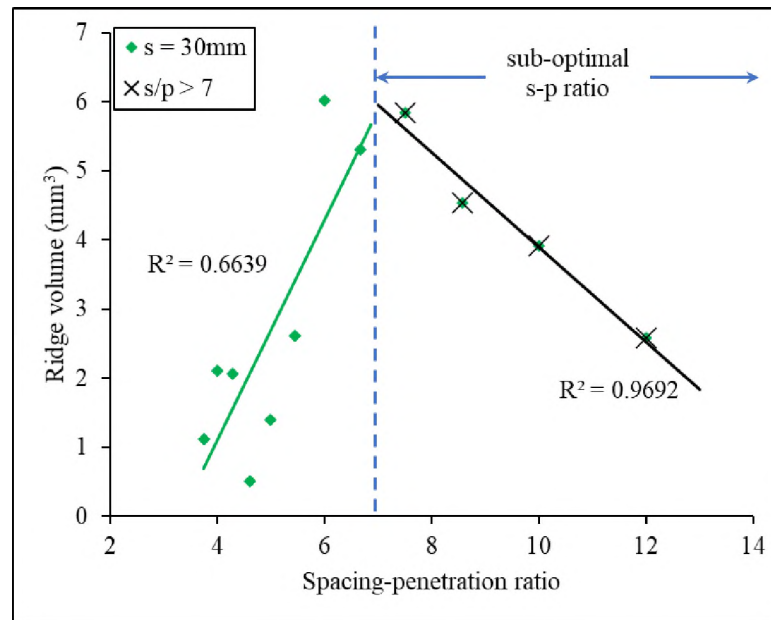


Figure 7.12. Relationship between ridge volume and s-p ratio at cut spacing 30 mm.

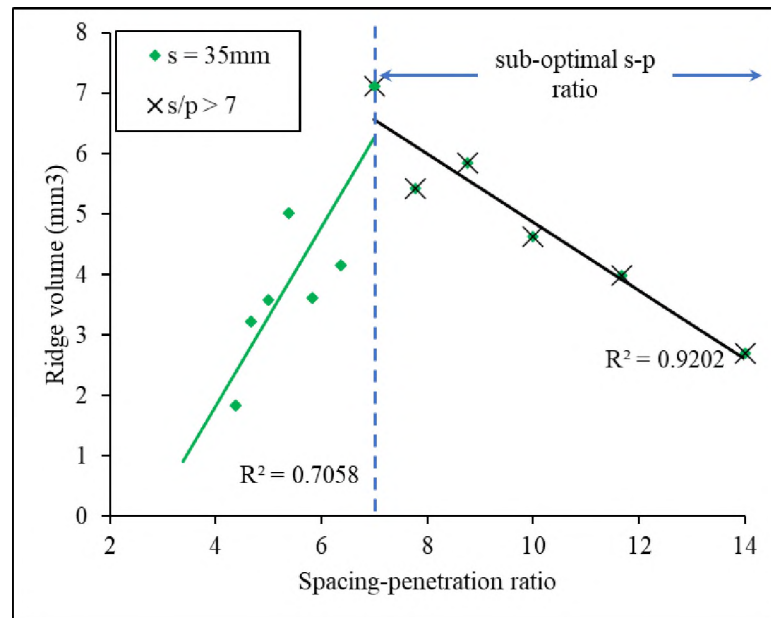


Figure 7.13. Relationship between ridge volume and s-p ratio at cut spacing 35 mm.

7.3.2. Effect of s-p Ratio on the Volume of Overbreak. Overbreaks in mechanical excavation result from inherent rock flaws, heterogeneities, and the cutting geometry. Overbreak depends partly on the cutting geometry, a unique relationship between the overbreak volume and the s-p ratio was expected. This relationship was investigated by plotting the overbreak volumes against the s-p ratio (Figure 7.14 and Figure 7.15).

The volume of overbreaks decreased with increasing s-p ratio until the s-p ratio reaches 7.0 (the optimum s-p ratio (e.g., Roxborough and Philips, 1975)), then remained relatively horizontal in the region of s-p ratio greater than 7.0 ratio (Figure 7.14 and Figure 7.15). When relieved cutting is achieved, the dependence of the overbreak volume on the cutting geometry becomes significant. A decrease in the s-p ratio below the optimum corresponds to deeper penetration which leads to more overbreaks (Figure 7.16). This explains the trend observed in the region of s-p ratio < 7.0 . At s-p ratio > 7.0 , unrelieved cutting is realized and there is no complete interaction between cuts. The volume of overbreaks in this region was independent of the depth of cutter penetration, thus the relatively horizontal trend shown in this region. These trends were also observed in the lab LCM test results discussed in Section 6.5.3 (see Figure 6.20).

The overbreak volume trends are complementary to the trends of the ridge volume, having the same turning point at s-p ratio = 7.0. The overbreak volume charts show more variation than the ridge volume charts because the overbreaks depend on other factors like inherent flaws in the rock models.

Based on these findings, evaluation of the irregularities of the excavation surface (determination of the volume of underbreaks and overbreaks) can be used to determine

whether or not optimal cutting conditions are achieved. Ridge and overbreak volumes can serve as additional tools for evaluating excavation efficiency.

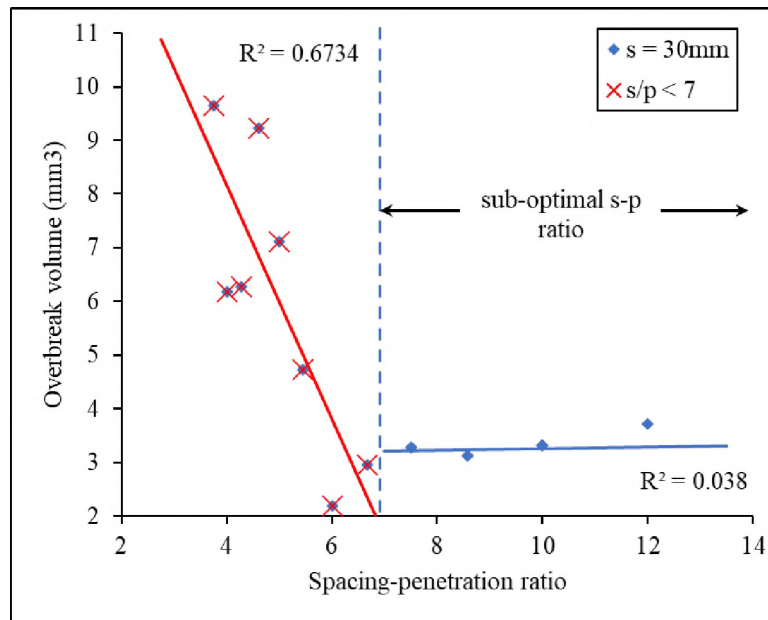


Figure 7.14. Relationship between overbreak volume and s-p ratio at cut spacing 30 mm.

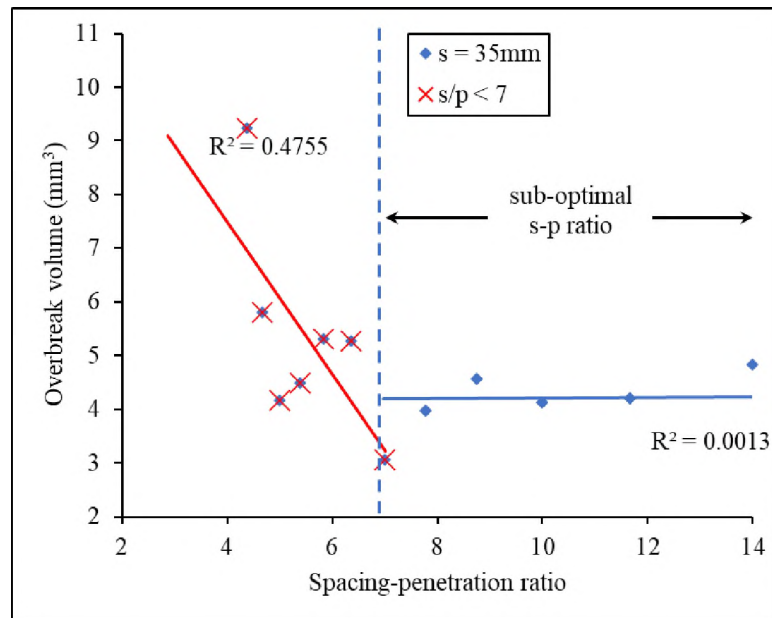


Figure 7.15. Relationship between overbreak volume and s-p ratio at cut spacing 35 mm.

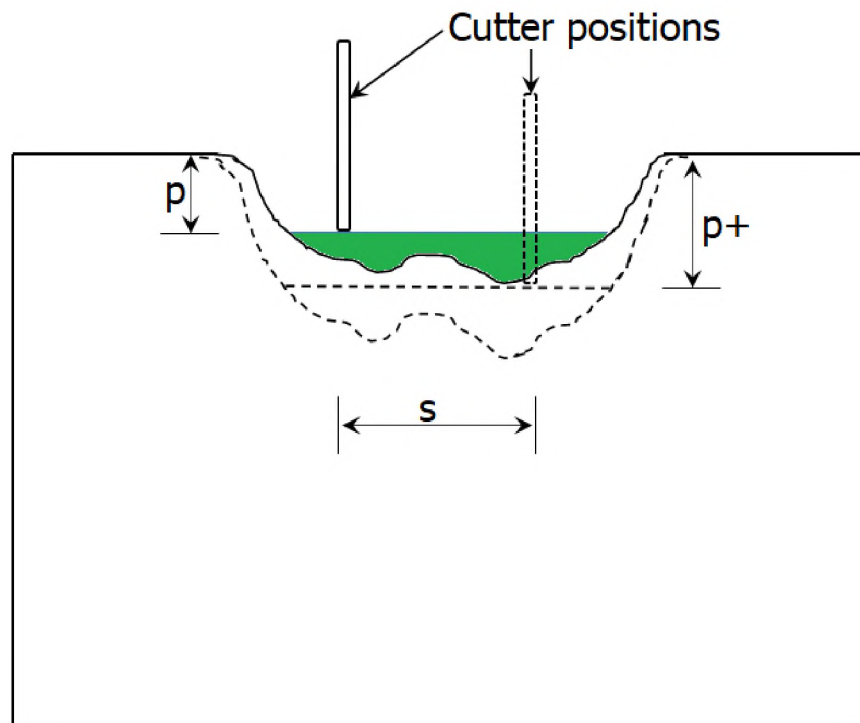


Figure 7.16. Illustration of deep relieved cutting having higher overbreak volume than shallow relieved cutting.

8. CONCLUSIONS AND RECOMMENDATIONS

This section presents a summary of the objectives and methods of this research and outlines the major conclusions and contributions to the body of knowledge. It also outlines recommendations for future work based on the challenges encountered and the limitations of this work.

8.1. CONCLUSIONS

This research conducted laboratory and numerical experimentations of linear rock cutting using a constant cross-section disc cutter, and it investigated the relationship between excavated rock surface properties (surface hardness and irregularities) and rock cutting parameters (cutting geometry, forces, and efficiency). The rock sample tested in this research was the Roubidoux Sandstone that was obtained from the Rosati quarry in northern Phelps County, Missouri. In the lab experiments, three cutter penetrations (6.35 mm, 9.525 mm, and 12.70 mm) were tested at a constant cut spacing (76.2 mm). For each level of penetration, four passes were cut and the cutting forces, surface irregularities, and hardness data were collected on each pass for analysis. The numerical experiments tested twelve cutter penetrations and three spacings resulting in 36 spacing-penetration combinations.

8.1.1. Relationships of Cutting Parameter. To study the relationships between the cutting forces, specific energy, instantaneous cutting rate, and cutting geometry, full-scale linear rock cutting was conducted using a disc cutter. Cutting forces were recorded during each cut and used to calculate excavation performance metrics, such as specific energy and instantaneous cutting rate. Numerical simulation of linear rock cutting was also conducted to extend the laboratory experiments to cover wide parameter variations.

Statistical analyses—including ANOVA, Tukey post hoc tests, and analysis of covariance—were conducted on the data from the laboratory and numerical experiments, and the following conclusions are drawn:

1. The average side forces in both the lab and numerical tests were largely negative with the negative sign being an indication of the cutter deflection towards the previous cut (the relieved side). Note that the sign of side forces, positive or negative, depends on the sign convention adopted. The magnitude of the side forces decreases with increasing s-p ratio, approaching zero at high s-p ratios where there is little or no cut interaction between adjacent cuts. This phenomenon can be used to assess whether relieved cutting is achieved or not, in an excavation project. Unrelieved cutting results in random and symmetrical deflection of the cutter, which leads to the average side forces approaching zero. Conversely, in relieved cutting, the cutter tends to deflect toward the previous cut, resulting in a negative average side force. The higher the magnitude of the average side force, the higher the deflection towards the previous cut.
2. The rolling, normal, and resultant forces decreased with increasing s-p ratios, consistent with previous research (e.g., Gertsch et al., 2007; Abu Bakar, 2012). This was observed in both the lab and numerical tests. The average rolling forces had a power relationship with the s-p ratio, and the normal and resultant forces had a linear relationship with the s-p ratio. This confirms that the numerical models were well-calibrated.
3. The specific energy had a positive correlation with the s-p ratio for the range of s-p ratios tested ($s/p = 6$ to $s/p = 12$). The degree of variation of the specific energy

increased with increasing s-p ratio. The high variability of the specific energy at high s-p ratio is attributed to the little or no interaction between cuts resulting in the production of an inconsistent quantity of rock material by the same cutting forces.

4. The cutting coefficient decreased with increasing s-p ratio. The cutting coefficient has a power relationship with the s-p ratio in the lab and numerical tests. This relationship was inherited from the relationship between the cutting forces and s-p ratios. This trend implies that the torque requirement of a TBM for a given thrust decreases with increasing s-p ratio.
5. The instantaneous cutting rate had a negative linear relationship with the s-p ratio. The instantaneous cutting rate had a power relationship with the specific energy with a negative gradient. This implies that as the cutting becomes more efficient (lower specific energy) due to deeper cutter penetration, the amount of rock fragments produced per unit time increases at a faster rate.
6. The cutting efficiency showed no unique relationship with the s-p ratio. At the lowest s-p ratio tested ($s/p = 6$), the cutting efficiency for all the passes were greater than 100%. Conversely, in the other two s-p ratios tested ($s/p = 8$ and $s/p = 12$), some passes recorded cutting efficiencies less than 100% while other passes recorded cutting efficiencies greater than 100%. This observation revealed that complete relieved cutting was achieved at s-p ratio 6, which resulted in more overbreaks than underbreaks resulting in over 100% cutting efficiency in all passes.

8.1.2. Relationship between Excavated Surface Parameters and Cutting

Parameters. To relate surface irregularities and surface hardness to the cutting parameters,

and establish a predictive model for specific energy estimation, measurements of the irregularities and hardness of the excavated surfaces were done, as summarized:

A structured laser light imaging system was used to record overlapping image frames of the cleaned excavated rock surfaces after excavating each pass. Image analysis was conducted in MATLAB to generate digital elevation models of each excavated surface. The volume of underbreaks (ridges) and overbreaks were calculated from the digital elevation models and their relationships with the cutting geometry were evaluated.

After the surface imaging, the hardness of the excavated surfaces was measured using an N-type Schmidt hammer. The hardness was measured in two lines on the ridges between the cuts in a staggered fashion to increase the measurement resolution. The hardness values were stored by the hammer and later transferred to Excel® files for analysis. The relationship between the surface hardness and the cutting geometry was evaluated, along with the cutting performance metrics.

From the analyses of the surface hardness, underbreak volume, and overbreak volume, the following conclusions are made:

1. At s-p ratios lower than the optimum s-p ratio, 7.0, there was a linear decrease in the ridge volume with decreasing s-p ratios (increasing penetration at constant spacing). In the region of sub-optimal cutting ($s/p > 7$ —no complete relieved cutting achieved), the ridge volume increased with decreasing s-p ratios. This behavior was observed in the laboratory experiments and numerical simulations (with numerical simulations having a wider s-p ratio range, from 3.125 to 14). This finding presents a means for obtaining the optimum s-p ratio from linear rock cutting experiments and by extension, in TBM excavations.

2. At s-p ratios greater than the optimum s-p ratio (the region of unrelieved cutting—s-p ratio > 7), the volume of overbreaks was low and less dependent on the s-p ratio—approximately horizontal. The numerical and laboratory experiments showed that, beyond the optimum s-p ratio ($s/p \approx 7$), increasing the penetration further at constant spacing increased the overbreak volume. This phenomenon provides another means for estimating the optimum s-p ratio from linear rock cutting experiments. It is complementary to the trend exhibited by the underbreak volume versus s-p ratio.
3. The surface hardness was significantly different in each s-p ratio tested based on the ANOVA conducted, with $s/p = 6$ yielding the lowest surface hardness and $s/p = 12$ having the highest surface hardness. This behavior is attributed to the increase in cutting forces with decreasing s-p ratios. Higher cutting forces lead to more fracturing of the rock, resulting in reduced rock surface hardness.
4. The specific energy of disc cutters decreased with increasing surface hardness. This implies that the harder the surface of the rock, the more tensile fractures that are generated from indentation, leading to more efficient cutting (lower specific energy). This finding indicates that rock cutting using disc cutters is more efficient in hard, brittle rocks than in soft, ductile rocks.
5. The specific energy of disc cutters can be estimated using a relation that involves the s-p ratio (s/p) and hardness (H) of the damaged rock surface (see Eq. 6.2). A plot of the specific energy predicted using Eq. 6.2 against the measured specific energy yielded an R^2 of 83.8%. For the range of s-p ratios tested (6 – 12), SE

increased with increasing s-p ratio at constant surface hardness. This relation may not be applicable outside this range of s-p ratios.

6. The instantaneous cutting rate was observed to be independent of the rock surface hardness.

8.1.3. Numerical Simulations. The objectives of the numerical simulations were to establish relationships for upscaling the rolling and normal forces for full-scale applications and to conduct sensitivity analyses of cutter size. To achieve these objectives, the numerical models were calibrated using the strength properties of the Roubidoux Sandstone. After the calibration, the sensitivity of the model scale was conducted by simulating linear rock cutting at different scales of the cutting geometry and cutter size. These analyses yielded logarithmic relationships for estimating rolling and normal forces at different model scales. Sensitivities of the cutter diameter and cutter tip thickness were also analyzed. The conclusions drawn from the analyses of the numerical simulation results are:

1. The effect of the scale of the cutter and cutting geometry on the rolling and normal forces are governed by logarithmic functions (see Eqs. 7.1 & 7.2). The rolling force scaling relationship has an R^2 of 98.0% and that of the normal force has an R^2 of 92.9%. Cutting forces from scaled numerical models can be upscaled to full-scale forces for use in design and construction purposes using these logarithmic functions. These functions are applicable when the spacing, penetration, cutter diameter, and cutter thickness are all scaled by the same factor.
2. The forces required to achieve the same level of penetration increased as the cutter size increased. There was a significant effect of the cutter size on the normal forces

at all levels of penetration. However, the effect of the cutter size on the rolling forces decreased with decreasing cutter penetration. As the penetration decreased, a limit was reached where there was no significant effect of the cutter size on the rolling force (the limit in this research was 0.95 mm). At this penetration, the cutter did not have enough bite of the rock to cause any cutting and the rolling resistance was minimal.

8.2. RECOMMENDATIONS

The following recommendations are for future research based on the limitations and challenges of this research:

1. The hardness relationships obtained in this research were from one rock block. Testing more than one rock with different surface hardness will verify the relationships observed in this study. This will eliminate the effect of the cutting forces on the surface hardness and highlight the main effects of the surface hardness on the cutting efficiency.
2. The hardness ranges of the rock sample tested were limited. Simulation of hardness measurement would enable the investigation of a wider hardness range to reveal the relationship between cutting performance measures and hardness beyond the tested range.
3. There were turning points in the underbreak and overbreak relationships with the cutting geometry that were not explicitly due to the sparse nature of the s-p ratios tested in the lab. Investigating more s-p combinations in the lab will confirm the trends of overbreak and underbreak volumes in relation to the cutting geometry.

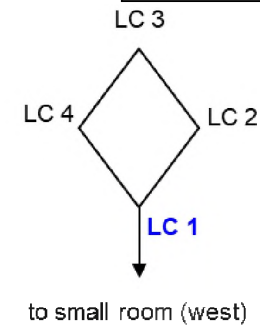
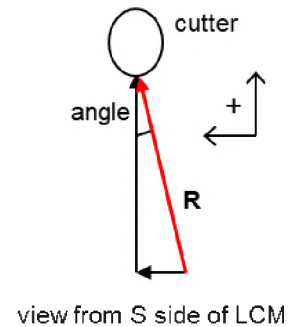
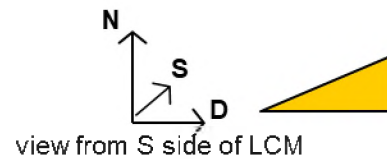
This could also reveal the relationship between the specific energy and overbreak and underbreak volumes.

4. The method used for measuring the surface irregularities in this research required about 91.44 cm clearance between the imaging instrumentation and the rock surface. However, the clearance between the cutterhead and the tunnel face is tight. Finding an alternative method for measuring overbreak and underbreak that can fit the tight clearances will be very useful for in situ measurements.

APPENDIX A.
CALIBRATION OF 3D LOAD CELLS AND LVDT

Table A.1. Calibration data for load cell 1.

LC1 Summary											
Wedge angle =7.5°; orientation = normal-rolling; July 2019											
UP-load	Resultant Load (R)	(kN)			Avg. output (Volts)				Output (Volts)		
		Normal	Rolling	Side	LC1	LC2	LC3	LC4	Normal	Rolling	Side
	0.00E+00	0.00E+00	0.00E+00		-3.91E-03	2.61E-03	-2.98E-03	1.26E-03	-3.03E-03	-5.61E-04	
	1.10E+04	4.87E+01	6.41E+00		-8.81E-03	1.03E-03	-6.42E-03	-1.07E-03	-1.53E-02	-1.46E-03	
	2.21E+04	9.74E+01	1.28E+01		-1.43E-02	-7.80E-04	-1.01E-02	-3.62E-03	-2.89E-02	-2.55E-03	
	3.31E+04	1.46E+02	1.92E+01		-1.97E-02	-2.60E-03	-1.38E-02	-6.09E-03	-4.22E-02	-3.57E-03	
	4.42E+04	1.95E+02	2.56E+01		-2.49E-02	-4.46E-03	-1.74E-02	-8.60E-03	-5.53E-02	-4.60E-03	
DOWN-load	5.52E+04	2.43E+02	3.20E+01		-3.04E-02	-6.41E-03	-2.10E-02	-1.12E-02	-6.90E-02	-5.76E-03	
	5.52E+04	2.43E+02	3.20E+01		-3.03E-02	-6.39E-03	-2.09E-02	-1.11E-02	-6.87E-02	-5.75E-03	
	4.42E+04	1.95E+02	2.56E+01		-2.92E-02	-6.04E-03	-2.01E-02	-1.07E-02	-6.60E-02	-5.57E-03	
	3.31E+04	1.46E+02	1.92E+01		-2.27E-02	-4.07E-03	-1.55E-02	-7.91E-03	-5.01E-02	-4.39E-03	
	2.21E+04	9.74E+01	1.28E+01		-1.60E-02	-2.01E-03	-1.09E-02	-4.89E-03	-3.37E-02	-3.12E-03	
	1.10E+04	4.87E+01	6.41E+00		-9.33E-03	1.85E-04	-6.40E-03	-1.89E-03	-1.74E-02	-1.79E-03	
	0.00E+00	0.00E+00	0.00E+00		-3.65E-03	2.35E-03	-2.73E-03	9.80E-04	-3.06E-03	-5.63E-04	
									(kN)		
calibration ram area =		1.10E+01	in ²						Slope	-2.80E-04	-1.67E-04
moment arm ratio =		6.10E-01							Intercept	-3.66E-03	-6.29E-04
									R ²	9.79E-01	9.70E-01



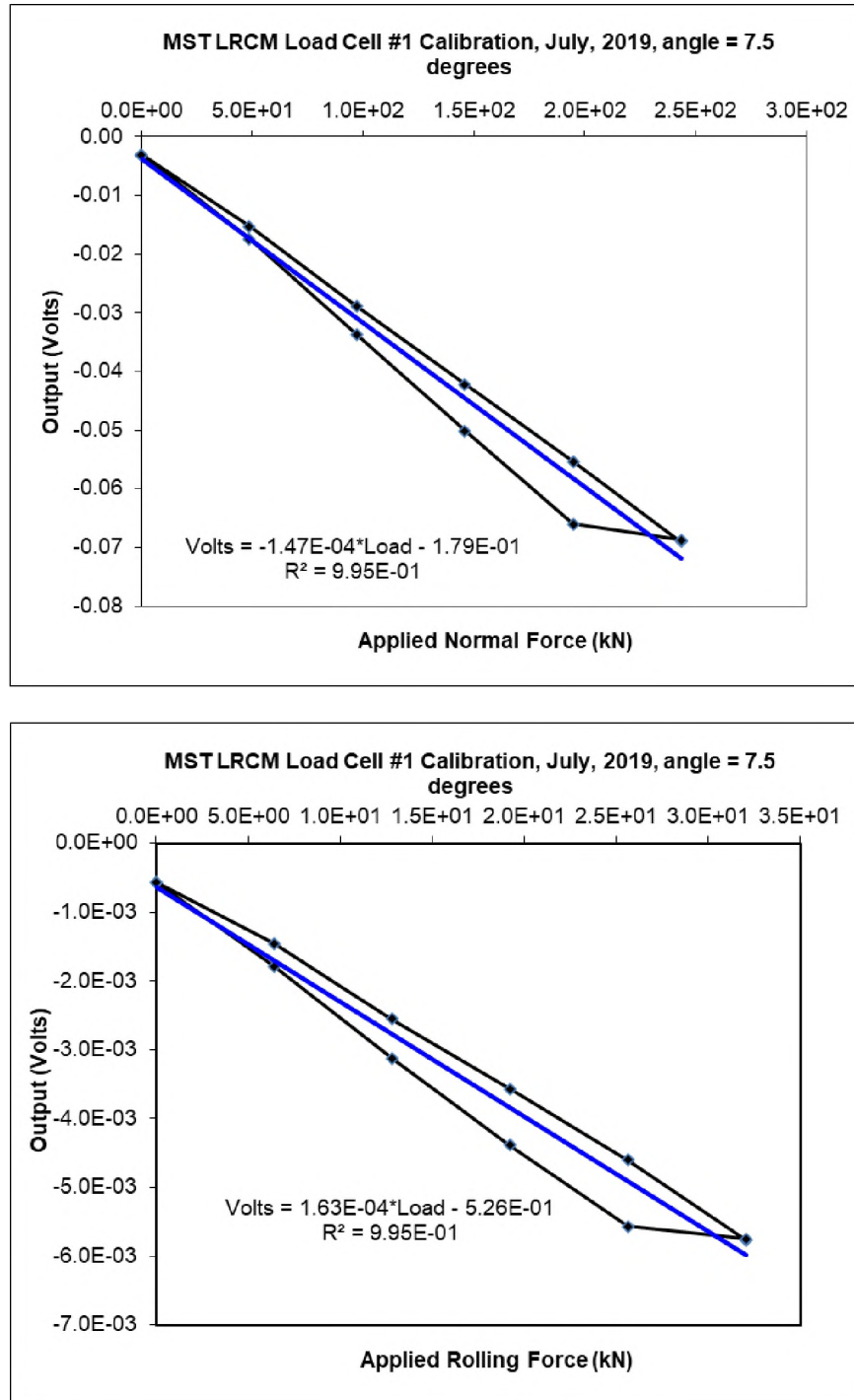
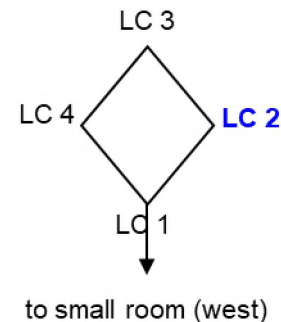
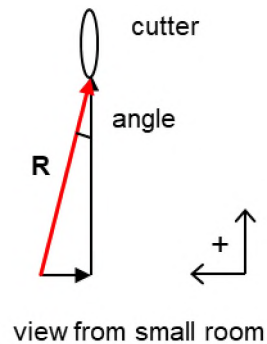


Figure A.1. Plots of calibration of load cell 1.

Table A.2. Calibration data for load cell 2.

LC2 Summary											
Wedge angle =7.5°; orientation = normal-side; July 2019											
	Resultant Load (R)	(kN)			Avg. output (Volts)				Output (Volts)		
		Normal	Rolling	Side	LC1	LC2	LC3	LC4	Normal	Rolling	Side
UP-load	0.00E+00	0.00E+00		0.00E+00	-3.67E-03	2.37E-03	-2.75E-03	1.01E-03	-3.04E-03		8.32E-04
	1.10E+04	4.87E+01		6.41E+00	-7.36E-03	1.79E-04	-7.09E-03	-5.91E-04	-1.49E-02		4.69E-04
	2.21E+04	9.74E+01		1.28E+01	-1.15E-02	-2.39E-03	-1.20E-02	-2.27E-03	-2.82E-02		-7.58E-05
	3.31E+04	1.46E+02		1.92E+01	-1.57E-02	-4.91E-03	-1.69E-02	-3.93E-03	-4.14E-02		-5.95E-04
	4.42E+04	1.95E+02		2.56E+01	-2.01E-02	-7.52E-03	-2.16E-02	-5.58E-03	-5.48E-02		-1.18E-03
	5.52E+04	2.43E+02		3.20E+01	-2.45E-02	-1.02E-02	-2.63E-02	-7.39E-03	-6.84E-02		-1.71E-03
DOWN-load	5.52E+04	2.43E+02		3.20E+01	-2.45E-02	-1.02E-02	-2.63E-02	-7.38E-03	-6.82E-02		-1.70E-03
	4.42E+04	1.95E+02		2.56E+01	-2.42E-02	-9.98E-03	-2.59E-02	-7.28E-03	-6.73E-02		-1.64E-03
	3.31E+04	1.46E+02		1.92E+01	-1.89E-02	-7.11E-03	-2.01E-02	-5.21E-03	-5.13E-02		-1.16E-03
	2.21E+04	9.74E+01		1.28E+01	-1.35E-02	-4.16E-03	-1.43E-02	-3.25E-03	-3.52E-02		-5.54E-04
	1.10E+04	4.87E+01		6.41E+00	-8.10E-03	-7.88E-04	-8.02E-03	-1.04E-03	-1.80E-02		1.55E-04
	0.00E+00	0.00E+00		0.00E+00	-3.63E-03	2.33E-03	-2.72E-03	9.66E-04	-3.05E-03		8.34E-04
								(kN)			
	calibration ram area =	1.10E+01	in ²					Slope	-2.79E-04		-8.21E-05
	moment arm ratio =	6.10E-01						Intercept	-3.88E-03		7.88E-04
								R ²	9.69E-01		9.50E-01



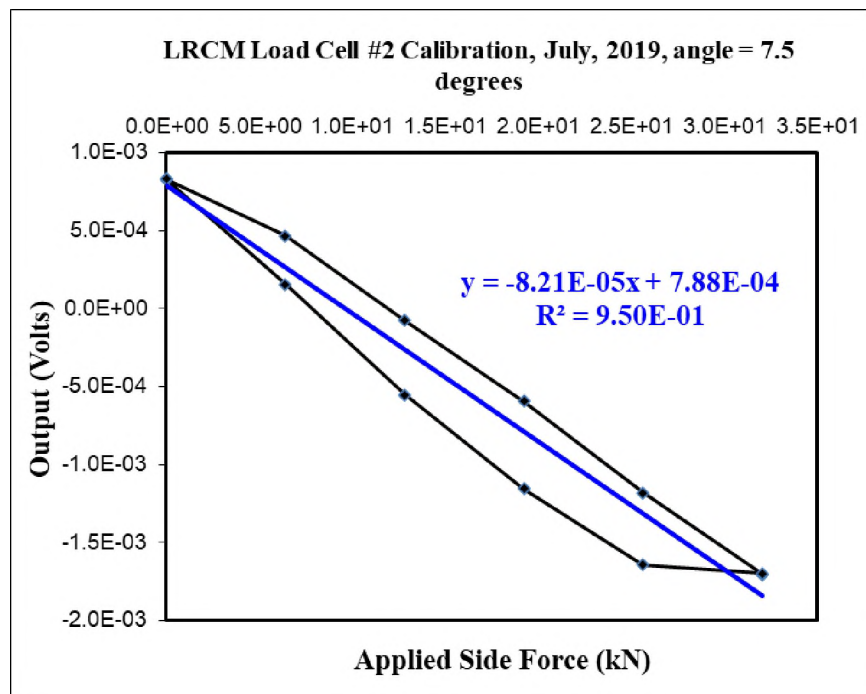
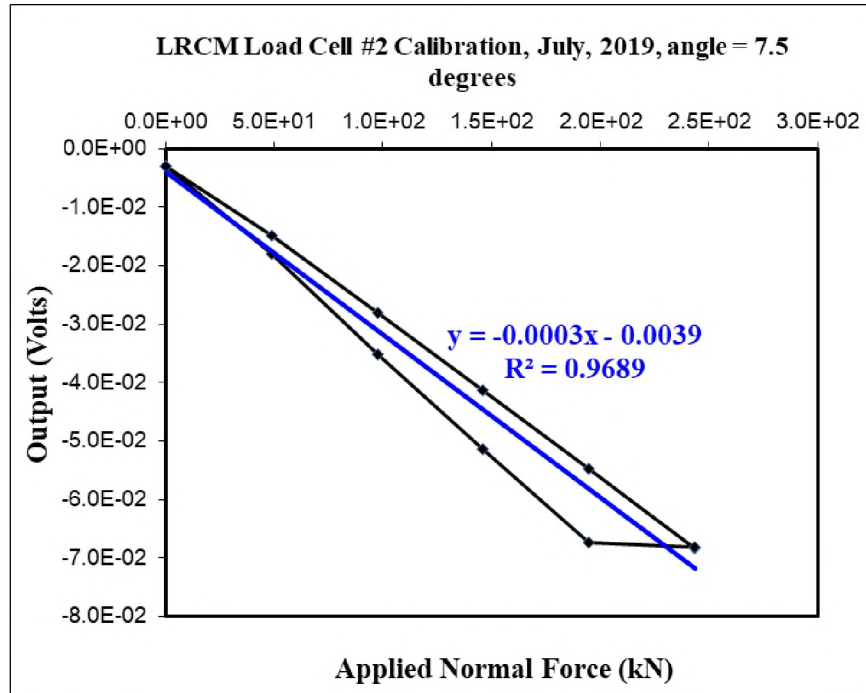
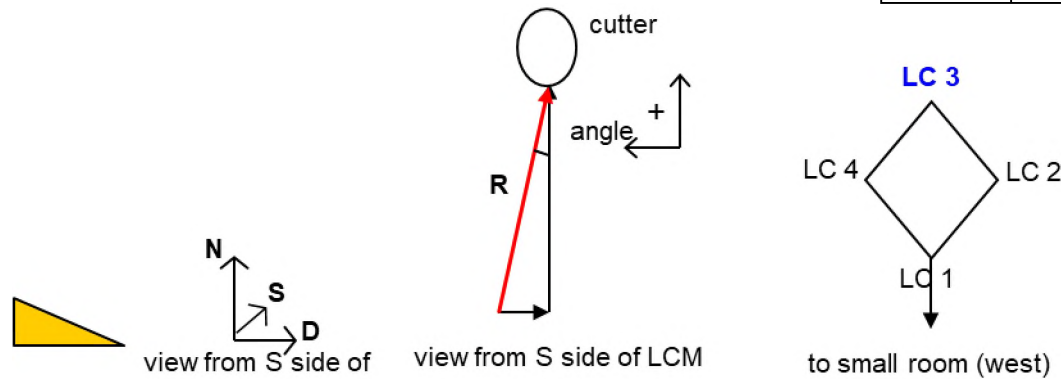


Figure A.2. Plots of calibration of load cell 2.

Table A.3. Calibration data for load cell 3.

Wedge angle =7.5°; orientation = normal-rolling; July 2019											
LC3 Summary	Resultant Load (R)	(kN)			Avg. output (Volts)				Output (Volts)		
		Normal	Rolling	Side	LC1	LC2	LC3	LC4	Normal	Rolling	Side
UP-load	0.00E+00	0.00E+00	0.00E+00		-3.65E-03	2.35E-03	-2.73E-03	9.71E-04	-3.06E-03	5.63E-04	
	1.10E+04	4.87E+01	6.41E+00		-6.67E-03	7.91E-04	-8.03E-03	-1.37E-03	-1.53E-02	-8.25E-04	
	2.21E+04	9.74E+01	1.28E+01		-1.02E-02	-1.10E-03	-1.42E-02	-3.82E-03	-2.94E-02	-2.44E-03	
	3.31E+04	1.46E+02	1.92E+01		-1.41E-02	-3.16E-03	-2.07E-02	-6.32E-03	-4.42E-02	-4.02E-03	
	4.42E+04	1.95E+02	2.56E+01		-1.73E-02	-4.84E-03	-2.61E-02	-8.55E-03	-5.68E-02	-5.37E-03	
DOWN-load	5.52E+04	2.43E+02	3.20E+01		-2.08E-02	-6.82E-03	-3.22E-02	-1.09E-02	-7.08E-02	-6.92E-03	
	5.52E+04	2.43E+02	3.20E+01		-2.08E-02	-6.80E-03	-3.21E-02	-1.09E-02	-7.05E-02	-6.88E-03	
	4.42E+04	1.95E+02	2.56E+01		-1.89E-02	-5.70E-03	-2.87E-02	-9.68E-03	-6.29E-02	-5.95E-03	
	3.31E+04	1.46E+02	1.92E+01		-1.50E-02	-3.77E-03	-2.21E-02	-7.25E-03	-4.82E-02	-4.33E-03	
	2.21E+04	9.74E+01	1.28E+01		-1.10E-02	-1.70E-03	-1.53E-02	-4.56E-03	-3.26E-02	-2.61E-03	
	1.10E+04	4.87E+01	6.41E+00		-7.05E-03	3.85E-04	-8.57E-03	-1.79E-03	-1.70E-02	-9.29E-04	
	0.00E+00	0.00E+00	0.00E+00		-3.64E-03	2.34E-03	-2.71E-03	9.63E-04	-3.05E-03	5.67E-04	
								kN			
	calibration ram area =	11.04	in ²					Slope	-2.84E-04	-2.38E-04	
	moment arm ratio =	0.609512						Intercept	-3.22E-03	5.47E-04	
								R ²	9.93E-01	9.95E-01	



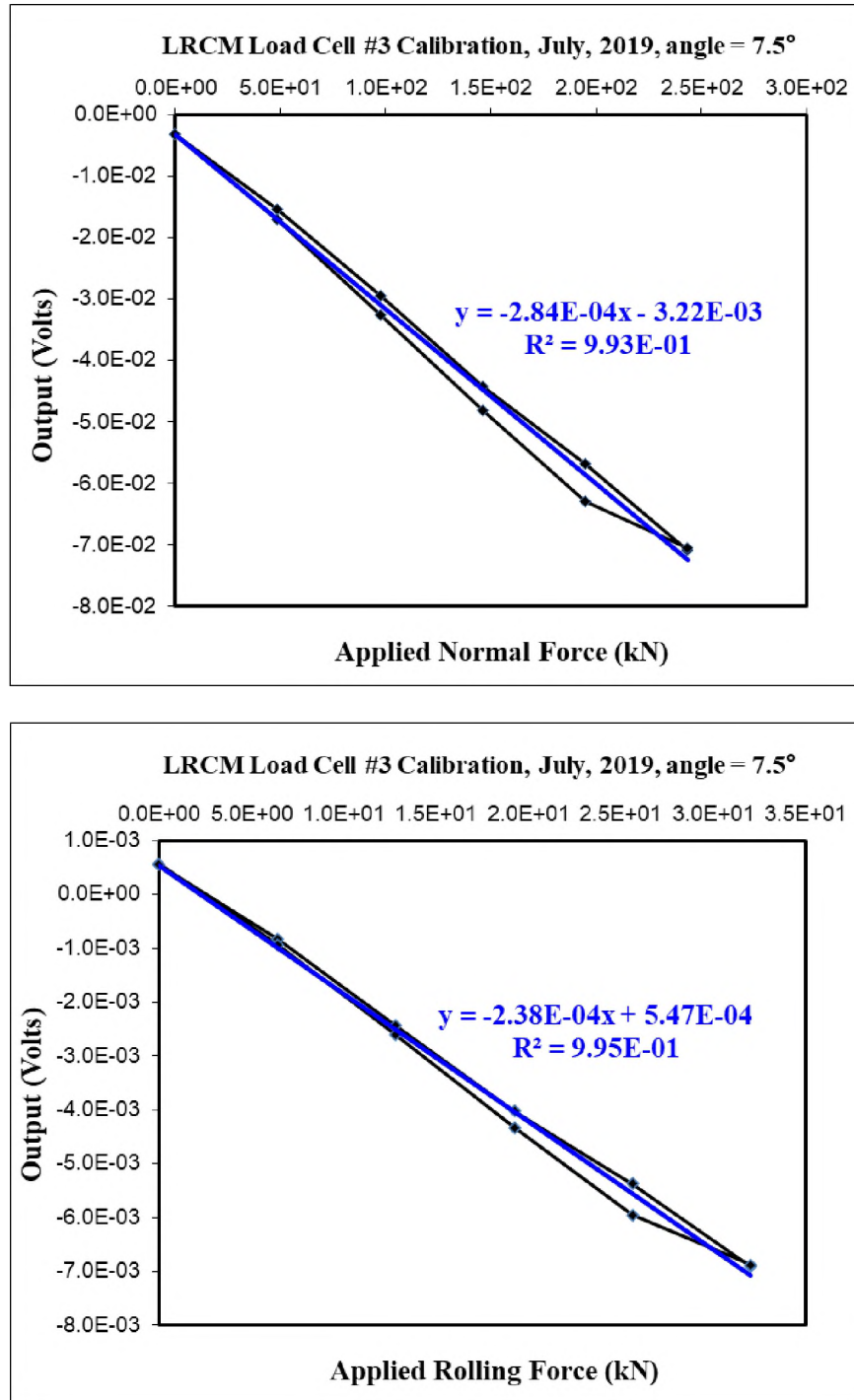
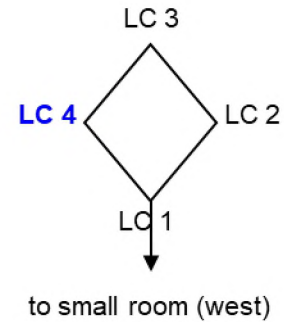
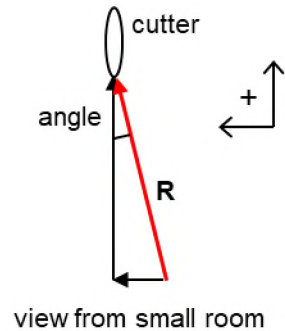


Figure A.3. Plots of calibration of load cell 3.

Table A.4. Calibration data for load cell 4.

LC4 Summary	Wedge angle =7.5°; orientation = normal-side; July 2019										
	Resultant Load (R)	(kN)			Avg. output (Volts)				Output (Volts)		
		Normal	Rolling	Side	LC1	LC2	LC3	LC4	Normal	Rolling	Side
UP-load	0.00E+00	0.00E+00		0.00E+00	-3.66E-03	2.35E-03	-2.73E-03	9.76E-04	-3.06E-03		-8.40E-04
	1.10E+04	4.87E+01		6.41E+00	-6.92E-03	1.30E-03	-7.07E-03	-1.58E-03	-1.43E-02		-1.75E-03
	2.21E+04	9.74E+01		1.28E+01	-1.10E-02	-2.35E-05	-1.22E-02	-4.43E-03	-2.77E-02		-2.68E-03
	3.31E+04	1.46E+02		1.92E+01	-1.52E-02	-1.55E-03	-1.73E-02	-7.22E-03	-4.12E-02		-3.46E-03
	4.42E+04	1.95E+02		2.56E+01	-1.94E-02	-3.12E-03	-2.23E-02	-9.86E-03	-5.47E-02		-4.11E-03
	5.52E+04	2.43E+02		3.20E+01	-2.38E-02	-4.79E-03	-2.74E-02	-1.26E-02	-6.86E-02		-4.74E-03
DOWN-load	5.52E+04	2.43E+02		3.20E+01	-2.37E-02	-4.78E-03	-2.73E-02	-1.25E-02	-6.84E-02		-4.73E-03
	4.42E+04	1.95E+02		2.56E+01	-2.31E-02	-4.56E-03	-2.65E-02	-1.22E-02	-6.63E-02		-4.64E-03
	3.31E+04	1.46E+02		1.92E+01	-1.82E-02	-2.87E-03	-2.08E-02	-9.28E-03	-5.11E-02		-3.91E-03
	2.21E+04	9.74E+01		1.28E+01	-1.30E-02	-1.06E-03	-1.47E-02	-6.03E-03	-3.48E-02		-3.03E-03
	1.10E+04	4.87E+01		6.41E+00	-7.96E-03	6.91E-04	-8.39E-03	-2.58E-03	-1.82E-02		-2.00E-03
	0.00E+00	0.00E+00		0.00E+00	-3.63E-03	2.33E-03	-2.71E-03	9.48E-04	-3.06E-03		-8.40E-04
								(kN)			
	calibration ram area =	1.10E+01	in ²					Slope	-2.79E-04		-1.24E-04
	moment arm ratio =	6.10E-01						Intercept	-3.71E-03		-1.07E-03
								R ²	9.71E-01		9.63E-01



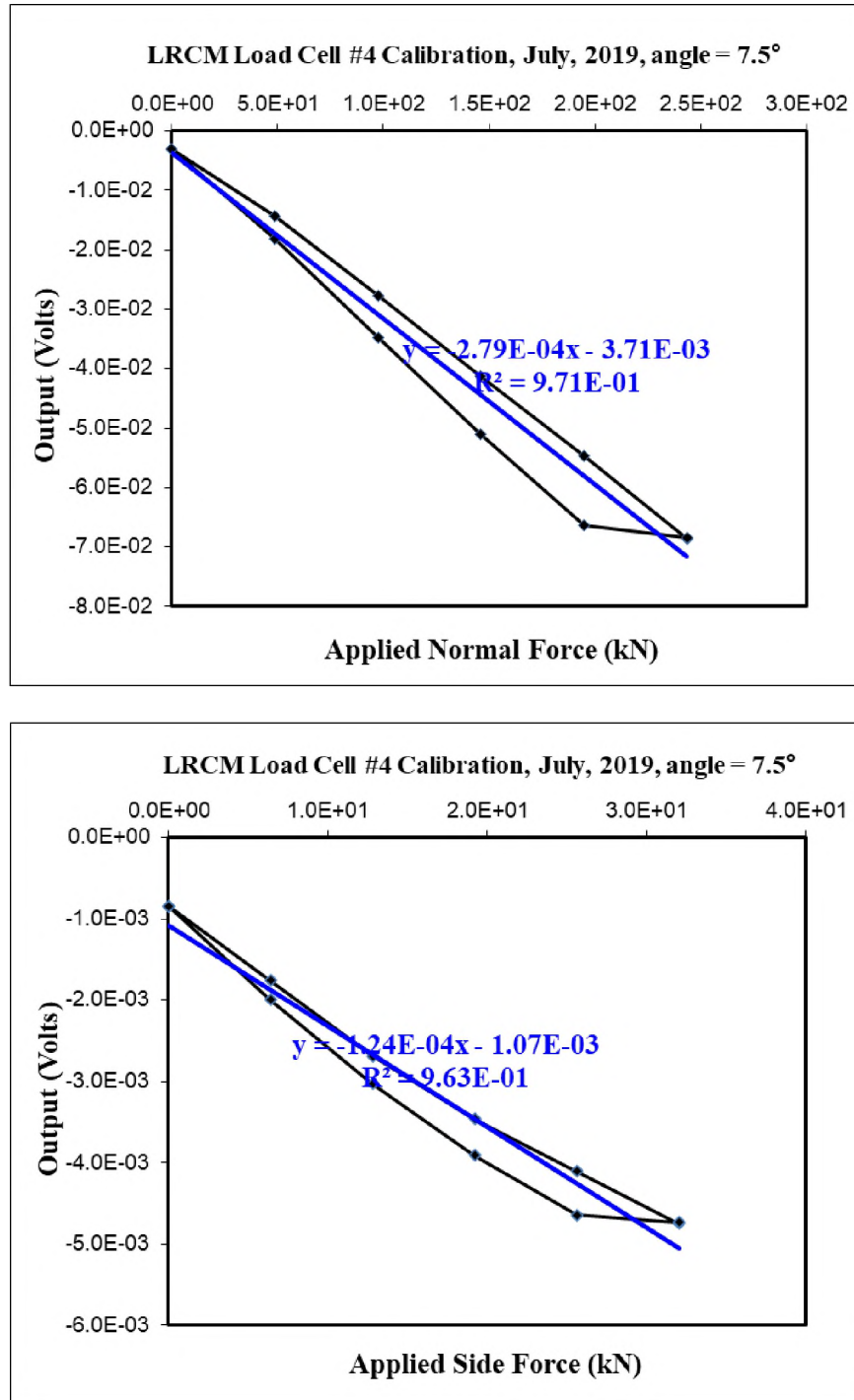


Figure A.4. Plots of calibration of load cell 4.

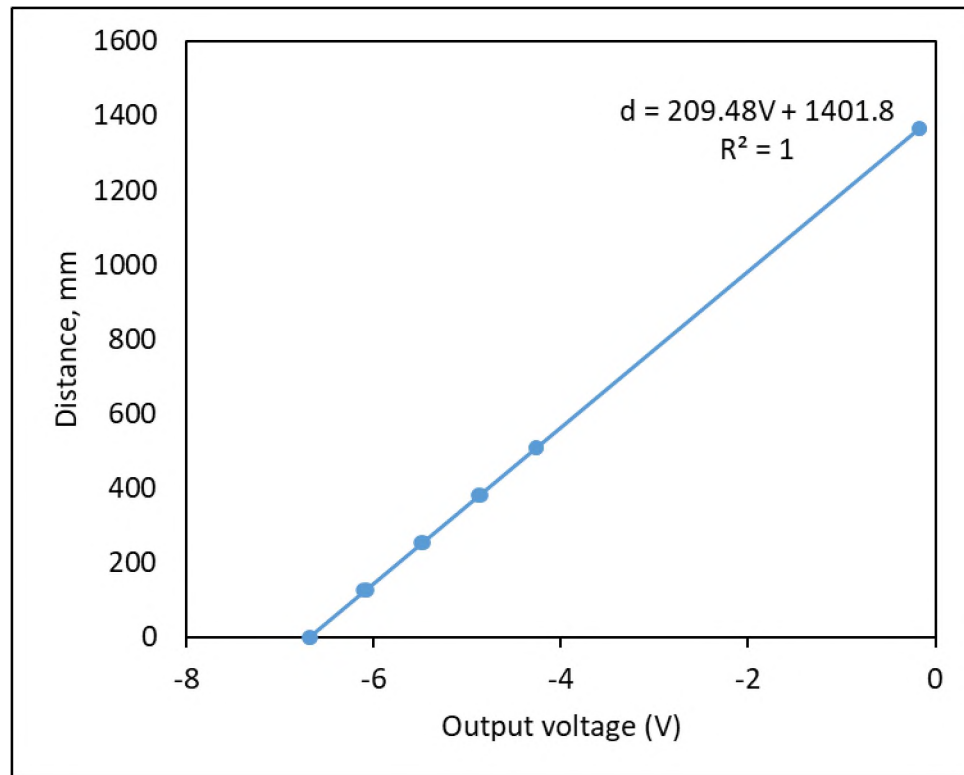
LVDT Calibration

Figure A.5. LVDT calibration.

APPENDIX B.
LAB CUTTING FORCES DATA

Table B.1. Average and peak cutting forces from lab experiments.

Penetration 6.35 mm	Pass 1						Pass 2					
Cut	2	3	4	5	6	7	2	3	4	5	6	7
Avg side force, kN	-15.1	-18.0	8.4	-1.4	4.6	1.2	-12.9	-24.2	-2.6	-2.7	-4.8	-1.1
Avg rolling force, kN	8.2	13.5	13.0	11.3	10.6	8.1	7.2	10.7	12.8	11.1	10.2	9.3
Avg normal force, kN	36.3	60.0	83.2	62.4	49.8	34.4	27.8	60.5	60.0	49.2	47.0	41.9
Avg resultant force, kN	40.2	64.1	84.6	63.5	51.2	35.4	31.5	66.0	61.4	50.5	48.3	42.9
Peak side force, kN	19.1	20.1	49.7	31.7	48.6	39.1	25.4	14.8	38.1	33.9	27.5	37.0
Peak rolling force, kN	27.3	38.0	37.2	32.2	39.7	88.4	30.6	32.2	33.1	42.2	38.8	36.4
Peak normal force, kN	126.8	149.3	178.5	123.9	147.3	128.8	82.9	178.5	129.7	129.7	136.6	152.2
Peak resultant force, kN	131.1	155.3	189.0	131.9	160.1	161.0	92.0	182.0	139.2	140.6	144.6	160.8
Penetration 6.35 mm	Pass 3						Pass 4					
Avg side force, kN	-16.8	-14.0	-4.8	-4.8	2.8	-0.3	-14.4	-14.3	4.6	0.9	11.5	-0.9
Avg rolling force, kN	10.3	9.6	10.8	11.5	11.3	9.8	10.1	7.8	14.1	11.4	13.2	9.3
Avg normal force, kN	45.2	50.0	56.8	60.2	60.2	51.6	52.9	50.9	64.1	63.1	63.5	39.5
Avg resultant force, kN	49.3	52.8	58.0	61.4	61.3	52.6	55.7	53.4	65.8	64.1	65.8	40.6
Peak side force, kN	19.1	26.5	33.9	30.7	32.8	45.5	23.3	13.8	47.6	30.7	42.3	49.7
Peak rolling force, kN	31.4	34.7	30.6	34.7	33.1	33.9	33.1	28.9	38.8	29.8	31.4	29.8
Peak normal force, kN	132.7	147.3	172.7	151.2	169.7	160.0	121.0	121.0	149.3	140.5	161.9	110.2
Peak resultant force, kN	137.7	153.6	178.6	158.1	176.0	169.7	127.6	125.1	161.4	146.8	170.3	124.5
Penetration 9.5 mm	Pass 1						Pass 2					
Avg side force, kN	-17.3	-14.7	-9.5	4.4	10.1	-11.1	-21.3	-20.7	-2.1	-4.1	8.8	-9.4
Avg rolling force, kN	10.0	13.7	19.3	15.2	10.4	9.4	16.9	17.8	21.8	18.9	21.5	13.0
Avg normal force, kN	36.3	55.3	86.0	66.6	52.8	35.8	65.2	83.9	91.0	80.8	78.1	56.2
Avg resultant force, kN	41.4	58.8	88.7	68.4	54.7	38.6	70.6	88.2	93.6	83.1	81.5	58.4
Peak side force, kN	6.4	25.4	26.5	43.4	41.2	24.3	37.1	43.4	50.8	42.3	52.9	22.2
Peak rolling force, kN	38.0	43.8	47.9	53.7	35.5	33.9	60.3	61.2	48.8	57.0	52.9	43.0
Peak normal force, kN	145.3	154.1	178.5	189.2	130.7	127.8	163.9	241.0	161.9	168.8	151.2	139.5
Peak resultant force, kN	150.4	162.2	186.7	201.4	141.6	134.4	178.6	252.4	176.6	183.1	168.7	147.7
Penetration 9.5 mm	Pass 3						Pass 4					
Avg side force, kN	-16.3	-19.1	-6.3	0.1	4.6	5.4	-28.5	-21.2	-8.1	4.3	-5.8	14.8
Avg rolling force, kN	12.4	14.5	15.6	13.9	18.6	16.5	12.3	20.3	18.8	14.4	12.8	17.5

Table B.1. Average and peak cutting forces from lab experiments (cont).

Avg normal force, kN	54.3	59.4	64.0	90.0	81.1	59.6	47.7	82.7	80.1	70.4	50.5	69.5
Avg resultant force, kN	58.0	64.1	66.2	91.0	83.3	62.1	57.0	87.8	82.7	72.0	52.4	73.2
Peak side force, kN	34.9	27.5	57.1	47.6	37.0	50.8	10.6	21.2	26.5	37.0	37.0	59.2
Peak rolling force, kN	36.4	44.6	45.5	43.8	52.1	69.4	36.4	49.6	55.4	48.8	50.4	64.5
Peak normal force, kN	132.7	161.0	155.1	173.6	221.4	194.1	120.0	224.3	174.6	200.0	194.1	204.8
Peak resultant force, kN	141.9	169.3	171.4	185.3	230.4	212.3	125.8	230.7	185.1	209.1	203.9	222.7
Penetration 12.7 mm	Pass 1						Pass 2					
Avg side force, kN	-20.6	-27.3	-17.5	0.5	7.5	-2.8	-28.0	-25.5	1.2	2.7	0.6	
Avg rolling force, kN	7.9	20.0	25.1	19.6	27.1	12.0	15.6	25.0	27.1	14.1	14.4	
Avg normal force, kN	32.5	74.3	90.3	76.5	89.7	44.0	60.7	83.3	90.7	53.5	57.5	
Avg resultant force, kN	39.3	81.6	95.3	79.0	94.0	45.7	68.7	90.6	94.7	55.4	59.3	
Peak side force, kN	19.1	8.5	29.6	51.8	51.8	33.9	18.0	31.7	47.6	46.5	46.5	
Peak rolling force, kN	33.9	56.2	61.2	66.9	66.9	54.5	57.9	72.7	71.9	46.3	61.2	
Peak normal force, kN	111.2	184.4	197.0	203.9	191.2	149.3	149.3	195.1	183.4	146.3	178.5	
Peak resultant force, kN	117.8	192.9	208.4	220.7	209.1	162.5	161.1	210.6	202.6	160.4	194.3	
Penetration 12.7 mm	Pass 3						Pass 4					
Avg side force, kN	-17.4	-24.1	14.0	-2.2	4.3		-20.1	-34.6	15.8	-10.6	4.4	
Avg rolling force, kN	13.3	19.7	19.2	17.0	13.8		16.1	22.6	22.3	17.3	17.5	
Avg normal force, kN	51.9	67.7	79.5	58.8	48.1		63.8	82.8	82.1	65.4	54.7	
Avg resultant force, kN	56.3	74.5	83.0	61.3	50.2		68.8	92.5	86.5	68.5	57.6	
Peak side force, kN	25.4	34.9	57.1	41.2	50.8		28.6	15.9	71.9	29.6	47.6	
Peak rolling force, kN	45.5	55.4	53.7	55.4	42.2		52.1	55.4	56.2	56.2	52.1	
Peak normal force, kN	157.1	192.2	221.4	163.9	154.1		156.1	209.7	168.8	168.8	134.6	
Peak resultant force, kN	165.5	203.0	234.9	177.8	167.7		167.0	217.5	191.8	180.3	152.0	

Table B.2. Fragment size distribution data.

	Pass 1		Pass 2		Pass 3		Pass 4	
Mesh size, mm	Mass retained (kg)	Cum. % retained	Mass retained (kg)	Cum. % retained	Mass retained (kg)	Cum. % retained	Mass retained (kg)	Cum. % retained
	Penetration 6.35 mm							
50.8	1.29	21.47	1.02	14.61	0.98	18.09	0.68	14.47
25.4	1.57	47.49	2.33	48.21	1.24	41.06	1.16	39.03
9.4	0.99	63.92	1.07	63.62	1.00	59.68	0.86	57.30
1.7	0.49	72.04	0.55	71.48	0.38	66.64	0.41	65.95
Pan	1.69	100.00	1.98	100.00	1.80	100.00	1.61	100.00
Total	6.03	304.93	6.95	297.93	5.39	285.47	4.71	276.75
	Penetration 9.5 mm							
50.8	0.64	8.77	1.61	15.20	2.00	20.63	1.41	16.65
25.4	2.24	39.51	3.04	43.86	2.72	48.61	2.33	44.05
9.4	1.19	55.92	1.60	58.95	1.60	65.10	1.34	59.78
1.7	0.58	63.90	0.78	66.26	0.69	72.22	0.59	66.77
Pan	2.63	100.00	3.58	100.00	2.70	100.00	2.82	100.00
Total	7.28	268.09	10.62	284.29	9.71	306.56	8.49	287.25
	Penetration 12.7 mm							
50.8	2.08	17.40	1.93	16.52	1.33	13.44	2.00	18.45
25.4	3.19	44.11	3.13	43.40	2.49	38.58	2.54	41.93
9.4	1.97	60.59	2.03	60.86	2.22	61.01	2.15	61.78
1.7	0.83	67.50	0.81	67.79	0.77	68.79	0.81	69.25
Pan	3.89	100.00	3.75	100.00	3.09	100.00	3.33	100.00
Total	11.95	289.60	11.65	288.57	9.89	281.81	10.82	291.42

APPENDIX C.

**NORMALITY AND OTHER STATISTICAL TESTS OF CUTTING
PARAMETER**

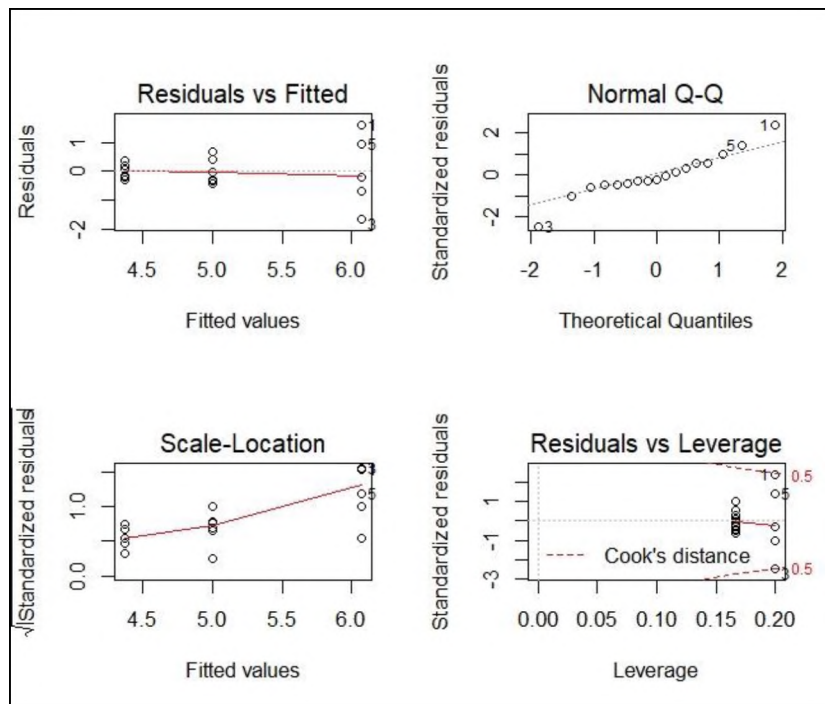


Figure C.1. Specific energy.

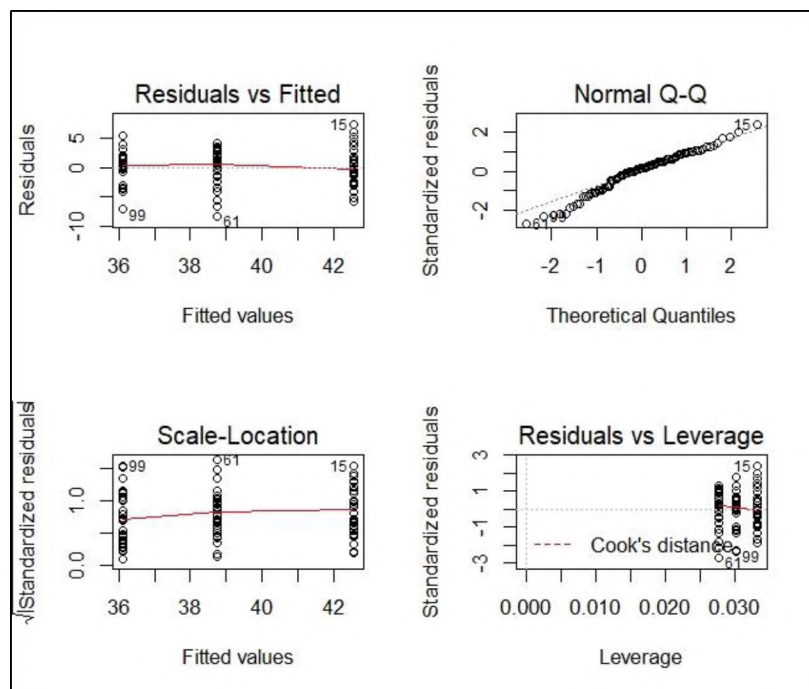


Figure C.2. Surface hardness.

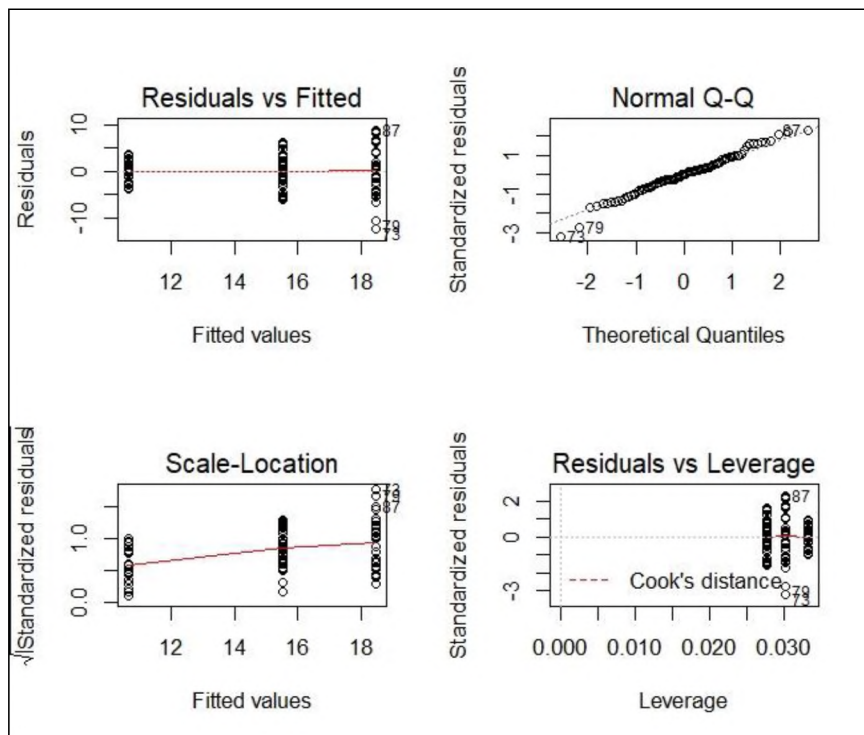


Figure C.3. Side force.

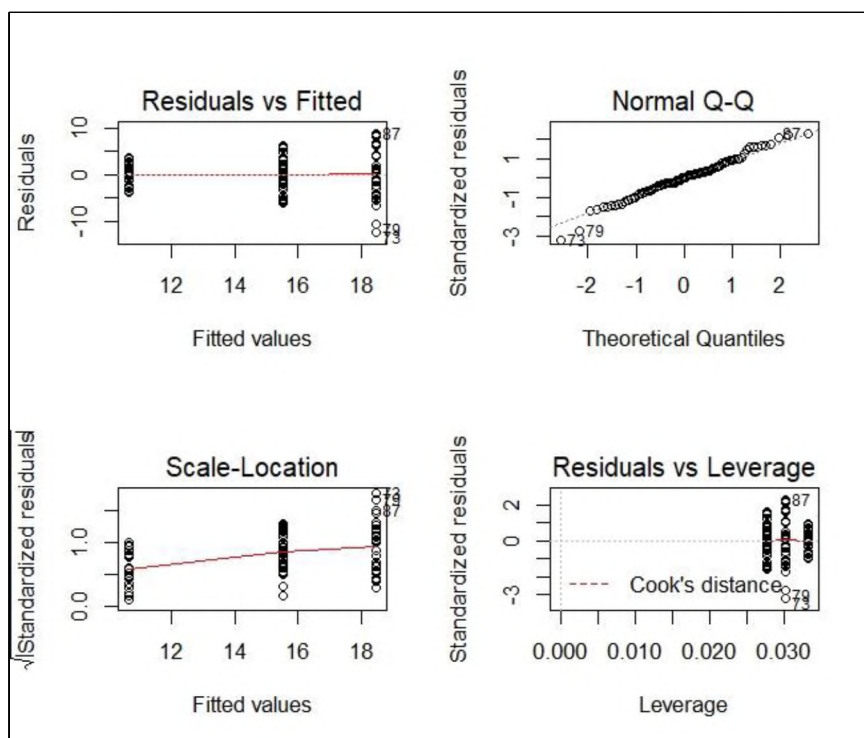


Figure C.4. Rolling force.

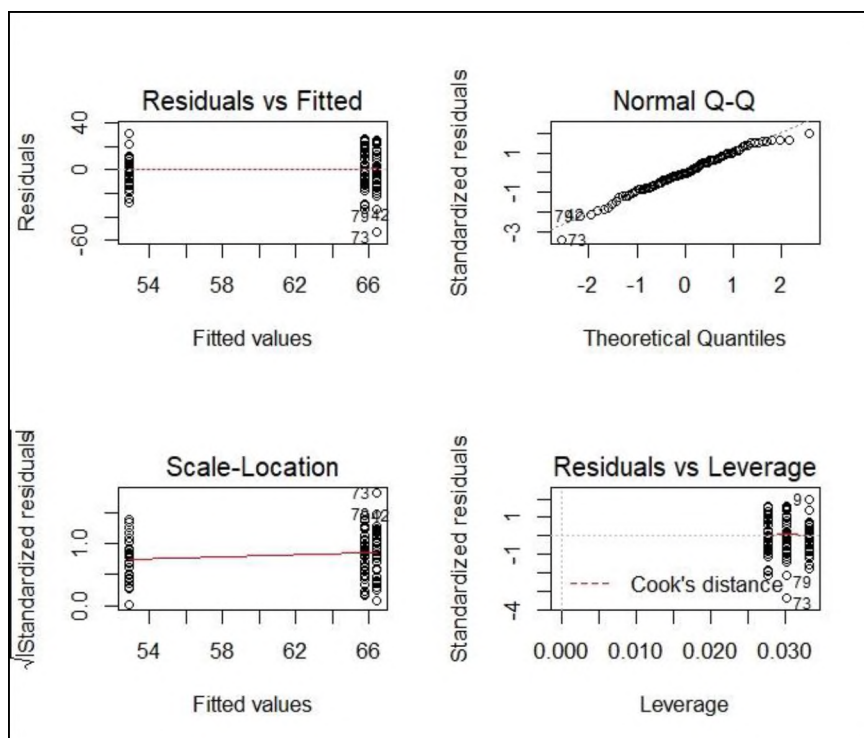


Figure C.5. Normal force.

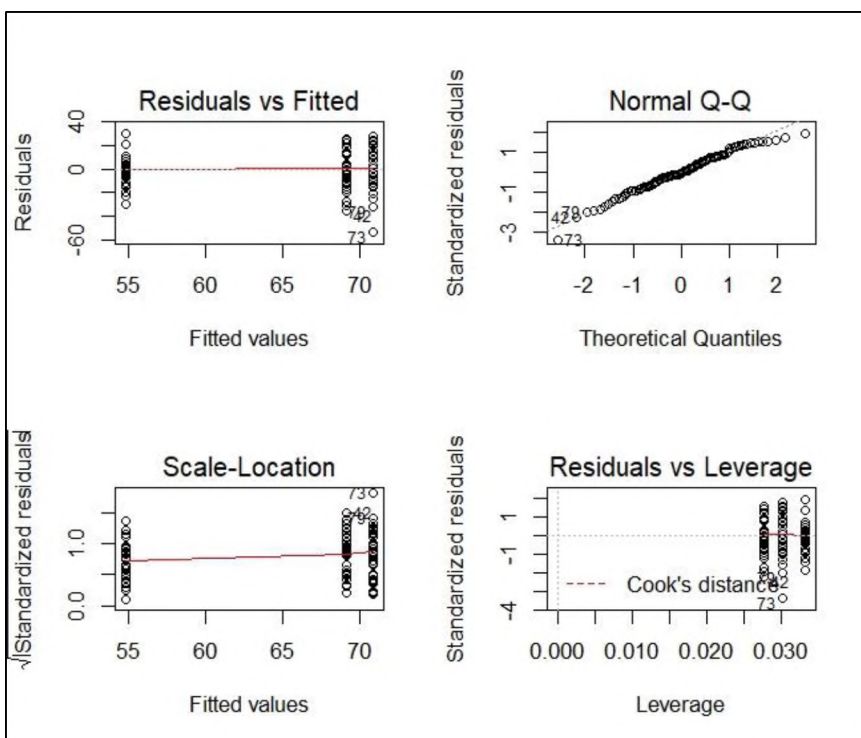


Figure C.6. Resultant force

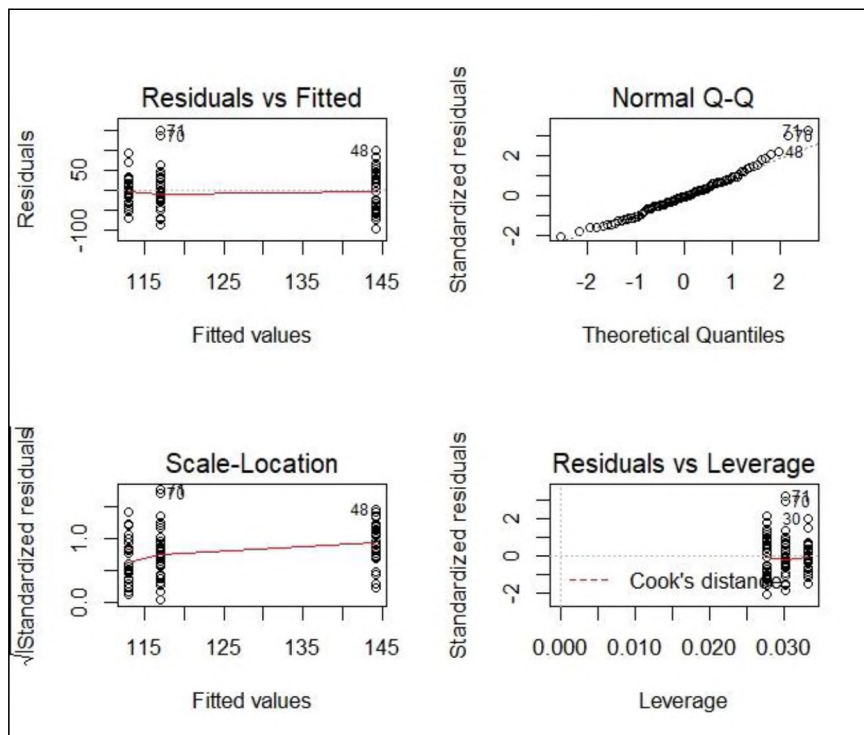


Figure C.7. Ridge volume.

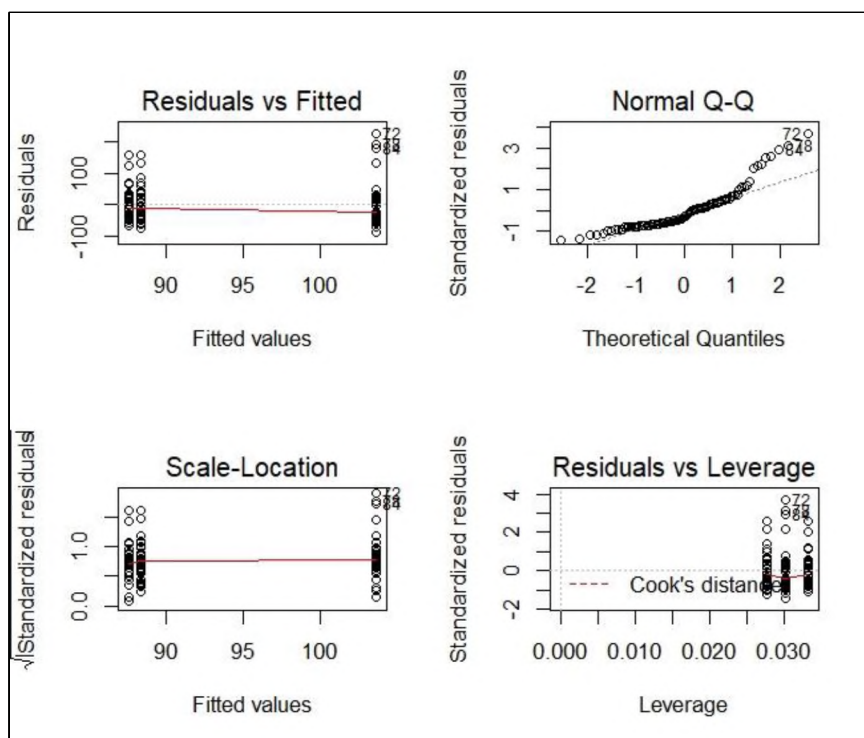


Figure C.8. Overbreak volume.

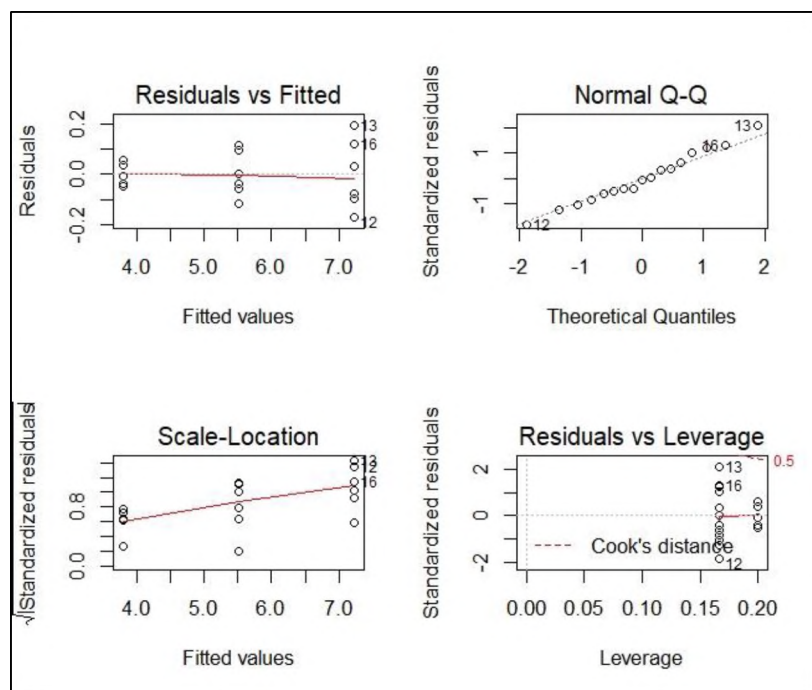


Figure C.9. Instantaneous cutting rate.

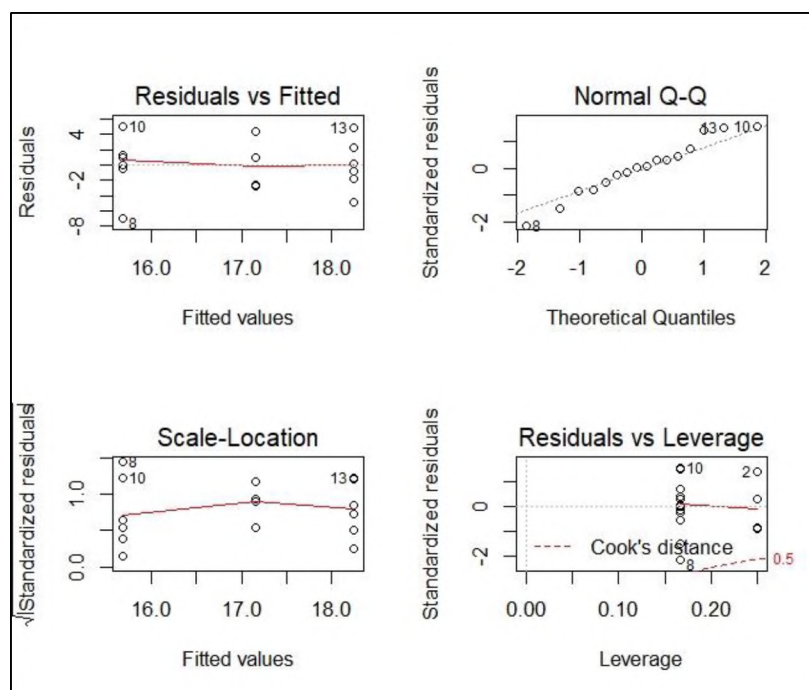


Figure C.10. Large fragment fraction.

APPENDIX D.
NUMERICAL MODEL CUTTING FORCES

Table D.1. Cutting forces from numerical simulations at three spacings.

Spacing, mm	Penetration, mm	s/p	cut1			cut2			cut3		
			Side forces, kN	Rolling forces, kN	Normal forces, kN	Side forces, kN	Rolling forces, kN	Normal forces, kN	Side forces, kN	Rolling forces, kN	Normal forces, kN
25	2.5	10.00	-1.84E-02	6.13E+00	4.07E+01	-1.69E+00	5.45E+00	3.56E+01	3.60E-01	5.71E+00	3.88E+01
25	3.0	8.33	4.61E-01	7.22E+00	4.90E+01	-2.02E+00	6.28E+00	4.44E+01	-2.90E-01	6.36E+00	4.24E+01
25	3.5	7.14	9.09E-01	8.27E+00	5.34E+01	-2.69E+00	7.06E+00	4.65E+01	-1.92E-01	7.09E+00	4.48E+01
25	4.0	6.25	5.10E-01	9.25E+00	5.45E+01	-2.56E+00	8.50E+00	4.58E+01	-1.97E-01	8.17E+00	4.07E+01
25	4.5	5.56	4.02E-01	1.10E+01	4.97E+01	-2.93E+00	9.01E+00	4.41E+01	-9.98E-01	8.28E+00	4.11E+01
25	5.0	5.00	3.68E-01	1.16E+01	5.38E+01	-2.25E+00	9.63E+00	4.51E+01	-1.12E+00	8.79E+00	4.19E+01
25	5.5	4.55	6.28E-01	1.28E+01	5.35E+01	-2.03E+00	1.06E+01	4.42E+01	-1.73E+00	9.24E+00	4.35E+01
25	6.0	4.17	2.34E-01	1.34E+01	6.18E+01	-1.62E+00	1.21E+01	5.05E+01	-1.64E+00	1.03E+01	4.58E+01
25	6.5	3.85	2.35E-01	1.55E+01	6.37E+01	-1.74E+00	1.31E+01	4.87E+01	-1.60E+00	1.10E+01	4.08E+01
25	7.0	3.57	6.01E-01	1.54E+01	5.97E+01	-1.19E+00	1.33E+01	4.80E+01	-2.22E+00	1.12E+01	4.22E+01
25	7.5	3.33	7.23E-01	1.69E+01	6.31E+01	-1.23E+00	1.46E+01	5.47E+01	-1.85E+00	1.15E+01	4.84E+01
25	8.0	3.13	8.84E-01	1.79E+01	6.32E+01	-9.88E-01	1.65E+01	6.02E+01	-2.28E+00	1.33E+01	4.53E+01
30	2.5	12.00	-1.21E-01	5.07E+00	3.71E+01	-3.76E-01	5.77E+00	4.14E+01	5.69E-01	5.29E+00	5.60E+01
30	3.0	10.00	-5.09E-01	5.82E+00	4.27E+01	-1.89E+00	6.53E+00	4.60E+01	-1.29E-01	6.94E+00	4.77E+01
30	3.5	8.57	-1.56E+00	6.93E+00	5.30E+01	-2.52E+00	7.40E+00	5.52E+01	-6.02E-01	7.57E+00	4.81E+01
30	4.0	7.50	-1.16E+00	8.83E+00	5.67E+01	-1.30E+00	9.53E+00	5.45E+01	-6.75E-02	8.82E+00	5.20E+01
30	4.5	6.67	-9.20E-01	1.05E+01	5.78E+01	-1.46E+00	1.01E+01	4.57E+01	-1.26E+00	9.27E+00	4.58E+01
30	5.0	6.00	-8.64E-01	1.16E+01	6.13E+01	-1.78E+00	1.15E+01	5.56E+01	-1.62E+00	9.60E+00	4.90E+01
30	5.5	5.45	2.09E-01	1.31E+01	6.70E+01	-1.56E+00	1.19E+01	5.61E+01	-1.65E+00	1.10E+01	5.08E+01
30	6.0	5.00	-2.88E-01	1.36E+01	6.01E+01	-1.81E-01	1.36E+01	5.45E+01	-2.63E+00	1.20E+01	5.93E+01
30	6.5	4.62	3.37E-01	1.44E+01	6.45E+01	-5.00E-01	1.43E+01	5.51E+01	-8.61E-01	1.23E+01	4.99E+01
30	7.0	4.29	1.33E-01	1.60E+01	7.05E+01	-9.14E-01	1.50E+01	5.64E+01	-1.53E+00	1.38E+01	5.79E+01
30	7.5	4.00	6.49E-02	1.65E+01	6.40E+01	-1.46E+00	1.54E+01	5.53E+01	-2.22E+00	1.41E+01	5.36E+01
30	8.0	3.75	-5.65E-02	1.96E+01	7.64E+01	-5.23E-01	1.65E+01	5.56E+01	-2.73E+00	1.52E+01	5.78E+01
35	2.5	14.00	6.33E-01	5.51E+00	3.88E+01	-4.02E-01	5.56E+00	5.03E+01	-3.35E-01	5.91E+00	5.04E+01
35	3.0	11.67	4.39E-01	6.34E+00	4.41E+01	2.73E-01	7.38E+00	4.50E+01	-9.88E-01	7.23E+00	5.12E+01
35	3.5	10.00	3.39E-01	7.20E+00	5.12E+01	1.13E-01	7.68E+00	5.37E+01	-7.56E-01	8.08E+00	5.32E+01
35	4.0	8.75	1.56E+00	8.61E+00	5.54E+01	-4.53E-01	9.17E+00	5.78E+01	-3.86E-01	1.00E+01	5.29E+01
35	4.5	7.78	8.30E-01	9.63E+00	5.56E+01	-5.52E-01	9.65E+00	5.19E+01	-3.08E-01	1.04E+01	5.36E+01
35	5.0	7.00	4.78E-01	1.13E+01	5.91E+01	-8.32E-01	1.11E+01	5.68E+01	-7.13E-01	1.10E+01	5.72E+01
35	5.5	6.36	6.38E-01	1.27E+01	6.43E+01	-8.11E-01	1.26E+01	6.19E+01	-2.37E-01	1.19E+01	5.92E+01
35	6.0	5.83	-1.47E+00	1.27E+01	6.62E+01	-3.00E-01	1.37E+01	6.32E+01	-7.30E-01	1.21E+01	6.12E+01
35	6.5	5.38	-1.46E-02	1.46E+01	6.73E+01	-2.76E-01	1.46E+01	5.73E+01	-9.51E-01	1.35E+01	5.76E+01
35	7.0	5.00	-1.57E+00	1.56E+01	6.38E+01	-2.10E-01	1.56E+01	6.61E+01	-7.83E-01	1.39E+01	5.97E+01
35	7.5	4.67	-9.25E-01	1.57E+01	6.29E+01	-7.11E-01	1.49E+01	6.63E+01	-6.43E-01	1.46E+01	6.62E+01
35	8.0	4.38	1.46E-02	1.75E+01	6.63E+01	-2.38E-01	1.64E+01	5.96E+01	-1.90E+00	1.53E+01	6.14E+01

BIBLIOGRAPHY

- Abu Bakar, M.Z., 2012. Saturation effects on mechanical excavatability of Roubidoux sandstone under selected rock cutting tools. Dr. Diss.
- Abu Bakar, M.Z., Gertsch, L.S., Rostami, J., 2013. Evaluation of Fragments from Disc Cutting of Dry and Saturated Sandstone. *Rock Mech. Rock Eng.* 47, 1891–1903. <https://doi.org/10.1007/s00603-013-0482-8>
- Afrasiabi, N., Rafiee, R., Noroozi, M., 2019. Investigating the effect of discontinuity geometrical parameters on the TBM performance in hard rock. *Tunn. Undergr. Sp. Technol.* <https://doi.org/10.1016/j.tust.2018.11.039>
- Albar, A., Osman, M.H., Kamaruddin, M.H., Hasan, D., Dollah, Z., 2019. Interaction of mineralogical content with engineering properties of selected weathered Semanggol formation mudrocks, in: *Journal of Physics: Conference Series*. Institute of Physics Publishing, p. 12012. <https://doi.org/10.1088/1742-6596/1349/1/012012>
- ASTM:D5873-14, 2014. Standard Test Method for Determination of Rock Hardness by Rebound Hammer Method 1, ASTM International. ASTM. <https://doi.org/10.1520/D5873-14>
- ASTM, 2000. Determination of Rock Hardness by Rebound Hammer Method1. ASTM D 5873 - 95 4.
- ASTM D4543-19, 2019. Standard Practices for Preparing Rock Core as Cylindrical Test Specimens and Verifying Conformance to Dimensional and Shape Tolerances. ASTM, West Conshohocken, PA.
- ASTM E111, 1981. Standard Test Method for Young ' s Modulus , Tangent Modulus , and Chord Modulus 1 (No. E111), Practice. West Conshohocken. <https://doi.org/10.1520/E0111-04R10>
- Aufmuth, R.E., 1975. A systematic determination of engineering criteria for rock. *Int. J. Rock Mech. Min. Sci. Geomech. Abstr.* 12, A2. [https://doi.org/10.1016/0148-9062\(75\)90749-4](https://doi.org/10.1016/0148-9062(75)90749-4)
- Ayawah, P.E., Gertsch, L.S., Sherizadeh, T., 2019. Using Roughness of Excavated Rock Surface to Predict Cutting Forces: A Numerical Approach. American Rock Mechanics Association, New York, New York, USA.
- Aydin, A., 2008. ISRM Suggested method for determination of the Schmidt hammer rebound hardness: Revised version. *Int. J. Rock Mech. Min. Sci.* <https://doi.org/10.1016/j.ijrmms.2008.01.020>

- Aydin, A., Basu, A., 2005. The Schmidt hammer in rock material characterization. *Eng. Geol.* 81, 1–14. <https://doi.org/10.1016/j.enggeo.2005.06.006>
- Bahrani, N., Kaiser, P.K., 2016. Numerical investigation of the influence of specimen size on the unconfined strength of defected rocks. *Comput. Geotech.* 77, 56–67. <https://doi.org/10.1016/J.COMPGEO.2016.04.004>
- Bain, F.H., Ulrich, E.O., 1905. *Copper Deposits Of Missouri*. Washington.
- Balci, C., 2009. Correlation of rock cutting tests with field performance of a TBM in a highly fractured rock formation: A case study in Kozyatagi-Kadikoy metro tunnel, Turkey. *Tunn. Undergr. Sp. Technol.* 24, 423–435. <https://doi.org/10.1016/j.tust.2008.12.001>
- Balci, C., Tumac, D., 2012. Investigation into the effects of different rocks on rock cuttability by a V-type disc cutter. *Tunn. Undergr. Sp. Technol.* 30, 183–193. <https://doi.org/10.1016/j.tust.2012.02.018>
- Barton, N., Lien, R., Lunde, J., 1974. Engineering classification of rock masses for the design of tunnel support. *Rock Mech. Felsmechanik Mécanique des Roches* 6, 189–236. <https://doi.org/10.1007/BF01239496>
- Benjumea, R., Sikarskie, D.L., 1969. A note on the penetration of a rigid wedge into a nonisotropic brittle material. *Int. J. Rock Mech. Min. Sci.* 6, 343–352. [https://doi.org/10.1016/0148-9062\(69\)90038-2](https://doi.org/10.1016/0148-9062(69)90038-2)
- Bieniawski, Z.T., 1979. *Tunnel Design By Rock Mass Classifications*. Washington DC.
- Bilgin, N., 1977. *Investigation into Mechanical Cutting Characteristics of Some Medium and High Strength Rocks*. University of Newcastle Upon Tyne, UK.
- Bilgin, N., Copur, H., Balci, C., 2014. *Mechanical Excavation in Mining and Civil Industries*. CRC Press, Boca Raton, FL.
- Boussinesq, J., 1885. *Application des Potentiels a l'Etude de l'Equilibre et du Mouvement des Solides Elastiques*, Gauthier-Viallars. Paris.
- Brezani, I., 2020. Rosin-Rammler Diagram plotting tool.
- Canny, J.F., 1986. A {C}omputational {A}pproach to {E}dge {D}etection. *Tpami* 8, 679–698. <https://doi.org/http://doi.acm.org/10.1145/11274.11275>
- Cargill, J.S., Shakoor, A., 1990. Evaluation of empirical methods for measuring the uniaxial compressive strength of rock. *Int. J. Rock Mech. Min. Sci.* 27, 495–503. [https://doi.org/10.1016/0148-9062\(90\)91001-N](https://doi.org/10.1016/0148-9062(90)91001-N)

- Castro-Filgueira, U., Alejano, L.R., Arzúa, J., Ivars, D.M., 2017. Sensitivity Analysis of the Micro-Parameters Used in a PFC Analysis Towards the Mechanical Properties of Rocks. *Procedia Eng.* 191, 488–495. <https://doi.org/10.1016/j.proeng.2017.05.208>
- Chen, L.H., Labuz, J.F., 2006. Indentation of rock by wedge-shaped tools. *Int. J. Rock Mech. Min. Sci.* 43, 1023–1033. <https://doi.org/10.1016/j.ijrmms.2006.03.005>
- Chen, P., 2017. Effects of Microparameters on Macroparameters of Flat-Jointed Bonded-Particle Materials and Suggestions on Trial-and-Error Method. *Geotech. Geol. Eng.* 35, 663–677. <https://doi.org/10.1007/s10706-016-0132-5>
- Cho, J.-W., Jeon, S., Jeong, H.-Y., Chang, S.-H., 2013. Evaluation of cutting efficiency during TBM disc cutter excavation within a Korean granitic rock using linear-cutting-machine testing and photogrammetric measurement. *Tunn. Undergr. Sp. Technol.* 35, 37–54. <https://doi.org/10.1016/j.tust.2012.08.006>
- Cho, J.-W., Jeon, S., Yu, S.-H., Chang, S.-H., 2010. Optimum spacing of TBM disc cutters: A numerical simulation using the three-dimensional dynamic fracturing method. *Tunn. Undergr. Sp. Technol.* 25, 230–244. <https://doi.org/10.1016/j.tust.2009.11.007>
- Choi, S.O., Lee, S.J., 2015. Three-dimensional numerical analysis of the rock-cutting behavior of a disc cutter using particle flow code. *KSCE J. Civ. Eng.* 19, 1129–1138. <https://doi.org/10.1007/s12205-013-0622-4>
- Cook, N.G.W., Hood, M., Tsai, F., 1984. Observations of crack growth in hard rock loaded by an indenter. *Int. J. Rock Mech. Min. Sci.* 21, 97–107. [https://doi.org/10.1016/0148-9062\(84\)91177-X](https://doi.org/10.1016/0148-9062(84)91177-X)
- Copur, H., Bilgin, N., Balci, C., Tumac, D., Avunduk, E., 2017. Effects of Different Cutting Patterns and Experimental Conditions on the Performance of a Conical Drag Tool. *Rock Mech. Rock Eng.* 50, 1585–1609. <https://doi.org/10.1007/s00603-017-1172-8>
- Daum, M., Dudek, G., 1998. On 3-D surface reconstruction using shape from shadows, in: *Proceedings of the IEEE Computer Society Conference on Computer Vision and Pattern Recognition*. IEEE Comp Soc, pp. 461–468. <https://doi.org/10.1109/cvpr.1998.698646>
- Deere, D.U., Miller, R.P., 1966. *Engineering Classification and Index Properties for Intact Rock*. New Mexico.
- Develi, K., Babadagli, T., Comlekci, C., 2001. A new computer-controlled surface-scanning device for measurement of fracture surface roughness. *Comput. Geosci.* 27, 265–277. [https://doi.org/10.1016/S0098-3004\(00\)00083-2](https://doi.org/10.1016/S0098-3004(00)00083-2)

- Dudt, J.-P., Delisio, A., 2016. The “penalty factors” method for the prediction of TBM performances in changing grounds. *Tunn. Undergr. Sp. Technol.* 57, 195–200. <https://doi.org/10.1016/j.tust.2016.01.006>
- Entacher, M., Lorenz, S., Galler, R., 2014a. Tunnel boring machine performance prediction with scaled rock cutting tests. *Int. J. Rock Mech. Min. Sci.* 70, 450–459. <https://doi.org/10.1016/j.ijrmms.2014.04.021>
- Entacher, M., Schuller, E., Galler, R., 2014b. Rock Failure and Crack Propagation Beneath Disc Cutters. *Rock Mech. Rock Eng.* 48, 1559–1572. <https://doi.org/10.1007/s00603-014-0661-2>
- Gertsch, R., 2000. Rock Toughness and Disc Cutting. Missouri University of Science and Technology.
- Gertsch, R., Gertsch, L., Rostami, J., 2007. Disc cutting tests in Colorado Red Granite: Implications for TBM performance prediction. *Int. J. Rock Mech. Min. Sci.* 44, 238–246. <https://doi.org/10.1016/j.ijrmms.2006.07.007>
- Glen, S., 2020. Confounding Variable: Simple Definition and Example" From StatisticsHowTo.com: Elementary Statistics for the rest of us! [WWW Document]. URL <https://www.statisticshowto.com/experimental-design/confounding-variable/> (accessed 11.19.20).
- Gong, Q.M., Zhao, J., Jiang, Y.S., 2007. In situ TBM penetration tests and rock mass boreability analysis in hard rock tunnels. *Tunn. Undergr. Sp. Technol.* 22, 303–316. <https://doi.org/10.1016/j.tust.2006.07.003>
- Grima, M.A., Bruines, P.A., Verhoef, P.N.W., 2000. Modeling Tunnel Boring Machine Performance by Neuro-Fuzzy Methods. *Tunn. Undergr. Sp. Technol.* 15, 259–269.
- Han, D.Y., Cao, P., Liu, J., Zhu, J.B., 2017. An Experimental Study of Dependence of Optimum TBM Cutter Spacing on Pre-set Penetration Depth in Sandstone Fragmentation. *Rock Mech. Rock Eng.* 50, 3209–3221. <https://doi.org/10.1007/s00603-017-1275-2>
- Hassanpour, J., Rostami, J., Zhao, J., 2011. A new hard rock TBM performance prediction model for project planning. *Tunn. Undergr. Sp. Technol.* 26, 595–603. <https://doi.org/10.1016/j.tust.2011.04.004>
- Heller, R.L., 1954. Stratigraphy and Paleontology of the Roubidoux Formation of Missouri. Rolla.
- Hood, M., Alehossein, H., 2000. A development in rock cutting technology. *Int. J. Rock Mech. Min. Sci.* 37, 297–305. [https://doi.org/10.1016/s1365-1609\(99\)00107-0](https://doi.org/10.1016/s1365-1609(99)00107-0)

- Huang, H., Lecampion, B., Detournay, E., 2013. Discrete element modeling of tool-rock interaction I: rock cutting. *Int. J. Numer. Anal. Methods Geomech.* 37, 1913–1929. <https://doi.org/10.1002/nag.2113>
- Ibarra, J.A., Maerz, N.H., Franklin, J.A., 1996. Overbreak and underbreak in underground openings Part 2: Causes and implications. *Geotech. Geol. Eng.* 14, 325–340. <https://doi.org/10.1007/BF00421947>
- ISRM, 2014. ISRM suggested methods for testing or measuring properties of rocks and rock masses, in: Ulusay, R. (Ed.), *The ISRM Suggested Methods for Rock Characterization, Testing and Monitoring: 2007-2014*. Springer International Publishing, p. 293. https://doi.org/10.1007/978-3-319-07713-0_2
- Itasca, 1988. 3-D Distinct element code. Itasca Consult. Group, Inc.
- James, M.R., Robson, S., 2012. Straightforward reconstruction of 3D surfaces and topography with a camera: Accuracy and geoscience application. *J. Geophys. Res. Earth Surf.* 117, n/a-n/a. <https://doi.org/10.1029/2011JF002289>
- Jang, H., Topal, E., 2013. Optimizing overbreak prediction based on geological parameters comparing multiple regression analysis and artificial neural network. *Tunn. Undergr. Sp. Technol.* 38, 161–169. <https://doi.org/10.1016/j.tust.2013.06.003>
- Kaba, A.G., 2018. Empirical Correlations Between Rock Cutting Parameters and Excavated Rock Surface Rebound Hardness. Missouri University of Science and Technology. <https://doi.org/10.9790/0837-2208010105>
- Karpuz, C., 1990. A classification system for excavation of surface coal measures. *Min. Sci. Technol.* 11, 157–163. [https://doi.org/10.1016/0167-9031\(90\)90303-A](https://doi.org/10.1016/0167-9031(90)90303-A)
- Khademi Hamidi, J., Shahriar, K., Rezai, B., Rostami, J., 2010. Performance prediction of hard rock TBM using Rock Mass Rating (RMR) system. *Tunn. Undergr. Sp. Technol.* 25, 333–345. <https://doi.org/10.1016/J.TUST.2010.01.008>
- Kidybiński, A., 1981. Bursting liability indices of coal. *Int. J. Rock Mech. Min. Sci.* 18, 295–304. [https://doi.org/10.1016/0148-9062\(81\)91194-3](https://doi.org/10.1016/0148-9062(81)91194-3)
- Koyama, T., Jing, L., 2007. Effects of model scale and particle size on micro-mechanical properties and failure processes of rocks—A particle mechanics approach. *Eng. Anal. Bound. Elem.* 31, 458–472. <https://doi.org/10.1016/J.ENGANABOUND.2006.11.009>
- Kumar, S., Talreja, R., Murthy, V.M.S.R., 2017. Development of a drill energy utilization index for aiding selection of drill machines in surface mines. *Int. J. Min. Sci. Technol.* 27, 393–399. <https://doi.org/10.1016/j.ijmst.2017.03.002>

- Labra, C., Rojek, J., Oñate, E., 2016. Discrete/Finite Element Modelling of Rock Cutting with a TBM Disc Cutter. *Rock Mech. Rock Eng.* 50, 621–638. <https://doi.org/10.1007/s00603-016-1133-7>
- Lawn, B.R., Swain, M. V., 1975. Microfracture beneath point indentations in brittle solids. *J. Mater. Sci.* 10, 113–122. <https://doi.org/10.1007/BF00541038>
- Ledgerwood III, L.W., Ledgerwood, L.W., Ledgerwood III, L.W., 2007. PFC modeling of rock cutting under high pressure conditions, in: 1st Canada-US Rock Mechanics Symposium. American Rock Mechanics Association, pp. 511–518.
- Li, K., Cheng, Y., Fan, X., 2018. Roles of model size and particle size distribution on macro-mechanical properties of Lac du Bonnet granite using flat-joint model. *Comput. Geotech.* 103, 43–60. <https://doi.org/10.1016/J.COMPGE0.2018.07.007>
- Liang, M., Mohamad, E.T., Komoo, I., Ma, C.K., 2017. An excavatability classification system for surface excavation in sedimentary rocks. *Bull. Eng. Geol. Environ.* 76, 241–251. <https://doi.org/10.1007/s10064-015-0807-9>
- Lim, W.L., 2004. Mechanics of railway ballast Mechanics of Railway Ballast Behaviour. University of Nottingham.
- Lin, L., Xia, Y., Wu, D., Kripka, M., 2019. Multiobjective Optimization Design for Structural Parameters of TBM Disc Cutter Rings Based on FAHP and SAMPGA. *Adv. Civ. Eng.* 2019. <https://doi.org/10.1155/2019/8438639>
- Lindqvist, P.-A., 1982. Rock Fragmentation By Indentation And Disc Cutting. University Of Luleå.
- Lisjak, A., Grasselli, G., 2014. A review of discrete modeling techniques for fracturing processes in discontinuous rock masses. *J. Rock Mech. Geotech. Eng.* 6, 301–314. <https://doi.org/10.1016/j.jrmge.2013.12.007>
- Lislerud, A., 1997. Principles of Mechanical Excavation, English. Helsinki, Finland.
- Ma, H., Gong, Q., Wang, J., Yin, L., Zhao, X., 2016. Study on the influence of confining stress on TBM performance in granite rock by linear cutting test. *Tunn. Undergr. Sp. Technol.* 57, 145–150. <https://doi.org/10.1016/j.tust.2016.02.020>
- Ma, H., Yin, L., Ji, H., 2011. Numerical study of the effect of confining stress on rock fragmentation by TBM cutters. *Int. J. Rock Mech. Min. Sci.* 48, 1021–1033. <https://doi.org/10.1016/j.ijrmms.2011.05.002>
- Maerz, N., Chepur, P., Myers, J., Linz, J., 2001. Concrete Roughness Characterization Using Laser Profilometry for Fiber-Reinforced Polymer Sheet Application. *Transp. Res. Rec. J. Transp. Res. Board* 1775, 132–139. <https://doi.org/10.3141/1775-16>

- Maerz, N.H., Hilgers, M.C., 2010. A method for matching fractured surfaces using shadow profilometry. *WIT Trans. Eng. Sci.* <https://doi.org/10.2495/TD100201>
- Maerz, N.H., Ibarra, J.A., Franklin, J.A., 1996. Overbreak and underbreak in underground openings Part 1: Measurement using the light sectioning method and digital image processing. *Geotech. Geol. Eng.* 14, 307–323. <https://doi.org/10.1007/BF00421946>
- Mah, J., Samson, C., McKinnon, S., Aikman, D., 2008. Triangulation-Based 3D Laser Imaging for Underground Rock Mass Characterization: Impact of Operational Parameters. American Rock Mechanics Association.
- Mah, J., Samson, C., Mckinnon, S.D., 2012. Surface roughness measurements using three-dimensional laser imaging. *International Society for Rock Mechanics and Rock Engineering*.
- Mah, Jason, Samson, C., McKinnon, S.D., Thibodeau, D., 2012. 3D laser imaging for surface roughness analysis. *Int. J. Rock Mech. Min. Sci.* 58, 111–117. <https://doi.org/10.1016/j.ijrmms.2012.08.001>
- Mahtab, M.A., Rossler, K., Kalamaras, G.S., Grasso, P., 1997. Assessment of Geological Overbreak for Tunnel Design and Contractual Claims. *Int. J. Rock Mech. Min. Sci.* 34.
- Mandal, S.K., Singh, M.M., 2009. Evaluating extent and causes of overbreak in tunnels. *Tunn. Undergr. Sp. Technol.* 24, 22–36. <https://doi.org/10.1016/J.TUST.2008.01.007>
- Mearz, N., Franklin, J., Bennett, C., 1990. Joint Roughness Measurements Using Shadow Profilometry. *Int. J. Rock Mech. Min. Sci. Geomech* 27, 15.
- Mishra, G., 2014. Rebound Hammer Test on Concrete - Principle, Procedure, Advantages & Disadvantages [WWW Document]. URL <https://theconstructor.org/concrete/rebound-hammer-test-concrete-ndt/2837/> (accessed 2.12.20).
- Moon, T., Oh, J., 2011. A Study of Optimal Rock-Cutting Conditions for Hard Rock TBM Using the Discrete Element Method. *Rock Mech. Rock Eng.* 45, 837–849. <https://doi.org/10.1007/s00603-011-0180-3>
- Nelson, P.P., 1993. TBM Performance Analysis with Reference to Rock Properties, in: Hudson, J.A. (Ed.), *Comprehensive Rock Engineering - Principles, Practice and Projects: Excavation, Support and Monitoring*. Pergamon Press, New York.
- Ozdemir, L., 1995. *Mechanical Tunneling*.
- Pang, S.S., Goldsmith, W., 1990. Investigation of crack formation during loading of brittle rock. *Rock Mech. Rock Eng.* 23, 53–63. <https://doi.org/10.1007/BF01020422>

- Pang, S.S., Goldsmith, W., Hood, M., 1989. A force-indentation model for brittle rocks. *Rock Mech. Rock Eng.* 22, 127–148. <https://doi.org/10.1007/BF01583958>
- Paterson, M.S., Wong, T., 2005. *Experimental rock deformation--the brittle field*. Springer.
- Paul, B., Sikarskie, D.L., 1965. A Preliminary Theory of Static Penetration by a Rigid Wedge into a Brittle Material, in: *SME Transactions*. pp. 372–383.
- Plácido, J.C.R., Friant, J.E., 2004. The Disc Bit-A Tool for Hard-Rock Drilling, in: 2003 SPE/IADC Drilling Conference. Amsterdam.
- Potyondy, D.O., 2015. The bonded-particle model as a tool for rock mechanics research and application: current trends and future directions. *Geosystem Eng.* 18, 1–28. <https://doi.org/10.1080/12269328.2014.998346>
- Potyondy, D.O., 2013. PFC3D flat joint contact model version 1. Tech. Memo. ICG7234-L, Itasca Consult. Gr.
- Potyondy, D.O., 2012. A flat-jointed bonded-particle material for hard rock, in: 46th US Rock Mechanics/Geomechanics Symposium. American Rock Mechanics Association.
- Potyondy, D.O., Cundall, P.A., 2004. A bonded-particle model for rock. *Int. J. Rock Mech. Min. Sci.* 41, 1329–1364. <https://doi.org/10.1016/j.ijrmms.2004.09.011>
- Proceq, 2020. Schmidt Rebound Hammers for Concrete Strength and Rock Testing [WWW Document]. Proceq SA. URL <https://www.proceq.com/compare/schmidt-hammers/> (accessed 12.1.20).
- Proceq, 2017. *Rock Schmidt Operating Instructions*.
- Qi, G., Wei, Z., Hao, M., 2016. An experimental research on the rock cutting process of the gage cutters for rock tunnel boring machine (TBM). *Tunn. Undergr. Sp. Technol.* 103, 215–229. <https://doi.org/10.1016/j.tust.2017.08.009>
- Ramezanzadeh, A., Hood, M., 2010. A state-of-the-art review of mechanical rock excavation technologies. *Int. J. Min. Environ. Issues* 1, 29–39. <https://doi.org/10.1088/2040-8978/12/12/124004>
- Ramezanzadeh, A., Rostami, J., Tadic, D., 2008. Impact of Rock Mass Characteristics on Hard Rock Tunnel Boring Machine Performance. 13th Aust. Tunn. Conf.
- Raviv, D., Pao, Y.H., Loparo, K.A., 1989. Reconstruction of Three-Dimensional Surfaces from Two-Dimensional Binary Images. *IEEE Trans. Robot. Autom.* 5, 701–710. <https://doi.org/10.1109/70.88087>
- Rizo, J.A.M., Mendoza Rizo, J.A., 2010. Modeling rock cutting using DEM with crushable particles. *Engineering* 86.

- Rojek, J., Labra, C., Onate, E., 2010. Discrete Element simulation of rock cutting process. 10th Int. Conf. Mod. Build. Mater. Struct. Tech. .
- Rojek, J., Oñate, E., Labra, C., Kargl, H., 2011. Discrete element simulation of rock cutting. *Int. J. Rock Mech. Min. Sci.* 48, 996–1010. <https://doi.org/10.1016/j.ijrmms.2011.06.003>
- Rosin, P., Rammler, E., Rammler, B., 1933. The Laws Governing the Fineness of powdered coal. *J. Inst. Fuel* 7, 29–36.
- Rostami, J., 2016. Performance prediction of hard rock Tunnel Boring Machines (TBMs) in difficult ground. *Tunn. Undergr. Sp. Technol.* 57, 173–182. <https://doi.org/10.1016/j.tust.2016.01.009>
- Rostami, J., 2013. Study of pressure distribution within the crushed zone in the contact area between rock and disc cutters. *Int. J. Rock Mech. Min. Sci.* 57, 172–186. <https://doi.org/10.1016/j.ijrmms.2012.07.031>
- Rostami, J., 2008. Hard Rock TBM Cutterhead Modeling for Design and Performance Prediction. *Geomech. und Tunnelbau* 1, 18–28. <https://doi.org/10.1002/geot.200800002>
- Rostami, J., 1997. Development Of A Force Estimation Model For Rock Fragmentation With Disc Cutters Through Theoretical Modeling And Physical Measurement Of Crushed Zone Pressure. Colorado School of Mines.
- Rostami, J., Chang, S.H., 2017. A Closer Look at the Design of Cutterheads for Hard Rock Tunnel-Boring Machines. *Engineering* 3, 892–904. <https://doi.org/10.1016/j.eng.2017.12.009>
- Rostami, J., Ozdemir, L., 1993. A new model for performance prediction of hard rock TBMs, in: *Proceedings of Rapid Excavation and Tunnelling Conference, USA*. pp. 794–809.
- Rostami, J., Ozdemir, L., Neil, D.M., 1994. Performance prediction: A key issue in mechanical hard rock mining, in: *Society of Mining, Metallurgy, and Exploration*.
- Roxborough, F.F., Philips, R.H., 1975. Rock excavation by disc cutter. *Int. J. Rock Mech. Min. Sci. Geomech.* 12, 6.
- Roxborough, F.F., Rispin, A., 1973. Investigation Into The Application Of Picks For Mechanized Tunnel Boring In The Lower Chalk. *Min. Eng* 1–13.
- Roxborough, F.F., Sen, G.C., 1986. Breaking Coal and Rock. *Australas. Coal Min. Pract.* 12, 13–147.

- Sachpazis, C.I., 1990. Correlating schmidt hardness with compressive strength and young's modulus of carbonate rocks. *Bull. Int. Assoc. Eng. Geol.* 42, 75–83. <https://doi.org/10.1007/BF02592622>
- Salimi, A., Rostami, J., Moormann, C., Delisio, A., 2016. Application of non-linear regression analysis and artificial intelligence algorithms for performance prediction of hard rock TBMs. *Tunn. Undergr. Sp. Technol.* 58, 236–246.
- Samson, C., English, C., Deslauriers, A., Christie, I., Blais, F., Ferrie, F., 2004. Neptec 3D Laser Camera System: From Space Mission STS-105 to Terrestrial Applications - NRC Publications Archive - Canada.ca, in: 2002 ASTRO Conference.
- Schick, F., 2019. Rebound hammer - ZfP - TUM Wiki [WWW Document]. URL <https://wiki.tum.de/display/zfp/Rebound+hammer> (accessed 8.21.20).
- Schmidt, E., 1951. Quality control of concrete by rebound hammer testing (Versuche mit dem neuen Beton-Prufhammer zur Qualitätsbestimmung des Betons). *Schweizer Arch. fur Angew. Wiss. und Tech.* (in Ger. 17, 139–143.
- Scholle, P.A., Ulmer-Scholle, D., 2003. Cements and Cementation, in: Middleton, Gerard, V., Church, M.J., Conglio, M., Hardie, L.A., Longstaffe, F.J. (Eds.), *Encyclopedia of Sediments and Sedimentary Rocks*. Kluwer Academic Publishers, Dordrecht, pp. 110–118.
- Selimoglu, O., 2009. A Fuzzy Logic Based Predictor Model For Disc Cutter Chip Production Rate. Missouri University of Science and Technology.
- Sheorey, P.R., Barat, D., Das, M.N., Mukherjee, K.P., Singh, B., 1984. Schmidt hammer rebound data for estimation of large scale in situ coal strength. *Int. J. Rock Mech. Min. Sci.* 21, 39–42. [https://doi.org/10.1016/0148-9062\(84\)90008-1](https://doi.org/10.1016/0148-9062(84)90008-1)
- Singh, R.N., Hassani, F.P., Elkington, P.A.S., 1983. The Application Of Strength And Deformation Index Testing To The Stability Assessment Of Coal Measures Excavations.
- Singh, S.P., Xavier, P., 2005. Causes, impact and control of overbreak in underground excavations. *Tunn. Undergr. Sp. Technol.* 20, 63–71. <https://doi.org/10.1016/j.tust.2004.05.004>
- Su, O., Ali Akcin, N., 2011. Numerical simulation of rock cutting using the discrete element method. *Int. J. Rock Mech. Min. Sci.* 48, 434–442. <https://doi.org/10.1016/j.ijrmms.2010.08.012>
- Summers, D.A., 1995. *Waterjetting Technology*, 1st ed. Taylor & Francis Routledge, New York.

- Teale, R., 1965. The concept of specific energy in rock drilling. *Int. J. Rock Mech. Min. Sci. Geomech. Abstr.* 2, 57–73. [https://doi.org/10.1016/0148-9062\(65\)90022-7](https://doi.org/10.1016/0148-9062(65)90022-7)
- Tiryaki, B., Dikmen, A.C., 2006. Effects of rock properties on specific cutting energy in linear cutting of sandstones by picks. *Rock Mech. Rock Eng.* <https://doi.org/10.1007/s00603-005-0062-7>
- Tumac, D., Balci, C., 2015. Investigations into the cutting characteristics of CCS type disc cutters and the comparison between experimental, theoretical and empirical force estimations. *Tunn. Undergr. Sp. Technol.* 45, 84–98. <https://doi.org/10.1016/j.tust.2014.09.009>
- Tumac, D., Bilgin, N., Feridunoglu, C., Ergin, H., 2007. Estimation of rock cuttability from shore hardness and compressive strength properties. *Rock Mech. Rock Eng.* 40, 477–490. <https://doi.org/10.1007/s00603-006-0108-5>
- Tuncdemir, H., Bilgin, N., Copur, H., Balci, C., 2008. Control of rock cutting efficiency by muck size. *Int. J. Rock Mech. Min. Sci.* 45, 278–288. <https://doi.org/10.1016/j.ijrmms.2007.04.010>
- USS, 2020. Underground Support Systems (USS) Inc. - Buy Tunnel Boring Machines (TBM), TBM Parts, Industrial Equipment and Parts [WWW Document]. URL <https://www.undergroundsupportsystems.com/parts.php#> (accessed 11.24.20).
- van Wyk, G., Els, D.N.J., Akdogan, G., Bradshaw, S.M., Sacks, N., 2014. Discrete element simulation of tribological interactions in rock cutting. *Int. J. Rock Mech. Min. Sci.* 65, 8–19. <https://doi.org/10.1016/j.ijrmms.2013.10.003>
- Verlet, L., 1967. Computer “experiments” on classical fluids. I. Thermodynamical properties of Lennard-Jones molecules. *Phys. Rev.* 159, 98–103. <https://doi.org/10.1103/PhysRev.159.98>
- Vogt, D., 2016. A review of rock cutting for underground mining: past, present, and future. *J. South. African Inst. Min. Metall.* 116, 1011–1026. <https://doi.org/10.17159/2411-9717/2016/v116n11a3>
- Walker, P.C., Maerz, N., Highers, G.M., 2005. Surface Reconstruction Using Shadow Profilometry, in: *ACM Symposium on Applied Computing*. ACM Press, New York, NY, Santa Fe, New Mexico, p. 2.
- Wang, C., Zhang, C., Zhao, X., 2018. Application of Similitude Rules in Calibrating Microparameters of Particle Mechanics Models. *KSCE J. Civ. Eng.* 22, 3791–3801. <https://doi.org/10.1007/s12205-018-1960-z>
- Willis, D., 2014. Main beam TBM makes great time in Mumbai [WWW Document]. URL <https://www.tunneltalk.com/Mumbai-India-25Feb14-Robbins-main-beam-TBM-makes-great-time-in-Mumbai.php> (accessed 11.21.20).

- Wu, S., Xu, X., 2016. A Study of Three Intrinsic Problems of the Classic Discrete Element Method Using Flat-Joint Model. *Rock Mech. Rock Eng.* 49, 1813–1830. <https://doi.org/10.1007/s00603-015-0890-z>
- Xia, Y., Shi, Y., Lin, L., Zhang, Y., Tan, Q., Yang, Y., 2018. Experimental evaluation of fragments from TBM disc cutting under different load cases. *Period. Polytech. Civ. Eng.* 62, 746–756. <https://doi.org/10.3311/PPci.11961>
- XU, S., GRASSO, P., MAHTAB, A., 1990. Use of Schmidt hammer for estimating mechanical properties of weak rock, in: *International Congress International Association of Engineering Geology*. 6. pp. 511–519.
- Xu, X., Wu, S., Gao, Y., Xu, M., 2016. Effects of Micro-structure and Micro-parameters on Brazilian Tensile Strength Using Flat-Joint Model. *Rock Mech. Rock Eng.* 49, 3575–3595. <https://doi.org/10.1007/s00603-016-1021-1>
- Yilmaz, I., Sendir, H., 2002. Correlation of Schmidt hardness with unconfined compressive strength and Young's modulus in gypsum from Sivas (Turkey). *Eng. Geol.* 66, 211–219. [https://doi.org/10.1016/S0013-7952\(02\)00041-8](https://doi.org/10.1016/S0013-7952(02)00041-8)
- Zhang, Z.X., Kou, S.Q., Lindqvist, P.A., 2003. In-situ measurements of cutter forces on boring machine at Äspö Hard Rock Laboratory. Part II. Characteristics of cutter forces and examination of cracks generated. *Rock Mech. Rock Eng.* 36, 63–83. <https://doi.org/10.1007/s00603-002-0037-x>
- Zhao, D., Liu, J.Q., Guo, W., 2012. The Simulation of Cutter-Rock Interaction in PFC. *Appl. Mech. Mater.* 170–173, 3385–3389. <https://doi.org/10.4028/www.scientific.net/AMM.170-173.3385>

VITA

Prosper Evaristus Akansah Ayawah was born in Tarkwa, in the Western Region of Ghana, West Africa. In July 2012, he obtained his undergraduate degree in Geological Engineering from the University of Mines and Technology, Tarkwa, Ghana. Upon completion, Prosper was adjudged the best graduating Geological Engineering student and given the G. O. Kesse Award in 2012. Prosper went on to pursue a master's degree in Petroleum Engineering at the African University of Science and Technology, Abuja, Nigeria under the Nelson Mandela scholarship scheme. He was awarded the Master of Science in Petroleum Engineering in December 2014. After graduation, Prosper worked for a geological exploration company in Ghana—MENART Geoventures—as a field geologist. He also worked as a research associate for the West African Institute of Mining, Metallurgy, and Petroleum (WAIMM).

In August 2017, Prosper was admitted into the Missouri University of Science and Technology, Rolla, Missouri (Missouri S&T) to pursue a Ph.D. in Geological Engineering. While at Missouri S&T, he took courses from the Information Science and Technology department and obtained a graduate certificate in Artificial Intelligence, Machine Learning, and Automation in Business in December 2020. Prosper worked as a graduate teaching assistant for all his time in Missouri S&T; instructing Introduction to Geology labs, Geomorphology and Terrain Analysis Labs, and Rock Engineering. He received his Ph.D. in Geological Engineering from Missouri S&T in May 2021.